Discontinuous Galerkin Methods for the Approximation of the Liouville-von Neumann Equation

von der

Fakultät für Elektrotechnik und Informationstechnik
der
Technischen Universität Dortmund

genehmigte

DISSERTATION

zur Erlangung des akademischen Grades
Doktor der Ingenieurwissenschaften (Dr.-Ing.)

vorgelegt von

Valmir Ganiu, M.Sc.

Referent: apl. Prof. Dr.-Ing. Dirk Schulz, Technische Universität Dortmund
Korreferent: Prof. Ming-Cheng Cheng, Ph.D., Clarkson University, USA

Tag der mündlichen Prüfung: 16.06.2026

Valmir Ganiu, M. Sc.
Discontinuous Galerkin Methods for the Approximation of the Liouville-von Neumann Equation

Genehmigte Dissertation zur Erlangung des akademischen Grades Doktor der Ingenieurwissenschaften (Dr.-Ing) der Fakultät Elektrotechnik und Informationstechnik der Technischen Universität Dortmund

Prüfungskommission:
Prof. Dr.-Ing. Martin Pfost, Technischen Universität Dortmund (Vorsitz)
apl. Prof. Dr.-Ing. Dirk Schulz, Technische Universität Dortmund
Prof. Ming-Cheng Cheng, Ph.D., Clarkson University, USA
Prof. Dr.-Ing. Stephan Frei, Technischen Universität Dortmund

Ort und Tag der mündlichen Prüfung: Dortmund, 16.06.2026

In the Name of God,
the Most Gracious, the Most Merciful.

Abstract

The rapid miniaturization of electronic devices has brought quantum mechanical effects to the forefront of semiconductor design, demanding accurate and efficient modeling frameworks for charge transport at the nanoscale. Conventional approaches such as the Non-Equilibrium Green's Function (NEGF) and the Quantum Transmitting Boundary Method (QTBM) deliver high accuracy but are computationally expensive, particularly for transient and multidimensional simulations. This dissertation develops and validates a novel framework based on the Discontinuous Galerkin (DG) method for the approximation of the Liouville-von Neumann equation (LVNE), establishing it as a competitive alternative to classical numerical schemes.
The work begins with a brief introduction into common quantum effects and phenomena that are relevant for the scope of this work. Furthermore, intraband and interband dynamics as well as systems with spatially varying effective mass are discussed and their descriptive quantum transport equations presented. Physically consistent boundary conditions are derived through inflow models based on Fermi-Dirac statistics and a Complex Absorbing Potential (CAP) for open-system truncation. Next, common approximation methods are presented and the DG scheme is analysed concerning its existence, uniqueness, stability, and the underlying numerical fluxes in detail. Three variants – Discontinuous Galerkin-Finite Volume (DGFV), Discontinuous Galerkin-Finite Element method (DGFEM), and Discontinuous Galerkin-Discontinuous Galerkin (DGDG) – are introduced, for the discretization of both spatial coordinates. Time discretization is performed with explicit Runge-Kutta schemes, and self-consistency with the Poisson equation is achieved via the Gummel algorithm. The Mode Space Approximation (MSA) is further integrated to extend the method toward two-dimensional simulations.
Comprehensive validation is conducted across canonical quantum devices. For Resonant Tunneling Diode (RTD)s, the DG method reproduces stationary and transient characteristics with good agreement to the reference results, including switching dynamics under non-equilibrium conditions. Intraband transport in Tunnel Field Effect Transistor (TFET)s and interband transport in Resonant Interband Tunneling Diode (RITD)s indicate physically plausible density matrix evolution and current-voltage characteristics. Finally, two-dimensional transport in Dual-Gate Field Effect Transistor (DGFET)s is simulated, showing close agreement with NEGF benchmark results while achieving significantly reduced runtimes.
High-Performance Computing (HPC) aspects are systematically investigated. Runtime analyses reveal that DG methods showed favorable runtime characteristics compared to the considered Finite Volume (FV) implementations, particularly when explicit time integration is leveraged. Resource management strategies show that functional programming drastically reduces memory usage, enabling parallelism at the cost of runtime, while slope limiter techniques enhance accuracy and accelerate convergence in self-consistent simulations. Overall, the DGDG achieved the best runtimeaccuracy trade-off among the investigated schemes under equal-error conditions.

Kurzfassung

Die rapide Miniaturisierung elektronischer Bauelemente hat quantenmechanische Effekte in den Vordergrund des Halbleiterentwurfs gerückt und erfordert präzise sowie effiziente Modellierungsrahmen für den Ladungstransport im Nanobereich. Konventionelle Ansätze wie die Non-Equilibrium Green's Function (NEGF) und die Quantum Transmitting Boundary Method (QTBM) liefern zwar eine hohe Genauigkeit, sind jedoch besonders für transiente und multidimensionale Simulationen rechenintensiv. Diese Dissertation entwickelt und validiert ein neuartiges Rahmenwerk basierend auf der Discontinuous Galerkin (DG)-Methode zur Approximation der Liouville-von Neumann equation (LVNE) und etabliert diese als wettbewerbsfähige Alternative zu klassischen numerischen Verfahren.
Die Arbeit beginnt mit einer kurzen Einführung in gängige Quanteneffekte und -phänomene, die für den Umfang dieser Arbeit relevant sind. Darüber hinaus werden intraband- und interbanddynamische Prozesse sowie Systeme mit räumlich variierender effektiver Masse diskutiert und deren beschreibende Quantentransportgleichungen vorgestellt. Physikalisch konsistente Randbedingungen werden durch Inflow-Modelle auf Basis der Fermi-Dirac-Statistik und ein Complex Absorbing Potential (CAP) zur Abgrenzung offener Systeme hergeleitet. Daraufhin werden gängige Approximationsmethoden vorgestellt und das DG-Schema im Hinblick auf Existenz, Eindeutigkeit, Stabilität sowie die zugrunde liegenden numerischen Flüsse detailliert analysiert. Drei Varianten – Discontinuous Galerkin-Finite Volume (DGFV), Discontinuous Galerkin-Finite Element method (DGFEM) und Discontinuous Galerkin-Discontinuous Galerkin (DGDG) – werden eingeführt, um beide Raumkoordinaten zu diskretisieren. Die Zeitdiskretisierung erfolgt mittels expliziter Runge-Kutta-Schemata, und die Selbstkonsistenz mit der Poisson-Gleichung wird durch den Gummel-Algorithmus erreicht. Zudem wird die Mode Space Approximation (MSA) integriert, um die Methode auf zweidimensionale Simulationen zu erweitern.
Eine umfassende Validierung wird an kanonischen Quantenbauelementen durchgeführt. Für eine Resonant Tunneling Diode (RTD) reproduziert die DG-Methode stationäre und transiente Charakteristika mit hoher Genauigkeit, einschlieSSlich Schaltverhalten unter Nichtgleichgewichtsbedingungen. Intrabandtransport in einem Tunnel Field Effect Transistor (TFET) und Interbandtransport in einer Resonant Interband Tunneling Diode (RITD) bestätigen die physikalische Korrektheit der Dichtematrizen sowie des Strom-Spannungs-Verhaltens. Letztlich wird der zweidimensionale Transport in einem Dual-Gate Field Effect Transistor (DGFET) simuliert, wobei eine exzellente Übereinstimmung mit Non-Equilibrium Green's Function (NEGF)-Referenzen erzielt wird – bei gleichzeitig deutlich reduzierten Laufzeiten.
High-Performance Computing (HPC)-Aspekte werden systematisch untersucht. Laufzeitanalysen zeigen, dass DG-Methoden Standard-Finite-Volumen-Schemata konsistent übertreffen, insbesondere bei Nutzung expliziter Zeitintegration. Ressourcenmanagement-Strategien verdeutlichen, dass funktionale Programmierung den Speicherverbrauch drastisch reduziert und Parallelisierung ermöglicht, allerdings auf Kosten der Laufzeit, während Slope-Limiter-Techniken die Genauigkeit erhöhen und die Konvergenz in selbstkonsistenten Simulationen beschleunigen. Insgesamt erweist sich die Variante DGDG als das effizienteste Schema unter gleichen Fehlertoleranzen.

Acknowledgements

This dissertation was carried out at TU Dortmund University under the supervision of apl. Prof. Dr.-Ing. Dirk Schulz, to whom I owe my deepest gratitude. His continuous guidance, constructive criticism, and willingness to provide support even beyond regular working hours or even vacation have been invaluable for the successful completion of this work.

Equally, I would like to express my sincere gratitude to Prof. Ming-Cheng Cheng from Clarkson University, who kindly agreed to serve as the second examiner of this dissertation after only a brief correspondence.

I am sincerely grateful to my parents, whose decision to come to Germany in 2001 laid the foundation for all academic opportunities that followed. Without their courage and sacrifices, the present dissertation would not exist.

Special thanks go to my darling, who provided encouragement and stability, particularly during the more challenging phases of this project.

I also wish to express my gratitude to my long-time friend Wladimir Plotnikov, who established the initial contact with Prof. Schulz and thus opened the door to my doctoral studies. His support has played a decisive role in enabling me to pursue this academic path.

Furthermore, I am indebted to my studious colleagues and fellow doctoral candidates at the Chair of Communication Technique. The collaborative working atmosphere, as well as numerous discussions during seminars and conferences, have greatly enriched both the professional and personal dimensions of my doctoral journey.

Finally, I would like to thank all readers of this dissertation. It is my hope that the ideas and methods presented here will contribute, in some measure, to the further development of quantum transport modeling.

Contents

1. Introduction

The simulation of quantum transport requires solving governing differential equations whose complexity strongly varies depending on the device at hand and the quantum effects to be considered. The governing equations are therefore approximated utilizing numerical methods. The most commonly used equations in this context are the Schrödinger equation (SE) [1], the Wigner transport equation (WTE) [2], which describes quantum transport in phase space, and the Liouville-von Neumann equation (LVNE) [3], which serves as its counterpart in real space. Analytical solutions to these transport equations are generally feasible under specific assumptions that simplify the governing equations. However, if one wishes to simulate devices under realistic operation conditions numerical approximations and the application of numerical methods become indispensable.
Typically, methods such as the Quantum Transmitting Boundary Method (QTBM) [4, 5], Monte Carlo-based integration techniques [6, 7], and the Non-Equilibrium Green's Function (NEGF) formalism [8, 9] are employed, mainly due to their high accuracy [4]. However, this high level of accuracy comes at the cost of substantial computational effort and long runtimes [7, 9, 10]. Therefore, transient simulations using QTBM or NEGF are possible, yet computationally inefficient [11, 12].
This has led to a demand for more efficient numerical methods that still provide sufficient accuracy to compete with the aforementioned benchmark techniques. Promising candidates have emerged in the form of Finite Difference (FD) methods [2, 13] and Finite Volume (FV) algorithms [3]. However, Finite Difference (FD) methods, which were implemented as an Upwinding Difference Scheme (UDS) in [2, 13, 14], already exhibited major drawbacks. When UDS is applied, the wave is split into forward- and backward-propagating components under the assumption of a vanishing Wigner potential [2, 13]. Once a potential is included, this leads to inherent simulation errors, as demonstrated mathematically in [15]. Therefore, UDS can be interpreted as an operator-splitting scheme with respect to the diffusion operator. As a result, UDS is associated with poor convergence behavior and non-physical results [16, 17].
Other research has also found that FD and FV methods tend to yield higher errors compared to continuous Finite Elemente methods (FEM) [18, 19]. Although FEM generally offers lower approximation error, it comes with significantly higher computational costs [20]. This is due to the coupling of finite elements via shared nodes, which introduces overlapping submatrices in the global matrix assembly. The resulting stair-step structure of the global matrices complicates matrix inversion and prevents efficient parallelization during computation.
Within the FEM family, an alternative method exists: the Discontinuous Galerkin (DG) method, originally introduced by Hill and Reed in 1973 [21]. Unlike traditional FEMs, the DG scheme uses elements that do not share nodes with their neighbors. Instead, each element has its own local degrees of freedom, resulting in local overlapping nodes but not global coupling of the individual elements. This has the decisive advantage that the global system matrix becomes block-diagonal, allowing for efficient inversion via independent inversion of element blocks. Furthermore, this structure enables straightforward parallelization across multiple CPU cores.

However, since the elements are decoupled, a mechanism is required to establish physical coupling between them. This is achieved by introducing a numerical flux, which governs the information transfer across element interfaces. This flux must be carefully constructed to ensure the physical consistency of the scheme. It also introduces two major challenges:

1. The accurate construction of the numerical flux requires a precise formulation of the Riemann problem [22].
2. An improperly formulated flux can lead to numerical instability, especially in the transient regime or in steady-state convergence [GS1], [23].

The DG method has already demonstrated significant advantages in Computational Fluid Dynamics (CFD), yielding more accurate results and reduced runtimes, as shown in the comprehensive work by Cockburn et al. [22]. This motivates its application in the field of quantum transport, with the hope of achieving similar runtime improvements.
The aim of this work is therefore to develop a DG method capable of solving quantum transport equations, such as those introduced above, with both high accuracy and computational efficiency. A strong emphasis is placed on the proper treatment of quantum effects.
Because the DG method is fundamentally based on matrix-vector multiplication, it is particularly well-suited for time-dependent simulations. Additionally, unlike conventional FEM, which is based on the continuous Galerkin method [24], the DG technique supports parallel computing due to its block-diagonal matrix structure, which allows partitioning the system matrix into smaller subproblems for parallel execution.
Another challenge in quantum transport modeling lies in the accurate treatment of boundary conditions in both real and phase space. The LVNE formally requires an unbounded domain in the relative coordinate direction to allow wave propagation toward infinity. In practice, however, this is non-trivial in numerical simulations, as the computational domain must be truncated. Simply terminating the domain results in serious issues:
Applying the Wigner-Weyl transformation [25] to the LVNE introduces a surface term. Neglecting this term is equivalent to imposing homogeneous Dirichlet boundary conditions, which physically corresponds to perfectly reflecting boundaries. As a result, waves propagating in the relative direction are reflected, interfering with other components of the statistical density matrix and ultimately leading to non-physical artifacts.
Several strategies have been proposed to address this issue. Boundary conditions may be defined as open [13], closed [26], or periodic [27]. While closed and periodic boundaries are suitable for applications in density functional theory of crystalline solids – due to their preservation of translational symmetry – they are less appropriate for quantum transport simulations. Open boundary conditions, on the other hand, allow separate modeling of the contacts and the device region, making them preferable for the problem considered here [26].
To implement open boundaries a CAP formalism is applied, which has been already successfully implemented in a previous work [28]. The goal is to integrate the CAP into the DG algorithm and analyze its influence on the results. An additional challenge is the accurate modeling of quantum effects such as tunneling, especially in layered device structures with varying potential levels. The numerical efficiency of the DG method makes it feasible to use higher-order integration schemes, such as Gauss-Lobatto quadrature [29], thereby improving accuracy.
Furthermore, scattering mechanisms must be considered for realistic simulations [30]. Particles in nanodevices can interact with lattice vibrations, defects, interfaces, or quasiparticles such as phonons, which can distort particle trajectories. These effects influence device performance by

increasing resistance and heat generation [31, 32]. While ballistic or quasi-ballistic models may suffice for small devices, their accuracy degrades with increasing size and temperature.
A comprehensive paper at the Chair for Communications Technique has demonstrated the conceptual feasibility of incorporating scattering into a DG framework [33]. However, since the goal of this work is to develop a DG concept first and foremost, scattering will be neglected.
In addition, a realistic quantum transport model must consider both intraband and interband transport. While intraband transport describes particle behavior within a single band, interband transport accounts for transitions between bands. Capturing these effects numerically requires an appropriate second-order numerical flux, especially since the diffusion operator contains a second derivative, making the Riemann problem more challenging.
As technological demands continue to grow, increasingly complex simulation models become necessary. These models must not only be accurate but also computationally efficient. As shall be shown, the DG method offers great potential in this regard.

This dissertation is structured into seven chapters.
Chapter 2 introduces the governing transport equations together with the relevant quantum effects. Building on this foundation, Chapter 3 presents the approximation models that underlie the simulations, with emphasis on the density matrix formalism, intraband and interband transport, and a spatially varying effective mass. The formulation of physically meaningful boundary conditions is the subject of Chapter 4. Attention then shifts in Chapter 5, which will lay out the mathematical foundation of the DG scheme analyzing its coercivity, stability, and uniqueness. Additionally, the models presented in Chapter 3 will be discretized in detail. Practical aspects are addressed in Chapter 6, which presents application-oriented examples such as simulations of an RTD, a TFET, a DGFET, and an RITD under various operational conditions. This chapter also serves to validate the proposed method. The dissertation concludes in Chapter 7 with a summary of the main results and an outlook on future developments.

2. Fundamentals of Quantum Theory

This chapter presents the theoretical foundations essential for the later derivation of the DG method and, in particular, for the introduction of the models to be approximated. To keep the scope of this work within reasonable limits, quantum theory will be discussed only to the necessary extent. Fundamental topics such as the electronic structure of crystals, band structure theory, and Bloch states can be found in standard textbooks [34, 35, 36].
Instead, this chapter focuses on the relevant quantum transport mechanisms, such as ballistic transport, and on quantum mechanical superposition. These topics are the focus of Section 2.1. An overview of transport equations is given in Section 2.2. The goal of this chapter is, furthermore, to arrive at the LVNE, starting from a formulation in the Schrödinger picture. Since the simulation of semiconductor devices represents a many-body problem, the many-body SE is introduced. Section 2.2.1 will present the transition from the many-body SE to the single-particle formulation [34, 36].
Subsequently, Section 2.2.2 derives a real-space formulation known as the LVNE or von Neumann equation [37, 38]. Lastly, Section 2.3 introduces the Poisson equation, which is necessary to ensure self-consistency.
Finally, in Section 2.2.3, following a Wigner-Weyl transformation [39, 40] into the phase space, the WTE is introduced [41].

2.1. Quantum Effects

Quantum effects is a broad term referring to mechanisms and phenomena in a system that cannot be explained by classical mechanics [42]. In systems where particles such as photons, phonons, or electrons dominate the dynamics, a variety of quantum effects may occur, including:

- *Wave-particle duality*: Particles can exhibit both particle-like and wave-like behavior [42].
- *Superposition*: A particle can exist in more than one state at the same time. Only upon measurement a definite state is assigned to the particle [43].
- *Quantum entanglement*: Multiple particles can be entangled with each other. Regardless of the distance between them, the particles interact instantaneously. This results in non-local effects that cannot be described by classical mechanics [44].
- *Quantum tunneling*: When an electron encounters a potential barrier that exceeds its energy, there remains a nonzero probability that the electron can still tunnel through the barrier [45].
- *Quantum coherence and decoherence*: Quantum coherence refers to the state in which quantum objects, such as electrons, remain in a superposition, allowing their wave functions

to interfere undisturbed. This enables quantum interference, where particle waves overlap and form interference patterns – either constructive or destructive [42]. When the system interacts with its environment and loses coherence, this is referred to as decoherence. As a result, quantum interference effects vanish, and the system begins to behave classically [46].

In addition, there are two further phenomena that are of particular importance for the scope of this work. These will be examined in more detail in the following.
Ballistic transport refers to the unhindered movement of an electron through a medium. During this process, interactions with other particles are negligible. One of many factors for causing scattering are length scales that are significantly larger than the device dimensions. This regime becomes increasingly relevant in nanoscale devices, where the physical dimensions are smaller than the mean free path of the electrons. Consequently, the resistance arises solely from the contacts, not from the material itself [31].
In an idealized ballistic regime, the scattering may in some cases be neglected, as no collective interactions are taken into account [45]. From a modeling perspective, the ballistic regime represents the simplest form of quantum transport since it disregards interaction terms altogether – though this idealization often does not hold in practice. In large scaled systems, where strong correlation effects are present and at least weak interactions must be considered, the scattering must therefore be taken into account and approximated [46].
Next, quantum mechanical superposition describes the non-uniqueness – or ambiguity – of a quantum system. That is, a quantum system can exist in multiple states simultaneously until, from the perspective of an observer, it assumes a single, definite state. Three attributes can be identified [42]:

1. *Wavefunction*: A quantum particle, such as an electron, is described by a wave function. This wave function is a mathematical representation of all possible states the particle may occupy. Closely related to the wave function is the density matrix, which additionally takes into account correlation effects. More on this later.

2. *Superposition states*: In a superposition state, the system does not occupy a definite classical state. Instead, it is described by a wave function that is a linear combination of several possible states (e.g., position eigenstates or energy levels). According to Borns probabilistic interpretation, the squared amplitude of the wave function is proportional to the probability of detecting an electron at a particular location [47].

3. *Measurement and collapse*: Once a measurement is performed, the system chooses one of the possible states, and the superposition ceases. This phenomenon is commonly referred to as the collapse of the wave function.

The possibility of quantum tunneling arises from the description of electrons in terms of wave functions. When the wave function of an electron encounters a potential barrier, $|\psi(x)|^2$ remains nonzero inside the classically forbidden region [42]. This implies a finite probability of detecting the electron beyond the barrier, even if its energy is lower than the barrier height. The tunneling probability depends on both the width and the height of the barrier [45, 46, 48].

Now that the most important quantum effects have been introduced, the following section will describe and categorize the equations governing quantum transport.

2.2. Overview of Common Transport Models

The description of quantum transport in solids is, in its essence, a many-body problem [45], since the state $|\Psi\rangle$ of a single particle typically cannot be considered independently of its immediate neighbors. Direct interactions with surrounding nuclei, as well as collective effects of electrons play a fundamental role. These include for the Hartree potential:

- *Electron-electron interaction*: Due to their electric charge, electrons in the crystal lattice of a solid repel each other. This interaction is often referred to as the Coulomb interaction. The resulting correlation effects influence the motion of the particles in such a way that the state of one electron cannot be described independently [36].
- *Electron-ion interaction*: Electrons move within the electrostatic potential generated by the positively charged atomic ions. This interaction essentially determines the structure of the periodic potential in the crystal and forms the foundation for the formation of energy band structures [36].
- *Ion-ion interaction*: Electrostatic repulsion also exists between the positively charged ion cores. The equilibrium between this repulsion and the electron-ion attraction determines the lattice structure of the solid [36].

For the perturbation these are:

- *Electron-phonon interaction*: Phonons are lattice vibrations, e.g., induced by thermal fluctuations, that disturb the motion of electrons. These interactions can lead to inelastic scattering events in which energy is exchanged, thereby impairing the electrical conductivity [46].
- *Impurity and defect scattering*: Depending on the purity of the material, the lattice may contain impurities or structural irregularities. Electrons may scatter at these imperfections, and it becomes relevant how multiple electrons behave in the vicinity of such defects [36].
- *Collective effects*: Electrons may also interact with plasmons – density oscillations of free electrons propagating along surfaces – or form superconducting states, where electrons pair up into so-called Cooper pairs. These phenomena can only be described through a collective treatment of many-particle systems [45].
- *Exchange and correlation effects*: Beyond classical Coulomb interaction, the Pauli exclusion principle and spin dependencies introduce additional quantum mechanical correlations. These exchange interactions are particularly significant in systems with strong electronic or magnetic coupling [42].

The common separation of electronic and ionic motion is based on the *Born-Oppenheimer approximation*, which exploits the fact that electrons move much faster than the heavier ions. This approximation is also a practical simplification that reduces the computational complexity of modeling many-body systems [49]. All the interactions mentioned above explicitly enter the Hamiltonian operator $\hat{H}$, which governs the total energy and dynamics of the system.

The following section introduces several approximations that allow the transition from the many-body SE to the single-particle SE.

2.2.1. Schrödinger Equation

The SE forms the foundation of the equations of motion in quantum mechanics. It describes the time evolution of a quantum state $|\Psi\rangle$ and is defined as

$$\imath\hbar\frac{\partial}{\partial t}|\Psi(t)\rangle = \mathcal{H}^{\mathrm{MB}}|\Psi(t)\rangle\,. \tag{2.1}$$

Here, $\hbar$ denotes the reduced Planck constant, $\Psi(t)$ is the time-dependent state vector, and $\mathcal{H}^{\mathrm{MB}}$ refers to the non-relativistic many-body Hamiltonian, which consists of both interacting and non-interacting terms. Eq. (2.1), therefore, represents the many-body SE.
To express the wave vector $|\Psi\rangle$ in the space domain, a wave function is introduced:

$$\langle \mathbf{r}_1,\ldots,\mathbf{r}_n,\mathbf{R}_1,\ldots,\mathbf{R}_N|\Psi\rangle = \Psi(\mathbf{r}_1,\ldots,\mathbf{r}_n,\mathbf{R}_1,\ldots,\mathbf{R}_N). \tag{2.2}$$

Here, $\mathbf{r}_j{\in}j = 1...n$ are the spatial coordinates of the n electrons, and $\mathbf{R}_k{\in}k = 1...N$ represent the positions of the N ions within the system. The potential is assumed to be ideally periodic, i.e., $V(\mathbf{r}) = V(\mathbf{r}+\mathbf{R})$.
To arrive at the single-particle SE, the Born-Oppenheimer approximation is introduced as a first step. This approximation states that, due to the significantly larger mass of atomic nuclei compared to electrons (by a factor of approximately 10^3), their motion can be considered marginally varying and, hence, decoupled from the electron movement. As a result, the SE can be separated into two equations [34]:

- one equation describing the motion of electrons for a fixed nuclear position,
- and one equation describing the motion of the nuclei itself.

Based on this, the Hamiltonian $\mathcal{H}^{MB}$ can be decomposed into two partial Hamiltonians:

$$\mathcal{H}^{MB} = \mathcal{H}_0 + \mathcal{H}_{\mathrm{ion},0}. \tag{2.3}$$

Here, $\mathcal{H}_0$ describes the motion of electrons within the fixed ion lattice, while $\mathcal{H}_{\mathrm{ion},0}$ accounts for the non-interacting components of the ions. This perspective enables a systematic analysis of the ionic influence on the electronic behavior. Since the Born-Oppenheimer approximation treats the ions as marginally varying, the Hamiltonian $\mathcal{H}_{\mathrm{ion},0}$ will not be further considered. Instead, the focus is placed on the operator $\mathcal{H}_0$, which is expanded as follows:

$$\mathcal{H}_0 = \mathcal{H}_{\mathrm{el},0} + \mathcal{H}_{\mathrm{el,el}} + \mathcal{H}_{\mathrm{ion,ion}} + \mathcal{H}_{\mathrm{el,ion}}. \tag{2.4}$$

In this expression, the Hamiltonians represent – in order – the non-interacting part of the electrons, electron-electron interaction, ion-ion interaction, and electron-ion interaction. As seen in Eq. (2.4), the system is still a many-body system. Therefore, an additional assumption is required to reduce this to a description based on the single-particle SE.

Through *mean-field theory*, complex many-body systems can be simplified by assuming that particles interact with an average field generated by the collective influence of all other particles. This leads to a significant reduction in complexity: rather than explicitly accounting for all pairwise interactions, their effect is replaced by an average field, effectively transforming the many-body equation into a system of coupled single-particle equations. One well-known

and relevant example for this is the *Hartree-Fock approximation* [46].
In the Hartree formalism, the many-body wave function is approximated as a product of single-particle wave functions (spin orbitals), which are antisymmetrized according to the *Pauli exclusion principle*. This approximation leads to the so-called Slater determinant, which consists of single-particle wave functions [34]. Based on this determinant, the total energy functional is defined as $E\{\Psi\} = \langle\Psi|\mathcal{H}^{HF}|\Psi\rangle \,/\, \langle\Psi|\Psi\rangle$. Assuming orthogonality of the single-particle functions Φ_j, and performing a variation with respect to the complex conjugate Φ_j^*, one arrives at the Hartree-Fock equation as derived in [34]:

$$E_j\mathbf{\Phi}_j(\mathbf{r}) = \left[-\frac{\hbar^2}{2m_0}\boldsymbol{\nabla}_{\mathbf{r}}^2 + V(\mathbf{r}) + \frac{q^2}{4\pi\epsilon_0}\sum\nolimits_{k\neq j}\int d\mathbf{r}'\frac{|\mathbf{\Phi}_k(\mathbf{r}')|^2}{|\mathbf{r}-\mathbf{r}'|} - \frac{q^2}{4\pi\epsilon_0}\sum\nolimits_{k\neq j}\int d\mathbf{r}'\frac{\mathbf{\Phi}_k^*(\mathbf{r}')\mathbf{\Phi}_j^*(\mathbf{r}')}{|\mathbf{r}-\mathbf{r}'|}\right]\mathbf{\Phi}_j(\mathbf{r}). \tag{2.5}$$

In Eq. (2.5), the first interaction term represents the Hartree term, while the second is referred to as the Fock term. If the non-local Fock contribution is neglected, one obtains the Hartree approximation, which is particularly relevant in the context of this work. For a conceptual understanding, the Hartree term represents the electric potential experienced by an electron due to the spatial distribution of the electron density. It accounts for the mean-field repulsion between electrons and thereby influences the energetic states of the system [42].
Due to the periodicity of the crystal lattice under consideration, the potential exhibits translational invariance, such that $V(\boldsymbol{r}+\boldsymbol{R}) = V(\boldsymbol{r})$, where $\boldsymbol{R}$ is a lattice vector. This invariance is inherited by the Hamiltonian, yielding $\mathcal{H}(\boldsymbol{r}+\boldsymbol{R}) = \mathcal{H}(\boldsymbol{r})$. As a consequence, the solutions to the Schrödinger equation take the form [34]:

$$\Psi_{\boldsymbol{k}}(\boldsymbol{r}) = e^{\imath\boldsymbol{k}\cdot\boldsymbol{r}}\cdot u_{\boldsymbol{k}}(\boldsymbol{r}), \tag{2.6}$$

which are known as Bloch waves. Here, $e^{\imath\boldsymbol{k}\cdot\boldsymbol{r}}$ is a plane wave characterized by the wave vector $\boldsymbol{k}$, and $u_{\boldsymbol{k}}(\boldsymbol{r})$ is the Bloch function [50, 51] with the periodicity of the crystal lattice, i.e., $u_{\boldsymbol{k}}(\boldsymbol{r}) = u_{\boldsymbol{k}}(\boldsymbol{r}+\boldsymbol{R})$ [46]. Since an energy eigenvalue exists for each wave vector $\boldsymbol{k}$, the electronic states form so-called energy bands in the solid. This explains why materials may behave as conductors, semiconductors, or insulators, depending on their band occupation [36]. The following material classes can be distinguished [52]:

1. **Insulators**: Large energy gap between valence and conduction bands; at room temperature, the conduction band is completely devoid of charge carriers. The valence band is filled with electrons, leaving no room for movement and, therefore, no conductivity.

2. **Semiconductors**: Smaller bandgap; at room temperature, electrons can be thermally excited into the conduction band, resulting in both electrons and holes acting as charge carriers.

3. **Metals**: Overlap between valence and conduction bands, and a partially filled conduction band, leading to high electrical conductivity.

By exploiting the periodicity of the lattice, the behavior of electrons together with the atomic nuclei can be described with an effective potential. This simplification significantly reduces the computational effort required to solve the Schrödinger equation for solids [52].
To approximate the band structure in the vicinity of a specific $\boldsymbol{k}$-point, especially near the band edges, the kp-formalism is commonly employed. In this approach, the Hamiltonian in $\boldsymbol{k}$-space is expanded as a perturbation around a reference point, allowing for the systematic determination

of effective masses and band curvatures [51, 53]. There are two main expansion schemes: the Kohn-Luttinger method [54] and the Kane approach [53]. The former has the advantage that band coupling mechanisms depend on the gradient of the external potential rather than on the gradient of the wave function [55, 56].
According to Blochs theorem, the electronic states in a periodic crystal can be expressed as Bloch functions characterized by wave vectors $\boldsymbol{k}$, which are typically mapped to the first Brillouin zone, since $\boldsymbol{k}$-vectors differing by a reciprocal lattice vector describe the same physical state [34]. Electrons excited by an external field behave like particles with an effective mass that depends on the curvature of the energy bands. This allows for the application of the *effective mass approximation*, as outlined in [53]. The Hartree equation is treated as an eigenvalue problem without external potential and is assumed to be known according to

$$E_\lambda(\boldsymbol{k})\boldsymbol{\Psi}_{\lambda,\boldsymbol{k}}(\boldsymbol{r}) = \Big[-\frac{\hbar^2}{2m_0}\boldsymbol{\nabla}^2 + V(\boldsymbol{r})\Big]\boldsymbol{\Psi}_{\lambda,\boldsymbol{k}}(\boldsymbol{r}) = \mathcal{H}_0\boldsymbol{\Psi}_{\lambda,\boldsymbol{k}}(\boldsymbol{r}), \tag{2.7}$$

where the eigenvalues $E_\lambda(\boldsymbol{k})$ describe the band structure of band λ and $\lambda^{'}$ for the wave vector $\boldsymbol{k}$. Deploying a lengthy transformation, which can be found in [57], the transformed equation results in

$$\begin{aligned}\Big(E_\lambda(0) + \frac{\hbar^2\boldsymbol{k}^2}{2m_0} + \sum\nolimits_{\alpha,\beta,\lambda'\neq\lambda}\frac{\hbar^2}{m_0^2}k_\alpha k_\beta\frac{p_{\lambda',\lambda,\alpha}p_{\lambda,\lambda',\beta}}{E_\lambda(0)-E_{\lambda'}(0)}\Big)B_\lambda(\boldsymbol{k}) + \int d\boldsymbol{k}^{'}\tilde{U}(\boldsymbol{k}-\boldsymbol{k}^{'})B_\lambda(\boldsymbol{k}^{'}) + \\ \sum\nolimits_{\lambda'\neq\lambda}\frac{\hbar}{m_0}\frac{\boldsymbol{p}_{\lambda,\lambda'}}{E_\lambda(0)-E_{\lambda'}(0)}\int d\boldsymbol{k}^{'}(\boldsymbol{k}-\boldsymbol{k}^{'})\tilde{U}(\boldsymbol{k}-\boldsymbol{k}^{'})B_{\lambda'}(\boldsymbol{k}) = EB_\lambda(\boldsymbol{k}).\end{aligned} \tag{2.8}$$

$\boldsymbol{p}_{\lambda,\lambda'}$ is the momentum element. The indices α and β represent the spatial components ($k_x, p_{\lambda,\lambda',z}$*etc.*) of the corresponding vectors and λ is the respective band. $B_\lambda(\boldsymbol{k})$ is the envelope function amplitude in momentum space for band λ. ccordingly, A subsequent transformation is carried out to express the momentum matrix elements as second- or higher-order terms [57]. This leads to the transformed eigenvalue equation with the effective mass m_λ as an expansion coefficient [54, 55, 57]:

$$E_\lambda(\boldsymbol{k}) = E_\lambda(0) + \frac{\hbar^2\boldsymbol{k}^2}{2m_\lambda} = E_\lambda(0) + \frac{\hbar^2\boldsymbol{k}^2}{2m_0} + \sum\nolimits_{\alpha,\beta,\lambda'\neq\lambda}\frac{\hbar^2}{m_0^2}k_\alpha k_\beta\frac{p_{\lambda',\lambda,\alpha}p_{\lambda,\lambda',\beta}}{E_\lambda(0)-E_{\lambda'}(0)}, \tag{2.9}$$

which accounts for the influence of the crystal lattice on the particle.
Since the wave function $\Psi_{\boldsymbol{k}}(\boldsymbol{r})$ no longer includes the rapidly oscillating part of the Bloch amplitude, it is referred to as the envelope function. From this, the SE for the envelope function can be obtained via an inverse Fourier transformation, as shown in [55]:

$$\imath\hbar\frac{\partial}{\partial t}\Phi_\lambda(\boldsymbol{r},t) = \underbrace{\Big[E_n(-\imath\boldsymbol{\nabla}) + V(\boldsymbol{r})\Big]}_{\mathcal{H}_{\lambda,\lambda}}\Phi_\lambda(\boldsymbol{r},t) - \sum\nolimits_{\lambda'\neq\lambda}\underbrace{\imath\boldsymbol{\nabla}V(\boldsymbol{r})\frac{\hbar}{m_0}\frac{\boldsymbol{p}_{\lambda,\lambda'}}{E_\lambda(0)-E_\lambda^{'}(0)}}_{\mathcal{H}_{\lambda,\lambda'}}\Phi_{\lambda'}(\boldsymbol{r},t). \tag{2.10}$$

In general, λ denotes the respective energy band. The term labeled $\mathcal{H}_{\lambda,\lambda}$ in Eq. (2.10) describes intraband transport and can therefore be interpreted as the SE in the effective mass approximation. In addition, the term labeled $\mathcal{H}_{\lambda,\lambda'}$ captures band coupling mechanisms and is used to analyze interband transport [54]. In the context of quantum transport, intraband transport refers to the motion of electrons and holes within the conduction or valence band, respectively.

Interband transport, on the other hand, describes the dynamics of these particles with explicit consideration of coupling between the bands [55]. This will become important at a later point in the discussion.
Closely associated with the wave function is the *statistical density operator*. The wave function is limited in that it can only describe systems in a pure quantum state – that is, the system is represented by a single wave function. This is rarely the case, especially when analyzing quantum devices. These often exist in a mixed state, which must be described by eigenstates. The relationship between the two becomes clear when considering the following expression for the statistical density operator

$$\hat{\rho} = \sum_i w_i \left|\psi_i\right\rangle \left\langle\psi_i\right| \tag{2.11}$$

as shown in [57]. Eq. (2.11) represents a sum of dyadic products of individual wave functions – where $\langle\psi_i|$ is the complex conjugate – each state i weighted by a coefficient w_i. Accordingly, the weights must satisfy the normalization condition $\sum_i w_i = 1$.
This approach is referred to as the density matrix formalism and has the advantage of offering a more compact and versatile representation than state-vector-based methods. It also enables the description of mixed states [58].
If the statistical density operator $\hat{\rho}$ is expressed in an arbitrary basis, it is referred to as the statistical density matrix. For this, it is assumed that each wave function can be expanded in a common basis $|\Phi_n\rangle$, with different coefficients a_n^i, such that $|\Psi_i\rangle = \sum_n a_n^i |\Phi_n\rangle$. The statistical density operator then becomes:

$$\hat{\rho} = \sum_m \left|\Phi_m\right\rangle \left\langle\Phi_m\right|\hat{\rho}\sum_n\left|\Phi_n\right\rangle \left\langle\Psi_n\right| = \sum_{m,n} = \rho_{m,n} \left|\Phi_m\right\rangle \left\langle\Phi_n\right|. \tag{2.12}$$

To describe multiband systems within the effective mass approximation, the statistical density operator $\hat{\rho}$ is defined using the eigenfunctions $\psi_{\lambda,\boldsymbol{k}}(\boldsymbol{r}) = \langle\boldsymbol{r}|\lambda,\boldsymbol{k}\rangle$ as:

$$\hat{\rho} = \sum_{\lambda,\lambda',\boldsymbol{k}} p_{\lambda,\lambda',\boldsymbol{k}} \left|\lambda,\boldsymbol{k}\right\rangle \left\langle\lambda',\boldsymbol{k}\right| = \sum_{\lambda,\lambda'} \hat{\rho}_{\lambda,\lambda'}. \tag{2.13}$$

For the position-space representation of the operator, the following expression is used:

$$\rho_{\lambda,\lambda'}(\boldsymbol{r},\boldsymbol{r}',t) = \langle\boldsymbol{r}|\hat{\rho}_{\lambda,\lambda'}|\boldsymbol{r}'\rangle = \sum_{\boldsymbol{k}} p_{\lambda,\lambda',\boldsymbol{k}} \cdot \psi_{\lambda,\boldsymbol{k}}(\boldsymbol{r},t)\psi^{\dagger}_{\lambda,\boldsymbol{k}}(\boldsymbol{r}',t), \tag{2.14}$$

where the sum $\sum_{\boldsymbol{k}}$ runs over all $\boldsymbol{k}$-states. From the statistical density matrix ρ, the charge carrier distribution n_λ in band λ can be derived as:

$$n_\lambda(\boldsymbol{r},t) = \rho_{\lambda,\lambda'}(\boldsymbol{r},\boldsymbol{r}',t)|_{\boldsymbol{r}=\boldsymbol{r}'} = \sum_{\boldsymbol{k}} p_{\lambda,\lambda',\boldsymbol{k}} \cdot |\psi_{\lambda,\boldsymbol{k}}(\boldsymbol{r},t)|^2, \tag{2.15}$$

which corresponds to the diagonal elements $\rho_{\lambda,\lambda}$ of the statistical density matrix in the space eigenbasis. Here, the squared magnitude of the wave function represents the probability of finding an electron in band λ, at position $\boldsymbol{r}$, and in state $\boldsymbol{k}$.
To obtain the second key physical quantity, an expression for the current density j_λ is required. Within the effective mass approximation, this is derived from the Hamiltonian operator as [59]:

$$j_\lambda(\boldsymbol{r},t) = \frac{\imath q\hbar}{2m_\lambda(\boldsymbol{r})}(\boldsymbol{\nabla}_{\boldsymbol{r}} - \boldsymbol{\nabla}_{\boldsymbol{r}'})\rho_{\lambda,\lambda'}(\boldsymbol{r},\boldsymbol{r}',t)|_{\boldsymbol{r}=\boldsymbol{r}'}. \tag{2.16}$$

2.2.2. Liouville-von Neumann Equation

To describe the time evolution of the statistical density operator, the LVNE will be introduced in this section.
Utilizing the product rule, as well as the definition of the statistical density operator in Eq. (2.11), the LVNE is defined according to

$$\imath\hbar\frac{\partial}{\partial t}\hat{\rho}(t) = [\mathcal{H}, \hat{\rho}(t)]. \tag{2.17}$$

One remarkable trait of the LVNE (or von Neumann equation), originally devised by Hungarian mathematician John von Neumann [37], is its definition in an abstract Hilbert space. A specific representation (e.g., in position, momentum, or phase space) is obtained once a basis is chosen. Depending on the choice, the von Neumann equation can be expressed in real space or phase space [38], making it particularly flexible with the use of inflow/outflow boundary conditions. This will be discussed in greater detail in Chapter 4.
In Eq. (2.17), the Hamiltonian $\mathcal{H}$ describes the underlying physical system. To find an explicit expression for the Hamiltonian $\mathcal{H}$, it is decomposed into a kinetic energy term and a potential energy term [60, 61, 62]. In first quantization, these are given by:

$$\mathcal{H} = \mathcal{H}_{\text{kin}} + \mathcal{H}_{\text{pot}} = -\frac{\hbar^2}{2m}\boldsymbol{\nabla}^2 + V(\boldsymbol{r}). \tag{2.18}$$

The external averaged potential $V(r)$ within $\mathcal{H}_{\text{pot}}$ arises from the previously introduced mean-field approximation (see Section 2.2.1). In the position representation, the well-known form of the LVNE is obtained as:

$$\imath\partial_t\rho(\boldsymbol{r}, \boldsymbol{r}', t) = \underbrace{\left\{\frac{\hbar}{2m}\left(\boldsymbol{\nabla}_{\boldsymbol{r}}^2 - \boldsymbol{\nabla}_{\boldsymbol{r}'}^2\right) + \frac{1}{\hbar}\Big(V(\boldsymbol{r}, t) - V(\boldsymbol{r}', t)\Big)\right\}}_{\mathcal{L}}\rho(\boldsymbol{r}, \boldsymbol{r}', t). \tag{2.19}$$

At this point, it should be noted that the reduced Planck constant $\hbar$ appearing on the left-hand side of Eq. (2.17) has been brought to the right-hand side in Eq. (2.19) by division. The expression $\mathcal{L}$ in braces denotes the *Liouville operator*, which plays a similar role to the Hamiltonian in the SE, describing the system's dynamics.
This form of the LVNE allows to distinguish between two scenarios:

- *Case 1:* The time-invariant (stationary) case, where $\partial_t\rho(\boldsymbol{r}, \boldsymbol{r}', t) = 0$.
- *Case 2:* The time-dependent (transient) case, where $\partial_t\rho(\boldsymbol{r}, \boldsymbol{r}', t) \neq 0$.

In a next step, a coordinate transformation of Eq. (2.19) is performed to center-mass and relative coordinates. This corresponds to a rotation of the original coordinate system defined by $\boldsymbol{r}$ and $\boldsymbol{r}'$ by an angle of $\frac{\pi}{4}$, as illustrated in Fig. 2.1. This transformation offers the following advantages:

1. As discussed in Section 2.2.1, the carrier distribution n_λ in Eq. (2.15) is obtained from the diagonal elements of the statistical density matrix $\rho_{\lambda,\lambda'}$. Due to the coordinate rotation, the carrier distribution now lies along one axis of the statistical density matrix. As a result, the contacts are no longer located at the corners but along a coordinate edge, which leads to improved resolution [46].

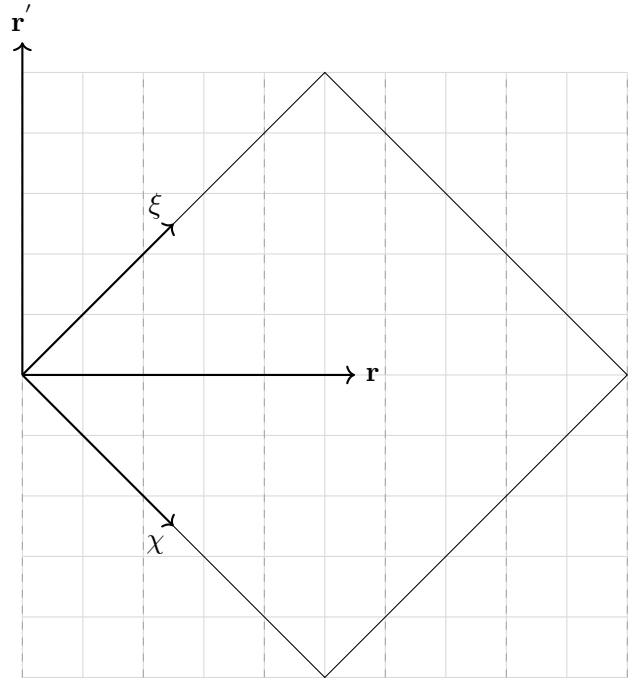

Figure 2.1.: Schematic representation of the coordinate transformation into center-mass coordinates.

2. Another advantage is the reduction of the gradient dimensionality in Eq. (2.19). A gradient – such as a temperature gradient or density gradient – induces motion in a closed system. A second-order gradient significantly increases the complexity of the numerical implementation of the LVNE, which will be discussed later in Section 5.2.1. This gradient is reduced to first order for the one-dimensional case of the LVNE through the coordinate transformation, as will be shown later in this section.

3. Moreover, the coordinate transformation serves as a preparatory step for quantum transport in phase space (see Section 2.2.3), which is essential for the formulation of boundary conditions (see Section 4.2) [45].

The coordinate rotation is performed according to the rule [58]

$$\begin{aligned} \boldsymbol{\chi} &= \frac{\boldsymbol{r}+\boldsymbol{r}'}{2} \qquad \text{and} \qquad \boldsymbol{\xi} = \boldsymbol{r}-\boldsymbol{r}', \text{ as well as} \\ \boldsymbol{r} &= \boldsymbol{\chi}+\frac{\boldsymbol{\xi}}{2} \qquad \text{and} \qquad \boldsymbol{r}' = \boldsymbol{\chi}-\frac{\boldsymbol{\xi}}{2}. \end{aligned} \tag{2.20}$$

Analogously, the corresponding transformation for the derivatives is given by

$$\begin{aligned} \frac{\partial}{\partial \mathbf{r}} &= \frac{1}{2}\frac{\partial}{\partial \boldsymbol{\chi}} + \frac{\partial}{\partial \boldsymbol{\xi}} \qquad \text{and} \qquad \frac{\partial}{\partial \mathbf{r}'} = \frac{1}{2}\frac{\partial}{\partial \boldsymbol{\chi}} - \frac{\partial}{\partial \boldsymbol{\xi}}, \text{ and for the second order} \\ \frac{\partial^2}{\partial \mathbf{r}^2} &= \frac{1}{4}\frac{\partial^2}{\partial \boldsymbol{\chi}^2} + \frac{\partial}{\partial \boldsymbol{\chi}}\frac{\partial}{\partial \boldsymbol{\xi}} + \frac{\partial^2}{\partial \boldsymbol{\xi}^2} \qquad \text{and} \qquad \frac{\partial^2}{\partial \mathbf{r}'^2} = \frac{1}{4}\frac{\partial^2}{\partial \boldsymbol{\chi}^2} - \frac{\partial}{\partial \boldsymbol{\chi}}\frac{\partial}{\partial \boldsymbol{\xi}} + \frac{\partial^2}{\partial \boldsymbol{\xi}^2}. \end{aligned} \tag{2.21}$$

The transformation rules (2.20) and (2.21) can now be applied to Eq. (2.19), resulting in the LVNE in center-mass (χ) and relative (ξ) coordinates:

$$\frac{\partial}{\partial t}\rho(\boldsymbol{\chi},\boldsymbol{\xi},t) = \underbrace{\imath\frac{\hbar}{2m}\frac{\partial}{\partial\boldsymbol{\chi}}\frac{\partial}{\partial\boldsymbol{\xi}}\rho(\boldsymbol{\chi},\boldsymbol{\xi},t)}_{\text{Diffusion operator}} \underbrace{-\imath\frac{q}{\hbar}\left[V\left(\boldsymbol{\chi}+\frac{\boldsymbol{\xi}}{2},t\right)-V\left(\boldsymbol{\chi}-\frac{\boldsymbol{\xi}}{2},t\right)\right]\rho(\boldsymbol{\chi},\boldsymbol{\xi},t)}_{\text{Drift operator}}. \tag{2.22}$$

The Wigner potential in Eq. (2.22) can be grouped as follows:

$$B(\chi,\xi,t) = q\left[V\left(\chi+\frac{\xi}{2},t\right)-V\left(\chi-\frac{\xi}{2},t\right)\right] \tag{2.23}$$

and will be referred to in the following as the *drift operator*. This term incorporates the motion of electrons caused by the device's band structure and by external potentials, and corresponds to $\mathcal{H}_{\text{pot}}$ from Eq. (2.18).
Likewise, the term referred to as the *diffusion operator* in Eq. (2.22) represents particle motion caused by the gradient of the statistical density matrix $\boldsymbol{\rho}(\boldsymbol{\chi},\boldsymbol{\xi},t)$ and corresponds to $\mathcal{H}_{\text{kin}}$ in Eq. (2.18).

In the following Section 2.2.3, the phase space representation will be introduced.

2.2.3. Wigner Transport Equation

In addition to analyzing a quantum system in one dimensional real space, it is also possible to perform the analysis in phase space. Here, the system is no longer described using the statistical density operator as in the case of the LVNE; instead, a so-called distribution function is employed. As a result, the system is no longer expressed in terms of two spatial coordinates, but rather in one position and one momentum coordinate [41].
This approach offers several advantages, which will be briefly outlined below:

- The WTE can be understood as the LVNE with a phase space basis. Using the Hamiltonian formalism, the time evolution of the distribution function can be described, which corresponds to the classical Liouville equation. This is the classical analog of the LVNE. In both cases, the system is described in position and momentum coordinates, which allows the expectation values to be determined from the moments of the distribution function [57]. Therefore, the WTE can be seamlessly integrated into simulations with classical trajectories.
- As previously mentioned, coupling to boundary conditions is often more favorable in the WTE framework compared to the LVNE. Since the Fermi-Dirac distribution already exists in phase space, no transformation is required [57].
- The WTE also provides a straightforward way to determine, whether the system under consideration exhibits quantum behavior. In such cases, the distribution function can attain negative values – something that is not possible in classical mechanics – and serves as an indicator of interference, superposition, or entangled states [57].

To derive an expression for the WTE, the statistical density operator – which already incorporates quantum effects – must first be transformed into a phase space representation.

This is achieved through **Weyl quantization** [63].

As a first step, the density operator $\hat{\rho}$ is redefined into an expression composed of the crystal momentum operator $\mathcal{K} = \mathcal{P}/\hbar$, where $\mathcal{P}$ is the momentum operator, and the position operator $\mathcal{R}$. Using distribution theory and the Fourier transformation, the definition reads:

$$\hat{\rho} = \frac{1}{(2\pi)^6}\int d\boldsymbol{r}\int d\boldsymbol{\zeta}\int d\boldsymbol{y}\int d\boldsymbol{k}\rho^*(\boldsymbol{r},\boldsymbol{k})e^{\imath\{\boldsymbol{\zeta}(\boldsymbol{r}-\mathcal{X})+\boldsymbol{y}(\boldsymbol{k}-\mathcal{K})\}} \tag{2.24}$$

Due to the Fourier transformation of the Dirac distribution, additional coordinates in position and crystal momentum, $\boldsymbol{y}$ and $\boldsymbol{\zeta}$ respectively, arise [6, 64]. The function $\rho^*(\boldsymbol{r},\boldsymbol{k})$ represents the operator $\hat{\rho}$ in phase space.
With the translation operator

$$e^{-\imath\boldsymbol{y}\mathcal{K}}\psi(\boldsymbol{z}) = e^{-\imath/\hbar\boldsymbol{y}\mathcal{P}}\psi(\boldsymbol{z}) = \psi(\boldsymbol{z}-\boldsymbol{y}) \tag{2.25}$$

and the Baker-Campbell-Hausdorff relation

$$e^{-\imath(\boldsymbol{\zeta}\mathcal{X}+\boldsymbol{y}\mathcal{K})} = e^{-\imath\boldsymbol{\zeta}\mathcal{X}}e^{-\imath\boldsymbol{y}\mathcal{K}}e^{\imath^2\{\boldsymbol{\zeta}\mathcal{X},\boldsymbol{y}\mathcal{K}\}/2}, \tag{2.26}$$

the action of the operator $\hat{\rho}$ on a state in real space can be expressed as [64]

$$\hat{\rho}\psi(\boldsymbol{z}) = \int\frac{d\boldsymbol{k}}{(2\pi)^3}\int d\boldsymbol{r}\,\rho^*\left(\boldsymbol{k},\frac{\boldsymbol{r}+\boldsymbol{z}}{2}\right)e^{\imath\boldsymbol{k}(\boldsymbol{z}-\boldsymbol{r})}\psi(\boldsymbol{r}) \tag{2.27}$$

Furthermore, a definition using an integral kernel $K_{\hat{\rho}}$ is needed, which is given by:

$$\hat{\rho}\psi(\boldsymbol{z}) = \int d\boldsymbol{r}\,K_{\hat{\rho}}(\boldsymbol{z},\boldsymbol{r})\psi(\boldsymbol{r}) \tag{2.28}$$

From Eqs. (2.27) and (2.28), an integral kernel representation of $\hat{\rho}$ in phase space can be extracted [64]. This yields:

$$K_{\hat{\rho}}(\boldsymbol{z},\boldsymbol{r}) = \int\frac{d\boldsymbol{k}}{(2\pi)^3}\rho^*\left(\boldsymbol{k},\frac{\boldsymbol{r}+\boldsymbol{z}}{2}\right)e^{\imath/\hbar\boldsymbol{k}(\boldsymbol{z}-\boldsymbol{r})} \tag{2.29}$$

Using the coordinate transformation introduced in Eq. (2.20), equation (2.29) can be rewritten in a form where the inverse transformation results as

$$K_{\hat{\rho}}\left(\boldsymbol{\chi}+\frac{\boldsymbol{\xi}}{2},\boldsymbol{\chi}-\frac{\boldsymbol{\xi}}{2}\right) = \int\frac{d\boldsymbol{k}}{(2\pi)^3}\rho^*(\boldsymbol{k},\boldsymbol{\chi})e^{\imath\boldsymbol{k}\boldsymbol{\xi}}. \tag{2.30}$$

From Eq. (2.30), the required transformation can now be derived that maps the statistical density operator $\hat{\rho}$ into phase space:

$$\rho^*(\boldsymbol{k},\boldsymbol{\chi}) = \int d\boldsymbol{\xi}\,e^{-\imath\boldsymbol{k}\boldsymbol{\xi}}K_{\hat{\rho}}\left(\boldsymbol{\chi}+\frac{\boldsymbol{\xi}}{2},\boldsymbol{\chi}-\frac{\boldsymbol{\xi}}{2}\right) \tag{2.31}$$

Moreover, using the relation from Eq. (2.14), an expression involving the distribution function ψ can be derived. Together with the integral kernel $K_{\rho_{\lambda,\lambda'}} = \sum_{\boldsymbol{k}}p_{\lambda,\lambda',\boldsymbol{k}}\cdot\psi_{\lambda,\boldsymbol{k}}(\boldsymbol{z})\psi^\dagger_{\lambda',\boldsymbol{k}}(\boldsymbol{r})$, the Wigner function $f_{\lambda,\lambda'}$ results in [58]:

$$\begin{aligned} f_{\lambda,\lambda'}(\boldsymbol{\chi},\boldsymbol{k},t) &= \int d\boldsymbol{\xi}\,e^{-\imath\boldsymbol{k}\boldsymbol{\xi}}\textstyle\sum_{\boldsymbol{k}'}p_{\lambda,\lambda',\boldsymbol{k}'}\cdot\psi_{\lambda,\boldsymbol{k}'}\left(\boldsymbol{\chi}+\frac{\boldsymbol{\xi}}{2}\right)\psi^\dagger_{\lambda',\boldsymbol{k}'}\left(\boldsymbol{\chi}-\frac{\boldsymbol{\xi}}{2}\right) \\ &= \int d\boldsymbol{\xi}\,e^{-\imath\boldsymbol{k}\boldsymbol{\xi}}\rho_{\lambda,\lambda'}\left(\boldsymbol{\chi}+\frac{\boldsymbol{\xi}}{2},\boldsymbol{\chi}-\frac{\boldsymbol{\xi}}{2}\right) \equiv \int d\boldsymbol{\xi}\,e^{-\imath\boldsymbol{k}\boldsymbol{\xi}}\rho^D_{\lambda,\lambda'}(\boldsymbol{\chi},\boldsymbol{\xi},t) \end{aligned} \tag{2.32}$$

with the inverse transformation

$$\rho^D_{\lambda,\lambda'}(\boldsymbol{\chi},\boldsymbol{\xi},t) = \int \frac{d\boldsymbol{k}}{(2\pi)^3}\, e^{\imath \boldsymbol{k}\boldsymbol{\xi}} f_{\lambda,\lambda'}(\boldsymbol{\chi},\boldsymbol{\xi},t) \tag{2.33}$$

where $\rho^D_{\lambda,\lambda'}(\boldsymbol{\chi},\boldsymbol{\xi},t) = \rho_{\lambda,\lambda'}\left(\boldsymbol{\chi}+\frac{\boldsymbol{\xi}}{2},\boldsymbol{\chi}-\frac{\boldsymbol{\xi}}{2}\right)$. The WTE then finally results:

$$\frac{\partial}{\partial t} f_{\lambda,\lambda'}(\boldsymbol{\chi},\boldsymbol{k},t) = -\frac{\hbar\boldsymbol{k}}{m}\frac{\partial}{\partial\chi} f_{\lambda,\lambda'}(\boldsymbol{\chi},\boldsymbol{k},t) + \frac{1}{\imath\hbar}\int \frac{d\boldsymbol{k'}}{2\pi} V(\boldsymbol{\chi},\boldsymbol{k}-\boldsymbol{k'})\cdot f_{\lambda,\lambda'}(\boldsymbol{\chi},\boldsymbol{k},t) \tag{2.34}$$

Since the WTE plays only a subordinate role in this work, the derivation provided so far shall be considered sufficient. For a more detailed discussion on the properties and characteristics of the WTE, the reader is referred to Section 2.4.3 in [58].

2.3. The Poisson Equation

The quantum transport equations presented so far describe the carrier transport as a function of the potential. This potential, in turn, depends on the charge carrier distribution due to carrier interaction mechanisms. In the Hartree approximation, this is referred to as a self-consistent problem [65, 66]. In order to capture this relationship correctly in the calculation, the Poisson equation is introduced.
It describes the electrostatic potential resulting from the charge distribution and is derived from Maxwells equations of electrodynamics as:

$$-\boldsymbol{\nabla}(\mathcal{E}(\boldsymbol{r})\boldsymbol{\nabla}\phi(\boldsymbol{r})) = \varrho(\boldsymbol{r}) = q(N_D(\boldsymbol{r}) - n(\boldsymbol{r}) + p(\boldsymbol{r}) - N_A(\boldsymbol{r})). \tag{2.35}$$

Here, ϱ denotes the space charge density and consists of donor atoms N_D and acceptor atoms N_A, which are spatially fixed. n and p represent the electron and hole densities, respectively. The permittivity $\mathcal{E}$ consists of the vacuum permittivity $\mathcal{E}_0$ and the position- and material-dependent component $\mathcal{E}_r$. The Hartree potential is linked to the electrostatic potential ϕ via the relation:

$$U(\boldsymbol{r}) = -q\phi(\boldsymbol{r}) \tag{2.36}$$

as given in [50, 65]. With the Hartree potential from Eq. (2.36), equation (2.35) becomes:

$$\boldsymbol{\nabla}(\mathcal{E}(\boldsymbol{r})\boldsymbol{\nabla}U(\boldsymbol{r})) = \varrho(\boldsymbol{r}) = q^2(N_D(\boldsymbol{r}) - n(\boldsymbol{r}) + p(\boldsymbol{r}) - N_A(\boldsymbol{r})). \tag{2.37}$$

The self-consistent problem aims to solve the quantum transport equation and the Poisson equation iteratively. In this approach, the carrier distribution n from the quantum transport equation serves as input for the Poisson equation. This iterative process is repeated until convergence is achieved. This procedure is referred to as the Gummel algorithm [67].
It is also possible to solve both equations simultaneously in a single step using the Newton-Raphson method. Although this offers higher stability compared to the Gummel algorithm, it requires greater memory consumption due to the higher dimensionality of the resulting linear system [58]. Therefore, this method is more suited for large time step widths, which are, however,

limited by the quantum transport equation and the underlying device structure.
To solve the Poisson equation numerically, appropriate boundary conditions must be applied, which are typically divided into two types [58]:

1. **Neumann boundary conditions**: In the stationary modeling of charge carrier transport, the contact regions are assumed to behave as quasi-neutral reservoirs. In these regions, the free carrier density compensates the doping profile, such that the total charge density satisfies $\rho = 0$. Under stationary conditions, the contacts are furthermore assumed to be in electrostatic equilibrium, meaning that no internal electric field is present within the bulk contact material. Consequently, the gradient of the Hartree potential vanishes in these regions. For this reason, homogeneous Neumann boundary conditions are imposed at the contacts. Since this equilibrium assumption generally does not hold in time-dependent simulations, the use of Neumann boundary conditions is typically restricted to stationary cases.

2. **Dirichlet boundary conditions**: The values of the Hartree potential are fixed at the boundary, as they are determined by externally applied voltages. Due to the lack of charge neutrality at the contact regions, these boundary conditions are suitable for transient simulations.

The numerical solution of the Poisson equation is discussed in Section 5.7.
Since the most relevant equations for determining quantum transport have now been covered, the approximation models required for the upcoming simulations can be introduced next.

Summary: This chapter discussed the fundamental quantum transport phenomena and equations, laying the foundation for the remainder of this work. Furthermore, detailed discussions were provided on *ballistic transport* and *quantum mechanical superposition*. The former describes the transport of a particle in a medium without perturbations. Such disturbances could include interactions with other surrounding particles or with the crystal lattice itself. *Quantum mechanical superposition*, on the other hand, describes the fact that a quantum system can exist in multiple states simultaneously, where the probabilities of those states are only determined upon measurement.
Finally, an overview of the three most important quantum transport equations was given. The foundation was provided by the SE, which describes the dynamics of the wave function in a quantum system. Although it contains the full information of the system, it is only valid for pure states. For quantum systems in mixed states, the *density matrix formalism* was introduced, along with the LVNE, which describes the time evolution of the statistical density operator. After a coordinate transformation into center-mass and relative coordinates, the WTE was derived via *Weyl quantization*, providing a phase-space formulation of quantum transport and thus completing the triad of transport equations. Lastly, the Poisson equations was introduced, enabling the inclusion of the charge carrier distribution in the potential and thereby the implementation of a self-consistent potential.

3. Approximation Models for Quantum Transport Simulation

As with any type of simulation – whether in mechanical engineering, computational fluid dynamics, thermodynamics, or electrodynamics – a model must first be constructed that realistically represents the underlying device. As previously mentioned, this model shall be based on the quantum transport equations discussed in Section 2.2. The foundational equation to be used is the LVNE.

A device typically consists of three spatial dimensions. Quantum devices, however, often exhibit structural invariance in the directions parallel to the material interfaces. To illustrate

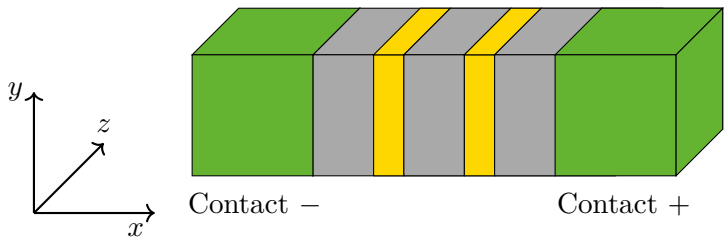

Figure 3.1.: 3D-schematic of an RTD.

this, Fig. 3.1 schematically depicts such a RTD structure. The heterostructure is layered along the x-direction, which corresponds to the transport direction perpendicular to the interfaces. In contrast, the device is assumed to be uniform in the transverse y- and z-directions. This translational invariance allows the problem to be reduced to a one-dimensional model along the x-axis, thereby significantly decreasing the computational effort.
The subsequent discussion begins in Section 3.1 with the one-dimensional transport problem, where the Quantum-Liouville Equation (QLE), a special case of the LVNE, is introduced. This is followed in Subsection 3.1.1, which develops the discretization strategy. Next, Subsection 3.1.2 then highlights the advantages of performing a basis transformation.
Furthermore, Section 3.2 introduces the model for intraband quantum transport. It accounts for the conduction and valence bands, albeit without coupling between them. Heterostructures, which arise from material variations (see Fig. 3.1) and require a spatially varying effective electron mass, are the focus of Section 3.3. This leads naturally to the appearance of a second-order derivative, a feature that will also play a key role in the interband transport model. Finally, Section 3.4 extends the intraband model by incorporating coupling between the two bands, thereby arriving at the interband formulation.

3.1. Quantum Liouville Equation

In Section 2.2.2, the LVNE was first introduced in the original coordinate system and subsequently transformed into the rotated coordinate system. This had the important advantage that the subtraction of second-order derivatives ($\boldsymbol{\nabla}_{r'}^2 - \boldsymbol{\nabla}_r^2$) in Eq. (2.19) transformed into a product of first-order derivatives $\partial_\chi \partial_\xi$ in Eq. (2.22). Nevertheless, this provides the advantage that both coordinates χ and ξ can be discretized consecutively utilizing a one-dimensional approximation method. Therefore, Instead of extending the DG method into a second dimension to discretize both coordinates simultaneously, two one-dimensional discretization approaches, can instead be coupled independently. In Fig. 3.2, the discretization procedure used in this work is illustrated.

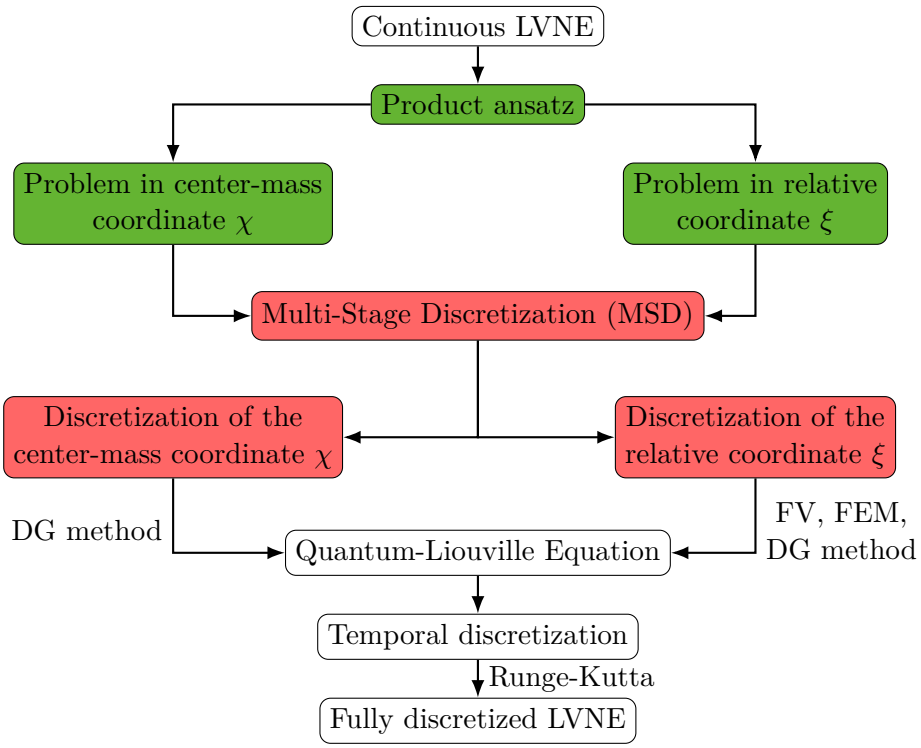

Figure 3.2.: Diagrammatic representation of the discretization procedure. First, the spatial coordinates of the LVNE are treated individually using the product ansatz. Subsequently, the MSD is used to separate the spatial discretization from the temporal one.

The untreated, continuous LVNE is split into two one-dimensional problems [50]. This separation is based on a *product ansatz*, i.e., the assumption that the statistical density matrix in center-of-mass coordinates can be written as a product of functions depending on the individual variables,

$$\rho(\chi, \xi) = \rho_\chi(\chi)\, \rho_\xi(\xi).$$

This product structure allows the transport direction χ and the relative coordinate ξ to be treated independently. First, the relative coordinate ξ is discretized using an arbitrary approximation method. Based on this ξ-discretization, the discretization of the center-mass coordinate χ is then carried out. This is followed by a discretization of the time domain to obtain the fully discretized LVNE, which is referred to as the *Multi-Stage Discretization (MSD)*. The spatial

discretizations are thereby combined with the temporal discretization, resulting in the fully discretized LVNE, hereinafter referred to as the QLE.

3.1.1. Multi-Stage Discretization

As shown in Fig. 3.2, there are several options for discretizing the separated spatial coordinates and the time domain. The center-mass coordinate χ is exclusively handled using the DG method. The simple reason is that the actual transport of electrons takes place in the χ direction. Since the aim of this work is to derive a DG concept for simulating quantum transport, it is, therefore, essential to utilize this method exclusively for the χ-coordinate. For the relative coordinate, there is more flexibility. The Finite Element method (FEM), Finite Volume (FV), or Discontinuous Galerkin (DG) methods may be used. Ultimately, both coordinates are discretized using the DG method. However, this does not constitute the two-dimensional variant of the method – rather, two one-dimensional methods are coupled. This is the standard procedure for each of the schemes. The workflow is the same in every case as follows:

1. Select a numerical method to handle the first coordinate (typically the relative coordinate).
2. Use the chosen numerical method to construct a so-called discretization matrix, as will be described in Section 5.3.1.
3. Extract the eigenvalues and eigenvectors of the semi-discretized system from the discretization matrix, which will also be explained in Section 5.3.1.
4. Use the previously determined eigenvalues and eigenvectors to discretize the second coordinate of the LVNE using another numerical method, which does not have to be the same as the first. This will be covered in Section 5.3.2.
5. Treat the spatially discretized LVNE with the Runge-Kutta 4th order (RK4) method [68].

This approach allows both coordinates to be processed by two (independent) one-dimensional numerical algorithms. Otherwise, a two-dimensional method would be required, significantly increasing computational effort and implementation complexity.
The derivation of eigenvalues and eigenvectors from step three is explained next.

3.1.2. Basis Transformation into the Eigenvalue Space

From Eq. (2.22), the ξ-dependence is first eliminated by discretizing it using the FEM, FV, or DG methods. Specifically:

$$\boldsymbol{A} = \frac{\partial}{\partial \xi} \rho(\xi)$$

is discretized. The exact procedure will be detailed in Section 5.3.1. After successful discretization of the relative coordinate ξ, the resulting discretization matrix $\boldsymbol{A}$ can be used to extract the eigenvalues $\boldsymbol{\Lambda}$ and eigenvectors $\boldsymbol{\Phi}$, with the columns of $\boldsymbol{\Phi}$ corresponding to the eigenvalues. The eigenvector matrix $\boldsymbol{\Phi}$ is unitary, such that $\boldsymbol{\Phi}^{-1} = \boldsymbol{\Phi}^{\dagger}$. This property can be exploited to transform the remaining χ-dependent terms in Eq. (2.22) into the so-called *eigenvalue space*,

according to:

$$0 = \imath\frac{\hbar}{m}\boldsymbol{\Phi}^{\dagger}\boldsymbol{A}\boldsymbol{\Phi}\frac{\partial}{\partial\chi}\rho(\chi) - \frac{\imath}{\hbar}\boldsymbol{\Phi}^{\dagger}(\boldsymbol{\mathcal{B}})\boldsymbol{\Phi}\rho(\chi). \tag{3.1}$$

The vector $\boldsymbol{\Lambda}$ contains the individual eigenvalues λ_j. This is recognized as an eigenvalue decomposition via $\boldsymbol{\Lambda} = \boldsymbol{\Phi}^{\dagger}\boldsymbol{A}\boldsymbol{\Phi}$.
With this transformation of the LVNE into the eigenvalue space, the notion of the QLE is introduced.
Now, the intraband transport model will be developed in the following section.

3.2. Intraband Transport

In the intraband case, the focus lies on transport within two bands – the conduction band and the valence band. Therefore, a brief overview of what these two bands represent will be given. In solids, the energy states of electrons are grouped into so-called bands. The conduction and valence bands form the main bands [52]. Regardless of how many conduction or valence bands exist, the valence band typically lies at a lower energy level than the conduction band. That is, electrons in a resting state remain in the valence band. The conduction band, in contrast, hosts the free electrons that are capable of conducting electricity. Meanwhile, electrons in the valence band can also move when there is at least one empty state. An electron can hop into this empty state and in turn leaves an empty state behind. The empty state is also known as a *hole*, which comes with its own set of properties [52]. This is recognized as hole movement, although the hole itself does not move. Therefore, charge carrier transport can also occur in the valence band [36, 52]. If a material is at a temperature near absolute zero (0 K), all electrons occupy the valence band due to their low energy. If electrons in the valence band are supplied with energy in the form of heat, light, or an electric field, they may transition to the conduction band and become available as charge carriers. The amount of energy required for this transition depends on the *bandgap energy*, which denotes the energy difference between the top of the valence band and the bottom of the conduction band. To move an electron from the valence to the conduction band, it must absorb at least the bandgap energy – a process known as excitation [52]. When a band transition occurs, the electron leaves behind a hole in the valence band, which behaves like a positive charge (absence of a negative electron). If more electrons transition to the conduction band, the valence band gains the capacity to accept electrons – for example, when charge carriers lose energy (e.g., via heat or light emission) and fall back to the valence band. This process is called recombination [52].
Since electrons in the valence band are static (when there are no empty states), quantum transport simulations often only consider the conduction band.
Nonetheless, analyzing the valence band is also beneficial, as holes can be understood as quasi-particles with their own effective mass, charge, and dynamics. This is particularly relevant for simulating semiconductor devices such as p-MOSFETs or photovoltaic cells, where hole transport is essential [69]. The valence band is also central in optoelectronic devices like LEDs and lasers, especially in photon absorption and emission processes [70]. However, these shall be of no further interest for this work.
For the following notation, the conduction band is denoted by the index $\lambda = c$ and the valence band by $\lambda^{'} = v$. Using the multiband SE (2.10), the multiband system can be written according

to [58]:

$$\imath\hbar\frac{\partial}{\partial t}\begin{pmatrix}\psi_c(\boldsymbol{r},t)\\ \psi_v(\boldsymbol{r},t)\end{pmatrix}=\begin{pmatrix}\mathcal{H}_{cc}\,\mathcal{H}_{cv}\\ \mathcal{H}_{vc}\,\mathcal{H}_{vv}\end{pmatrix}\cdot\begin{pmatrix}\psi_c(\boldsymbol{r},t)\\ \psi_v(\boldsymbol{r},t)\end{pmatrix} \tag{3.2}$$

Here, $\mathcal{H}_{cc}$ denotes the Hamiltonian for the conduction band and $\mathcal{H}_{vv}$ for the valence band. Applying the effective mass approximation from Eq. (2.9) to Eq. (2.10), [58]:

$$\mathcal{H}_{cc}=-\frac{\hbar^2}{2}\boldsymbol{\nabla}\frac{1}{m_c(\boldsymbol{r})}\boldsymbol{\nabla}+E_c(\boldsymbol{r})+U(\boldsymbol{r})\qquad\text{and}\qquad\mathcal{H}_{vv}=-\frac{\hbar^2}{2}\boldsymbol{\nabla}\frac{1}{m_v(\boldsymbol{r})}\boldsymbol{\nabla}+E_v(\boldsymbol{r})+U(\boldsymbol{r}), \tag{3.3}$$

are obtained. Here, $U(\boldsymbol{r})$ is the Hartree potential. The effective masses of the conduction and valence bands, $m_c(\boldsymbol{r})$ and $m_v(\boldsymbol{r})$, respectively, are spatially dependent and will become important in Section 3.3. To avoid a negative effective electron mass in the valance band due to missing electrons, the positive quantity $m_v(\boldsymbol{r})$ is introduced which represents the effective mass of a hole [14, 36, 71]. The off-diagonal elements $\mathcal{H}_{cv}$ and $\mathcal{H}_{vc}$ represent interband coupling mechanisms and are described by the following relation [58]:

$$\mathcal{H}_{cv}=\mathcal{H}_{vc}=-\frac{\hbar^2 P}{m_0 E_g}\boldsymbol{\nabla}U(\boldsymbol{r}). \tag{3.4}$$

Here, P is Kane's momentum matrix element, and the bandgap energy $E_g=E_c-E_v$ is derived from the energy difference between the conduction band edge E_c and valence band edge E_v. As established earlier the heterostructure is uniform in the transverse directions, the material parameters and potentials depend solely on the transport coordinate. The spatial dependence is therefore reduced from the three-dimensional position vector $\boldsymbol{r}$ to the one-dimensional coordinate x. To define the two-band LVNE, the Hamiltonians from (3.3)-(3.4) are substituted into (3.2) [58]:

$$\begin{aligned}\imath\hbar\frac{\partial}{\partial t}\hat{\Phi}_c(x,t)&=\underbrace{\left\{-\frac{\hbar^2}{2}\frac{\partial}{\partial x}\frac{1}{m_c(x)}\frac{\partial}{\partial x}+E_c(x)+U(x)\right\}}_{\mathcal{H}_{cc}(x)}\hat{\Phi}_c(x,t)\underbrace{-\frac{\hbar^2 P}{m_0E_g}\frac{\partial}{\partial x}}_{\mathcal{H}_{cv}(x)}\hat{\Phi}_v(x,t)\\ \imath\hbar\frac{\partial}{\partial t}\hat{\Phi}_v(x,t)&=\underbrace{\left\{-\frac{\hbar^2}{2}\frac{\partial}{\partial x}\frac{1}{m_v(x)}\frac{\partial}{\partial x}+E_v(x)+U(x)\right\}}_{\mathcal{H}_{vv}(x)}\hat{\Phi}_v(x,t)\underbrace{-\frac{\hbar^2 P}{m_0E_g}\frac{\partial}{\partial x}}_{\mathcal{H}_{vc}(x)}\hat{\Phi}_c(x,t).\end{aligned} \tag{3.5}$$

Finally, by inserting the quantum mechanical identity operator $\int dx^{''}\left|x^{''}\right\rangle\left\langle x^{''}\right|$ into the LVNE (2.17), the multiband quantum transport model can be written as:

$$\imath\hbar\frac{\partial}{\partial t}\begin{pmatrix}\hat{\rho}_{cc}\\ \hat{\rho}_{vv}\end{pmatrix}=\begin{pmatrix}\mathcal{H}_{cc}(x)-\mathcal{H}_{cc}^{\dagger}(x^{'}) & \mathcal{H}_{cv}^{\dagger}(x)\\ -\mathcal{H}_{vc}^{\dagger}(x^{'}) & \mathcal{H}_{vv}(x)-\mathcal{H}_{vv}^{\dagger}(x^{'})\end{pmatrix}\begin{pmatrix}\hat{\rho}_{cc}\\ \hat{\rho}_{vv}\end{pmatrix}. \tag{3.6}$$

From the multiband model (3.6), under the assumption that coupling is not considered, the relevant equations for intraband transport in the separated conduction and valence bands can be extracted:

$$\imath\hbar\frac{\partial}{\partial t}\hat{\rho}_{cc}(x,x^{'},t)=\left[\mathcal{H}_{cc}(x)-\mathcal{H}_{cc}^{\dagger}(x^{'})\right]\hat{\rho}_{cc}(x,x^{'},t) \tag{3.7}$$

and

$$\imath\hbar\frac{\partial}{\partial t}\hat{\rho}_{vv}(x,x^{'},t)=\left[\mathcal{H}_{vv}(x)-\mathcal{H}_{vv}^{\dagger}(x^{'})\right]\hat{\rho}_{vv}(x,x^{'},t). \tag{3.8}$$

One will recognize that, through a coordinate transformation according to (2.20), the LVNE is obtained in the form of Eq. (2.22). With this, the model for intraband quantum transport is sufficiently established, and the model involving a spatially varying effective mass can be introduced.

3.3. Spatially Varying Effective Electron Mass

Since nanoelectronic devices typically consist of different material layers (see Fig. 3.1), the electrons moving within them have a spatially dependent effective mass. This is referred to as spatially varying effective mass [14], which is also reflected in the spatial dependence of $m_{c(v)}(x)$ in Eq. (3.5).
From the difference of the Hamilton operators in Eq. (3.7) and Eq. (3.8), and by considering the wave vector $\boldsymbol{k}=\{\boldsymbol{k}_{||},\boldsymbol{k}_x\}$, where $\boldsymbol{k}_{||}$ is the lateral component and $\boldsymbol{k}_x$ corresponds to the transport direction, the LVNE for spatial variation of the effective mass becomes [58]:

$$\mathcal{H}(x)-\mathcal{H}^{\dagger}(x^{'})=-\frac{\hbar^2}{2}\left\{\frac{\partial}{\partial x}\frac{1}{m(x)}\frac{\partial}{\partial x}-\frac{\partial}{\partial x^{'}}\frac{1}{m(x^{'})}\frac{\partial}{\partial x^{'}}\right\}+\{V(x)-V(x^{'})\}+\frac{\hbar^2\boldsymbol{k}_{||}^2}{2}\left\{\frac{1}{m(x)}-\frac{1}{m(x^{'})}\right\}. \tag{3.9}$$

If the effective mass is spatially constant, the lateral term (last term in Eq. (3.9)) can be neglected. This is the case, for instance, in devices with a homogeneous material composition [2, 13, 15, 65, 72, 73, 74].
Using the coordinate transformation from Eq. (2.20), expressions for the effective masses can be written as [58]:

$$m_{\pm}(\chi,\xi)=\frac{1}{m\left(\chi+\frac{\xi}{2}\right)}\pm\frac{1}{m\left(\chi-\frac{\xi}{2}\right)}. \tag{3.10}$$

Additionally, the derivatives of the masses in Eq. (3.10) are defined as [14, 58]:

$$\begin{aligned}\frac{\partial}{\partial x}\frac{1}{m(x^{'})}=0=+\frac{\partial}{\partial x^{'}}\frac{1}{m(x)}&\rightarrowtail\frac{\partial}{\partial\xi}m_{+}(\chi,\xi)=\frac{1}{2}\frac{\partial}{\partial\chi}m_{-}(\chi,\xi)\\ \frac{\partial}{\partial x}\frac{1}{m(x^{'})}=0=-\frac{\partial}{\partial x^{'}}\frac{1}{m(x)}&\rightarrowtail\frac{\partial}{\partial\xi}m_{-}(\chi,\xi)=\frac{1}{2}\frac{\partial}{\partial\chi}m_{+}(\chi,\xi).\end{aligned} \tag{3.11}$$

It is common practice to convert derivatives with respect to the relative coordinate ξ into derivatives with respect to the center-mass coordinate χ [14, 75].
Thus, by inserting the transformations (3.10) and (3.11) into the difference of the Hamiltonians in Eq. (3.9), the LVNE for the spatially varying effective mass becomes:

$$\begin{aligned}\frac{\partial}{\partial t}\rho =& \frac{\imath\hbar}{2}m_- \frac{1}{4}\frac{\partial^2}{\partial\chi^2}\rho + \frac{\imath\hbar}{2}\left\{\left(\frac{\partial}{\partial\chi}m_-\right)\frac{1}{2} + m_+\frac{\partial}{\partial\xi}\right\}\frac{\partial}{\partial\chi}\rho \\ &+\frac{\imath\hbar}{2}\left\{\left(\frac{\partial}{\partial\chi}m_+\right)\frac{\partial}{\partial\xi} + m_-\frac{\partial^2}{\partial\xi^2}\right\}\rho + \frac{1}{\imath\hbar}B\cdot\rho - \frac{\imath\hbar}{2}\boldsymbol{k}_{||}^2 m_-\rho.\end{aligned} \tag{3.12}$$

For better readability, the shorthand notation $\rho = \rho(\chi, \xi, t)$ for the statistical density matrix and $m_\pm = m_\pm(\chi, \xi)$ in Eq. (3.12) is used.
A further simplification can be made regarding the lateral wave vector component $\boldsymbol{k}_{||}$ in Eq. (3.12). Since electron transport typically occurs near the Fermi level at the band extrema [76], the contribution of the lateral wave vector $\boldsymbol{k}_{||}$ can be assumed to be negligibly small. Additionally, the difference of the effective mass $m_-(\chi, \xi)$ takes only small values or vanishes entirely, so that the last term in Eq. (3.12) can also be neglected [58].
While this second derivative introduces challenges when defining the numerical flux for the DG method – as will be discussed in Section 5.2.1 – it is nonetheless required for the interband approximation model, which will be introduced in the following section.

3.4. Interband Transport

As discussed previously in Section 3.2, the transition of a valence band electron into the conduction band can be induced by the supply of energy. However, this is not the only possible mechanism. Since a quantum system is analyzed, an electron can also tunnel into the energetically next higher band without a change in energy. This process is crucial in devices dominated by tunneling effects, such as an RITD [77] or a TFET [78].
To extend the intraband quantum transport model (3.6) with band coupling mechanisms, a definition of the derivative of the potential U is required, which is connected to the electric field. This coupling formulation is commonly referred to as the Multiband Envelope Function (MEF) method, which provides a systematic framework for describing interband transport within the effective mass approximation [53]. Using the definition for $\mathcal{E}$ [52]:

$$\mathcal{E}^{\pm}\left(\chi \pm \frac{\xi}{2}\right) = \left(\frac{1}{2}\frac{\partial}{\partial\chi} \pm \frac{\partial}{\partial\xi}\right)\cdot U\left(\chi \pm \frac{\xi}{2}\right), \tag{3.13}$$

the electric field can be introduced. With this, the system of equations (3.6) can be extended by the two density matrices ρ_{cv} and ρ_{vc}, which describe the coupling between conduction and valence bands. According to [58], the multiband model (3.6) becomes a 4×4 system:

$$\imath\hbar\frac{\partial}{\partial t}\begin{pmatrix}\rho_{cc}\\ \rho_{cv}\\ \rho_{vc}\\ \rho_{vv}\end{pmatrix} = \begin{pmatrix}\mathcal{H}_{cc}(x) - \mathcal{H}_{cc}^{\dagger}(x') & -\mathcal{H}_{cv}^{\dagger}(x') & \mathcal{H}_{cv}(x) & 0\\ -\mathcal{H}_{vc}^{\dagger}(x') & \mathcal{H}_{cc}(x) - \mathcal{H}_{vv}^{\dagger}(x') & 0 & \mathcal{H}_{cv}(x)\\ \mathcal{H}vc(x) & 0 & \mathcal{H}_{vv}(x) - \mathcal{H}_{cc}^{\dagger}(x') & -\mathcal{H}_{cv}^{\dagger}(x')\\ 0 & \mathcal{H}_{vc}(x) & -\mathcal{H}_{vc}^{\dagger}(x') & \mathcal{H}_{vv}(x) - \mathcal{H}_{vv}^{\dagger}(x')\end{pmatrix}\begin{pmatrix}\rho_{cc}\\ \rho_{cv}\\ \rho_{vc}\\ \rho_{vv}\end{pmatrix}. \tag{3.14}$$

Using this equation of motion (3.14) and the previously defined Hamiltonians from Eq. (3.5), the LVNE for interband quantum transport can be established. First, two additional quantities essential for this new model must be introduced: the effective masses for each band and their

couplings, as well as expressions for their derivatives. These are defined as [58]:

$$m^{\pm}_{\lambda\lambda'}(\chi,\xi) = \frac{1}{m_\lambda\left(\chi+\frac{\xi}{2}\right)} \pm \frac{1}{m_{\lambda'}\left(\chi-\frac{\xi}{2}\right)} \tag{3.15}$$

and

$$\begin{aligned} \frac{\partial}{\partial x}\frac{1}{m(x')} = 0 = +\frac{\partial}{\partial x'}\frac{1}{m_v(x)} &\rightarrowtail \frac{\partial}{\partial\xi}m^-_{cv}(\chi,\xi) = \frac{1}{2}\frac{\partial}{\partial\chi}m^+_{vc}(\chi,\xi) \\ \frac{\partial}{\partial x}\frac{1}{m_c(x')} = 0 = -\frac{\partial}{\partial x'}\frac{1}{m_v(x)} &\rightarrowtail \frac{\partial}{\partial\xi}m^+_{cv}(\chi,\xi) = \frac{1}{2}\frac{\partial}{\partial\chi}m^+_{vc}(\chi,\xi), \end{aligned} \tag{3.16}$$

Furthermore, the drift term $B_{\lambda\lambda'}$ is required, which accounts for the band coupling mechanisms [58]:

$$B_{\lambda\lambda'}(\chi,\xi) = V_\lambda\left(\chi+\frac{\xi}{2}\right) - V_{\lambda'}\left(\chi-\frac{\xi}{2}\right). \tag{3.17}$$

Together with the spatially varying masses from Eq. (3.15), their derivatives in Eq. (3.16), the drift operator in Eq. (3.17), and the electric field term $\mathcal{E}$ from Eq. (3.13), the equations in the rotated coordinate system are given as [58]:

$$\begin{aligned} \frac{\partial}{\partial t}\rho_{cc} =& + \frac{\imath\hbar}{2}\left\{\left(\frac{\partial}{\partial\chi}m^-_{cc}\right)\frac{1}{2}\frac{\partial}{\partial\chi} + \left(\frac{\partial}{\partial\chi}m^+_{cc}\right)\frac{\partial}{\partial\xi} + m^-_{cc}\frac{1}{4}\frac{\partial^2}{\partial\chi^2} + m^+_{cc}\frac{\partial}{\partial\chi}\frac{\partial}{\partial\xi} + m^-_{cc}\frac{\partial^2}{\partial\xi^2}\right\}\rho_{cc} \\ &+ \frac{1}{\imath\hbar}B_{cc}\rho_{cc} + \frac{\imath\hbar P}{m_0E_g}\mathcal{E}\left(\chi-\frac{\xi}{2}\right)\rho_{cv} - \frac{\imath\hbar P}{m_0E_g}\mathcal{E}\left(\chi+\frac{\xi}{2}\right)\rho_{vc} \\ \frac{\partial}{\partial t}\rho_{cv} =& + \frac{\imath\hbar}{2}\left\{\left(\frac{\partial}{\partial\chi}m^+_{cv}\right)\frac{1}{2}\frac{\partial}{\partial\chi} + \left(\frac{\partial}{\partial\chi}m^-_{cv}\right)\frac{\partial}{\partial\xi} + m^+_{cv}\frac{1}{4}\frac{\partial^2}{\partial\chi^2} + m^-_{cv}\frac{\partial}{\partial\chi}\frac{\partial}{\partial\xi} + m^+_{cv}\frac{\partial^2}{\partial\xi^2}\right\}\rho_{cv} \\ &+ \frac{1}{\imath\hbar}B_{cv}\rho_{cv} + \frac{\imath\hbar P}{m_0E_g}\mathcal{E}\left(\chi-\frac{\xi}{2}\right)\rho_{cc} - \frac{\imath\hbar P}{m_0E_g}\mathcal{E}\left(\chi+\frac{\xi}{2}\right)\rho_{vv} \\ \frac{\partial}{\partial t}\rho_{vc} =& - \frac{\imath\hbar}{2}\left\{\left(\frac{\partial}{\partial\chi}m^+_{vc}\right)\frac{1}{2}\frac{\partial}{\partial\chi} + \left(\frac{\partial}{\partial\chi}m^-_{vc}\right)\frac{\partial}{\partial\xi} + m^+_{vc}\frac{1}{4}\frac{\partial^2}{\partial\chi^2} + m^-_{vc}\frac{\partial}{\partial\chi}\frac{\partial}{\partial\xi} + m^+_{vc}\frac{\partial^2}{\partial\xi^2}\right\}\rho_{vc} \\ &+ \frac{1}{\imath\hbar}B_{vc}\rho_{vc} + \frac{\imath\hbar P}{m_0E_g}\mathcal{E}\left(\chi-\frac{\xi}{2}\right)\rho_{vv} - \frac{\imath\hbar P}{m_0E_g}\mathcal{E}\left(\chi+\frac{\xi}{2}\right)\rho_{cc} \\ \frac{\partial}{\partial t}\rho_{vv} =& - \frac{\imath\hbar}{2}\left\{\left(\frac{\partial}{\partial\chi}m^-_{vv}\right)\frac{1}{2}\frac{\partial}{\partial\chi} + \left(\frac{\partial}{\partial\chi}m^+_{vv}\right)\frac{\partial}{\partial\xi} + m^-_{vv}\frac{1}{4}\frac{\partial^2}{\partial\chi^2} + m^+_{vv}\frac{\partial}{\partial\chi}\frac{\partial}{\partial\xi} + m^-_{vv}\frac{\partial^2}{\partial\xi^2}\right\}\rho_{vv} \\ &+ \frac{1}{\imath\hbar}B_{vv}\rho_{vv} + \frac{\imath\hbar P}{m_0E_g}\mathcal{E}\left(\chi-\frac{\xi}{2}\right)\rho_{vc} - \frac{\imath\hbar P}{m_0E_g}\mathcal{E}\left(\chi+\frac{\xi}{2}\right)\rho_{cv}. \end{aligned} \tag{3.18}$$

Note that, for clarity, the arguments (χ,ξ,t) in Eq. (3.18), as well as the full notation of the effective masses $m_{\lambda\lambda'}(\chi,\xi)$ were omitted.

Also here, the lateral component of the wave vector $\boldsymbol{k}_{||}$ can be neglected [13, 79]. Since the case of spatially varying mass has already been considered separately (cf. Section 3.3), it is now appropriate to assume the effective masses in Eq. (3.18) to be constant and equal [55, 79]. Consequently, the band edge energies E_c and E_v should posses a positional dependence due to different material layers. However, since all potential contributions from the heterostructure and other external sources are grouped into a single drift term $B_{\lambda,\lambda'}(\chi,\xi)$ [55], the band edge energy for the conduction band E_c and for the valence band E_v can be treated as global reference values that omit the positional dependence. This is done due to conceptual reasons and have the

following advantages. First, both band edge energies do not need to be integrated additionally, thus simplifying the overall calculation. Second, with both effective masses m_c and m_v being equal in absolute value such that electrons and holes are treated formally similar [55, 79, 80], it is, therefore, adequate to also assume their respective band edges as spatially invariant. While these assumptions are not strictly realistic for an actual heterostructure with type I/II/III-heterogeneous junctions [50], they are justified in the context of formulating a DG concept and instrumental for comparability with other numerical methods.
With these assumptions, the equations in (3.18) can be further simplified into [58]:

$$
\begin{aligned}
\frac{\partial}{\partial t}\rho_{cc} =& + \frac{\imath\hbar}{m}\frac{\partial}{\partial\chi}\frac{\partial}{\partial\xi}\rho_{cc} + \frac{1}{\imath\hbar}B\rho_{cc} - \frac{\imath\hbar P}{m_0 E_g}\mathcal{E}\left(\chi-\frac{\xi}{2}\right)\rho_{cv} + \frac{\imath\hbar P}{m_0 E_g}\mathcal{E}\left(\chi+\frac{\xi}{2}\right)\rho_{vc} \\
\frac{\partial}{\partial t}\rho_{cv} =& + \frac{\imath\hbar}{m}\left\{\frac{1}{4}\frac{\partial^2}{\partial\chi^2} + \frac{\partial^2}{\partial\xi^2}\right\}\rho_{cv} + \frac{1}{\imath\hbar}\left\{+E_g + B\right\}\rho_{cv} - \frac{\imath\hbar P}{m_0 E_g}\mathcal{E}\left(\chi-\frac{\xi}{2}\right)\rho_{cc} \\
&+ \frac{\imath\hbar P}{m_0 E_g}\mathcal{E}\left(\chi+\frac{\xi}{2}\right)\rho_{vv} \\
\frac{\partial}{\partial t}\rho_{vc} =& - \frac{\imath\hbar}{m}\left\{\frac{1}{4}\frac{\partial^2}{\partial\chi^2} + \frac{\partial^2}{\partial\xi^2}\right\}\rho_{vc} + \frac{1}{\imath\hbar}\left\{-E_g + B\right\}\rho_{vc} - \frac{\imath\hbar P}{m_0 E_g}\mathcal{E}\left(\chi-\frac{\xi}{2}\right)\rho_{vv} \\
&+ \frac{\imath\hbar P}{m_0 E_g}\mathcal{E}\left(\chi+\frac{\xi}{2}\right)\rho_{cc} \\
\frac{\partial}{\partial t}\rho_{vv} =& - \frac{\imath\hbar}{m}\frac{\partial}{\partial\chi}\frac{\partial}{\partial\xi}\rho_{vv} + \frac{1}{\imath\hbar}B\rho_{vv} - \frac{\imath\hbar P}{m_0 E_g}\mathcal{E}\left(\chi-\frac{\xi}{2}\right)\rho_{vc} + \frac{\imath\hbar P}{m_0 E_g}\mathcal{E}\left(\chi+\frac{\xi}{2}\right)\rho_{cv}.
\end{aligned}
\tag{3.19}
$$

Again, the arguments on χ, ξ, and t are omitted for clarity.
Now that all approximation models for describing quantum systems have been covered, the following Chapter 4 will address the formulation of appropriate boundary conditions.

Summary: This chapter presented approximation models for the analysis of quantum transport processes. The starting point was the LVNE, serving as the foundation for all simulations.
Initially, the transport in the conduction and valence bands was described using an intraband model that omitted band coupling.
Then, a model for heterostructures was introduced by extending the LVNE with a second-order derivative and incorporating a spatially varying effective mass, which is necessary to account for the varying material layers in heterostructure devices.
Subsequently, the intraband model was extended by introducing coupling between the bands, forming an interband model based on the MEF method.

4. Formulation of Boundary Conditions

Boundary conditions terminate open systems. Just as in classical mechanics simulations, appropriate boundary values can be used either to substitute missing material or to include external influences from the environment.
In quantum transport, this is in the same manner essential. As introduced earlier in Section 2.2.2, the primary tool in this work is the LVNE in center-of-mass and relative coordinates χ and ξ, respectively. Accordingly, discretizing these two coordinates results in two computational domains, Ω_χ and Ω_ξ. Both computational domains must be finite, i.e., clearly defined start and end points are essential. Thus, boundary conditions must be formulated for both domains.
Section 4.1 will therefore address the boundaries of the computational domain Ω_ξ, while Section 4.2 will deal with the contacts, which form the boundaries of Ω_χ.

4.1. Complex Absorbing Potential

From a physical perspective, the quantum transport equation demands that the distribution function in the direction of the relative coordinate ξ extends to infinity. Consequently, the computational domain Ω_ξ must theoretically be infinitely long to allow propagating waves to vanish into infinity [81].
However, this directly contradicts the earlier statement that numerical domains must be finite. If implemented without precaution, the propagating wave function will encounter a *perfectly reflecting wall* at the boundaries of Ω_ξ. This leads to the following phenomenon, which negatively affects the final results (including the statistical density matrix). Before addressing how to mitigate this, it is important to understand the origin.
In the NEGF formalism, the system Hamiltonian describes the isolated device region. Coupling to external contacts and scattering environments is incorporated through self-energies, which modify the Greens functions and account for carrier injection, escape, and dissipation processes [45]. After a Wigner transformation, these self-energies give rise to surface terms which, if neglected, effectively correspond to applying Dirichlet boundary conditions: $\boldsymbol{\rho}(\chi, \xi = \pm L/2, t) = 0$ at both the left ($\xi = -L/2$) and right ($\xi = +L/2$) boundaries of the computational domain Ω_ξ [2, 13, 75]. In essence, the density matrix is set to zero in these regions. Intuitively, this creates perfectly reflecting boundaries, as mentioned before. The problem arises when the reflections interfere with the ongoing wave propagation, leading to interference patterns.
To appropriately terminate the computational domain Ω_ξ, several options exist, which are briefly outlined below:

- **Periodic boundary conditions**: If a device exhibits translational symmetry or if the crystal lattice is periodic in the relevant direction [27], the infinite extent of a crystal or layer structure can be approximated. Periodic boundary conditions are particularly useful when no external perturbations affect the system.

- **Closed boundary conditions**: If a quantum system is to be analyzed without external perturbations, closed boundary conditions can be employed. In the context of quantum transport, this applies particularly to systems in thermodynamic equilibrium – but not when contact coupling is required [26].
- **Open boundary conditions**: If the system interacts with its surroundings at the domain boundaries, open boundary conditions are used. An example is thermal nonequilibrium, in which the quantum device experiences an external voltage [8, 13].

Since open boundary conditions align with the open nature of the quantum transport equations, they will be used throughout this work. There are several ways to implement open boundaries as listed below:

1. **Transparent Boundary Conditions**: These rely on approximating the open boundary behavior from within the domain. However, they are computationally expensive and thus inefficient for time domain simulations [82].
2. **Perfectly Matched Layer (PML)**: A PML is an artificial absorbing layer defined in the Schrödinger picture. It suppresses reflections but must be formulated in the original coordinate system, which also affects the contact regions of the device [83, 84].
3. **Complex Absorbing Potential (CAP)**: Similar in function to the PML, the CAP is instead defined in the rotated coordinate system, leaving the contact regions unaffected and avoiding computationally expensive boundary matching [28].

The approach adopted here will be the CAP method for the above given reasons and because it has proven to be effective in previous works [28]. Next, Section 4.1.1 introduces its working principle, followed by the mathematical derivation in Section 4.1.2.

4.1.1. Working Principle of the CAP

To illustrate the working principle of the CAP, Fig. 4.1a is considered. The entire computational domain $\Omega_\Gamma = \Omega_\chi \times \Omega_\chi$ is shown, where the shaded area indicates the active region of the CAP with width δ. It is essential that the CAP satisfies the following conditions:

1. The CAP must depend exclusively on the ξ coordinate. This ensures that the contacts located at the boundaries of the χ transport direction remain unaffected.
2. The CAP should contribute no values outside the active regions, indicated by the shaded area in Fig. 4.1a within the interval $[-L_\xi/2 + \delta, +L_\xi/2 - \delta]$. This guarantees that the actual charge carrier distribution at the center of the computational domain Ω_Γ remains unaltered.
3. Furthermore, the amplitude of the CAP within the shaded active region shown in Fig. 4.1a should increase monotonically, reaching its maximum at the domain boundaries $\xi = -L_\xi/2$ and $\xi = +L_\xi/2$. It is crucial that this increase occurs smoothly, i.e., with a continuous and low gradient, to avoid artificial reflections caused by the CAP itself [28].
4. The CAP must attain a sufficient amplitude such that the statistical density matrix $\boldsymbol{\rho}$ converges to zero at the domain boundaries, i.e., $\boldsymbol{\rho}(\chi, \xi = \pm L/2, t) \to 0$.

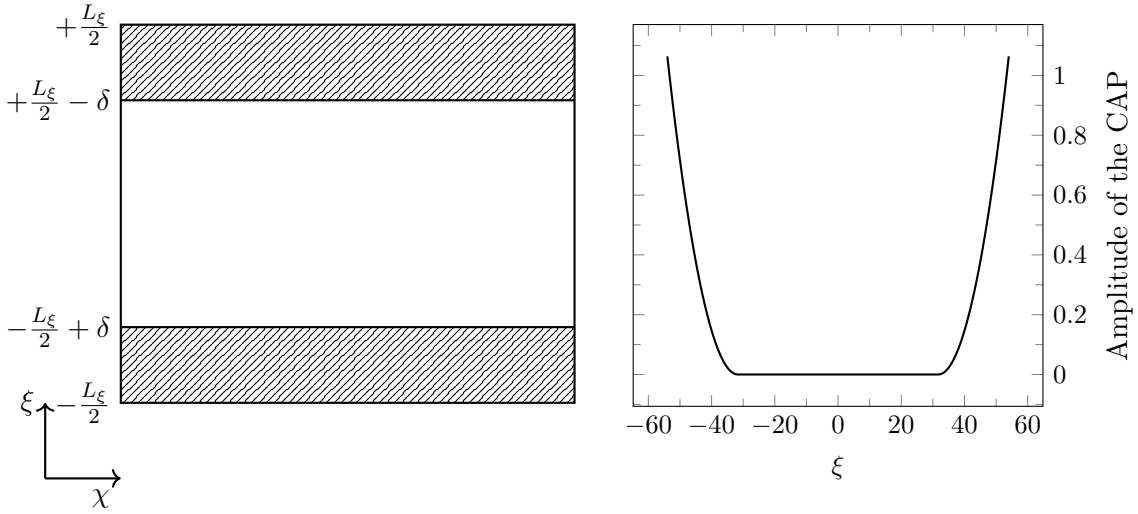

(a) Effective region of the CAP.

(b) Amplitude of the CAP.

Figure 4.1.: The computational domain is spanned by the center-of-mass and relative coordinates χ and ξ. At the boundaries of the ξ domain, the effective region of the CAP with layer thickness δ is indicated by the shaded region. The domain in relative direction is defined over the interval $\Omega_\xi = [-L_\xi/2, +L_\xi/2]$.

As illustrated in Fig. 4.1b, the amplitude begins to rise at the junction $\xi = \pm L_\xi/2 \mp \delta$ and increases continuously until it reaches its respective maximum at the computational domain edges $\xi = \pm L_\xi/2$. This ensures that no artificial reflections are generated due to an abrupt increase in the CAP, and that the physically relevant region at the center of the domain $\Omega_\xi|_{\xi=0}$ remains unaffected.
With the operational principle of the CAP now established, the derivation can be carried out next.

4.1.2. Derivation of the Complex Absorbing Potential Formalism

As explained in Section 4.1.1, the quantum transport equation requires an infinitely extended domain in the relative direction ξ. Mathematically speaking, this means that the statistical density ρ must asymptotically vanish. If the domain Ω_ξ is bounded by $[-L_\xi/2, +L_\xi/2]$, this condition can be expressed using Eq. (2.23) as [28]

$$\lim_{L_\xi \to \infty} \imath \frac{\hbar}{m} \frac{\partial}{\partial \chi} \rho(\chi, t) - \imath \frac{q}{\hbar} B(\chi, t) \rho(\chi, t) \Big|_{\xi=-L_\xi/2}^{\xi=+L_\xi/2} = 0. \tag{4.1}$$

Eq. (4.1) results from the L^2 integrability condition [28]. For finite L_ξ, this condition cannot be satisfied.
To derive a suitable CAP, which depends exclusively on the relative coordinate ξ and is compatible with the QLE, the properties of the drift term $B(\chi, \xi, t)$ in Eq. (2.23) must be analyzed. This term consists of a real part $\Re\{B(\chi, \xi, t)\}$, representing the conduction band potential and external fields, as well as an imaginary part $\Im\{B(\chi, \xi, t)\}$, which includes the

CAP. Notably, the real part exhibits odd symmetry with respect to ξ, whereas the imaginary part is even. These symmetry properties allow the drift term to be decomposed as follows [28]:

$$\Re\{B(\chi,\xi,t)\} = \mathcal{R}(\chi,\xi,t) = R(\chi+\frac{\xi}{2},t) - R(\chi-\frac{\xi}{2},t) \tag{4.2}$$

$$\Im\{B(\chi,\xi,t)\} = \mathcal{W}(\chi,\xi,t) = W(\chi+\frac{\xi}{2},t) + W(\chi-\frac{\xi}{2},t). \tag{4.3}$$

Next, the statistical density $\rho(\chi,\xi,t)$ from Eq. (2.23) must be expressed. Following the reasoning in Section 3.1.2, the density can be expanded in an arbitrary basis as [28]:

$$\rho(\chi,\xi,t) = \sum_j c_j(\chi,t)\cdot\mathbf{\Phi}_j(\xi) = \sum_j c_j(\chi,t)\cdot\sqrt{\frac{\Delta\xi}{L_\xi}}\exp(\imath k\cdot\xi), \tag{4.4}$$

where $c_j(\chi,t)$ are the expansion coefficients and $\mathbf{\Phi}_j(\xi)$ denotes the chosen basis. In this case, a plane wave basis is used, corresponding to $\sqrt{\Delta\xi/L_\xi}\,\exp(\imath k\cdot\xi)$. This leads to a system of coupled advection-reaction equations with respect to χ:

$$\imath\frac{\frac{\partial}{\partial\chi}c_j(\chi)}{c_j(\chi)} = \imath\frac{mq}{\hbar^2}B(\chi,\xi)\frac{\mathbf{\Phi}_j(\xi)}{\frac{\partial}{\partial\xi}\mathbf{\Phi}_j(\xi)} = \frac{mq}{\hbar^2 k}B(\chi,\xi). \tag{4.5}$$

Eq. (4.5) can be solved by combining the individual solutions into:

$$\rho(\chi,\xi)\propto\exp(\imath k\cdot\xi)\exp\left(-\imath\frac{mq}{\hbar^2 k}(\mathcal{R}(\chi,\xi)-\imath\mathcal{W}(\chi,\xi))\chi\right). \tag{4.6}$$

From this, an additional factor involving the imaginary part of $B(\chi,\xi)$ emerges. Since this term enters as a subtractive component, it becomes clear that for positive CAP values, this component has a damping effect. If the term vanishes, the statistical density remains unaffected. This satisfies the second condition from Section 4.1.1. However, the explicit χ-dependence of the imaginary part $\imath\mathcal{W}(\chi,\xi)$ violates the first requirement. Consequently, the imaginary potential must be reformulated to depend solely on ξ while preserving its even symmetry. Following [28], the CAP can be redefined as:

$$\mathcal{W}(\chi,\xi) := \mathcal{C}(\xi). \tag{4.7}$$

To integrate this into the QLE, a monomial basis depending on ξ is introduced [28]:

$$\mathcal{C}(\xi) = \begin{cases} \sum_m \beta\cdot(|\xi| - (\frac{L}{2}-\delta))^m, & \text{if } \frac{L}{2}-\delta < |\xi| < \frac{L}{2} \\ 0, & \text{otherwise.} \end{cases} \tag{4.8}$$

Here, δ denotes the layer thickness as shown in Fig. 4.1a, existing in the intervals $[-L_\xi/2, -L_\xi/2+\delta]$ and $[+L_\xi/2-\delta, +L_\xi/2]$. The monomial form (4.8) preserves the same symmetry as $\mathcal{W}(\chi,\xi)$ about the center $\xi=0$ of the domain Ω_ξ. The coefficient β is given by $\beta = W_0/\delta$, where W_0 represents the amplitude of the CAP. For the constant monomial $(|\xi| - (\frac{L}{2}-\delta))^0$, the coefficient β must be set to zero to avoid artificially induced reflections [28], thereby satisfying the third requirement. To fulfill the integrability condition (4.1), it is required that the statistical density vanishes at $|\xi| = L_\xi/2$ completely. Finally, the CAP can be introduced as an additional subtractive term in the drift expression (2.23):

$$B(\chi,\xi,t) = V\left(\chi+\frac{\xi}{2},t\right) - V\left(\chi-\frac{\xi}{2},t\right) - \imath\mathcal{C}(\xi). \tag{4.9}$$

4.2. Inflow Boundary Conditions

This section discusses the so-called inflow boundary conditions, which are used to describe the contact regions of a quantum device. The contacts are located at the left and right boundaries of the transport domain along the coordinate χ. Specifically, the left contact is positioned at $\chi = 0$ and the right contact at $\chi = L_\chi$. This defines a directed transport configuration along the positive χ-axis, where carriers are injected at one contact and collected at the opposite boundary.
Since this work primarily considers the transport of fermions (particles with half-integer spin [34]), the *Fermi-Dirac statistics* is applied. It describes the probability that a fermion occupies a given quantum state at a particular location, temperature, and chemical potential. Fermions are subject to the Pauli exclusion principle [34].
First, the statistical density matrix for an infinitely extended reservoir must be defined. Here, transversal wave propagation must be taken into account [58]:

$$\boldsymbol{\rho}(x, x^{'}) = \frac{1}{A}\sum_{\boldsymbol{k}_x}\sum_{\boldsymbol{k}_{||}} f_{3D}^{FD}(E(\boldsymbol{k}_{||}, \boldsymbol{k}_x) - \mu)\phi_{\boldsymbol{k}_x}(x)\phi_{\boldsymbol{k}_x}^{\dagger}(x^{'}). \tag{4.10}$$

$\boldsymbol{k}_x$ is the longitudinal wave vector component along the transport direction, and $\boldsymbol{k}_{||}$ is the lateral component perpendicular to the transport direction. f_{3D}^{FD} denotes the three-dimensional Fermi-Dirac distribution that determines the occupancy of states, μ is the Fermi level, and $\phi_{\boldsymbol{k}_x}(x)$ is the electron wavefunction. As outlined in Section 2.2.3, the lateral wave vector component $\boldsymbol{k}_{||}$ is neglected [2, 14]. Its summation $\sum_{\boldsymbol{k}_{||}}$ is evaluated via the integral expression $A/(2\pi)^2 \int d\boldsymbol{k}_{||}\, 2\pi\boldsymbol{k}_{||}$ [58]. This yields the simplified form:

$$\boldsymbol{\rho}(x, x^{'}) = \sum_{\boldsymbol{k}_x} f_{2D}^{FD}(E(\boldsymbol{k}_x) - \mu)\phi_{\boldsymbol{k}_x}(x)\phi_{\boldsymbol{k}_x}^{\dagger}(x^{'}). \tag{4.11}$$

The two-dimensional Fermi gas is defined as [58]:

$$f_{2D}^{FD}(E(\boldsymbol{k}_x) - \mu) = \frac{m k_B T}{2\pi\hbar^2} \cdot \ln\left\{1 + e^{-\frac{E(\boldsymbol{k}_x)-\mu}{k_B T}}\right\}. \tag{4.12}$$

The unknown wavefunction in the reservoir is modeled as a plane wave, $\phi_{\boldsymbol{k}_x}(x) = \exp(\imath \boldsymbol{k}_x x)/\sqrt{L}$, where L is a normalization constant [2]. The statistical density matrix in center-of-mass and relative coordinates is then given by:

$$\boldsymbol{\rho}(\chi, \xi) = \frac{1}{L}\sum_{\boldsymbol{k}_x} f_{2D}^{FD}(E(\boldsymbol{k}_x) - \mu)\exp(\imath \boldsymbol{k}_x \xi). \tag{4.13}$$

This makes clear why the choice of basis introduced in Section 3.1 is advantageous for determining the boundary conditions in the χ-coordinate: in both cases, an expansion into plane waves allows the LVNE (or QLE) to share the same basis as the boundary conditions in the χ-direction, enabling direct computation.
It is now important to distinguish between incoming waves and out-flowing ones. If a basis of plane waves is used, this can be done, for example, via the sign of the wave vector $\boldsymbol{k}$. If, as discussed in Section 3.1, the basis was obtained from a discretization matrix, then the eigenvalues λ_j correspond to the elements inside the wave vector $k_j = \lambda_j$. Consequently, the boundary conditions g and the wave packet assignment are defined as follows [GS2]:

$$g(\chi, \xi) = \begin{cases} 2_{Spin} \cdot f_{2D}^{FD}(E_L(\lambda) - \mu_L) & \text{for } \chi = 0,\ \lambda_j > 0, \\ 2_{Spin} \cdot f_{2D}^{FD}(E_R(\lambda) - \mu_R) & \text{for } \chi = L_\chi,\ \lambda_j < 0. \end{cases} \tag{4.14}$$

Next, it must be ensured that the statistical density matrix remains spatially constant at the transition between reservoir and device [2, 14, 71]:

$$\frac{\partial}{\partial\chi}g(\chi=0,\xi)=0 \qquad \text{and} \qquad \frac{\partial}{\partial\chi}g(\chi=L_\chi,\xi)=0. \tag{4.15}$$

Next, the boundary conditions for the multiband models shall be established. Since the MEF method is used, band coupling mechanisms only exist in regions where the potential gradient is non-zero, i.e., $\partial_\chi V \neq 0$ [79]. Therefore, no band coupling occurs within the reservoirs, where the potential is constant. Based on this, the inflow boundary conditions for electrons entering the conduction band are:

$$g_{cc}(\chi,\xi)=2_{Spin}\cdot f_{2D}^{FD}(E_{c,L}(\lambda)-\mu_L) \qquad \text{for } \chi=0,\ \lambda_j>0, \tag{4.16}$$

and for electrons exiting the conduction band:

$$g_{cc}(\chi,\xi)=2_{Spin}\cdot f_{2D}^{FD}(E_{c,R}(\lambda)-\mu_R) \qquad \text{for } \chi=L_\chi,\ \lambda_j<0. \tag{4.17}$$

Similarly, the inflow of holes into the valence band is given by:

$$g_{vv}(\chi,\xi)=2_{Spin}\cdot f_{2D}^{FD}(-E_{v,L}(\lambda)+\mu_L) \qquad \text{for } \chi=0,\ \lambda_j>0, \tag{4.18}$$

and their outflow by:

$$g_{vv}(\chi,\xi)=2_{Spin}\cdot f_{2D}^{FD}(-E_{v,R}(\lambda)+\mu_R) \qquad \text{for } \chi=L_\chi,\ \lambda_j<0. \tag{4.19}$$

From a physical standpoint, g_{vv} describes the injection of holes at those contacts where electrons leave the device. This relation follows the boundary condition concept introduced in [56].
In addition to the terms ρ_{cc} and ρ_{cv}, the interband transport model introduced in Chapter 3 contains the off-diagonal density matrix elements ρ_{cv} and ρ_{vc}, which describe the quantum coherence between conduction and valence bands.
The inflow boundary conditions specified above apply only to the aforementioned components, since these correspond to particles injected from thermal reservoirs characterized by Fermi-Dirac statistics. In contrast, the contacts are assumed not to introduce any coherent superposition between bands.
In the present model, interband mixing at the contracts is neglected. Consequently, the contacts do not act as sources or sinks of interband coherence. The only physically required condition is therefore the absence of the net coherence flux across the boundary.
This leads to the natural Neumann boundary condition [58]

$$\frac{\partial}{\partial\chi}g_{cv}=0, \qquad \frac{\partial}{\partial\chi}g_{vc}=0, \tag{4.20}$$

which ensures conservation of the coherence and preservers the self adjointness of the transport operator [32].
A Dirichlet condition $g_{cv}=0$ would correspond to strong dephasing or pair-breaking contacts that completely suppress interband coherence and is therefor not appropriate for the present device model.
The Neumann condition is equivalent to requiring that the interband coherence current vanishes at the contacts, consistent with a purely reflecting boundary for the coherent component [31, 32].

With both computational domains Ω_χ and Ω_ξ and their boundary conditions now fully defined, the next Chapter 5 will thoroughly discuss the numerical methods used to approximate the quantum transport models introduced in Chapter 3.

Summary: Chapter 4 addressed the necessary boundary conditions for the numerical approximation of quantum transport. The two computational domains Ω_ξ and Ω_χ required a physically meaningful termination at their respective boundaries. In the ξ-direction, wave propagation to infinity had to be ensured. Since this is not feasible numerically, a CAP was introduced to completely attenuate the wave packets at both ends $\partial\Omega_\xi$.
At the boundaries $\partial\Omega_\chi$, so-called inflow boundaries based on the Fermi-Dirac distribution were formulated. These conditions ensure the physically correct injection and absorption of charge carriers at the simulation domain boundaries.

5. Numerical Approximation with the Discontinuous Galerkin Method

In Chapter 2, the quantum transport equations – particularly the LVNE – were introduced as the foundation for modeling charge carrier transport. Building on this foundation, Chapter 3 derived various approximation models, including those for one-dimensional transport, intraband and interband transport, as well as for systems with a spatially varying effective electron mass. Subsequently, Chapter 4 established boundary conditions for the computational domains Ω_χ and Ω_ξ. In Ω_χ, inflow conditions based on Fermi-Dirac statistics were defined to describe the injection and transmission of electrons and holes. For the domain Ω_ξ, which theoretically extends to infinity, open boundary conditions were imposed. To this end, the CAP was introduced to attenuate all propagating wave packets at the domain boundaries $\partial\Omega_\xi$ without reflections, thus avoiding undesired interference effects.
This main chapter is structured as follows. After a historical overview of the DG method and an introduction to common numerical approximation techniques in Section 5.1, Section 5.2 presents several preliminary considerations relevant to the method. These include a discussion of the general operating principle (5.2.1), existence and uniqueness of solutions (5.2.2), as well as stability and consistency (5.2.3), all of which are examined from a mathematical standpoint. To this end, the LVNE is discretized using the DG method, and error rates and convergence behavior are analyzed by comparison with a model equation and a reference solution.
Section 5.3 will then address the discretization of the intraband quantum transport model introduced in Section 3.2. Section 5.4 follows with the incorporation of a spatially varying effective mass into the DG simulation scheme. Furthermore, Section 5.5 subsequently discusses the discretization of the interband quantum transport model from Section 3.4. After all transport models have been spatially discretized, Section 5.6 outlines the treatment of the time domain using explicit time integration methods. Finally, Section 5.7 presents the numerical approximation of the Poisson equation introduced in Section 2.3, which is used to ensure self-consistency.

5.1. Historical Background and Comparison with Classical Methods

Historical Background: The DG method was first introduced by Reed and Hill in 1973 [21] for computing neutron flux. The method owes its name, however, to the Galerkin approach. This technique was developed by the Russian mathematician Boris Grigorievich Galerkin [85] to solve Partial Differential Equations (PDEs) numerically. Galerkin introduced the principle of the *least residual*, where the residual denotes the deviation between the exact and the approximate solution. The approximation itself is expressed as a linear combination of so-called basis functions [24]. By requiring that the residual be minimized, test functions are introduced that belong to the

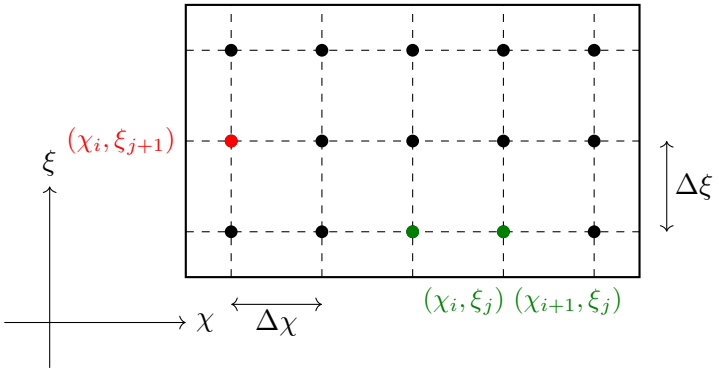

Figure 5.1.: Schematic representation of the discretization of a two-dimensional computational domain using the FD method.

same vector space as the solution. From a mathematical perspective, this corresponds to the orthogonality between the residual and the test functions and can be expressed according to:

$$\int \mathcal{R}_h(x,t) l_j(x) dx = 0, \tag{5.1}$$

where $\mathcal{R}_h$ is the residual and l_j the test functions.
When both, the basis and test functions, are defined element-wise, the resulting approach is known as the FEM [24]. Similarly, for the Galerkin method the basis and test functions are chosen to be identical as well. In the FEM, the elements are inherently coupled, resulting in a continuous model across the domain. The reason for this coupling will be discussed in more detail later. In their seminal 1973 work [21], Reed and Hill decoupled the finite elements, thereby deriving a *discontinuous* Galerkin method from the FEM. The advantages – and disadvantages – of this approach will be explored in the following sections.
Evaluation of yet another numerical method, given the multitude of available schemes for approximating PDEs, might seem redundant. To justify this, it is helpful to take a brief look at the most common finite approximation techniques, particularly the FD, FV, and FEM methods.

Finite Difference (FD) Method: The FD method is a discretization technique that divides the computational domain into a fixed number of discrete grid points. If the domain is two-dimensional – for instance, consisting of a transport direction χ and a relative direction ξ, as illustrated in Fig. 5.1 – then a grid of equidistant points is formed. Assigning the discrete positions along the transport direction χ with an index i, the solution at these locations can be approximated as follows [86]:

$$\begin{aligned} \text{Forward differences:} \quad & u_i' = \frac{u_{i+1} - u_i}{\Delta\chi} \\ \text{Backward differences:} \quad & u_i' = \frac{u_i - u_{i-1}}{\Delta\chi} \\ \text{Central differences:} \quad & u_i' = \frac{u_{i+1} - u_{i-1}}{2\Delta\chi}. \end{aligned} \tag{5.2}$$

Here, u represents the function value being sought, and $\Delta\chi$ is the spacing between two neighboring grid points, as depicted in Fig. 5.1. The equations in (5.2) have a simple,

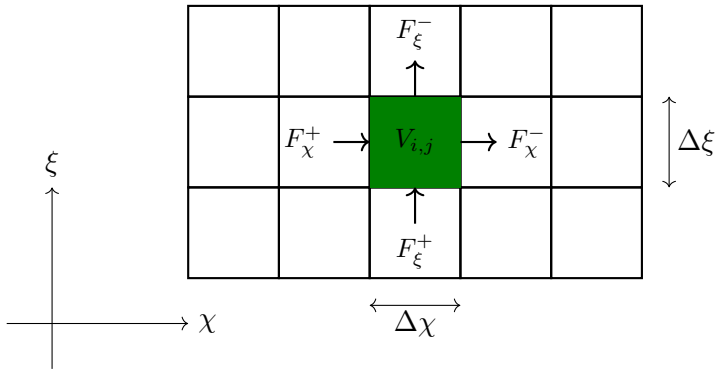

Figure 5.2.: Schematic representation of the discretization of a two-dimensional computational domain using the FV method.

straightforward structure, keeping their implementation and computational cost relatively low [86]. This simplicity constitutes the primary advantage of the method. However, when more complex geometries than a simple rectangle are to be considered, the strengths of the FD method quickly diminish – for example, representing curved boundaries such as circles is difficult using a regular Cartesian grid. Moreover, this method is unsuitable for problems governed by conservation laws [87]. These typically include scenarios in which mass, energy, or momentum conservation is of utmost importance. This shortcoming arises from the fact that the FD method does not adequately enforce the integral form of the governing equations [87]. In such cases, the FV method is more appropriate.

Finite Volume (FV) Technique: Especially in computational fluid dynamics, the enforcement of conservation laws is essential. In this context, so-called fluxes play a central role, as they must enter and exit a control volume in equal measure. In Fig. 5.2, these fluxes are shown as $F_\chi^\pm$, representing the inflow and outflow in the transport direction χ, as well as $F_\xi^\pm$, which analogously denote the inflow and outflow in the relative direction ξ. The control volume $V_{i,j}$, with a volume of $V_{i,j} = \Delta\chi \cdot \Delta\xi$, is highlighted in green. The fluxes shown in Fig. 5.2 are numerical fluxes that regulate the flow of information between neighboring elements [87]. In the FV technique, these elements are referred to as finite volumes (hence the name of the method). They are chosen to be infinitesimally small in order to discretize the domain of interest. The numerical flux ensures that the amount exiting one volume ($F_{\chi,\xi}^-$) enters the adjacent volume ($F_{\chi,\xi}^+$). This allows the FV method to more accurately approximate a problem, where the propagation of shock waves in incompressible fluids is of primary importance [87]. Numerically, the FV method is more stable in handling discontinuities and steep gradients than the FD method. This is due to the fact that the FV method solves the integral form of the conservation equations, thereby preserving conserved quantities such as mass, momentum, and energy. In contrast, the FD method is based on the differential form, which does not explicitly account for steep gradients or discontinuities [86, 88].

Nonetheless, there are two major drawbacks to both methods:

1. The FD method is limited to simple geometries. For curved or sharply-edged domains, the accuracy near boundaries suffers significantly, which can have a substantial impact on the results [86].

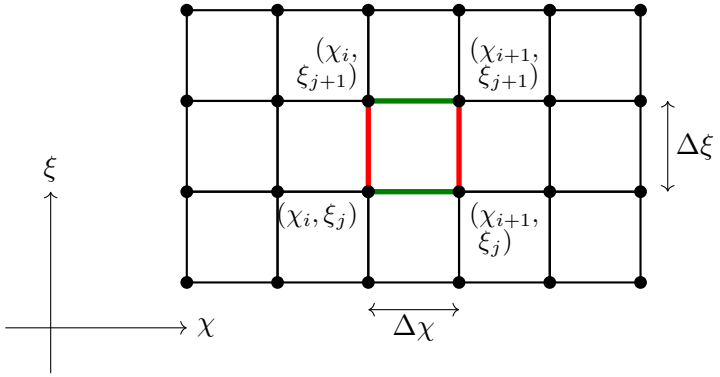

Figure 5.3.: Schematic illustration of the discretization of a two-dimensional computational domain using the finite element method (FEM). Dark green: bar elements in χ-direction; red: bar elements in ξ-direction.

2. In the FV technique, low-order polynomial approximations are often used within a control volume to keep the computational effort manageable. However, this comes at the expense of local accuracy [87].

When analyzing structures with highly complex geometries, where the formulation of appropriate boundary conditions is essential, the FEM is employed.

Finite Element method (FEM): As previously mentioned, the FEM is based on the continuous Galerkin method, with the distinctive feature that finite elements are used to subdivide the computational domain into smaller regions, see Fig. 5.3. The elements used are infinitesimally small, similar to the finite volumes in the FV method. As with the previous schemes, the smaller the elements, the higher the computational cost [24]. In the FD method, the accuracy can be improved either by reducing the grid spacing (h-refinement) or by increasing the order of the finite difference stencil based on higher-order Taylor expansions. In the latter case, additional neighboring grid points are incorporated into the approximation without necessarily reducing the grid size.
By contrast, the FEM provides two analogous mechanisms for improving accuracy: the element size can be reduced (h-refinement), and the polynomial order of the shape functions within each element can be increased (p-refinement). The polynomial degree determines the order of the approximation (linear, quadratic, cubic, etc.), enabling systematic control over the discretization accuracy [24].
Higher-order functions are capable of capturing curvature more accurately, thereby reducing the residual and improving the overall accuracy of the solution. While both FD and FEM allow accuracy improvement through refinement and higher-order approximations, FEM offers additional advantages such as geometric flexibility, variational consistency, and the possibility of local h- and p-refinement. These properties are particularly beneficial for complex, coupled quantum transport problems.
The term 'nodes' refers to the points that define and delimit each element. As indicated in Fig. 5.3, an element in its simplest form (one-dimensional) consists of two nodes, which mark the start and end of the line element shown in green (or red). In this example, $\Delta\chi$ denotes the length of a horizontal element (green) and $\Delta\xi$ the length of a vertical element (red). In the FEM, two types of representations are typically used, which are briefly described below.

1. **Nodal representation**
   The solution is represented using trial functions (basis functions) that are defined locally at the mesh nodes. These functions are typically described by using Lagrange polynomials [24, 89]. The number of nodes directly correlates with the polynomial degree of the Lagrange functions according to the definition $N = N_p - 1$, where N_p is the number of nodes.
   The unknowns in this approach are the function values at the nodal points [89].
   This type of representation is particularly straightforward to implement and well-suited for linear or low-order elements [89]. It is predominantly used in simulations involving structural mechanics, heat conduction, and fluid dynamics [22].

2. **Modal representation**
   This representation is based on global basis functions constructed from orthogonal polynomials. Here, the unknowns are not the nodal values, but the coefficients of the basis functions themselves.
   This means that the solution is not represented at discrete nodal points, but rather over the entire length of the element. Therefore, the modal representation is often used in vibration analysis. However, its implementation and computational cost are higher, especially for complex geometries or nonlinear problems [89].

In the FD method, reducing the grid spacing $\Delta\chi$ decreases the truncation error and thereby improves the accuracy of the numerical solution. However, such h-refinement does not change the formal order of convergence of the scheme, which is determined by the chosen difference stencil. An increase in the approximation order requires the explicit construction of a higher-order FD scheme, typically involving a wider stencil and additional neighboring grid points. In contrast, within the FEM framework, the polynomial degree of the approximation functions can be increased locally and independently of the mesh size. This enables p-refinement without enlarging the computational stencil, as the approximation remains element-local [18, 19, 24, 86, 89].
It is now known that finite elements are defined and bounded by nodes. The next step is to demonstrate how continuity is maintained across multiple finite elements.
The transport direction χ is subdivided into a fixed number of one-dimensional finite elements N_χ. For example, if a row of discretization elements in the transport direction χ is extracted from Fig. 5.3, it is discretized into five finite elements. Each of these elements has two nodes, and the shape functions are of degree $N = N_p - 1 = 2 - 1 = 1$. This results in the linear profiles of the two shape functions $N_1(\chi)$ (dark green) and $N_2(\chi)$ (red) shown in Fig. 5.4. It now remains to clarify how continuity between finite elements is maintained. After all, it must be ensured that effects acting on the left side of the computational domain Ω_χ are actually transmitted to the right side via the approximating elements.
Although a single finite element consists of two nodes, one of these nodes is shared with the adjacent element. In the case of five finite elements discretizing the entire transport direction χ, this means that only six nodes exist in total. Put differently: the right node of the first element is simultaneously the left node of the second element. This has certain implications for the implementation, which directly reveal the primary disadvantage of the FEM method.

In terms of implementation, matrices are used, which arise from the shape of the finite elements, with their dimension corresponding to the number of nodes N_p. In the specific case shown in Fig. 5.3, the resulting matrices have dimension 2×2. If continuity is guaranteed, the five finite elements can be assembled

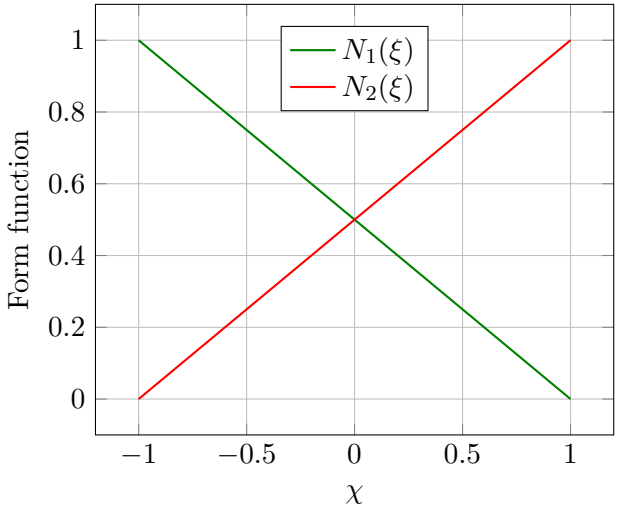

Figure 5.4.: Visualization of the linear shape functions for a one-dimensional finite element with $N_p = 2$ nodes.

to describe the entire transport domain χ according to the following schema [24]:

$$\boldsymbol{S}_{\text{local}} = \begin{pmatrix} a & b \\ c & d \end{pmatrix}$$

$$\boldsymbol{S}_{\text{global}} = \begin{pmatrix} a & b & 0 & 0 & 0 & 0 \\ c & a+d & b & 0 & 0 & 0 \\ 0 & c & a+d & b & 0 & 0 \\ 0 & 0 & c & a+d & b & 0 \\ 0 & 0 & 0 & c & a+d & b \\ 0 & 0 & 0 & 0 & c & d \end{pmatrix} \tag{5.3}$$

Here, $\boldsymbol{S}_{\text{local}}$ in Eq. (5.3) represents an arbitrary matrix corresponding to a single finite element. Since all finite elements in the transport direction χ are identical, this matrix applies equally to all considered elements. If one now wishes to derive a system that encompasses all elements and describes the entire computational domain in Ω_χ, the matrix $\boldsymbol{S}_{\text{global}}$ is constructed as shown in Eq. (5.3). It contains the local matrix $\boldsymbol{S}_{\text{local}}$ along its main diagonal. One can observe that the elements a and d are added for $\boldsymbol{S}^{i,i}_{\text{global}}$ with $i = 2...5$. As previously discussed, this includes the nodes that are shared between two neighboring elements. The addition of the matrix entries ensures continuity of the overall system. The drawback of such a matrix, however, is the inefficiency of its inversion [68].

The structure of the global matrix shown in Eq. (5.3) resembles a staircase form. Typically, a successful application of the FEM to one-dimensional problems results in a final equation of the form $\boldsymbol{S}_{\text{global}} \cdot \boldsymbol{x} = \boldsymbol{b}$, where the vector $\boldsymbol{x}$ contains the unknowns and $\boldsymbol{b}$ contains the boundary conditions. To solve this system, the matrix $\boldsymbol{S}_{\text{global}}$ must be inverted and multiplied by $\boldsymbol{b}$. The inversion of a matrix with such structure tends to be computationally inefficient, since the matrix must be inverted in its entirety [89]. A more desirable structure would be a so-called *block-diagonal* matrix. It is at this point that the DG method plays a decisive role.

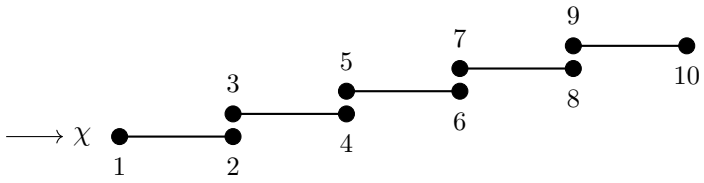

Figure 5.5.: Schematic representation of the discretization of a one-dimensional computational domain using the discontinuous Galerkin (DG) method. In this example, the finite elements are stacked to illustrate the overlap.

5.2. Preliminary Considerations for the Discontinuous Galerkin Method

In order for the DG method to be used for the numerical discretization of the intraband and interband quantum transport models from Chapter 3, the general functionality of the method and its advantages as well as disadvantages must be outlined first.

5.2.1. General Functionality

As established earlier, the FEM is based on the continuous Galerkin method. Accordingly, the DG method can be seen as an extension of the FEM. Here, too, finite elements are used, but unlike in FEM, these no longer share nodes – instead, each element possesses its own set of nodes. As illustrated in Fig. 5.5, the finite elements are overlapping, i.e., two nodes exist at the same spatial location, which is emphasized by the staggered layout. Consequently, the node pairs $(2,3)$, $(4,5)$, $(6,7)$, and $(8,9)$ share the same spatial coordinate in the χ domain. In the literature, these are referred to as overlapping finite elements [24]. Furthermore, it is apparent that a total of ten nodes are created with this new type of discretization. From a mathematical perspective, the decoupling of the discretization elements results in a significant advantage. If once again the local matrix $\boldsymbol{S}_{\text{local}}$ from Eq. (5.3) is considered, a new global matrix can be derived. Since the same finite elements with two nodes (as in FEM) are used, this approach is justified [89]. The global matrix $\boldsymbol{S}_{\text{global}}$ for the DG method is then constructed as follows:

$$\boldsymbol{S}_{\text{global}} = \begin{pmatrix} a & b & 0 & 0 & 0 & 0 & 0 & 0 & 0 & 0 \\ c & d & 0 & 0 & 0 & 0 & 0 & 0 & 0 & 0 \\ 0 & 0 & a & b & 0 & 0 & 0 & 0 & 0 & 0 \\ 0 & 0 & c & d & 0 & 0 & 0 & 0 & 0 & 0 \\ 0 & 0 & 0 & 0 & a & b & 0 & 0 & 0 & 0 \\ 0 & 0 & 0 & 0 & c & d & 0 & 0 & 0 & 0 \\ 0 & 0 & 0 & 0 & 0 & 0 & a & b & 0 & 0 \\ 0 & 0 & 0 & 0 & 0 & 0 & c & d & 0 & 0 \\ 0 & 0 & 0 & 0 & 0 & 0 & 0 & 0 & a & b \\ 0 & 0 & 0 & 0 & 0 & 0 & 0 & 0 & c & d \end{pmatrix}. \tag{5.4}$$

This clearly shows that the discretization elements in Fig. 5.5 are indeed decoupled. Two key observations follow:

1. The global matrix of the DG method in Eq. (5.4) is block-diagonal. This allows local

inversion, i.e., the blocks along the main diagonal can be inverted independently, resulting in increased computational efficiency [68].

2. The global matrix in Eq. (5.4) has a higher dimension than the one in Eq. (5.3). This arises because the DG method involves more nodes, and due to the separation of the finite elements, the resulting matrix is larger. The following relationships apply:

   - The number of nodes N_p^{FEM} in FEM is given by the number of discretization elements N_χ as $N_p^{\mathrm{FEM}} = (N_p^{\mathrm{local}} - 1)N_\chi + 1$, where N_p^{local} is the number of nodes in a single finite element. The global matrix thus has dimension $N_p^{\mathrm{FEM}} \times N_p^{\mathrm{FEM}}$.
   - The number of nodes N_p^{DG} in the DG method is given by $N_p^{\mathrm{DG}} = N_p^{\mathrm{local}} \cdot N_\chi$. Accordingly, the global matrix has dimension $N_p^{\mathrm{DG}} \times N_p^{\mathrm{DG}}$.

Obviously, no physical process can be accurately reproduced with completely decoupled elements. For instance, if Fig. 5.5 represented the discretization of a device with contacts at both ends, one would need to ensure that the incoming current exits at the opposite end. With decoupled elements, no transmission would occur. Furthermore, the existence of two independent nodes may lead to discontinuities in the solution, contradicting the conservative nature of the quantum transport equation and leading to an overdetermined system from a mathematical standpoint [68]. In the literature, this overdetermination problem is known as the *Riemann problem* [21, 22, 68, 87].

Addressing the Riemann Problem

The Riemann problem refers to solving a system of PDEs with an initial condition that contains a discontinuity (e.g., a jump). In the case of the DG method, such discontinuities occur at the edges of the finite elements, since neighboring elements are defined independently of each other. As a result, two different function values can exist at the same spatial coordinate.
To resolve this, a concept from the FV technique – already introduced earlier – is employed: the numerical flux. Since each element interface is affected, this is referred to as a local

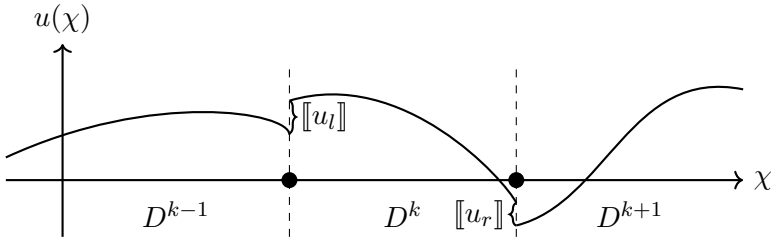

Figure 5.6.: Visualization of discontinuities at element interfaces, arising from discontinuous approximation functions within a finite element D^k. The jump at the left interface is labeled $[\![u_l]\!]$ and at the right interface $[\![u_r]\!]$.

Riemann problem [68]. The goal is to find a suitable expression for each interface that couples adjacent element nodes and thereby resolves the discontinuity. This transforms the originally overdetermined system into a consistent and solvable one. There are two main approaches [90]:

1. **Exact solution of the Riemann problem**: These methods compute the exact wave structure from the initial discontinuity at the element interface. This is often computationally expensive due to the need for detailed analysis of the governing equations [91].

2. **Approximate solution of the Riemann problem**: These approaches use numerical or approximate methods to solve the Riemann problem. Common examples include the Lax-Friedrichs, Roe, or HartenLaxvan Leer fluxes, which are less computationally intensive and widely used in practice [87].

In the following, the Riemann problem is illustrated using a simple advection equation with similar structure:

$$\frac{\partial}{\partial t}u(x,t) + \frac{\partial}{\partial x}f(u(x,t)) = 0 \tag{5.5}$$

with flux function $f(u(x,t)) = s \cdot u(x,t)$, where s is the propagation speed of the shock wave. The equation is subject to the discontinuous initial condition

$$u(x, t=0) = \begin{cases} u^-, & x < 0 \\ u^+, & x > 0. \end{cases} \tag{5.6}$$

Even at discontinuous transitions like jumps, it must be ensured that conserved quantities – such as mass, energy, or momentum – are transmitted correctly. No mass or energy must be lost. This is guaranteed by the *Rankine-Hugoniot condition* [87], which in the scalar case reads:

$$\begin{aligned} su &= f(u) \\ \Leftrightarrow s(u^- - u^+) &= (f^- - f^+). \end{aligned} \tag{5.7}$$

Eq. (5.7) establishes a relation between the propagation speed s, the states before (u^+) and after (u^-) the discontinuity, and their respective fluxes [87]. If the Rankine-Hugoniot condition is expressed as a linear system with $f(u) = \boldsymbol{A}u$, it can be assumed that the matrix $\boldsymbol{A}$ has real, distinct eigenvalues $\lambda_p \in p = 1, ..., m$ and is therefore diagonalizable, according to the linear decomposition:

$$\boldsymbol{A} = \boldsymbol{\Phi}\boldsymbol{\Lambda}\boldsymbol{\Phi}^{-1}. \tag{5.8}$$

Here, $\boldsymbol{\Phi} = [\boldsymbol{\phi}_1, \boldsymbol{\phi}_2, ..., \boldsymbol{\phi}_m]$ is the transformation matrix whose columns are the eigenvectors of $\boldsymbol{A}$, corresponding to the eigenvalues λ_p within the vector $\boldsymbol{\Lambda}$. From this, the eigenvalue equation

$$\boldsymbol{A}\boldsymbol{\phi}_p = \lambda_p \boldsymbol{\phi}_p \tag{5.9}$$

can be constructed. Furthermore, the two discontinuities u^- and u^+ can be represented in their respective eigenvector bases as

$$u^- = \sum_{p=1}^{m} \alpha_p \boldsymbol{\phi}_p \qquad \text{and} \qquad u^+ = \sum_{p=1}^{m} \beta_p \boldsymbol{\phi}_p. \tag{5.10}$$

With $v = \boldsymbol{\Phi}^{-1}u$, and due to the characteristic structure of the advection equation, it follows that

$$v_p(x,t) = \begin{cases} \alpha_p, & x - \lambda_p t < 0 \\ \beta_p, & x - \lambda_p t > 0. \end{cases}$$

If m' is the last index p for which $x - \lambda_p t > 0$ still holds, then the sums from Eq. (5.10) can be limited as

$$u(x,t) = \sum_{p=1}^{m'} \beta_p \boldsymbol{\phi}_p + \sum_{m'}^{m} \alpha_p \boldsymbol{\phi}_p.$$

Within the individual segments, the solution is constant but jumps at the p-th characteristic $x_p = \lambda_p t$. This jump is defined as

$$-[\![u_p]\!] = (\beta_p - \alpha_p)\boldsymbol{\phi}_p. \tag{5.11}$$

From the linear system $f(u) = \boldsymbol{A}u$, the flux at the discontinuity can be derived as

$$[\![f]\!]_p = \boldsymbol{A}[\![u]\!]_p \overset{(5.11)}{=} -(\beta_p - \alpha_p)\boldsymbol{A}\boldsymbol{\phi}_p \overset{(5.9)}{=} -(\beta_p - \alpha_p)\lambda_p\boldsymbol{\phi}_p = \lambda_p[\![u]\!]_p.$$

To obtain the numerical flux $\hat{f}$ for the DG method, u must be evaluated at the element interfaces ($x = 0$ or $x = \Delta\chi$) of each finite element. However, since the right edge of the reference element coincides with the left edge of the neighboring element, the left-side discontinuities from u^- or the right-side discontinuities from u^+ can be summed, depending on the chosen perspective. This yields

$$\begin{aligned} u(x=0) &= u^- - \textstyle\sum_{\lambda_p<0}(\beta_p - \alpha_p)\boldsymbol{\phi}_p = u^+ - \sum_{\lambda_p>0}(\beta_p - \alpha_p)\boldsymbol{\phi}_p \\ \Rightarrow u(x=0) &= \frac{u^- + u^+}{2} + \frac{1}{2}\left\{\textstyle\sum_{\lambda_p<0}(\beta_p - \alpha_p)\boldsymbol{\phi}_p - \sum_{\lambda_p>0}(\beta_p - \alpha_p)\boldsymbol{\phi}_p\right\}. \end{aligned} \tag{5.12}$$

Finally, this is multiplied by the linear decomposition from Eq. (5.8), where $\boldsymbol{\Lambda} = \boldsymbol{\Lambda}^+ + \boldsymbol{\Lambda}^-$ is split into its positive ($\boldsymbol{\Lambda}^+$) and negative ($\boldsymbol{\Lambda}^-$) components. It is also used that $\sum_j(\boldsymbol{\Phi}^{-1})_{i,j}(\boldsymbol{\phi}_p)_j = \delta_{i,p}\boldsymbol{I}_p$, where $\boldsymbol{I}_p$ denotes a unit vector. This results in the numerical flux $\hat{f}$ as

$$\begin{aligned} \hat{f} &= \boldsymbol{A}\{u\} + \frac{1}{2}\left\{\boldsymbol{\Phi}(\boldsymbol{\Lambda}^+ + \boldsymbol{\Lambda}^-)\boldsymbol{\Phi}^{-1}\right\}\textstyle\sum_{\lambda_p<0}(\beta_p - \alpha_p)\boldsymbol{\phi}_p \\ &\quad - \frac{1}{2}\left\{\boldsymbol{\Phi}(\boldsymbol{\Lambda}^+ + \boldsymbol{\Lambda}^-)\boldsymbol{\Phi}^{-1}\right\}\textstyle\sum_{\lambda_p>0}(\beta_p - \alpha_p)\boldsymbol{\phi}_p \\ &= \boldsymbol{A}\{u\} + \frac{1}{2}\left\{\boldsymbol{\Phi}\boldsymbol{\Lambda}^-\boldsymbol{\Phi}^{-1}\textstyle\sum_{\lambda_p<0}(\beta_p - \alpha_p)\boldsymbol{\phi}_p - \boldsymbol{\Phi}\boldsymbol{\Lambda}^+\boldsymbol{\Phi}^{-1}\sum_{\lambda_p>0}(\beta_p - \alpha_p)\boldsymbol{\phi}_p\right\}, \end{aligned}$$

where $\{u\} = (u^- + u^+)/2$. Introducing the shorthand notation $|\boldsymbol{A}| = (|\boldsymbol{A}|)_{i,j} = |\boldsymbol{A}_{i,j}|$, the numerical flux $\hat{f}$ can be further simplified as

$$\begin{aligned} \hat{f} &= \boldsymbol{A}\{u\} + \frac{1}{2}\left\{-\boldsymbol{\Phi}|\boldsymbol{\Lambda}^-|\boldsymbol{\Phi}^{-1}\textstyle\sum_{\lambda_p<0}(\beta_p - \alpha_p)\boldsymbol{\phi}_p - \boldsymbol{\Phi}\boldsymbol{\Lambda}^+\boldsymbol{\Phi}^{-1}\sum_{\lambda_p>0}(\beta_p - \alpha_p)\boldsymbol{\phi}_p\right\} \\ &= \boldsymbol{A}\{u\} - \frac{1}{2}\underbrace{\left(\boldsymbol{\Phi}|\boldsymbol{\Lambda}^-|\boldsymbol{\Phi}^{-1} + \boldsymbol{\Phi}\boldsymbol{\Lambda}^+\boldsymbol{\Phi}^{-1}\right)}_{=\boldsymbol{\Phi}|\boldsymbol{\Lambda}|\boldsymbol{\Phi}^{-1}\equiv|\boldsymbol{A}|}\textstyle\sum_p(\beta_p - \alpha_p)\boldsymbol{\phi}_p \\ &\overset{(5.12)}{=} \boldsymbol{A}\{u\} - \frac{1}{2}|\boldsymbol{A}|(u^+ - u^-) \\ &= \boldsymbol{A}\{u\} + \frac{1}{2}|\boldsymbol{A}|[\![u]\!]. \end{aligned}$$

The same applies if $\boldsymbol{A}$ is already a diagonal matrix. Finally, the transformation $u = \boldsymbol{\Phi}v$ is carried out so that the advection equation (5.5) in the new basis becomes

$$\frac{\partial}{\partial t}v + \frac{\partial}{\partial x}\boldsymbol{\Lambda}v = 0.$$

As shown earlier, the upwinding flux follows as

$$\hat{f} = \hat{\boldsymbol{\Lambda}}v = \boldsymbol{\Lambda}\{v\} + \frac{1}{2}|\boldsymbol{\Lambda}|[\![v]\!], \tag{5.13}$$

which is exactly the numerical upwind flux [68, 87]. In its weighted form, the numerical flux is also given as [68]

$$\hat{f} = \mathbf{\Lambda}\{v\} + \frac{1-\alpha}{2}|\mathbf{\Lambda}|[\![v]\!], \tag{5.14}$$

where the parameter α allows for exclusion of the jump $[\![v]\!]$ entirely ($\alpha = 1$), resulting in the central flux consisting only of the mean value $\{v\}$. For all other values $0 < \alpha < 1$, the contribution of the jump term can be controlled, eventually recovering the standard upwind flux when $\alpha = 0$ as is given in Eq. (5.13) [68].

The advantages of the upwind flux over other numerical fluxes and its derivation specifically for the DG method will be discussed in the following section.

The Numerical Flux

The numerical flux is an approximate method used to treat the Riemann problem. It makes use of the Rankine-Hugoniot condition to ensure that the density flux remains consistent even at discontinuities. Combined with decoupled finite elements, the numerical flux makes the DG method one of the most flexible numerical approximation techniques, as highlighted in Tab. 5.1 [68]. The DG method combines the high local accuracy of the FEM with the flexibility

Table 5.1.: Suitability of the presented numerical approximation methods for solving different classes of PDEs. A ✗ indicates that the method is unsuitable for a particular type of PDE. A ✓ denotes suitability, and (✓) means the method is applicable but not ideal [68].

	Complex Geometries	***hp*-Adaptivity**	**Expl. Semi-Discrete Form**	**Conservation Laws**	**Elliptic Problems**
FD	✗	✓	✓	✓	✓
FV	✓	✗	✓	✓	(✓)
FEM	✓	✓	✗	(✓)	✓
DG	✓	✓	✓	✓	(✓)

of the FV approach. Fig. 5.7 provides a visual representation of the numerical flux. In practical terms, the numerical flux connects the discontinuities between adjacent elements [68], effectively merging the overlapping nodes into a single point. In mathematical terms, the single-valued numerical flux replaces the two-valued flux [GS2].
It remains to be discovered what advantage this provides in terms of computational efficiency. To address this, it must be considered how the global system matrix changes when the numerical flux is included. Based on Fig. 5.6, the numerical flux for a one-dimensional finite element with two nodes is derived. For this purpose, the notation used in Fig. 5.6 is adapted. The normal vectors $n^{\pm}$ in Fig. 5.8 are oriented orthogonally to the element interfaces and thus to the wave propagation direction. The superscript '$-$' refers to internal information, i.e., inside the reference element, while the superscript '$+$' denotes external information, i.e., outside the reference element. Based on the function values in Fig. 5.8 and Eq. (5.14), the upwind flux can

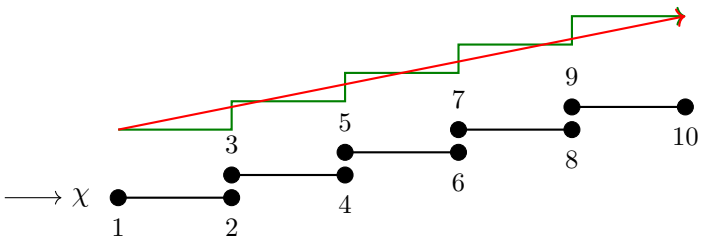

Figure 5.7.: Schematic representation of the discretization of a one-dimensional domain using the DG method. The red arrow indicates the single-valued numerical flux, while the green stepped path illustrates the two-valued flux.

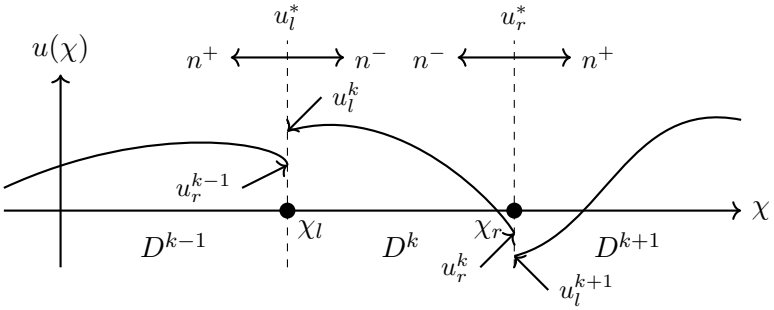

Figure 5.8.: Different flux values of the element D^k and its neighboring elements D^{k-1} and D^{k+1}. The double-valued fluxes are indicated as u_r^{k-1} and u_l^k at the left edge u_l^*, and u_r^k and u_l^{k+1} at the right edge u_r^*. Indices l and r denote the left and right interfaces, respectively, marked by the dashed vertical lines.

now be formulated. The left element interface is focused first, where the jump $[\![u_l]\!]$ is located and shown in Fig. 5.8. For the upwind flux at the left and right element interfaces at the locations χ_l and χ_r, the expressions are given by

$$u_l^* = -u_l^k + \left(\frac{u_l^k + u_r^{k-1}}{2} + \frac{1}{2} \left[-u_l^k + u_r^{k-1} \right] \right) \quad \text{and} \quad u_r^* = u_r^k - \left(\frac{u_r^k + u_l^{k+1}}{2} + \frac{1}{2} \left[-u_r^k + u_l^{k+1} \right] \right). \tag{5.15}$$

Additionally, the central flux can be simply derived by setting $\alpha = 1$, which removes the second summand in Eq. (5.14). This yields:

$$u_l^* = -u_l^k + \left(\frac{u_l^k + u_r^{k-1}}{2} \right) \qquad \text{and} \qquad u_r^* = u_r^k - \left(\frac{u_r^k + u_l^{k+1}}{2} \right) \tag{5.16}$$

for the left and right element interfaces in Fig. 5.8, respectively. To obtain a matrix representation, Eq. (5.16) can be rewritten as a system of equations. This is demonstrated in the following:

$$\begin{pmatrix} u_l^* \\ u_r^* \end{pmatrix} = \underbrace{\left(\begin{array}{cc:cc:cc} 0 & \frac{1}{2} & -\frac{1}{2} & 0 & 0 & 0 \\ 0 & 0 & 0 & \frac{1}{2} & -\frac{1}{2} & 0 \end{array} \right)}_{\boldsymbol{F}_{\text{local}}} \cdot \begin{pmatrix} u_l^{k-1} \\ u_r^{k-1} \\ u_l^k \\ u_r^k \\ u_l^{k+1} \\ u_r^{k+1} \end{pmatrix}.$$

The matrix $\boldsymbol{F}_{\text{local}}$ is referred to as the local flux matrix. The vertical dashed lines indicate the two element interfaces in Fig. 5.8. Its dimensions are $N_p \times 3N_p$. The number of columns in $\boldsymbol{F}_{\text{local}}$ arises from the fact that three finite elements are considered. Additionally, the state vector on the right-hand side is extended with the missing values u_l^{k-1} and u_r^{k+1}. To construct the global flux matrix, the local matrix is assembled along the main diagonal according to the following scheme. The example is again based on five finite elements:

$$\boldsymbol{F}_{\text{global}} = \begin{pmatrix} -\frac{1}{2} & 0 & 0 & 0 & 0 & 0 & 0 & 0 & 0 & 0 \\ 0 & \frac{1}{2} & -\frac{1}{2} & 0 & 0 & 0 & 0 & 0 & 0 & 0 \\ 0 & \frac{1}{2} & -\frac{1}{2} & 0 & 0 & 0 & 0 & 0 & 0 & 0 \\ 0 & 0 & 0 & \frac{1}{2} & -\frac{1}{2} & 0 & 0 & 0 & 0 & 0 \\ 0 & 0 & 0 & \frac{1}{2} & -\frac{1}{2} & 0 & 0 & 0 & 0 & 0 \\ 0 & 0 & 0 & 0 & 0 & \frac{1}{2} & -\frac{1}{2} & 0 & 0 & 0 \\ 0 & 0 & 0 & 0 & 0 & \frac{1}{2} & -\frac{1}{2} & 0 & 0 & 0 \\ 0 & 0 & 0 & 0 & 0 & 0 & 0 & \frac{1}{2} & -\frac{1}{2} & 0 \\ 0 & 0 & 0 & 0 & 0 & 0 & 0 & \frac{1}{2} & -\frac{1}{2} & 0 \\ 0 & 0 & 0 & 0 & 0 & 0 & 0 & 0 & 0 & \frac{1}{2} \end{pmatrix}. \tag{5.17}$$

It is apparent that the global flux matrix begins and ends with matrix entries at positions (1,3) and (2,4) of $\boldsymbol{F}_{\text{local}}$. In both cases, these correspond to the respective reference element in the local flux matrix $\boldsymbol{F}_{\text{local}}$. A block from the matrix above is denoted as:

$$\boldsymbol{F}_{\text{gl,blck}} = \begin{pmatrix} \frac{1}{2} & -\frac{1}{2} \\ \frac{1}{2} & -\frac{1}{2} \end{pmatrix} = \begin{pmatrix} w & x \\ y & z \end{pmatrix}.$$

To obtain the final global matrix of the DG method, the global flux matrix is superimposed with the matrix from Eq. (5.4). This yields the following sparsity pattern:

$$\boldsymbol{K} = \begin{pmatrix} a+z & b & 0 & 0 & 0 & 0 & 0 & 0 & 0 & 0 \\ c & d+w & x & 0 & 0 & 0 & 0 & 0 & 0 & 0 \\ 0 & y & a+z & b & 0 & 0 & 0 & 0 & 0 & 0 \\ 0 & 0 & c & d+w & x & 0 & 0 & 0 & 0 & 0 \\ 0 & 0 & 0 & y & a+z & b & 0 & 0 & 0 & 0 \\ 0 & 0 & 0 & 0 & c & d+w & x & 0 & 0 & 0 \\ 0 & 0 & 0 & 0 & 0 & y & a+z & b & 0 & 0 \\ 0 & 0 & 0 & 0 & 0 & 0 & c & d+w & x & 0 \\ 0 & 0 & 0 & 0 & 0 & 0 & 0 & y & a+z & b \\ 0 & 0 & 0 & 0 & 0 & 0 & 0 & 0 & c & d+w \end{pmatrix}.$$

As is apparent, this breaks the block diagonal structure of the matrix. This would be true if the entire computational domain, i.e., $\Omega_\chi \times \Omega_\xi$, were described by $\boldsymbol{K}$. In most cases, and particularly for QLEs, a two-dimensional computational domain is discretized. For the sake of clarity, only the transport direction χ was shown in Figs. 5.5 and 5.7. When also considering the relative direction ξ, the DG method yields the same mesh as in the FEM shown in Fig. 5.3. Thus, Fig. 5.5 can be extended by an additional set of finite elements running parallel in the relative direction ξ. For clarity, the system is reduced to three elements in the transport

direction. For two layers in the ξ domain, the following matrix is obtained:

$$\boldsymbol{K} = \tag{5.18}$$

$$\left(\begin{array}{cccccc:cccccc}
a+z & b & 0 & 0 & 0 & 0 & 0 & 0 & 0 & 0 & 0 & 0 \\
c & d+w & x & 0 & 0 & 0 & 0 & 0 & 0 & 0 & 0 & 0 \\
0 & y & a+z & b & 0 & 0 & 0 & 0 & 0 & 0 & 0 & 0 \\
0 & 0 & c & d+w & x & 0 & 0 & 0 & 0 & 0 & 0 & 0 \\
0 & 0 & 0 & y & a+z & b & 0 & 0 & 0 & 0 & 0 & 0 \\
0 & 0 & 0 & 0 & c & d+w & 0 & 0 & 0 & 0 & 0 & 0 \\
\hdashline
0 & 0 & 0 & 0 & 0 & 0 & a+z & b & 0 & 0 & 0 & 0 \\
0 & 0 & 0 & 0 & 0 & 0 & c & d+w & x & 0 & 0 & 0 \\
0 & 0 & 0 & 0 & 0 & 0 & 0 & y & a+z & b & 0 & 0 \\
0 & 0 & 0 & 0 & 0 & 0 & 0 & 0 & c & d+w & x & 0 \\
0 & 0 & 0 & 0 & 0 & 0 & 0 & 0 & 0 & y & a+z & b \\
0 & 0 & 0 & 0 & 0 & 0 & 0 & 0 & 0 & 0 & c & d+w
\end{array}\right).$$

By dividing the matrix above with vertical and horizontal dashed lines, it becomes evident that the block-diagonal structure is preserved. This allows certain principles of HPC to be exploited, which are discussed in more detail in Section 6.5. The coupling between the two layers is described in detail in Section 5.3.

Following this detailed explanation of the functioning of the DG method, its fundamental mathematical properties, such as coercivity, stability, and the uniqueness and existence of solutions shall be analyzed next.

5.2.2. Uniqueness and Existence

DG methods aim to solve a specific abstract problem, which is formulated as follows [92]:

Problem 5.1. *Find a $u \in X$ such that $a(u,v) = \ell(v)$ holds for all $v \in X$.*

Here, X is a Banach space, $a : X \times X \to \mathbb{R}$ is a bilinear form, and $\ell : X \to \mathbb{R}$ is a linear functional [93].
To ensure the existence and well-posedness (i.e., uniqueness) of the solution to Eq. (4.5), the Lax-Milgram theorem is employed [94].

Lemma 5.1 (Lax-Milgram)**.** *Let X be a Hilbert space and suppose $a \in \mathcal{L}(X \times X, \mathbb{R})$ and $\ell \in \mathcal{L}(X, \mathbb{R}) = X^*$, then the variational problem 5.1 is well-posed if the bilinear form a is bounded and coercive. Moreover, the following a priori estimate holds:*

$$||u||_X \leq \frac{1}{\beta} ||\ell||_{X^*}.$$

To apply Lemma 5.1, the definitions of coercivity and boundedness of a bilinear form are needed [92]:

Definition 5.1 (Coercivity and Boundedness of a Bilinear Form)**.** *Let X be a Hilbert space and let $a \in \mathcal{L}(X \times X, \mathbb{R})$ and $b \in \mathcal{L}(X \times X, \mathbb{C})$ be bilinear forms. It follows that a is coercive on X if there exists a constant $\beta > 0$ such that*

$$\forall v \in X: \qquad \beta ||v||_X^2 \leq a(v,v).$$

Furthermore, b is coercive on X if there exists a constant $\beta > 0$ such that

$$\forall v \in X: \qquad \beta ||v||_X^2 \leq \Re(b(v,v)).$$

Finally, a and b are said to be bounded if there exists a constant $C > 0$ such that

$$\forall v, w \in X: \qquad |a(v,w)| \leq C||v||_X ||w||_X.$$

A PDE has a *weak formulation* (variational formulation) in the space $X = W^{k,p}(\Omega)$, if it is multiplied with test functions $w \in X$ and integrated over the open, bounded domain $\Omega \subset \mathbb{R}^d$ with Lipschitz boundary $\Gamma = \partial\Omega$. Here, $W^{k,p}(\Omega)$ is the Sobolev space defined by

$$W^{k,p}(\Omega) = \{\varphi \in L^p(\Omega) : D^\alpha \varphi \in L^p(\Omega) \text{ for all } |\alpha| \leq k\} \tag{5.19}$$

with the associated semi-norm

$$||\varphi||_p = \left\{ \sum_{|\alpha|=k} ||D^\alpha \varphi||_p^p \right\}^{1/p},$$

where α is a multi-index and $D^\alpha \phi$ denotes the so-called weak derivative [95]. The solution to the weak formulation is called the *weak solution*. In contrast to classical solutions, it does not require classical differentiability. Instead, it suffices that the function is regular enough for its weak derivatives to exist and be square-integrable. This relaxes the regularity requirements of the underlying variational problem to those imposed by Sobolev space membership, such as $H^1(\Omega)$. This relaxation allows solutions with kinks, jumps, or other singularities to be admitted [86, 96].

To derive the weak formulation of the LVNE, the computational domain Ω_χ is triangulated using a fixed number N_χ of non-overlapping finite elements. Each individual element is defined as $D^k[\chi_{k-1/2}, \chi_{k+1/2}]$. The triangulation is denoted by τ. A discrete solution v_τ is sought, which belongs to the finite element space

$$X_\tau = (X_{\tau,1})^{N_\xi} \equiv \left(\{v \in L^1(\Omega_\chi) : v|_{D^k} \in \mathcal{P}_N(D^k) \ \forall k = 1, ..., N_\chi\} \right)^{N_\xi} \tag{5.20}$$

where $\mathcal{P}_N$ denotes the $(N+1) = N_p$-dimensional polynomial space of degree N. The space $X_{\tau,1}$ is a subset of the broken Sobolev space $H^1(\tau) = \{v \in L^2(\Omega_\chi) : v|_{D^k} \in H^1(D^k) \ \forall D^k \in \tau\}$. Note that $H^1(\tau)$ is *not* a subset of the solution space $X = H^1(\Omega)$, which again emphasizes the non-conforming nature of the method. Nevertheless, $H^1(\tau)$ is a subset of a Hilbert space, so Lemma 5.1 can be applied.
As the name of the method implies, the finite element space in which the DG method exists permits discontinuities between adjacent elements. Values at these discontinuities are denoted with the superscript '$-$' when located to the left. If the values are located to the right, this is indicated by a superscript '$+$'. The interpretation always depends on the edge of the reference element where the definition is made, since, as mentioned above, the '$+$' index indicates external information and the '$-$' index always represents internal information.

Definition 5.2 (Jump and Average)**.** *Let $F = \cup_{D^k \in \tau} \partial D^k$ denote the union of all element edges. The interior edges $e \in F_i = F \setminus \partial\Omega_\chi$ are defined by*

$$[\![u_\tau]\!]_e = u_\tau^-\big|_e - u_\tau^+\big|_e \qquad \textit{as well as} \qquad \{u_\tau\}_e = \frac{1}{2}(u_\tau^-\big|_e + u_\tau^+\big|_e)$$

and are referred to as the jump $[\![u_\tau]\!]_e$ and the average $\{u_\tau\}_e$, respectively, for all $u_\tau \in X_\tau$ [97]. On boundary nodes $e \in F_e = F \setminus F_i$, the definition is extended as

$$[\![u_\tau]\!]_e \equiv \begin{cases} -u_{\tau,l}^+ \equiv -u_\tau(\chi_{1/2}), & \textit{left} \\ u_{\tau,r}^- \equiv u_\tau(\chi_{N_\chi+1/2}), & \textit{right} \end{cases} \qquad \textit{and} \qquad \{u_\tau\}_e = \begin{cases} u_{\tau,l}^+, & \textit{left} \\ u_{\tau,r}^-, & \textit{right} \end{cases} \tag{5.21}$$

Analogously, the jump and average are also defined for $u \in X_{\tau,1}$. For $u, v \in X_\tau$, the following relation holds:

$$[\![u^\dagger v]\!] = c([\![u]\!]^\dagger \{v\} + \{u\}^\dagger [\![v]\!]) \tag{5.22}$$

where $c = 1$ for interior edges and $c = 1/2$ for boundary edges.

To construct the DG method, the weak formulation of the QLE (3.1) must be derived. Furthermore, the bilinear form a and the linear form ℓ must satisfy the following conditions:

1. *Consistency*: For every weak solution $u \in H^1(\Omega)$ of the LVNE and any function $v \in L^2(\Omega)$ that lies elementwise in $H^1(D^k)$, it holds that $a_\tau(u, v) = \ell_\tau(v)$.
2. *Boundedness and Coercivity* of the bilinear form as defined in Definition 5.1 are essential.

The first point is satisfied by including the jump terms in the formulation and evaluating them for a solution $u \in H^1(\Omega)$. Due to the mathematical properties of the solution u, these jumps vanish. To understand this, the *Sobolev Embedding Theorem* must be introduced [95].

Lemma 5.2 (Second Sobolev Embedding Theorem)**.** *Let $\Omega \subseteq \mathbb{R}^n$ be a bounded domain with Lipschitz boundary, and let $m \in \mathbb{N}_0$, $1 \leq p \leq \infty$. Then:*

1. *If the **Sobolev number** $s = m - n/p$ is positive ($s > 0$), then the Sobolev space $W^{m,p}(\Omega)$ embeds continuously into the Hölder space $C^{l,\alpha}(\bar{\Omega})$, where*
   - $l = \lfloor s \rfloor$,
   - $0 < \alpha = s - l < 1$.
2. *For the case $p = 2$, $m = 1$, $n = 1$, i.e. for the space $H^1(\Omega) := W^{1,2}(\Omega)$, it holds that:*
   - *The Sobolev number is $sob(H^1(\Omega)) = 1 - n/2 = 1 - 1/2 = 1/2 > 0$.*
   - *Thus, every function in $H^1(\Omega)$ is continuous and lies in the space $C^0(\bar{\Omega})$.*

When jump terms are included, they do not contribute significantly because they vanish upon integration over the entire computational domain Ω. This is due to the fact that functions in $H^1(\Omega)$ are inherently free from jumps or discontinuities, since the Sobolev number, as shown above, is positive [95].
The second condition, however, is not trivially fulfilled and depends on the choice of a suitable numerical flux.

Theorem 5.1 (Weak formulation of the LVNE)**.** *Find a $v_\tau \in X_\tau$ such that for all test functions $\varphi \in X_\tau$, the relation $a_\tau^w(v_\tau,\varphi) + b_\tau(v_\tau,\varphi) = \ell_\tau(\varphi)$ holds. The individual terms are defined as*

$$
\begin{aligned}
a_\tau^w(v_\tau,\varphi) &= \sum\nolimits_{D^k\in\tau}\int_{D^k}\left(-(\partial_\chi\varphi^\dagger)f(v_\tau) + \varphi^\dagger G v_\tau\right) + \sum\nolimits_{e\in F}\int_e [\![\varphi^\dagger]\!]\left(\mathbf{\Lambda}\{v\} + \frac{1-\mu}{2}|\mathbf{\Lambda}|[\![v]\!]\right)\\
b_\tau^w(v_\tau,\varphi) &= \sum\nolimits_{D^k\in\tau}\int_{D^k}\varphi^\dagger\partial_t v_\tau\\
\ell_\tau(\varphi) &= -\int_{e_r}[\![\varphi^\dagger]\!]\frac{1-\mu}{2}(\mathbf{\Lambda}-|\mathbf{\Lambda}|)g - \int_{e_l}[\![\varphi^\dagger]\!]\frac{1-\mu}{2}(\mathbf{\Lambda}+|\mathbf{\Lambda}|)g.
\end{aligned}
$$

Within the flux terms involving the flux function f, μ is a scalar regulating the jump contribution of the numerical flux, as explained in Section 5.2.1. The matrix $\mathbf{\Phi}$ is obtained from the eigenvalue decomposition $\mathbf{\Lambda} = \mathbf{\Phi}^\dagger\hat{\boldsymbol{A}}\mathbf{\Phi}$ and contains the eigenvectors $\boldsymbol{\phi}_j$ in its columns, which correspond to the eigenvalues λ_j.

Proof. Starting from the semi-discrete QLE (3.1), the individual terms are multiplied by test functions $\varphi\in X_\tau$. Additionally, the expression is simplified by defining $G = -\imath q/\hbar\mathbf{\Phi}^\dagger\boldsymbol{B}\mathbf{\Phi}$ and $f(v_\tau) = \imath\hbar/m\mathbf{\Phi}^\dagger\boldsymbol{A}\mathbf{\Phi}\rho(\chi,t)$. The transformed governing equation, multiplied by the test functions, reads:

$$\varphi^\dagger\partial_t v_\tau = \varphi^\dagger\partial_\chi f(v_\tau) + \varphi^\dagger G v_\tau.$$

Next, all terms are integrated over each finite element and summed over all elements of the triangulation:

$$\sum\nolimits_{D^k\in\tau}\int_{D^k}\varphi^\dagger\partial_t v_\tau = \sum\nolimits_{D^k\in\tau}\int_{D^k}\varphi^\dagger\partial_\chi f(v_\tau) + \sum\nolimits_{D^k\in\tau}\int_{D^k}\varphi^\dagger G v_\tau.$$

Along with a straightforward integration by parts of the diffusion operator, this yields:

$$\sum\nolimits_{D^k\in\tau}\int_{D^k}\varphi^\dagger\partial_t v_\tau = \sum\nolimits_{D^k\in\tau}\oint_{\partial D^k}\varphi^\dagger\hat{n}f(v_\tau) - \sum\nolimits_{D^k\in\tau}\int_{D^k}(\partial_\chi\varphi^\dagger)f(v_\tau) + \sum\nolimits_{D^k\in\tau}\int_{D^k}\varphi^\dagger G v_\tau. \tag{5.23}$$

The contour integral in Eq. (5.23) includes the sum over all interior edges as well as the two boundaries at the endpoints of the domain Ω. With this, the two bilinear forms a_τ^w and b_τ^w are defined. The expression for the linear form ℓ_τ in Theorem 5.1 arises from the two boundary integrals of the domain and the boundary condition g, which corresponds here to the Fermi-Dirac statistics, as introduced in Section 4.2. □

At this point, it is worth noting that the missing matrix elements in the global matrix (5.18) are contained in the linear form ℓ_τ. Moreover, it is important to understand that the weak formulation in Theorem 5.1 does *not yet* incorporate the numerical flux [22].

Theorem 5.2 (Coercivity of the DG Method)**.** *Coercivity according to Definition 5.1 is necessary to guarantee an energy minimum and thus a unique solution. There must exist a positive constant C_c for the bilinear form such that [GS1],[97]*

$$a_\tau(\varphi_\tau,\varphi_\tau) \geqq C_c\|\varphi_\tau\|_{DG}^2, \qquad \forall\varphi_\tau\in X_\tau.$$

The natural DG norm is defined as

$$\|\varphi\|_{DG}^2 = \|\nabla\varphi\|_{\Omega,\tau}^2 + \|h^{-1/2}[\![\varphi]\!]\|_{\Gamma_i}^2 + \|h^{-1/2}\varphi\|_{\Gamma_e}^2, \tag{5.24}$$

where h is the element width, defined as $h = \min((h^k)^-, (h^k)^+)$. Additionally, the boundary norms are given by

$$\|\varphi\|_{\Gamma_i}^2 = \oint_{\Gamma_i} \varphi^2 \,\mathrm{d}\chi \qquad \textit{and} \qquad \|\varphi\|_{\Gamma_e}^2 = \oint_{\Gamma_e} \varphi^2 \,\mathrm{d}\chi. \tag{5.25}$$

Proof. First, the trace inequality proved by Warburton and Hesthaven [68] for orthogonal polynomials is employed:

$$\|v_\tau\|_{\partial D} \leq \sqrt{\frac{(N+1)(N+d)}{d}\frac{|\partial D|}{|D|}}\|v_\tau\|_D, \quad \forall v_\tau \in \mathrm{P}_N(\mathrm{D}), \tag{5.26}$$

where d is the dimension of the simplex D. Moreover, since $\frac{|\partial D|}{|D|} \propto h^{-1}$, this results in the classical inverse inequality $\|v_\tau\|_{\partial D} \leq C_i h^{-1/2}\|v_\tau\|_D$ [92]. The constant C_i depends on the polynomial degree N and the shape of the simplex. The model problem can then be formulated as

$$a_\tau(v_\tau, \varphi_\tau) = \|\nabla\varphi_\tau - \mathcal{L}(\varphi_\tau)\|_{\Omega,\tau}^2 - \gamma\|\mathcal{L}(\varphi_\tau)\|_{\Omega,\tau}^2 + \mathcal{I}(\varphi_\tau, \varphi_\tau), \tag{5.27}$$

where $\mathcal{L}(\varphi_\tau)$ is the lift operator, and γ is a constant which includes the internal penalty form if $\gamma = 1$ and excludes it otherwise ($\gamma = 0$). The stabilizing term $\mathcal{I}(\varphi_\tau, \varphi_\tau)$ ensures the invertibility of the method and is defined as

$$\mathcal{I}(\varphi_\tau, \varphi_\tau) = \oint_{\Gamma_i} \kappa[\![\varphi_\tau]\!]^2 \,\mathrm{d}\chi + \oint_{\Gamma_e} \kappa\varphi_\tau^2 \,\mathrm{d}\chi, \tag{5.28}$$

where κ is the local stabilization factor, given by $\kappa = \tilde{\kappa}^k/h$. This yields

$$\begin{aligned}\mathcal{I}(\varphi_\tau, \varphi_\tau) &= \|\kappa^{1/2}[\![\varphi_\tau]\!]\|_{\Gamma_i}^2 + \|\kappa^{1/2}\varphi_\tau\|_{\Gamma_e}^2 \\ &= \|(\tilde{\kappa}^k)^{1/2}h^{-1/2}[\![\varphi_\tau]\!]\|_{\Gamma_i}^2 + \|(\tilde{\kappa}^k)^{1/2}h^{-1/2}\varphi_\tau\|_{\Gamma_e}^2.\end{aligned} \tag{5.29}$$

Using the inverse inequality from Eq. (5.26), one obtains

$$\|\mathcal{L}(\varphi_\tau)\|_{\Omega,\tau}^2 \leq C_l^2\left(\|h^{-1/2}[\![\varphi_\tau]\!]\|_{\Gamma_i}^2 + \|h^{-1/2}\varphi_\tau\|_{\Gamma_e}^2\right). \tag{5.30}$$

Moreover, it holds that

$$\|\nabla\varphi_\tau - \mathcal{L}(\varphi_\tau)\|_{\Omega,\tau}^2 = \|\nabla\varphi_\tau\|_{\Omega,\tau}^2 + \|\mathcal{L}(\varphi_\tau)\|_{\Omega,\tau}^2 - 2\textstyle\sum_{k=1}^K(\nabla\varphi_\tau, \mathcal{L}(\varphi_\tau))_{D^k}. \tag{5.31}$$

Applying the arithmetic-geometric inequality $2ab \leq \epsilon a^2 + \epsilon^{-1}b^2$ to the summation in Eq. (5.31), it follows that:

$$\|\nabla\varphi_\tau - \mathcal{L}(\varphi_\tau)\|_{\Omega,\tau}^2 \geq (1-\epsilon)\|\nabla\varphi_\tau\|_{\Omega,\tau}^2 + (1-\epsilon^{-1})\|\mathcal{L}(\varphi_\tau)\|_{\Omega,\tau}^2. \tag{5.32}$$

For $\epsilon < 1$, the term $(1-\epsilon)$ is positive, while $(1-\epsilon^{-1})$ is negative. Using Eq. (5.30),

$$\begin{aligned}a_\tau(\varphi_\tau, \varphi_\tau) \geq &(1 - \epsilon + C_l^2(1-\gamma-\epsilon^{-1}))\|\nabla\varphi_\tau\|_{\Omega,\tau}^2 + (C_l^2((1-\gamma)-\epsilon^{-1}) + \tilde{\kappa}) \\ &\cdot\left(\|h^{-1/2}[\![\varphi_\tau]\!]\|_{\Gamma_i}^2 + \|h^{-1/2}\varphi_\tau\|_{\Gamma_e}^2\right)\end{aligned} \tag{5.33}$$

results. Here, $\tilde{\kappa} \leq \min_k(\tilde{\kappa}^k)$. Two cases can be distinguished:

- *Case* $\gamma = 0$: Both terms are positive provided $C_l^2/(C_l^2 + \tilde{\kappa}) < \epsilon < 1$, which is guaranteed if $\tilde{\kappa} > 0$.
- *Case* $\gamma = 1$: The condition $\tilde{\kappa} - C_l^2/\epsilon > 0$ must hold. This requires $\tilde{\kappa} > \kappa^*$, where κ^* depends on C_l and the regularity of the discretization mesh. According to [97], the following inequality must be satisfied:

$$\tilde{\kappa}^k \geq \frac{(N+1)(N+d)}{d} \frac{|\partial D^k|}{|D^k|}.$$

Hence, the constant C_c is positive, and the bilinear form a_τ is coercive. □

If the expressions $a_\tau(v_\tau, \varphi_\tau)$ with $(v_\tau, \varphi_\tau) \in X_\tau$ are evaluated using the definition of the DG norm in Eq. (5.24) and the Cauchy-Schwarz inequality, then the coercivity of a_τ can be shown as follows:

$$\begin{aligned}
\sum_{D^k \in \tau} \int_{D^k} \varphi^\dagger \partial_\chi f(\varphi) =& \kappa \partial_\chi \sum_{D^k \in \tau} \int_{D^k} \varphi^\dagger f(\varphi) = \kappa \partial_\chi \sum_{e \in F} \int_e [\![\varphi^\dagger f(\varphi)]\!] \\
\overset{(5.22)}{=}& \kappa \partial_\chi \left\{ \sum_{e \in F_i} \int_e [\![\varphi^\dagger]\!] \{f(\varphi)\} + \{\varphi^\dagger\} [\![f(\varphi)]\!] + \sum_{e \in F_e} \int_e [\![\varphi^\dagger]\!] \{f(\varphi)\} + \{\varphi^\dagger\} [\![f(\varphi)]\!] \right\} \\
=& \kappa \partial_\chi \left\{ \sum_{e \in F_i} \int_e \{\varphi^\dagger\} [\![f(\varphi)]\!] + \sum_{e \in F_e} \int_e [\![\varphi^\dagger]\!] \{f(\varphi)\} \right\} \\
\overset{(5.21)}{=}& \kappa \partial_\chi \left\{ \sum_{e \in F_i} \int_e \{\varphi^\dagger\} [\![f(\varphi)]\!] + \int_{e_r} [\![\varphi^\dagger]\!] [\![f(\varphi)]\!] - \int_{e_l} [\![\varphi^\dagger]\!] [\![f(\varphi)]\!] \right\},
\end{aligned} \tag{5.34}$$

with $\varphi \in X_\tau$. Since $f(\varphi)$ no longer depends on χ at this point, the derivative ∂_χ can be separated from the integral. As a result, integration is only required over the element interfaces. At the interfaces, only the jump remains, leaving the expression $[\![\varphi^\dagger f(\varphi)]\!]$. Furthermore, Eq. (5.22) is applied to $[\![\varphi^\dagger f(\varphi)]\!]$, yielding a new expression for the interface terms and enabling further simplifications. Finally, Eq. (5.21) is applied to the second integral $\int_e [\![\varphi^\dagger]\!] \{f(\varphi)\}$, which ultimately results in Eq. (5.34).

With the proof of coercivity, not only is the essential foundation for the well-posedness of the problem established, but it is also ensured that the system possesses positive energy – which, in turn, guarantees the existence and uniqueness of the solution. In a subsequent step, the consistency of the method will be analyzed and verified.

5.2.3. Stability and Consistency

So far, it has been shown that the considered system is well-posed and that the underlying problem is properly represented. Now, it remains to be investigated whether the method converges and small errors do not significantly affect the results.
In particular, for transient simulations, a stable method is essential; otherwise, the results may diverge. As announced in Section 3.1, time discretization is performed using the Runge-Kutta 2nd order (RK2) and Runge-Kutta 4th order (RK4) methods. Their stability requirement demands that the eigenvalues of the system matrix (i.e., the matrix representing the complete spatial discretization) all lie in the left half of the complex plane [22, 68].

Theorem 5.3 (Stability of the DG method)**.** *The stability of the DG algorithm is influenced by the jump term within the flux and the potential term $\hat{\boldsymbol{G}}$. Stability is ensured if the following inequality holds [GS1]:*

$$g_0 \sum_{D^k \in \tau} \int_{D^k} v^\dagger v + |\lambda_{min}| \sum_{e \in F} \int_e [\![v^\dagger]\!][\![v]\!] > 0 \tag{5.35}$$

Since the first term in Eq. (5.35) *can be both positive and negative, the second term must be larger than the absolute value of the first. Moreover, the eigenvalues contained in $\boldsymbol{\Lambda}$ must not include $\lambda_j = 0$, as this would contradict the above requirement. Additionally, a zero eigenvalue would result in a singularity in the system matrix due to multiplication with zero in Eq.* (3.1)*.*

To prove Theorem 5.3, the strong formulation of the bilinear form a_τ^w is needed.

Theorem 5.4 (Strong Formulation of the LVNE)**.** *The strong formulation a_τ^s requires higher regularity and is defined as [GS1]*

$$a_\tau^s(v_\tau, \varphi) = \sum_{D^k \in \tau} \int_{D^k} (\varphi^\dagger \partial_\chi f(v_\tau) + \varphi^\dagger \hat{\boldsymbol{G}} v_\tau) + \sum_{e \in F} \int_e ([\![\varphi^\dagger]\!] \frac{1-\mu}{2} |\boldsymbol{\Lambda}| - \{\varphi^\dagger\}\boldsymbol{\Lambda})[\![v_\tau]\!], \tag{5.36}$$

where the definitions of the bilinear form $b_\tau^w(v_\tau, \varphi)$ and the linear form $l_\tau(\varphi)$ from Theorem 5.1 are retained.

Proof. The strong formulation results from applying a second partial integration to the gradient term in Eq. (5.23):

$$\begin{aligned} \sum_{D^k \in \tau} \int_{D^k} \varphi^\dagger \partial_t v_\tau \, dD^k =& \sum_{D^k \in \tau} \oint_{\partial D^k} \varphi^\dagger \hat{n} f(v_\tau) \, d\partial D^k - \sum_{D^k \in \tau} \oint_{\partial D^k} \varphi^\dagger \hat{n} \hat{f}(v_\tau) \, d\partial D^k \\ &+ \sum_{D^k \in \tau} \int_{D^k} \varphi^\dagger \partial_\chi f(v_\tau) \, dD^k + \sum_{D^k \in \tau} \int_{D^k} \varphi^\dagger G v_\tau \, dD^k. \end{aligned} \tag{5.37}$$

Here, the numerical flux $\hat{f}$ is introduced, which has been discussed extensively in Section 5.2.1. □

Proof. From Section 5.2.2, it is known that the bilinear form $a_\tau(v_\tau, \varphi)$ is coercive. The terms responsible for the stability of the DG method can be extracted by subtracting $a_\tau(v_\tau, \varphi)$ from the strong form a_τ^s:

$$\begin{aligned} a_\tau^s(v_\tau, \varphi) - a_\tau(v_\tau, \varphi) =& \sum_{D^k \in \tau} \int_{D^k} (\varphi^\dagger \partial_\chi f(v_\tau) + \varphi^\dagger \hat{\boldsymbol{G}} v_\tau) \\ &+ \sum_{e \in F_i} \int_e ([\![\varphi^\dagger]\!] \frac{1-\mu}{2} |\boldsymbol{\Lambda}| - \{\varphi^\dagger\}\boldsymbol{\Lambda})[\![v_\tau]\!] \\ &+ \int_{e_r} [\![\varphi^\dagger]\!] \frac{1-\mu}{2} (-\boldsymbol{\Lambda} + |\boldsymbol{\Lambda}|)[\![v_\tau]\!] + \int_{e_l} [\![\varphi^\dagger]\!] \frac{1-\mu}{2} (\boldsymbol{\Lambda} + |\boldsymbol{\Lambda}|)[\![v_\tau]\!] \\ &- \partial_\chi \Big\{ \sum_{e \in F_i} \int_e \{\varphi^\dagger\} [\![f(\varphi)]\!] + \int_{e_r} \kappa [\![\varphi^\dagger]\!][\![f(\varphi)]\!] - \int_{e_l} \kappa [\![\varphi^\dagger]\!][\![f(\varphi)]\!] \Big\} \\ =& \sum_{D^k \in \tau} \int_{D^k} v^\dagger (\hat{\boldsymbol{G}} + \hat{\boldsymbol{G}}^\dagger) v + \sum_{e \in F} \int_e [\![v^\dagger]\!] |\boldsymbol{\Lambda}| [\![v]\!]. \end{aligned} \tag{5.38}$$

The terms in Eq. (5.38) remain and are therefore responsible for the method's stability. In order for the eigenvalues of the system matrix to lie in the left half-plane, it must hold that $\Re\{\lambda_i\} < 0$. To determine the real part of the bilinear form a_τ^s, the complex conjugate of the term $\hat{\boldsymbol{G}}$ is added:

$$2\Re\{a_\tau^s(v,v)\} = \sum_{D^k\in\tau}\int_{D^k} v^\dagger(\hat{\boldsymbol{G}}+\hat{\boldsymbol{G}}^\dagger)v + \sum_{e\in F}\int_e [\![v^\dagger]\!]|\boldsymbol{\Lambda}|[\![v]\!] \tag{5.39}$$

From the Hermitian sum $\hat{\boldsymbol{G}}+\hat{\boldsymbol{G}}^\dagger$, a scalar value g_0 can be extracted, which lies in the range $-g_{\max} < g_0 < +g_{\max}$. Similarly, the smallest absolute eigenvalue of $\boldsymbol{\Lambda}$ can be extracted from the second term in Eq. (5.39). This leads to the inequality:

$$g_0\sum_{D^k\in\tau}\int_{D^k} v^\dagger v + |\lambda_{\min}|\sum_{e\in F}\int_e [\![v^\dagger]\!][\![v]\!] > 0 \tag{5.40}$$

Since the second term in Eq. (5.40) is always positive, only the first term can become problematic. To ensure the condition in Eq. (5.40), the first term must remain below the threshold set by g_0 and the second term must dominate. As long as this condition is fulfilled, the bilinear form remains coercive and thus the method is stable. Otherwise, the method is unstable.
The eigenvalue spectrum of $\hat{\boldsymbol{G}}(\chi)+\hat{\boldsymbol{G}}^\dagger(\chi)$ corresponds to that of $\boldsymbol{B}(\xi)+\boldsymbol{B}^\dagger(\xi)$ since both are connected via the unitary transformation $\hat{\boldsymbol{G}} = \Phi^\dagger\boldsymbol{B}\Phi$. As shown in Section 5.3.1, the matrix $\boldsymbol{B}$ is symmetric, and therefore $\boldsymbol{B}+\boldsymbol{B}^\dagger = 2\Re\{\boldsymbol{B}\}$. From Eq. (4.9), it follows that the CAP is exclusively contained in $\boldsymbol{B}$. Hence, $\Re\{\boldsymbol{B}\}$ is positive definite for $\beta > 0$ (see Eq. (4.8)). Thus, the terms in Eq. (5.39) contribute to the stability of the method. Again, it is essential that $\lambda_{\min} \neq 0$ at all times. Therefore, it is advisable to use an even number N_ξ of finite elements for the discretization of the ξ-domain to avoid a zero crossing [98]. □

It has been mathematically demonstrated that initial numerical errors of the method do not grow uncontrollably. It is therefore worth analyzing the absolute error of the method. While relative error measures can be informative, they may become misleading in regions where the reference solution approaches zero. For this reason, the validation focuses on the absolute error. To that end, a relatively simple model problem, which will be given in the following, is considered and solved both analytically as well as using the DG method. The analytical solution is given by $u(\chi,\xi) = \exp(\imath a(\xi)\chi)$, where $a(\xi) = \sin(2\pi\xi/L_\xi)$ and L_ξ denotes the length of the computational domain in the ξ-direction. This analytical solution can then be used to determine the absolute error of the DG method. It is also desirable to compute the iterative error. For this purpose, the number of finite elements N_χ is doubled iteratively, starting from $N_\chi = 16$ up to $N_\chi = 256$. The analytical and iterative errors are defined as [GS2]:

$$\begin{aligned} e_r^\alpha &= \|\Re(u-u_\tau^\alpha)\|_{L^2}\,, \qquad \text{and} \\ e_{\tau,r}^\alpha &= \left\|\Re(u_\tau^\alpha - u_\tau^{\alpha-1})\right\|_{L^2}\,, \end{aligned} \tag{5.41}$$

where u is the exact solution and u_τ the approximate one. The index α denotes the iteration step in which the spatial resolution in χ-direction is refined (i.e., the number of elements is increased), and it is always positive ($\alpha > 0$). The number of elements is given by $N_\chi = 2^\alpha$. Fig. 5.9 shows the absolute error e_r^α obtained by comparing the DG solution with the analytical expression for $u(\chi,\xi)$. The number of elements in ξ-direction is fixed at $N_\xi = 180$ throughout. It can be observed that for polynomial order $N = 3$, an error of approximately 10^{-8} is already

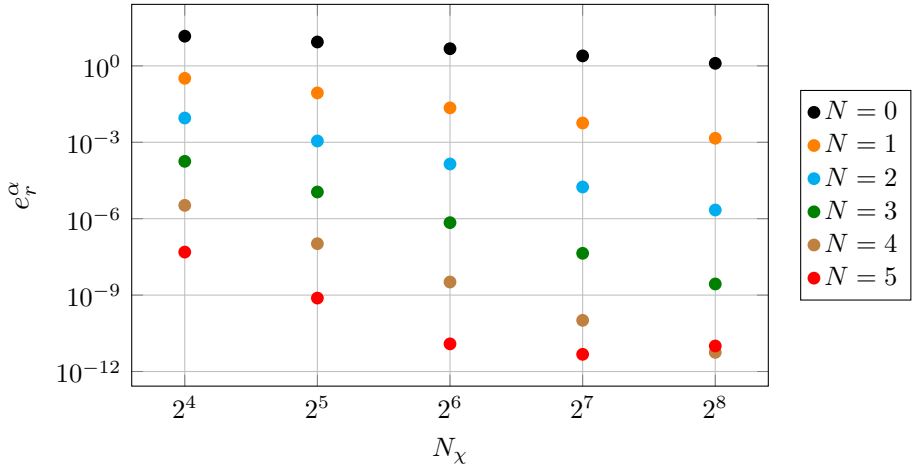

Figure 5.9.: Absolute error of the DG method compared to the analytical solution $u(\chi, \xi)$. The number of elements N_χ is doubled at each iteration, with $N_\chi = 2^\alpha$, $\alpha = 4, \ldots, 8$. The order of the basis functions ranges from $N = 0$ to $N = 5$.

achieved. Interestingly, for order $N = 5$, the error is slightly higher than for $N = 4$ when using $N_\chi = 2^8$ elements. This is most likely due to numerical inaccuracies, as the values fall in the range of 10^{-12}, which is the amplitude of CPU accuracy [GS2].
In addition to the absolute error, the iterative error can also be plotted against the number of elements. Here again, the number of elements in the ξ-direction is fixed at $N_\xi = 180$. As

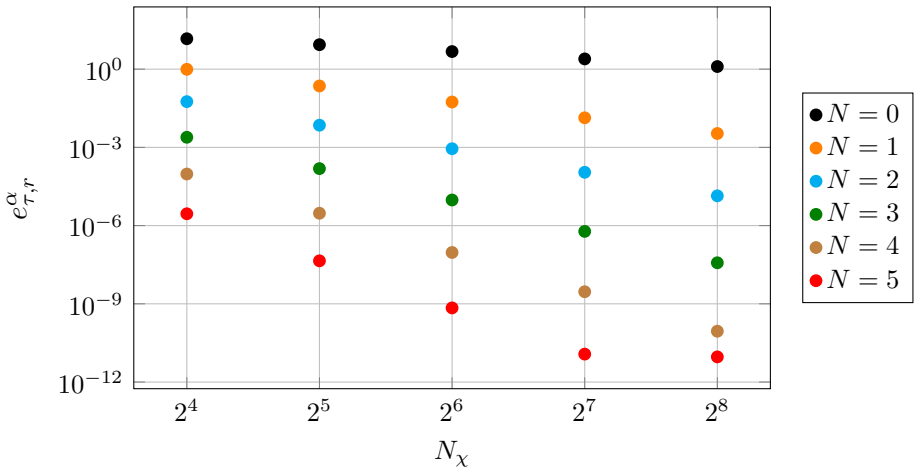

Figure 5.10.: Iterative error of the DG method. The number of elements N_χ is doubled at each step, using $N_\chi = 2^\alpha$, $\alpha = 4, \ldots, 8$. The order of the basis functions ranges from $N = 0$ to $N = 5$.

shown in Fig. 5.10, the DG method achieves an accuracy on the order of the CPU precision (for $N = 5$) [GS2]. It is also insightful to examine the convergence rates, which are defined as

follows [GS2]:

$$r_r^\alpha \equiv \frac{\ln(e_r^\alpha) - \ln(e_r^{\alpha-1})}{\ln(N_\chi^{\alpha-1}) - \ln(N_\chi^\alpha)}, \qquad \text{and}$$
$$r_{\tau,r}^\alpha \equiv \frac{\ln(e_{\tau,r}^\alpha) - \ln(e_{\tau,r}^{\alpha-1})}{\ln(N_\chi^{\alpha-1}) - \ln(N_\chi^\alpha)}. \tag{5.42}$$

Following standard procedures such as in [99], the following *a priori* error estimate can also be used:

$$e \leq c\Delta\chi^{N_\chi+1}, \tag{5.43}$$

where the positive constant $c > 0$ is independent of the element size $\Delta\chi$. This behavior is also reflected in the convergence rates, which are listed in Tab. 5.2 for various polynomial orders $N = 0 \dots 5$. As can be seen, the DG method already achieves near-optimal convergence at a

Table 5.2.: Convergence rates r_r and r_i for the real and imaginary parts of the absolute error e_r^α, and convergence rates $r_{\tau,r}$ and $r_{\tau,i}$ for the real and imaginary parts of the iterative error $e_{\tau,r}^\alpha$.

Order N	r_r	r_i	$r_{\tau,r}$	$r_{\tau,i}$
0	0.86 ± 0.07	0.83 ± 0.08	0.63 ± 0.16	0.57 ± 0.18
1	1.94 ± 0.03	1.95 ± 0.03	2.06 ± 0.05	2.05 ± 0.04
2	3.0 ± 0.0	3.0 ± 0.0	3.0 ± 0.0	3.0 ± 0.0
3	4.0 ± 0.0	4.0 ± 0.0	4.0 ± 0.0	4.0 ± 0.0
4	5.0 ± 0.0	5.0 ± 0.0	5.0 ± 0.0	5.0 ± 0.0
5	4.55 ± 2.04	4.6 ± 1.97	5.97 ± 0.04	5.97 ± 0.04

polynomial order of $N = 3$, in accordance with Eq. (5.43).

With these preliminary considerations, it can be proceeded to approximate the transport models introduced in Chapter 3 using the DG method.

Intermediate summary: At the beginning of Chapter 5, the various numerical approximation methods were introduced. The advantages and disadvantages of the FD, FV, and FEM methods were discussed. It was shown that the FEM method provides higher local accuracy and geometrical flexibility, though at the expense of computational efficiency due to its matrix structures. To address this, the DG method was introduced. In the subsequent Section 5.2, the basic operation of the DG method was presented, including a treatment of the Riemann problem and the derivation of the numerical flux. This was followed by a rigorous mathematical analysis of uniqueness, existence, stability, and consistency. It was shown that the DG method yields not only a unique solution (with minimal energy), but also correctly represents the physical problem, as confirmed by the strong formulation. Furthermore, numerical validation against an analytical solution revealed that both absolute and iterative errors reach magnitudes as low as 10^{-12}, with optimal convergence behavior.

5.3. Intraband Transport

The intraband quantum transport model was introduced in Section 3.2. In order to approximate the model using the DG method, Section 5.3.1 will first describe the discretization of the relative coordinate ξ. Then, the procedures of the FV, FEM, and DG methods will be presented. This will be followed by the discretization of the transport direction χ using the DG algorithm in Section 5.3.2.

5.3.1. Discretization of the ξ-Coordinate

The model developed by Frensley [13] is based on a phase-space description in which the density matrix is Fourier-transformed with respect to the relative coordinate ξ, while the transport direction χ remains in real space. In order to solve the resulting system numerically, a cell formalism is introduced in the χ-direction, dividing the computational domain into discrete cells. Each of these cells can be coupled to its neighbors through continuity conditions on the resulting Wigner distribution function in the discretized phase space. As a result, the discretization scheme in phase space must be consistently applied to each cell. This can be accomplished using the FV, FEM, or DG methods. To isolate the effects of the DG method and its numerical flux on the transport direction χ, initially the FV method in the ξ-direction is employed. A direct application of the DG approach in both χ and ξ directions would not allow for such clear separation. Since both methods are combined, the resulting approach is considered a hybrid scheme.

The Finite Volume Method

First, a uniform mesh of finite volumes is generated to discretize the computational domain Ω_ξ. The relative domain Ω_ξ is defined over the interval $\Omega_\xi = [-L_\xi/2, +L_\xi/2]$. This domain is then divided into a fixed, even number N_ξ of finite volumes, each of which has a width $\Delta\xi$. The LVNE (2.17) is thereby transformed into a semi-discrete system of coupled advection equations, which depend only on the center-mass coordinate χ. The result is given by [GS2]

$$\frac{\partial}{\partial t}\boldsymbol{\rho}(\chi,t) = \boldsymbol{A}\frac{\partial}{\partial \chi}\boldsymbol{\rho}(\chi,t) - \boldsymbol{B}(\chi,t)\boldsymbol{\rho}(\chi,t). \tag{5.44}$$

In this formulation, the density vector $\boldsymbol{\rho}(\chi,t)$ contains the values of the density matrix $\boldsymbol{\rho}$ at the discrete positions ξ_j. A central flux is used to approximate the gradient ∂_ξ, which corresponds to Eq. (5.13) with $\alpha = 1$. The matrix elements $A_{i,j}$ of the diffusion matrix $\boldsymbol{A}$ are given as

$$A_{i,i+1} = c_A, \qquad A_{i,i-1} = -c_A, \qquad \text{with} \qquad c_A = \frac{\imath\hbar}{2m\Delta\xi}. \tag{5.45}$$

Since the FV method is implemented in its lowest-order form, this approach corresponds to the FD method as discussed in [100]. The diffusion matrix $\boldsymbol{A}$, therefore, has a tridiagonal structure, which will become important shortly. Next, the drift matrix $\boldsymbol{B}(\chi,t)$ must be considered, which includes potential terms such as the (self-consistent) Hartree potential, potential barriers due to

the heterostructure, and any external potential. For the numerical integration of the drift in the relative direction ξ, the trapezoidal rule is applied. This yields the matrix elements $\boldsymbol{B}_{i,j}$ as

$$\begin{aligned} B_{i,i}(\chi,t) &= \frac{1}{4}\cdot c_B\left(B(\chi,\xi_{i-\frac{1}{2}},t)+B(\chi,\xi_{i+\frac{1}{2}},t)\right), \\ B_{i,i\pm1}(\chi,t) &= \frac{1}{4}\cdot c_B\cdot B(\chi,\xi_{i\pm\frac{1}{2}},t), \\ \text{with}\qquad c_B &= \frac{\imath q}{\hbar}. \end{aligned} \tag{5.46}$$

The values $\xi_{i\pm\frac{1}{2}}$ refer to the locations at the cell interfaces. Like the diffusion matrix $\boldsymbol{A}$, the drift matrix $\boldsymbol{B}$, introduced in Section 2.2.2, also has a tridiagonal structure. To improve the efficiency of the numerical algorithm at this point, a key property of tridiagonal matrices can be exploited: their eigenvalues and eigenvectors can be obtained analytically [101]. As described in Section 3.1, the eigenvectors of the diffusion matrix $\boldsymbol{A}$ are needed to derive the QLE. The eigenvalues can be obtained using the formula [100]

$$k_n = 2\cos\left(\frac{\pi n}{N_\xi+1}\right), \tag{5.47}$$

and the corresponding eigenvectors (also referred to as basis functions) are given by [100]

$$\boldsymbol{\Phi}_n = \left(i^{1/2}\sin\left(\frac{1\pi n}{N_\xi+1}\right),\ldots,i^{N_\xi/2}\sin\left(\frac{N_\xi\pi n}{N_\xi+1}\right)\right)^T. \tag{5.48}$$

The quantity k_n defined in Eq. (5.47) represents the eigenvalue of the discrete operator in the ξ-direction. It is a dimensionless spectral parameter associated with the discrete mode index n, rather than a physical wave number or momentum. Two essential conditions for the application of the inflow boundary condition scheme [13] (cf. Section 4.2) are, first, the coercivity of the approximation method (see Section 5.2.2) and second, the definition of propagation direction [100]. To that end, it is essential that the eigenvalue spectrum k_n is symmetrically distributed and that the value $k_n = 0$ is excluded in order to avoid singularities [98]. Consequently, the number of discretization elements N_ξ used for the expansion of the semi-discrete density matrix must be even. The matrix $\boldsymbol{\Phi}$ contains the eigenvectors as its columns, while the eigenvalues k_n are stored along the main diagonal of the matrix $\boldsymbol{\Lambda}$. Since the eigenvalues k_n in Eq. (5.47) correspond exactly to the wavenumbers k, this approach is equivalent to a Fourier transformation and allows for a basis transformation into phase space. This greatly simplifies the incorporation of boundary conditions in the transport direction χ (cf. Section 4.2). The k-values can also be used to classify forward- and backward-propagating waves, which are important not only for defining inflow boundary conditions [13] but also for specifying the upwind flux [22, 87]. Using this basis, the density matrix can be expanded according to [24]

$$\boldsymbol{\rho}(\chi,t) = \textstyle\sum_{n=1}^{N_\xi}\boldsymbol{\Phi}_n\cdot c_n(\chi,t) = \boldsymbol{\Phi}\cdot\boldsymbol{c}(\chi,t), \tag{5.49}$$

where the coefficients $c_n(\chi,t)$ are stored in the vector $\boldsymbol{c}(\chi,t)$. The basis functions are chosen to be orthogonal, so that $\boldsymbol{\Phi}_n^\dagger\cdot\boldsymbol{\Phi}_m = \delta_{n,m}$. This allows solving for $\boldsymbol{c}(\chi,t)$ by multiplying Eq. (5.49) from the left with $\boldsymbol{\Phi}^\dagger$:

$$\boldsymbol{c}(\chi,t) = \boldsymbol{\Phi}^\dagger\cdot\boldsymbol{\rho}(\chi,t). \tag{5.50}$$

Finally, this expansion is inserted into the LVNE and multiplied from the left by the self-adjoint matrix $\mathbf{\Phi}^\dagger$ to project into the eigenvalue space (also called image space):

$$\frac{\partial}{\partial t}\boldsymbol{c}(\chi,t) = \mathbf{\Lambda}\frac{\partial}{\partial \chi}\boldsymbol{c}(\chi,t) - \mathbf{\Phi}^\dagger \boldsymbol{B}(\chi,t)\mathbf{\Phi}\cdot\boldsymbol{c}(\chi,t). \tag{5.51}$$

The matrices $\boldsymbol{A}$, $\boldsymbol{B}$, $\mathbf{\Lambda}$, and $\mathbf{\Phi}$ all have the dimension $N_\xi \times N_\xi$. The diagonalization of the diffusion matrix $\boldsymbol{A}$ is carried out via the eigenvalue decomposition $\mathbf{\Lambda} = \mathbf{\Phi}^\dagger \boldsymbol{A}\mathbf{\Phi}$.

The Finite Element Method

For the discretization of the same computational domain Ω_ξ over the same interval, N_ξ finite elements are employed for triangulation. This results in a uniform mesh of one-dimensional elements, each having the length $\Delta\xi$. As discussed in Section 5.1, neighboring elements share a node, so the total number of nodes across the entire domain is $N_{\xi p} = N_\xi + 1$, when two nodes per element are considered. In the more general case, where three or more nodes per element are used, the total number of nodes becomes $N_{\xi p} = N_\xi \cdot (N_p - 1) + 1$, where N_p denotes the number of nodes per element. The order of the shape functions $l_{i,j}(\xi)$ then follows as $N = N_p - 1$, which corresponds to linear shape functions in this case. Each finite element is then integrated individually. The semi-discrete form of the LVNE in integral form reads:

$$\sum_{i=1}^{N_\xi}\int_{D^k}\frac{\partial}{\partial t}\boldsymbol{\rho}(\xi)l_i(\xi)dD^k = \sum_{i=1}^{N_\xi}\int_{D^k}\frac{\partial}{\partial \xi}\boldsymbol{\rho}(\xi)l_i(\xi)dD^k - \sum_{i=1}^{N_\xi}\int_{D^k}B(\xi)\boldsymbol{\rho}(\xi)l_i(\xi)dD^k. \tag{5.52}$$

The density matrix can be expanded using the test functions $l_j(\xi)$ as proposed in [24]:

$$\boldsymbol{\rho}(\xi) = \sum_{j=1}^{N_p} l_j(\xi)\tilde{\boldsymbol{\rho}}. \tag{5.53}$$

For clarity, the summation over all elements $\sum_{i=1}^{N_\xi}$ is temporarily omitted in the following. Inserting Eq. (5.53) into Eq. (5.52), and integrating the diffusion term (which includes ∂_ξ) by parts twice, yields:

$$\sum_{j=1}^{N_p}\int_{D^k}\frac{\partial}{\partial t}l_j(\xi)\tilde{\boldsymbol{\rho}}l_i(\xi)dD^k = \sum_{j=1}^{N_p}\int_{D^k}\left(\frac{\partial}{\partial \xi}l_j(\xi)\tilde{\boldsymbol{\rho}}\right)l_i(\xi)dD^k - \sum_{j=1}^{N_p}\int_{D^k}B(\xi)l_j(\xi)\tilde{\boldsymbol{\rho}}l_i(\xi)dD^k. \tag{5.54}$$

It should be noted that the repeated integration by parts generates two boundary terms that normally account for boundary conditions. However, since the CAP model is applied at the boundaries of Ω_ξ (cf. Section 4.1), it suffices to refer to the existence of the imaginary term $iW(\xi)$ in $\boldsymbol{B}$ (see Eq. (4.9)) [28]. The multiplication of test and trial functions $l_i(\xi)\cdot l_j(\xi)$ leads to the so-called mass and stiffness matrices [24], whose entries are defined as [GS3]:

$$\begin{aligned}\boldsymbol{M}^k_{i,j}(\sigma) &\equiv \int_{D^k} l^k_i(\sigma)l^k_j(\sigma)d\sigma, \qquad \text{and}\\ \boldsymbol{S}^k_{i,j}(\sigma) &\equiv \int_{D^k} l^k_i(\sigma)\frac{\partial}{\partial\sigma}l^k_j(\sigma)d\sigma, \qquad \text{with} \quad \sigma = \chi,\xi.\end{aligned} \tag{5.55}$$

The coordinate σ is used here in a general sense, since both matrices appear in the FEM and DG formulations, and are valid for both computational domains Ω_χ and Ω_ξ.

In the next step, the global mass and stiffness matrices can be assembled according to the standard FEM procedure given in Eq. (5.3). Both matrices are tridiagonal. Inserting the relations from Eq. (5.55) into Eq. (5.54) yields the compact form:

$$\boldsymbol{M}\frac{\partial}{\partial t}\tilde{\boldsymbol{\rho}} = c_A\boldsymbol{S}\tilde{\boldsymbol{\rho}} - c_B\boldsymbol{B}\boldsymbol{M}\tilde{\boldsymbol{\rho}}, \qquad \text{with} \quad c_A = \frac{\imath\hbar}{2m\Delta\xi} \quad \text{and} \quad c_B = \frac{\imath q}{\hbar}.$$

Since the stiffness matrix originates from the gradient ∂_ξ, it is used to compute eigenvalues and eigenvectors. Similar to the FV approach above, the eigenvalues and eigenvectors are stored in the matrices $\boldsymbol{\Lambda}$ and $\boldsymbol{\Phi}$, respectively. The expansions from Eqs. (4.4) and (5.50) can then be applied again.
The potential values in the drift matrix $\boldsymbol{B}$ still need to be integrated over each element. The nonzero entries are defined as:

$$\boldsymbol{B}_{i,j}(\chi,t) = c_B\left(B(\chi,\xi_{i-\frac{1}{2}},t) + B(\chi,\xi_{i+\frac{1}{2}},t)\right)\cdot\boldsymbol{M}^k(\chi). \tag{5.56}$$

The integration is performed using the so-called Gauss-Lobatto algorithm, which, similar to the trapezoidal rule, is a numerical quadrature method for evaluating integrals [102]. The result reads:

$$\tilde{\boldsymbol{B}}_{j,m} = \textstyle\sum_{a=1}^{N_{GL}}(\tilde{V}V^{-1})_{ai}(\tilde{V}V^{-1})_{aj}B_{j,m}(\chi,t)w_aJ^k. \tag{5.57}$$

Here, V is the Vandermonde matrix, w_a are the Gauss-Lobatto weights, and J^k is the Jacobian. The indices j and m refer to the rows and columns of the drift matrix.
Finally, the semi-discrete QLE can be written as:

$$\boldsymbol{M}\frac{\partial}{\partial t}\boldsymbol{c}(\chi,t) = c_A\boldsymbol{\Lambda}\frac{\partial}{\partial\chi}\boldsymbol{c}(\chi,t) - \boldsymbol{\Phi}^\dagger\tilde{\boldsymbol{B}}(\chi,t)\boldsymbol{\Phi}\cdot\boldsymbol{c}(\chi,t), \tag{5.58}$$

where the matrix $\boldsymbol{\Lambda}$ now results from the eigenvalue decomposition $\boldsymbol{\Lambda} = \boldsymbol{\Phi}^\dagger\boldsymbol{S}_{\text{global}}\boldsymbol{\Phi}$. It is important to note that, once again, the avoidance of singularities is crucial. This can only be ensured if the number of elements N_ξ is ***odd*** for the linear case $N_p = 2$, since the total number of eigenvalues in $\boldsymbol{\Lambda}$ depends on the total number of nodes $N_{\xi p} = N_\xi\cdot(N_p-1)+1$. A zero crossing in the eigenvalue spectrum is avoided if an even number of eigenvalues exists.

The Discontinuous Galerkin Method in the Relative Direction

The computational domain Ω_ξ over the finite interval $[-L_\xi/2, +L_\xi/2]$ is discretized using the same one-dimensional finite elements as in the FEM. The total number of nodes is given by $N_{\xi p} = N_p\cdot N_\xi$, since each element has its own set of nodes. The same ansatz and test functions $l_{i,j}(\xi)$ as well as the same mass and stiffness matrices apply. Based on the expansion in Eq. (5.49), one obtains the integral form of Eq. (5.54), with one exception:
As already shown for the FEM, two boundary terms arise after performing integration by parts twice. In contrast to the FEM, where continuity at cell interfaces is ensured via shared nodes (and boundary terms only appear at the outermost boundaries $\xi(-L_\xi/2)$ and $\xi(+L_\xi/2)$), the boundary terms in the DG method are essential for defining the numerical flux to ensure continuity at cell interfaces.
However, there is a restriction in defining the numerical flux. As derived in Section 5.2.1, the

upwind flux requires knowledge of the propagation direction of the wave packets. Although this information is encoded in the sign of the eigenvalues λ_j or the wave numbers k_n, they are only obtained *after* discretization in the ξ-direction. Therefore, at this stage, no information about wave propagation is available, and the central flux must be used instead, which has been derived in detail in Section 5.2.1 and can be constructed without this knowledge. Only the flux matrix $\boldsymbol{F}$ is introduced, with dimension $N_\xi \times N_\xi$. Nearly analogous to the FEM case, the semi-discrete QLE becomes:

$$\begin{aligned} \boldsymbol{M}\frac{\partial}{\partial t}\boldsymbol{c}(\chi,t) &= c_A\boldsymbol{\Lambda}\frac{\partial}{\partial\chi}\boldsymbol{c}(\chi,t) - \boldsymbol{\Phi}^\dagger\tilde{\boldsymbol{B}}(\chi,t)\boldsymbol{\Phi}\cdot\boldsymbol{c}(\chi,t), \\ \text{with} \qquad \boldsymbol{\Lambda} &= \boldsymbol{\Phi}^\dagger(\underbrace{\boldsymbol{S}_{\text{global}}}_{\text{cf. Eq. (5.4)}} - \underbrace{\boldsymbol{F}}_{\text{cf. Eq. (5.17)}})\boldsymbol{\Phi}. \end{aligned} \tag{5.59}$$

The eigenvalue decomposition is performed based on the difference between the global stiffness matrix and the flux matrix. The integrated drift term $\tilde{\boldsymbol{B}}$ is identical to that used in Eq. (5.57).

5.3.2. Discretization of the χ-Coordinate

In the first stage of the MSD, the relative coordinate ξ was discretized (see. Fig. 3.2). With the eigenvalues λ_n in the vector $\boldsymbol{\Lambda}$ (or the wave numbers k_n) and the eigenvectors in the transformation matrix $\boldsymbol{\Phi}$, the transport direction χ can subsequently be treated using the DG method. This corresponds to the second stage of the MSD approach.

The computational domain Ω_χ lies in the interval $[0, L_\chi]$ with Lipschitz boundary $\partial\Omega_\chi\in\mathbb{R}$. This domain is subdivided into N_χ one-dimensional finite elements. As in the DG method for the relative direction ξ, each finite element has its own set of nodes, so that the total number of nodes in the domain Ω_χ is given by $N_{\chi p} = N_p \cdot N_\chi$.
The basis for the discretization is the QLE from Eq. (5.51) (FV), (5.58) (FEM), or (5.59) (DG). Accordingly, the matrices $\boldsymbol{\Lambda}$ and $\boldsymbol{\Phi}$ are taken from the respective method.
In each case, an advection-reaction system is present, with the initial condition at time $t = 0$

$$\boldsymbol{c}(\chi,0) = (c(\xi_1,\chi,0),...,c(\xi_{N_\xi},\chi,0))^T = \boldsymbol{c}_0(\chi) \tag{5.60}$$

and the flux vector

$$\boldsymbol{f}(\chi,t) = \boldsymbol{\Lambda}\cdot\boldsymbol{c}(\chi,t), \tag{5.61}$$

with vector components $f_j(\chi,t)$. Each finite element D^k is defined in the interval $[D]^k = [\chi_l^k, \chi_r^k]$, where χ_l^k and χ_r^k denote the left and right boundaries, respectively, as shown in Fig. 5.8. D^k is the reference element on which the integration is to be evaluated and applies to all other elements in the domain Ω_χ. The totality of discretization elements will hereafter be referred to as the triangulation τ.
In the next step, test functions $l_i(\chi)$ are introduced. These are piecewise-defined polynomials corresponding to the test functions of the FEM and the previous DG method. They are of order N, which results from the number of nodes per element as $N = N_p - 1$. The terms in Eqs. (5.51), (5.58), or (5.59) are multiplied by the test functions and integrated over the interval

$[D]^k$, yielding

$$\begin{aligned}&\int_{D^k}\frac{\partial}{\partial t}c_j^k(\chi,t)l_i(\chi)-\mathbf{\Lambda}\int_{D^k}\frac{\partial}{\partial\chi}f_j^k(\chi,t)l_i(\chi)\\&+\sum_{m=1}^{N_\xi}\int_{D^k}G_{jm}^k(\chi)c_m^k(\chi,t)l_i(\chi)=0\quad,\quad\forall i=1,...,N_p,\end{aligned}\tag{5.62}$$

where $G_{jm}^k(\chi)$ denotes the matrix entries of the partially discretized drift matrix $\mathbf{\Phi}^\dagger\boldsymbol{B}\mathbf{\Phi}$. To couple the values at the element interfaces, Eq. (5.62) must be partially integrated over all $[D]^k\in\tau$ (cf. Theorem 5.1). This yields

$$\begin{aligned}&\int_{D^k}\partial_t c_j^k(\chi,t)l_i(\chi)+\int_{D^k}f_j^k(\chi,t)\partial_\chi l_i(\chi)\\&+\sum_{m=1}^{N_\xi}\int_{D^k}G_{jm}^k(\chi)c_m^k(\chi,t)l_i(\chi)=-\oint_{\partial D^k}\hat{n}^-f_j^k(\chi,t)l_i(\chi).\end{aligned}\tag{5.63}$$

The contour integral introduces the flux $f_j^k(\chi,t)$, which is double-valued at element boundaries. For a visual representation, see Fig. 5.7. This must subsequently be replaced by a unique, single-valued numerical flux $f_j^{k,*}(\chi,t)$. Since the eigenvalues from the first stage of the MSD method are now known, an upwind flux can be chosen for this DG method.
Next, the function $c_j^k(\chi,t)$ is expanded using the already defined test functions $l_i(\chi)$. The nodal representation is chosen (see Section 5.1):

$$\chi\in D^k:\quad c_j^k(\chi,t)=\sum_{n=1}^{N_p}c_j^k(\chi_n^k,t)l_n^k(\chi).\tag{5.64}$$

The flux $f_j^k(\chi,t)$ is expanded analogously:

$$\chi\in D^k:\quad f_j^k(\chi,t)=\sum_{n=1}^{N_p}f_j^k(\chi_n^k,t)l_n^k(\chi).\tag{5.65}$$

From these expansions, the vectors

$$\boldsymbol{c}_j^k\equiv(c_j^k(\chi_1^k,t),...,c_j^k(\chi_{N_\xi}^k,t))^T\qquad\text{and}\qquad\boldsymbol{f}_j^k\equiv(f_j^k(\chi_1^k,t),...,f_j^k(\chi_{N_\xi}^k,t))^T$$

are obtained, containing the expansion coefficients $c_j^k(\chi_n)$ and $f_j^k(\chi_n)$. The basis functions $l_n^k(\chi)$ are Lagrange polynomials that satisfy the condition $l_n^k(\chi_m^k)=\delta_{n,m}$ [98].
Additionally, the term $\boldsymbol{G}_{jm}(\chi)\boldsymbol{c}_m(\chi,t)l_i(\chi)$ must be evaluated. Analogous to the nodal expansion, the following ansatz is used [GS2]:

$$\begin{aligned}\boldsymbol{G}_{jm}^k(\chi)c_m^k(\chi,t)&=\sum_{n=1}^{N_p}\boldsymbol{G}_{jm}^k(\chi_n)c_m^k(\chi_n)l_n(\chi)\\&=\boldsymbol{l}\cdot\mathrm{diag}(\boldsymbol{G}_{jm}^k)\cdot\boldsymbol{c}_m^k,\end{aligned}\tag{5.66}$$

with

$$\boldsymbol{l}\equiv(l_1(\chi),l_2(\chi),...,l_{N_p}(\chi))^T.$$

The main diagonal $\mathrm{diag}(\boldsymbol{G}_{jm}^k)$ contains the values $G_{jm}^k(\chi_1),...,G_{jm}^k(\chi_{N_p})$. Eq. (5.66) can therefore be rearranged and integrated over the reference element as follows:

$$\begin{aligned}\sum_{m=1}^{N_\xi}\int_{D^k}G_{jm}(\chi)c_m^k(\chi,t)l_i(\chi)d\chi&=\sum_{m=1}^{N_\xi}\sum_{n=1}^{N_p}G_{jm}^k(\chi_n)c_m^k(\chi_n)\int_{D^k}l_n(\chi)l_i(\chi)d\chi\\&=\boldsymbol{M}_j^k\sum_{m=1}^{N_\xi}\mathrm{diag}(\underline{G}_{jm}^k)\,\underline{c}_m^k.\end{aligned}\tag{5.67}$$

With Eq. (5.67), the mass matrix from Eq. (5.55) is introduced, which results from the integral over the basis and test functions. Together with the definition of the stiffness matrix from Eq. (5.55), the weak formulation of the semi-discrete QLE can be written as follows [GS2]:

$$\boldsymbol{M}^k \partial_t \boldsymbol{c}_j^k + \boldsymbol{S}^k \boldsymbol{f}_j^k + \boldsymbol{M}^k \sum_{m=1}^{N_\xi} \mathrm{diag}(\boldsymbol{G}_{jm}^k) \boldsymbol{c}_m^k = -\oint_{\partial D^k} f_j^k(\chi, t) \hat{n} \boldsymbol{l}(\chi). \tag{5.68}$$

The contour integral in Eq. (5.68) introduces a coupling between adjacent cells. By performing a second partial integration of the diffusion term $\boldsymbol{S}^k \boldsymbol{f}_j^k$ in Eq. (5.68), one obtains the strong formulation:

$$\boldsymbol{M}^k \partial_t \boldsymbol{c}_j^k - \boldsymbol{S}^k \boldsymbol{f}_j^k + \boldsymbol{M}^k \sum_{m=1}^{N_\xi} \mathrm{diag}(\boldsymbol{G}_{jm}^k) \boldsymbol{c}_m^k = \oint_{\partial D^k} (f_j^k(\chi, t) - f_j^{k,*}(\chi, t)) \hat{n} \boldsymbol{l}(\chi), \tag{5.69}$$

which introduces the numerical flux $f_j^{k,*}$. The flux f_j^k is evaluated at the internal nodes of element k.

An alternative approach exists for evaluating the drift term $\int_{D^k} G_{jm}^k$ in Eq. (5.62): instead of multiplying with the mass matrix, the Gauss-Lobatto quadrature rule can be applied [102], as was already illustrated for the discretization of the ξ-coordinate using the DG method. Using the Vandermonde matrix V of size $N_p \times N_p$, a second Vandermonde matrix $\tilde{V}$ of size $N_{GL} \times N_p$, and the Gauss-Lobatto weights w_a, the drift term $\boldsymbol{G}_{jm}$ can be expressed in the stationary case as

$$\sum_{m=1}^{N_\xi} \int_{D^k} \boldsymbol{G}_{jm}^k(\chi) c_m^k(\chi, t) l_i(\chi) = (\boldsymbol{M}^k)^{-1} \sum_{a=1}^{N_{GL}} (\tilde{V} V^{-1})_{ap} (\tilde{V} V^{-1})_{aq} G_{jm} w_a J^k, \tag{5.70}$$

where N_{GL} denotes the number of Gauss-Lobatto support points and J^k is the Jacobian of the element transformation. It is worth noting that the mass matrix $\boldsymbol{M}^k$ to be inverted has a relatively small dimension of $N_p \times N_p$. In contrast, for the FEM, one would need to invert a mass matrix of size $N_\chi \cdot (N_p - 1) + 1 \times N_\chi \cdot (N_p - 1) + 1$, which would represent a significant computational effort.
For the strong formulation from Eq. (5.69), this leads to the alternative expression

$$\boldsymbol{M}^k \partial_t \boldsymbol{c}_j^k - \boldsymbol{S}^k \boldsymbol{f}_j^k + \sum_{a=1}^{N_{GL}} (\tilde{V} V^{-1})_{ap} (\tilde{V} V^{-1})_{aq} G_{jm} w_a J^k = \oint_{\partial D^k} (f_j^k(\chi, t) - f_j^{k,*}(\chi, t)) \hat{n} \boldsymbol{l}(\chi), \tag{5.71}$$

which allows the distinction of two numerical methods [GS2]:

- ***Method 1 (M1)*** refers to the procedure defined by Eq. (5.69).
- ***Method 2 (M2)*** refers to the procedure defined by Eq. (5.70).

Ultimately, the diffusion and drift terms can be moved to the right-hand side and multiplied from the left with the inverse mass matrix $(\boldsymbol{M}^k)^{-1}$, in order to isolate the time derivative on the left-hand side.
At this point, it is appropriate to compare both proposed methods M1 and M2 in terms of accuracy. Therefore, the same model problem from Section 5.2.3 is used to asses the absolute error of both methods. The number N_ξ of finite elements in Ω_ξ is kept the same for both methods, while the number of N_χ finite elements in Ω_χ is incremented according to $N_\chi = 2^\alpha$. As for the order of the test functions, a quadratic order $N = 2$ is chosen. The comparison can

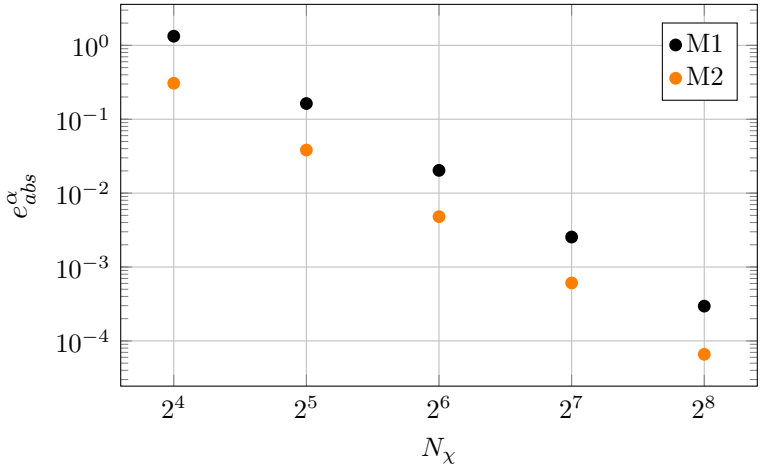

Figure 5.11.: Comparison between the methods M1 and M2. The number of elements N_χ is doubled at each iteration, with $N_\chi = 2^\alpha$, $\alpha = 4, \ldots, 8$. The order of the basis functions is set to $N = 2$.

be summed up in the following Fig. 5.11. As is visible, the Gauss-Lobatto quadrature (M2) delivers a smaller absolute error when compared to the integration by a mass matrix (M1) throughout all increments of the number of elements N_χ [GS2]. Therefore, method M2 shall be used for all approximations for the remainder of this work.

Finally, the numerical flux for the transport direction χ must be formulated. In the context of hydrodynamics, it is common to consider only the homogeneous part of the PDE. However, in a quantum transport problem, the reactive term $\boldsymbol{B}(\chi)\boldsymbol{\rho}(\chi)$ must also be taken into account. If the discretization width $\Delta\chi$ is sufficiently small, the reactive term $\boldsymbol{B}(\chi_0)\boldsymbol{\rho}(\chi)$ in the interval $\chi_l \leq \chi_0 \leq \chi_r$ can be assumed to be approximately constant [GS2]. With the ansatz

$$\boldsymbol{\rho}(\chi) = e^{\boldsymbol{B}(\chi_0)\chi}\boldsymbol{\rho}'(\chi) \tag{5.72}$$

the semi-discrete advection-reaction equations (5.51), (5.58), and (5.59) can be rewritten as [GS2]

$$\frac{\partial}{\partial t}\boldsymbol{\rho}'(\chi,t) - \frac{\partial}{\partial \chi}\boldsymbol{A}\exp(\boldsymbol{B}(\chi_0)\chi)\boldsymbol{\rho}'(\chi,t) = 0. \tag{5.73}$$

Considering the norm of the matrix $\|\boldsymbol{B}\| = 10^5$ A/J together with the relatively small discretization width $\Delta\chi = 10^{-10}$ m, the exponential term in Eq. (5.72) tends toward 1, such that the corresponding term in Eq. (5.73) can practically be neglected [GS2]. This justifies the approach of considering only the diffusive part of the PDE for the formulation of the numerical flux. Using the previously determined eigenvalues and eigenvectors from Section 5.3.1, the argumentation from Section 5.2.1 regarding the upwinding flux can be applied. Since the inverse mass matrix is multiplied with the time derivative, so-called lift operators can be introduced according to [22, 24]:

$$\boldsymbol{e}_r \equiv (\boldsymbol{M}^k)^{-1}\boldsymbol{l}(\chi_r^k) = (\boldsymbol{M}^k)^{-1}\cdot(0,...,0,1)^T \tag{5.74}$$

$$\boldsymbol{e}_l \equiv (\boldsymbol{M}^k)^{-1}\boldsymbol{l}(\chi_l^k) = (\boldsymbol{M}^k)^{-1}\cdot(1,0,...,0)^T \tag{5.75}$$

where $\chi_l^k, \chi_r^k = \chi_1, \chi_{N_p}$ for polynomials of degree $N \geq 1$. This leads to the following expression for the contour integral in Eq. (5.71):

$$\oint_{\partial D^k} (f_j^k(\chi,t) - f_j^{k,*}(\chi,t))\hat{n}(\boldsymbol{M}^k)^{-1}\boldsymbol{l}(\chi) = \left(\frac{\lambda_j - |\lambda_j|}{2}\right)\hat{n}_r^- [\![f_r]\!]\boldsymbol{e}_r - \left(\frac{\lambda_j + |\lambda_j|}{2}\right)\hat{n}_l^- [\![f_l]\!]\boldsymbol{e}_l. \tag{5.76}$$

Together with the numerical flux from Eq. (5.76), the final strong formulation – and thereby the implementation foundation – can be written as

$$\begin{aligned}\partial_t \boldsymbol{c}_j^k =& (\boldsymbol{M}^k)^{-1}\boldsymbol{S}^k\boldsymbol{f}_j^k - (\boldsymbol{M}^k)^{-1}\textstyle\sum_{a=1}^{N_{GL}}(\tilde{V}V^{-1})_{ap}(\tilde{V}V^{-1})_{aq}G_{jm}w_a J^k \\ &+ \left(\frac{\lambda_j - |\lambda_j|}{2}\right)\hat{n}_r^- [\![f_r]\!]\boldsymbol{e}_r - \left(\frac{\lambda_j + |\lambda_j|}{2}\right)\hat{n}_l^- [\![f_l]\!]\boldsymbol{e}_l.\end{aligned} \tag{5.77}$$

This concludes the second stage of the MSD, and the LVNE is now fully discretized in space. Within the framework of intraband quantum transport, Eq. (5.77) is the foundation for both the valence and conduction bands, differing only in the respective physical constants.
To compute the carrier density n and current density j, the following relation is used [58]:

$$n(\chi,t) = \Re\{\boldsymbol{\rho}\}|_{\xi=0} \qquad \text{and} \qquad j(\chi,t) = q\frac{\hbar}{m\Delta\xi}\Im\{\boldsymbol{\rho}\}|_{\xi=0}. \tag{5.78}$$

In the following, the model with spatially varying effective mass will be discretized.

Intermediate summary: In this Subsection 5.3, the LVNE has been discretized using the MSD in two separate stages. First, the relative coordinate ξ was discretized using the FV, FEM, and DG methods. This yielded eigenvalues and eigenvectors required for a basis transformation into phase space or eigenspace, which transformed the LVNE into the QLE. Subsequently, the center-mass coordinate χ was discretized using the DG method, leading to the strong formulation that serves as the foundation for the implementation as given in Eq. (5.78).

5.4. Discretization of the Spatially Varying Effective Mass

The model including the spatially varying effective mass introduces not only the new variable $m(\chi)$ but also a second derivative with respect to the transport coordinate χ. As a result, the straightforward formulation of the numerical flux as previously presented in Section 5.5 is no longer directly applicable. The basis for the upcoming discretization is Eq. (3.12). In a first step, the equation is simplified by introducing three operators D_0, D_1, and D_2. Additionally, the relative coordinate ξ is discretized using the FV method, since this yields the smallest matrix dimension and allows for a plane wave basis. Eq. (3.12) can thus be rewritten as

$$\frac{\partial}{\partial t}\boldsymbol{\rho}(\chi,t) = \boldsymbol{D}_2(\chi)\frac{\partial^2}{\partial\chi^2}\boldsymbol{\rho}(\chi,t) + \boldsymbol{D}_1(\chi)\frac{\partial}{\partial\chi}\boldsymbol{\rho}(\chi,t) + \boldsymbol{D}_0(\chi)\boldsymbol{\rho}(\chi,t), \tag{5.79}$$

where the matrix elements of $\boldsymbol{D}_2$, $\boldsymbol{D}_1$, and $\boldsymbol{D}_0$ are given by [GS4],[58]

$$\begin{aligned}
D_2^{l,l'}(\chi) &= \frac{\imath\hbar}{8} m_-(\chi,\xi_l)\cdot\delta_{l,l'},\\
D_1^{l,l'}(\chi) &= \frac{\imath\hbar}{4}\frac{\partial}{\partial\chi} m_-(\chi,\xi_l) + \frac{\imath\hbar}{2} m_+(\chi,\xi_l)\cdot\left(\frac{\delta_{l,l'-1}-\delta_{l,l'+1}}{2\Delta\xi}\right),\\
D_0^{l,l'}(\chi) &= \frac{\imath\hbar}{2}\frac{\partial}{\partial\chi} m_+(\chi,\xi_l)\cdot\left(\frac{\delta_{l,l'-1}-\delta_{l,l'+1}}{2\Delta\xi}\right) + \frac{\imath\hbar}{2} m_-(\chi,\xi_l)\cdot\left(\frac{\delta_{l,l'-1}-2\delta_{l,l'}+\delta_{l,l'+1}}{\Delta\xi^2}\right),\\
d_0^{l,l'}(\chi) &= \frac{1}{\imath\hbar}\cdot\left(V\left(\chi+\frac{\xi_l}{2}\right) - V\left(\chi-\frac{\xi_l}{2}\right) - \imath W(\xi_l)\right).
\end{aligned} \tag{5.80}$$

Here, $m_\pm(\chi)$ denotes the spatially varying effective mass introduced in Eq. (3.10). The matrix $\boldsymbol{d}_0(\chi)$ contains the potential terms V and the CAP $\imath W(\xi)$. The term $d_0^{l,l'}(\chi)$ can generally be interpreted as the drift term. Its evaluation follows the same scheme as the drift term G_{jm} in Section 5.3.2. To reduce the second-order derivative, a substitution is introduced with

$$\boldsymbol{u}(\chi) = \frac{\partial}{\partial\chi}\boldsymbol{\rho}(\chi,t). \tag{5.81}$$

Inserting Eq. (5.81) into Eq. (5.79) yields:

$$\frac{\partial}{\partial t}\boldsymbol{\rho}(\chi,t) = \boldsymbol{D}_2(\chi)\frac{\partial}{\partial\chi}\boldsymbol{u}(\chi) + \boldsymbol{D}_1(\chi)\boldsymbol{u}(\chi) + \boldsymbol{D}_0(\chi)\boldsymbol{\rho}(\chi,t). \tag{5.82}$$

This results in a coupled system of Eqs. (5.81) and (5.82) for the two unknown vectors $\boldsymbol{u}$ and $\boldsymbol{\rho}$. Since both equations contain the gradient ∂_χ, suitable numerical fluxes must be defined for each. The discretization in ξ based on plane waves yields eigenvalues and eigenvectors, $\boldsymbol{\Lambda}$ and $\boldsymbol{\Phi}$, which are used for the subsequent basis transformation. The statistical density matrix $\boldsymbol{\rho}$ and the substitution variable $\boldsymbol{u}$ are transformed utilizing the expansions from Eqs. (5.64) and (5.65), while the substitution variable $\boldsymbol{u}$ is expanded according to $\tilde{\boldsymbol{u}}(\chi) = \boldsymbol{\Phi}^\dagger\cdot\boldsymbol{u}(\chi)$. Multiplying both equations by test functions $l_i(\chi)$ and integrating over a finite element, followed by two partial integrations to derive the strong formulation and insert the numerical flux, one obtains:

$$\boldsymbol{M}^k\tilde{\boldsymbol{u}}_j^k - \boldsymbol{S}^k\boldsymbol{f}_j^k = \oint_{\partial D^k}\left(f_j^k(\chi,t) - f_j^{k,*}(\chi,t)\right)\hat{n}\boldsymbol{l}(\chi), \tag{5.83}$$

$$\boldsymbol{M}^k\frac{\partial}{\partial t}\boldsymbol{c}_j^k - \boldsymbol{D}_2\boldsymbol{S}^k\tilde{\boldsymbol{u}}_j^k + \boldsymbol{D}_1\boldsymbol{M}^k\tilde{\boldsymbol{u}}_j^k + \boldsymbol{D}_0\boldsymbol{M}^k\boldsymbol{c}_j^k + \boldsymbol{d}_0\boldsymbol{c}_j^k = \boldsymbol{D}_2\oint_{\partial D^k}\left(u_j^k(\chi) - u_j^{k,*}(\chi)\right)\hat{n}\boldsymbol{l}(\chi). \tag{5.84}$$

Using the mass and stiffness matrices defined in Eq. (5.55), the matrix form of Eqs. (5.83) and (5.84) is obtained. The right-hand sides include the numerical flux. Note that the last term $\boldsymbol{d}_0\boldsymbol{c}_j^k$ does not require a mass matrix since it is integrated using Gauss-Lobatto quadrature (see M2 in Section 5.3.2).

Based on the known eigenvalues from the ξ-discretization, an upwind flux with $\alpha = 0$ is applied to both equations:

$$\oint_{\partial D^k}(f_j^k - f_j^{k,*})\hat{n}l_i(\chi) = \lambda_j\left(\frac{f_{r/l}^- + f_{r/l}^+}{2}\right) + |\lambda_j|\frac{1-\alpha}{2}[\![f_{r/l}]\!], \tag{5.85}$$

$$\oint_{\partial D^k}(u_j^k - u_j^{k,*})\hat{n}l_i(\chi) = \left\{\lambda_j\left(\frac{u_{r/l}^- + u_{r/l}^+}{2}\right) + |\lambda_j|\frac{1-\alpha}{2}[\![u_{r/l}]\!]\right\}\cdot\boldsymbol{e}_{r/l}, \tag{5.86}$$

where $\boldsymbol{e}_{r/l}$ are the lift operators defined in Eq. (5.74). The flux values from Eq. (5.85) are assembled into a matrix $\boldsymbol{F}_f^k$, and those from Eq. (5.86) into a matrix $\boldsymbol{F}_u^k$.
Multiplying Eq. (5.84) from the left by the inverse mass matrix and rearranging all terms to the right-hand side yields the system in compact matrix-vector form:

$$\begin{pmatrix} 0 \\ \frac{\partial}{\partial t}\boldsymbol{c}_j^k \end{pmatrix} = \begin{pmatrix} \boldsymbol{M}^k & -(\boldsymbol{S}^k - \boldsymbol{F}_f^k) \\ (\boldsymbol{M}^k)^{-1}\boldsymbol{D}_2(\boldsymbol{S}^k - \boldsymbol{F}_u^k) - \boldsymbol{D}_1 & -\boldsymbol{D}_0 - (\boldsymbol{M}^k)^{-1}\boldsymbol{d}_0 \end{pmatrix} \cdot \begin{pmatrix} \tilde{\boldsymbol{u}}_j^k \\ \boldsymbol{c}_j^k \end{pmatrix}. \tag{5.87}$$

Since $\boldsymbol{u}(\chi)$ is only an auxiliary variable, the flux $\boldsymbol{F}_u$ does not contribute boundary conditions to the system. The flux $\boldsymbol{F}_f$, however, does, resulting in Dirichlet boundary conditions imposed via the Fermi-Dirac distribution (cf. Section 4.2). For the boundaries in ξ, the CAP is included through $\imath W(\xi)$ in Eq. (5.80) [GS4].
Regarding matrix dimensions, the substitution in Eq. (5.81) doubles the size of the system compared to the basic intraband model. While the submatrices (e.g., $\boldsymbol{S}$) remain of size $N_\chi N_p \times N_\chi N_p$, the total system has a dimension of $2 \cdot N_\xi N_\chi N_p \times 2 \cdot N_\xi N_\chi N_p$, since two equations are solved.

Next, the discretization of the interband transport model is presented.

5.5. Interband Transport

The fundamental equation for the discretization of the interband quantum model is given by Eq. (3.19). In total, four equations must be solved, two of which contain second-order derivatives. These are specifically the coupling equations of motion for ρ_{cv} and ρ_{vc}, which require special attention to formulate an appropriate numerical flux.

5.5.1. Discretization of the ξ-Coordinate

Also in this case, only the FV method is employed to discretize the relative coordinate ξ. This choice is made due to the matrix size, which can be given by $4 \cdot N_\xi N_\chi N_p \times 4 \cdot N_\xi N_\chi N_p$. The FV method further allows analytical expressions for the eigenvalues and basis vectors. Additionally, the resulting matrices are smaller compared to the DG method, allowing the concept to run on limited hardware. The discretization is based on the formulations in Eq. (3.19).

The terms in Eq. (3.19) can again be written in matrix form:

$$\begin{aligned}
T_{cc}^{l,l'} &= -T_{vv}^{l,l'} = \frac{\hbar}{\imath m}\left(\frac{\delta_{l,l'-1}-\delta_{l,l'+1}}{2\Delta_\xi}\right),\\
D_{cv}^{l,l'} &= -D_{vc}^{l,l'} = \frac{\hbar}{\imath 4m}\cdot\delta_{l,l'},\\
O_{\pm}^{l,l'}(\chi) &= \pm\frac{\hbar P}{\imath m_0 E_g}\mathcal{E}^{\pm}\cdot\delta_{l,l'},\\
Z_{cc}^{l,l'}(\chi) &= Z_{vv}^{l,l'}(\chi) = \frac{1}{\imath\hbar}\left\{\frac{\tilde{B}^{+}}{4}\cdot\delta_{l,l'-1}+\frac{\tilde{B}^{-}}{4}\cdot\delta_{l,l'+1}+\frac{\tilde{B}^{+}+\tilde{B}^{-}}{4}\cdot\delta_{l,l'}\right\},\\
Z_{cv}^{l,l'}(\chi) &= \left\{\frac{\hbar}{\imath m}\left(\frac{\delta_{l,l'-1}-2\delta_{l,l'}+\delta_{l,l'+1}}{\Delta\xi^2}\right)+\frac{E_g}{\imath\hbar}\delta_{l,l'}\right\}+Z_{cc}^{l,l'}(\chi),\\
Z_{vc}^{l,l'}(\chi) &= \left\{-\frac{\hbar}{\imath m}\left(\frac{\delta_{l,l'-1}-2\delta_{l,l'}+\delta_{l,l'+1}}{\Delta\xi^2}\right)-\frac{E_g}{\imath\hbar}\delta_{l,l'}\right\}+Z_{vv}^{l,l'}(\chi),
\end{aligned} \tag{5.88}$$

where $\tilde{B}^{\pm}$ contain the potential values and are defined as $\tilde{B}^{\pm}=\tilde{V}(\chi,\xi_{l\pm1/2})-\imath W(\xi_{l\pm1/2})$. Using the operators from Eq. (5.88), the semi-discrete matrices can be constructed. These operators are then assembled into the matrix form:

$$\begin{aligned}
\boldsymbol{D}_2 &= \begin{pmatrix}
\mathbf{0} & \mathbf{0} & \mathbf{0} & \mathbf{0}\\
\mathbf{0} & \boldsymbol{\Phi}_{cv}^{\dagger}\boldsymbol{D}_{cv}\boldsymbol{\Phi}_{cv} & \mathbf{0} & \mathbf{0}\\
\mathbf{0} & \mathbf{0} & \boldsymbol{\Phi}_{vc}^{\dagger}\boldsymbol{D}_{vc}\boldsymbol{\Phi}_{vc} & \mathbf{0}\\
\mathbf{0} & \mathbf{0} & \mathbf{0} & \mathbf{0}
\end{pmatrix},\\
\boldsymbol{D}_1 &= \begin{pmatrix}
\boldsymbol{\Phi}_{cc}^{\dagger}\boldsymbol{T}_{cc}\boldsymbol{\Phi}_{cc} & \mathbf{0} & \mathbf{0} & \mathbf{0}\\
\mathbf{0} & \mathbf{0} & \mathbf{0} & \mathbf{0}\\
\mathbf{0} & \mathbf{0} & \mathbf{0} & \mathbf{0}\\
\mathbf{0} & \mathbf{0} & \mathbf{0} & \boldsymbol{\Phi}_{vv}^{\dagger}\boldsymbol{T}_{vv}\boldsymbol{\Phi}_{vv}
\end{pmatrix} \quad \text{and}\\
\boldsymbol{D}_0 &= \begin{pmatrix}
\boldsymbol{\Phi}_{cc}^{\dagger}\boldsymbol{Z}_{cc}(\chi)\boldsymbol{\Phi}_{cc} & \boldsymbol{\Phi}_{cc}^{\dagger}\boldsymbol{O}_{-}(\chi)\boldsymbol{\Phi}_{cv} & \boldsymbol{\Phi}_{cc}^{\dagger}\boldsymbol{O}_{+}(\chi)\boldsymbol{\Phi}_{vc} & \mathbf{0}\\
\boldsymbol{\Phi}_{cv}^{\dagger}\boldsymbol{O}_{-}(\chi)\boldsymbol{\Phi}_{cc} & \boldsymbol{\Phi}_{cv}^{\dagger}\boldsymbol{Z}_{cv}(\chi)\boldsymbol{\Phi}_{cv} & \mathbf{0} & \boldsymbol{\Phi}_{cv}^{\dagger}\boldsymbol{O}_{+}(\chi)\boldsymbol{\Phi}_{vv}\\
\boldsymbol{\Phi}_{vc}^{\dagger}\boldsymbol{O}_{+}(\chi)\boldsymbol{\Phi}_{cc} & \mathbf{0} & \boldsymbol{\Phi}_{vc}^{\dagger}\boldsymbol{Z}_{vc}(\chi)\boldsymbol{\Phi}_{vc} & \boldsymbol{\Phi}_{vc}^{\dagger}\boldsymbol{O}_{-}(\chi)\boldsymbol{\Phi}_{vv}\\
\mathbf{0} & \boldsymbol{\Phi}_{vv}^{\dagger}\boldsymbol{O}_{+}(\chi)\boldsymbol{\Phi}_{cv} & \boldsymbol{\Phi}_{vv}^{\dagger}\boldsymbol{O}_{-}(\chi)\boldsymbol{\Phi}_{vc} & \boldsymbol{\Phi}_{vv}^{\dagger}\boldsymbol{Z}_{vv}(\chi)\boldsymbol{\Phi}_{vv}
\end{pmatrix}.
\end{aligned} \tag{5.89}$$

Here, the basis transformations are defined via the matrices $\boldsymbol{\Phi}_{cc}$, $\boldsymbol{\Phi}_{cv}$, $\boldsymbol{\Phi}_{vc}$, and $\boldsymbol{\Phi}_{vv}$. The semi-discrete QLE can then be written as:

$$\frac{\partial}{\partial t}\boldsymbol{\mathcal{P}}(\chi,t) = \boldsymbol{D}_2\frac{\partial^2}{\partial\chi^2}\boldsymbol{\mathcal{P}}(\chi,t)+\boldsymbol{D}_1\frac{\partial}{\partial\chi}\boldsymbol{\mathcal{P}}(\chi,t)+\boldsymbol{D}_0(\chi)\boldsymbol{\mathcal{P}}(\chi,t), \tag{5.90}$$

where the vector $\boldsymbol{\mathcal{P}}(\chi,t)$ collects the components of the semi-discrete density vectors $\boldsymbol{\rho}_{\lambda,\lambda'}(\chi,t)$ according to [58]

$$\boldsymbol{\mathcal{P}}(\chi,t) = \left(\boldsymbol{\rho}_{cc}(\chi,t),\boldsymbol{\rho}_{cv}(\chi,t),\boldsymbol{\rho}_{vc}(\chi,t),\boldsymbol{\rho}_{vv}(\chi,t)\right)^{T}.$$

There are two strategies for obtaining the basis vector matrices and their corresponding eigenvalues:

1. ***Analytical approach***: The eigenvalues and vectors are determined via Eqs. (5.47) and (5.48).

2. ***Approach using the discretization matrix***: A discretization matrix is constructed for the ξ-coordinate, and its eigenvalues and eigenvectors are used in the further procedure.

If the analytical approach is chosen, then the eigenvalues $\boldsymbol{\Lambda}_{cc}$ are derived from Eq. (5.47) for a given number of finite volumes N_ξ. Similarly, the basis vectors $\boldsymbol{\Phi}_{cc}$ follow from Eq. (5.48). The eigenvalues and basis vectors for the valence band are then set as $\boldsymbol{\Lambda}_{vv} = -\boldsymbol{\Lambda}_{cc}$ and $\boldsymbol{\Phi}_{vv} = -\boldsymbol{\Phi}_{cc}$. This approach is used in [56], although it is questionable whether it sufficiently resolves the Riemann problem. One issue is that the second-order derivative ∂_ξ^2 is entirely neglected. A more precise method is the one using the discretization matrix as proposed in point two.
As can be seen in Eq. (3.19), the ξ-derivatives mainly appear in the matrices $\boldsymbol{D}_1$ and $\boldsymbol{D}_2$. The discretization matrix $\hat{\boldsymbol{A}}$ can be written analytically as [GS5]:

$$\bar{\mathcal{A}} \cdot \boldsymbol{\rho} + \mathcal{A}^* \cdot \boldsymbol{\rho} = \underbrace{\begin{pmatrix} \partial_\xi & 0 & 0 & 0 \\ 0 & \boldsymbol{I} & 0 & 0 \\ 0 & 0 & \boldsymbol{I} & 0 \\ 0 & 0 & 0 & \partial_\xi \end{pmatrix}}_{\bar{\mathcal{A}}} \partial_\chi \begin{pmatrix} \boldsymbol{\rho}_{cc} \\ \partial_\chi \boldsymbol{\rho}_{cv} \\ \partial_\chi \boldsymbol{\rho}_{vc} \\ \boldsymbol{\rho}_{vv} \end{pmatrix} + \underbrace{\begin{pmatrix} 0 & 0 & 0 & 0 \\ 0 & \partial_\xi^2 & 0 & 0 \\ 0 & 0 & \partial_\xi^2 & 0 \\ 0 & 0 & 0 & 0 \end{pmatrix}}_{\mathcal{A}^*} \begin{pmatrix} \boldsymbol{\rho}_{cc} \\ \boldsymbol{\rho}_{cv} \\ \boldsymbol{\rho}_{vc} \\ \boldsymbol{\rho}_{vv} \end{pmatrix}. \tag{5.91}$$

Now, the discretization matrix $\hat{\boldsymbol{A}}$ can be diagonalized using the eigenvalue decomposition $\boldsymbol{\Lambda} = \boldsymbol{\Phi}^\dagger \hat{\boldsymbol{A}} \boldsymbol{\Phi}$. A mathematical property of the matrix $\hat{\boldsymbol{A}}$ can be exploited here to simplify the assignment of eigenvalues and eigenvectors to the individual states. Since only the main diagonal of $\hat{\boldsymbol{A}}$ is populated, as shown in Eq. (5.91), the matrix elements $\hat{\boldsymbol{A}}(i,i)$ for $i = 1, \ldots, 4$ can be diagonalized individually and identified as follows:

$$\begin{aligned} \hat{\boldsymbol{A}}(1,1) \to \hat{\boldsymbol{A}}_{cc} \to \boldsymbol{\Lambda}_{cc} &= \boldsymbol{\Phi}_{cc}^\dagger \hat{\boldsymbol{A}}(1,1) \boldsymbol{\Phi}_{cc}, \\ \hat{\boldsymbol{A}}(2,2) \to \hat{\boldsymbol{A}}_{cv} \to \boldsymbol{\Lambda}_{cv} &= \boldsymbol{\Phi}_{cv}^\dagger \hat{\boldsymbol{A}}(2,2) \boldsymbol{\Phi}_{cv}, \\ \hat{\boldsymbol{A}}(3,3) \to \hat{\boldsymbol{A}}_{vc} \to \boldsymbol{\Lambda}_{vc} &= \boldsymbol{\Phi}_{vc}^\dagger \hat{\boldsymbol{A}}(3,3) \boldsymbol{\Phi}_{vc}, \\ \hat{\boldsymbol{A}}(4,4) \to \hat{\boldsymbol{A}}_{vv} \to \boldsymbol{\Lambda}_{vv} &= \boldsymbol{\Phi}_{vv}^\dagger \hat{\boldsymbol{A}}(4,4) \boldsymbol{\Phi}_{vv}. \end{aligned} \tag{5.92}$$

The signs of the eigenvalues $\lambda_{\lambda\lambda',j}$ in the eigenvalue vectors $\boldsymbol{\Lambda}_{\lambda\lambda'}$ correspond to the propagation direction of the wave packets and can therefore be used for formulating the numerical flux and inflow boundary conditions, enabling an appropriate treatment of the Riemann problem. The eigenvector matrices are orthogonal, i.e., $\boldsymbol{\Phi}_{\lambda\lambda'}^\dagger \boldsymbol{\Phi}_{\lambda\lambda'} = \boldsymbol{I}$.
Subsequently, the spatial coordinate χ is discretized next.

5.5.2. Discretization of the χ-Coordinate

The transport direction χ is again discretized using the DG method. The closed computational domain with interval $\Omega_\chi = [0, L_\chi]$ is discretized into N_χ one-dimensional finite elements. The triangulation then consists of $N_{\chi p} = N_\chi \cdot N_p$ nodes, where N_p is the number of nodes per element. The terms are then multiplied by the test functions $l_j(\chi)$ and integrated over the reference element D^k. After twofold partial integration of all terms in Eq. (3.19), the following relations

result [GS5]:

$$\begin{aligned}
\int_{D^k} \partial_t \boldsymbol{\rho}'_{cc} l_j^k &= +\int_{D^k} \partial_\chi f^k_{cc,j} l_j^k + \int_{D^k} \hat{U} \boldsymbol{\rho}'_{cc} l_j^k + \int_{D^k} \mathcal{E}^- \boldsymbol{\rho}'_{cv} l_j^k - \int_{D^k} \mathcal{E}^+ \boldsymbol{\rho}'_{vc} l_j^k \\
&\quad - \left\{ [f^k_{cc,j} l_j^k] - [f^{k,*}_{cc,j} l_j^k] \right\}_{\partial D^k}, \\
\int_{D^k} \partial_t \boldsymbol{\rho}'_{cv} l_j^k &= +\int_{D^k} \left\{ \frac{1}{4}\partial_\chi^2 + \mathcal{I} \right\} f^k_{cv,j} l_j^k + \int_{D^k} \left\{ +E_g + \hat{U} \right\} \boldsymbol{\rho}'_{cv} l_j^k + \int_{D^k} \mathcal{E}^- \boldsymbol{\rho}'_{cc} l_j^k - \int_{D^k} \mathcal{E}^+ \boldsymbol{\rho}'_{vv} l_j^k \\
&\quad - \left\{ [\partial_\chi f^k_{cv,j} l_j^k] - [\partial_\chi f^{k,*}_{cv,j} l_j^k] \right\}_{\partial D^k}, \\
\int_{D^k} \partial_t \boldsymbol{\rho}'_{vc} l_j^k &= -\int_{D^k} \left\{ \frac{1}{4}\partial_\chi^2 + \mathcal{I} \right\} f^k_{vc,j} l_j^k + \int_{D^k} \left\{ -E_g + \hat{U} \right\} \boldsymbol{\rho}'_{vc} l_j^k + \int_{D^k} \mathcal{E}^- \boldsymbol{\rho}'_{vv} l_j^k - \int_{D^k} \mathcal{E}^+ \boldsymbol{\rho}'_{cc} l_j^k \\
&\quad - \left\{ [\partial_\chi f^k_{vc,j} l_j^k] - [\partial_\chi f^{k,*}_{vc,j} l_j^k] \right\}_{\partial D^k}, \\
\int_{D^k} \partial_t \boldsymbol{\rho}'_{vv} l_j^k &= -\int_{D^k} \partial_\chi f^k_{vv,j} l_j^k + \int_{D^k} \hat{U} \boldsymbol{\rho}'_{vv} l_j^k + \int_{D^k} \mathcal{E}^- \boldsymbol{\rho}'_{vc} l_j^k - \int_{D^k} \mathcal{E}^+ \boldsymbol{\rho}'_{cv} l_j^k \\
&\quad - \left\{ [f^k_{vv,j} l_j^k] - [f^{k,*}_{vv,j} l_j^k] \right\}_{\partial D^k}.
\end{aligned} \tag{5.93}$$

Here, $\mathcal{I}$ is the identity matrix and $\boldsymbol{\rho}'_{\lambda\lambda'} = \sum_{i=1}^{N_p} c_j^k l_i^k$ is the expansion of the statistical density matrix $\boldsymbol{\rho}_{\lambda\lambda'}$. The expressions in curly brackets represent the flux terms $f^k_{\lambda\lambda',j}$ and the numerical flux $f^{k,*}_{\lambda\lambda',j}$. As before, the single-valued numerical flux replaces the double-valued flux, ensuring continuity across element interfaces. While the flux can be clearly defined for $\boldsymbol{\rho}'_{cc}$ and $\boldsymbol{\rho}'_{vv}$, it cannot be directly applied to $\boldsymbol{\rho}'_{cv}$ and $\boldsymbol{\rho}'_{vc}$ due to the second order derivative. Thus, a substitution is introduced:

$$\boldsymbol{u}_{cv} = \frac{\partial}{\partial\chi}\boldsymbol{\rho}'_{cv}, \qquad \boldsymbol{u}_{vc} = \frac{\partial}{\partial\chi}\boldsymbol{\rho}'_{vc}. \tag{5.94}$$

Substituting into Eq. (5.93) yields:

$$\begin{aligned}
\int_{D^k} \partial_t \boldsymbol{\rho}'_{cv} l_j^k &= +\int_{D^k} \left\{ \frac{1}{4}\partial_\chi \boldsymbol{u}_{cv} + \mathcal{I} f^k_{cv,j} \right\} l_j^k + \int_{D^k} (E_g + \hat{U}) \boldsymbol{\rho}'_{cv} l_j^k + \int_{D^k} \mathcal{E}^- \boldsymbol{\rho}'_{cc} l_j^k - \int_{D^k} \mathcal{E}^+ \boldsymbol{\rho}'_{vv} l_j^k \\
&\quad - \left\{ [u^k_{cv,j} l_j^k] - [u^{k,*}_{cv,j} l_j^k] \right\}_{\partial D^k}, \\
\int_{D^k} \partial_t \boldsymbol{\rho}'_{vc} l_j^k &= -\int_{D^k} \left\{ \frac{1}{4}\partial_\chi \boldsymbol{u}_{vc} + \mathcal{I} f^k_{vc,j} \right\} l_j^k + \int_{D^k} (-E_g + \hat{U}) \boldsymbol{\rho}'_{vc} l_j^k + \int_{D^k} \mathcal{E}^- \boldsymbol{\rho}'_{vv} l_j^k - \int_{D^k} \mathcal{E}^+ \boldsymbol{\rho}'_{cc} l_j^k \\
&\quad - \left\{ [u^k_{vc,j} l_j^k] - [u^{k,*}_{vc,j} l_j^k] \right\}_{\partial D^k}.
\end{aligned} \tag{5.95}$$

Once again, a flux with respect to $\boldsymbol{u}_{\lambda,\lambda'}$ and a flux with respect to $\boldsymbol{\rho}_{\lambda,\lambda'}$ arises. The latter is obtained by multiplying the substitution equations (5.94) with test functions $l_i(\chi)$, integrating over the reference element, and subsequently performing two partial integrations, which results in

$$\begin{aligned}
\int_{D^k} \boldsymbol{u}_{cv} l_j^k &= \int_{D^k} \frac{\partial}{\partial\chi} f_{cv} l_j^k - \left\{ [f^k_{cv} l_j^k] - [f^{k,*}_{cv} l_j^k] \right\} \qquad \text{and} \\
\int_{D^k} \boldsymbol{u}_{vc} l_j^k &= \int_{D^k} \frac{\partial}{\partial\chi} f_{vc} l_j^k - \left\{ [f^k_{vc} l_j^k] - [f^{k,*}_{vc} l_j^k] \right\}.
\end{aligned} \tag{5.96}$$

The substitutions $\boldsymbol{u}_{cv}$ and $\boldsymbol{u}_{vc}$ are themselves expanded using test functions, and after transforming all equations with the mass matrix $\boldsymbol{M}$, stiffness matrix $\boldsymbol{S}$, and lift operators $\boldsymbol{e}_{l/r}$, the full matrix form becomes:

$$
\begin{aligned}
\partial_t \boldsymbol{\rho}'_{cc} &= +(\boldsymbol{M})^{-1}\boldsymbol{D}_1(\boldsymbol{S}-\boldsymbol{F}_f)\boldsymbol{\rho}'_{cc} + (\boldsymbol{M})^{-1}\boldsymbol{Z}_{cc}\boldsymbol{\rho}'_{cc} + (\boldsymbol{M})^{-1}\boldsymbol{O}^{-}\boldsymbol{\rho}'_{cv} - (\boldsymbol{M})^{-1}\boldsymbol{O}^{+}\boldsymbol{\rho}'_{vc},\\
\partial_t \boldsymbol{\rho}'_{cv} &= +(\boldsymbol{M})^{-1}\boldsymbol{D}_2(\boldsymbol{S}-\boldsymbol{F}_u)\boldsymbol{u}_{cv} + \boldsymbol{D}_2\boldsymbol{\rho}'_{cv} + (\boldsymbol{M})^{-1}\boldsymbol{Z}_{cv}\boldsymbol{\rho}'_{cv} + (\boldsymbol{M})^{-1}\boldsymbol{O}^{-}\boldsymbol{\rho}'_{cc}\\
&\quad -(\boldsymbol{M})^{-1}\boldsymbol{O}^{+}\boldsymbol{\rho}'_{vv},\\
0 &= -\boldsymbol{M}\boldsymbol{u}_{cv} + (\boldsymbol{S}-\boldsymbol{F}_f)\boldsymbol{\rho}'_{cv},\\
\partial_t \boldsymbol{\rho}'_{vc} &= -(\boldsymbol{M})^{-1}\boldsymbol{D}_2(\boldsymbol{S}-\boldsymbol{F}_u)\boldsymbol{u}_{vc} + \boldsymbol{D}_2\boldsymbol{\rho}'_{vc} + (\boldsymbol{M})^{-1}\boldsymbol{Z}_{vc}\boldsymbol{\rho}'_{vc} + (\boldsymbol{M})^{-1}\boldsymbol{O}^{-}\boldsymbol{\rho}'_{vv}\\
&\quad -(\boldsymbol{M})^{-1}\boldsymbol{O}^{+}\boldsymbol{\rho}'_{cc},\\
0 &= -\boldsymbol{M}\boldsymbol{u}_{vc} + (\boldsymbol{S}-\boldsymbol{F}_f)\boldsymbol{\rho}'_{vc},\\
\partial_t \boldsymbol{\rho}'_{vv} &= -(\boldsymbol{M})^{-1}\boldsymbol{D}_1(\boldsymbol{S}-\boldsymbol{F}_f)\boldsymbol{\rho}'_{vv} + (\boldsymbol{M})^{-1}\boldsymbol{Z}_{vv}\boldsymbol{\rho}'_{vv} + (\boldsymbol{M})^{-1}\boldsymbol{O}^{-}\boldsymbol{\rho}'_{vc} - (\boldsymbol{M})^{-1}\boldsymbol{O}^{+}\boldsymbol{\rho}'_{cv}.
\end{aligned}
\tag{5.97}
$$

Note that the matrices $\boldsymbol{Z}_{\lambda,\lambda'}$ and $\boldsymbol{O}^{\pm}$ are evaluated using Gauss-Lobatto quadrature for higher accuracy. Accordingly, the left multiplication by the inverse mass matrix $(\boldsymbol{M})^{-1}$ is also applied to these terms.

Intermediate summary: The interband quantum model from Section 3.4 has now been spatially fully discretized. The ξ-coordinate was discretized using a low-order FV technique. The operators in Eq. (5.88) were constructed and transformed to the eigenbasis using the basis vector matrices derived from the discretization matrix $\hat{\boldsymbol{A}}$, itself resulting from the FV method. Subsequently, the transport coordinate χ was discretized using the DG approach. The terms of the interband equations (3.19) were treated using this method. Since two of these equations contained second-order derivatives, suitable substitution was applied to reduce the differential order. This resulted in a total of six equations, as shown in Eqs. (5.93), (5.95), and (5.96). After multiplying each equation with test functions, integrating over a reference element D^k, and applying twofold integration by parts, the strong formulation was derived. With the eigenvalues from the discretization matrix $\hat{\boldsymbol{A}}$, a numerical flux was introduced. Finally, the mass and stiffness matrices were incorporated and the resulting matrix system, shown in Eq. (5.97), was formulated – serving as the foundation for simulation.

5.6. Discretization of the Time Domain

In the previous chapters, the stationary case was assumed throughout. However, the time axis must also be discretized. This forms the third stage of the MSD approach and the final step in Fig. 3.2, leading to a fully discretized QLE. Within the stationary formulation, all terms have already been left-multiplied by the local inverse mass matrix $(\boldsymbol{M}^k)^{-1}$. Consequently, explicit time discretization methods can be applied, which are generally more efficient than implicit methods [103] and are therefore well suited for combination with the DG method. In this work, the Runge-Kutta 2nd order (RK2) and Runge-Kutta 4th order (RK4) methods are implemented for this purpose.
The RK2 method satisfies the Total Variation Diminishing Methods (TVDM) property [68]

$$
\sum\nolimits_{D^k\in\mathcal{T}\setminus D^{N_\chi}} |\bar{v}_\tau^{k+1,n+1} - \bar{v}_\tau^{k,n+1}| \leq \sum\nolimits_{D^k\in\mathcal{T}\setminus D^{N_\chi}} |\bar{v}_\tau^{k+1,n} - \bar{v}_\tau^{k,n}|, \tag{5.98}
$$

and is thus considered *strong stability preserving*. The TVDM class comprises numerical schemes used in the solution of PDEs, particularly for hyperbolic equations. The TVD property ensures that the total variation of a solution does not increase over time, which is essential for avoiding spurious oscillations and instabilities [68].
For the RK2 method, the following update scheme is used:

$$\begin{aligned} p^{(1)} &= \boldsymbol{v}_\tau^n + \Delta t \mathcal{F}(\boldsymbol{v}_\tau^n, t^n), \\ \boldsymbol{v}_\tau^{n+1} &= \frac{1}{2}\left(\boldsymbol{v}_\tau^n + p^{(1)} + \Delta t \mathcal{F}(p^{(1)}, t^n + \Delta t)\right). \end{aligned} \tag{5.99}$$

Here, $\mathcal{F}(\boldsymbol{v}_\tau^n, t^n)$ denotes the right-hand side of the final transient system of equations of the form $\partial_t \boldsymbol{v} = -\boldsymbol{A}\boldsymbol{v} + \boldsymbol{b} \equiv \mathcal{F}(\boldsymbol{v}_\tau^n, t^n)$, where $\boldsymbol{A}$ is the system matrix, $\boldsymbol{v}$ the solution vector, and $\boldsymbol{b}$ represents the boundary conditions. Δt is the time step size, which can be chosen using two different strategies. One is the estimation [68]

$$\Delta t \leq \frac{1}{2N+1}\, c\, \frac{\Delta\chi}{\Delta\xi \max(\boldsymbol{\Lambda})}, \tag{5.100}$$

with $c = 0.2$ for the RK2 method and $c = 0.4$ for the RK4 method. Alternatively, the time step can be chosen numerically by computing all eigenvalues γ_j of the system matrix $\boldsymbol{A}$. The step size is then based on the largest absolute eigenvalue $\max(|\gamma_j|)$. However, for large system matrices – typically encountered in real simulations – this eigenvalue analysis can be very time-consuming. Thus, the estimate given in Eq. (5.100) is recommended.
The RK4 method uses the following update rules:

$$\begin{aligned} p^{(0)} &= \boldsymbol{v}_\tau^n, \\ q^{(i)} &= a_i q^{(i-1)} + \Delta t \mathcal{F}(p^{(i-1)}, t^n + c_i \Delta t) \qquad \forall i \in \{1, ..., 5\}, \\ p^{(i)} &= p^{(i-1)} + b_i q^{(i)}, \\ \boldsymbol{v}_\tau^{n+1} &= p^{(5)}. \end{aligned} \tag{5.101}$$

The coefficients a_i, b_i, and c_i can be found in the literature [68]. Although the RK4 method requires more function evaluations per step, this is compensated by the fact that Eq. (5.100) allows a time step twice as large (via $c = 0.4$), helping to avoid a significant increase in total simulation time.

Now that the time domain has also been discretized, a fully discrete QLE system is available. The final step is to implement the self-consistent coupling introduced in Section 2.3, which is achieved using the so-called Gummel algorithm.

5.7. Discretization of the Poisson Equation

For the discretization of the Poisson equation from Subsection 2.3, a FD scheme is applied. It should be noted that the FD scheme exhibits a lower order of accuracy compared to the DG method. It would be interesting to investigate to what extent the runtime of the Gummel algorithm could be reduced if the Poisson equation were discretized using a DG method. Since

a DGFET is simulated in Section 6.4, the two-dimensional formulation will also be considered. For a one-dimensional transport problem, the Poisson equation [58] is given by

$$\frac{\partial}{\partial z}\left(\mathcal{E}(z)\frac{\partial}{\partial z}U(z)\right) = q(N_D(z) - n(z) + p(z) - N_A(z)), \tag{5.102}$$

where $\mathcal{E}$ denotes the permittivity. With N_z equidistant grid points, the transport axis of the device, given over the physical device length L, is discretized. The grid points are spaced at intervals of Δz, and the discrete values of the Hartree potential U_i are located at each point z_i, such that $U(z_i) = U_i$. At the inner nodes, the Poisson equation (5.102) is approximated using the difference equation [65]

$$\frac{\mathcal{E}_{i+\frac{1}{2}}}{\Delta z^2}U_{i+1} - \frac{\mathcal{E}_{i+\frac{1}{2}} + \mathcal{E}_{i-\frac{1}{2}}}{\Delta z^2}U_i + \frac{\mathcal{E}_{i-\frac{1}{2}}}{\Delta z^2}U_{i-1} = \varrho_i = q(N_{D_i} - n_i + p_i - N_{A_i}). \tag{5.103}$$

At the boundary nodes, U_1 and U_{N_z}, the potential values must be incorporated into the boundary conditions. The intermediate grid values can be computed using the arithmetic mean, e.g., $\mathcal{E}_{i+1/2} = (\mathcal{E}(z_i) + \mathcal{E}(z_{i+1}))/2$, since the permittivity can be determined analytically. The system can then be cast into a matrix-vector formulation according to [58].

$$\underbrace{\begin{pmatrix} \gamma_2 & \alpha_2 & & & & & \\ \alpha_2 & \gamma_3 & \alpha_3 & & & & \\ & \ddots & \ddots & \ddots & & & \\ & & \alpha_{i-1} & \gamma_i & \alpha_{i+1} & & \\ & & & \ddots & \ddots & \ddots & \\ & & & & \alpha_{N-3} & \gamma_{N-2} & \alpha_{N-2} \\ & & & & & \alpha_{N-2} & \gamma_{N-1} \end{pmatrix}}_{\boldsymbol{P}} \underbrace{\begin{pmatrix} U_2 \\ \vdots \\ U_{i-1} \\ U_i \\ U_{i+1} \\ \vdots \\ U_{N-1} \end{pmatrix}}_{\boldsymbol{U}} = \underbrace{\begin{pmatrix} \varrho \\ \vdots \\ \varrho_{i-1} \\ \varrho_i \\ \varrho_{i+1} \\ \vdots \\ \varrho_{N-1} \end{pmatrix}}_{\boldsymbol{\varrho}} - \underbrace{\begin{pmatrix} \alpha_1 U_1 \\ 0 \\ \vdots \\ 0 \\ \vdots \\ 0 \\ \alpha_{N-1} U_N \end{pmatrix}}_{\boldsymbol{b}} \tag{5.104}$$

The non-zero matrix elements are given by $\alpha_i = \mathcal{E}_{i+1/2}/\Delta z^2$ and $\gamma_i = -(\mathcal{E}_{i+1/2} + \mathcal{E}_{i-1/2})/\Delta z^2$ [58]. To implement Dirichlet boundary conditions, one side is set as a reference using $U_1 = 0$, and the external voltage is included via $U_{N_z} = -qV$. For Neumann boundary conditions, the following applies:

$$\frac{\partial}{\partial z}U(z)\big|_{z=z_1} = 0 \rightarrow U_1 = U_2 \quad \text{and} \quad \frac{\partial}{\partial z}U(z)\big|_{z=z_N} = 0 \rightarrow U_{N-1} = U_N. \tag{5.105}$$

The Neumann boundary conditions from Eq. (5.105) are then integrated into the system matrix $\boldsymbol{P}$. The matrix elements $\boldsymbol{P}(1,1)$ and $\boldsymbol{P}(N-2, N-2)$ are set to $\boldsymbol{P}(1,1) = \gamma_2 + \alpha_1 = -\alpha_2$ and $\boldsymbol{P}(N-2, N-2) = \gamma_{N-1} + \alpha_{N-2} = -\alpha_{N-2}$, respectively. This results in a matrix-vector product [58].

$$\underbrace{\begin{pmatrix} -\alpha_2 & \alpha_2 & & & & & \\ \alpha_2 & \gamma_3 & \alpha_3 & & & & \\ & \ddots & \ddots & \ddots & & & \\ & & \alpha_{i-1} & \gamma_i & \alpha_{i+1} & & \\ & & & \ddots & \ddots & \ddots & \\ & & & & \alpha_{N-3} & \gamma_{N-2} & \alpha_{N-2} \\ & & & & & \alpha_{N-2} & -\alpha_{N-2} \end{pmatrix}}_{\tilde{\boldsymbol{P}}} \underbrace{\begin{pmatrix} U_2 \\ \vdots \\ U_{i-1} \\ U_i \\ U_{i+1} \\ \vdots \\ U_{N-1} \end{pmatrix}}_{\boldsymbol{U}} = q \underbrace{\begin{pmatrix} \varrho \\ \vdots \\ \varrho_{i-1} \\ \varrho_i \\ \varrho_{i+1} \\ \vdots \\ \varrho_{N-1} \end{pmatrix}}_{\boldsymbol{\varrho}} \tag{5.106}$$

The Gummel algorithm proceeds by solving the transport and Poisson equations successively. Using the carrier density $n(z)$, obtained from solving the transport equation, the Poisson equation (5.106) is solved [65]. The result is a potential that approaches self-consistency with each iteration. In each new iteration, the density operator is constructed using this updated potential as described in Eq. (5.70).
Furthermore, the two-dimensional Poisson equation must be discretized, which is essential for the self-consistent solution of the LVNE. It is defined as

$$\frac{\partial}{\partial z}\left(\mathcal{E}(x,z)\frac{\partial}{\partial z}U(x,z)\right)+\frac{\partial}{\partial x}\left(\mathcal{E}(x,z)\frac{\partial}{\partial x}U(x,z)\right)=\varrho(x,z). \tag{5.107}$$

Again, an FD scheme is used, where the x-direction is discretized using N_x points and the z-direction using N_z points. The finite difference approximation of the differential equation follows [58]:

$$\begin{aligned}&\frac{\mathcal{E}_{i+\frac{1}{2},j}}{\Delta z^2}U_{i+1,j}-\left(\frac{\mathcal{E}_{i+\frac{1}{2},j}+\mathcal{E}_{i-\frac{1}{2},j}}{\Delta z^2}+\frac{\mathcal{E}_{i,j+\frac{1}{2}}+\mathcal{E}_{i,j-\frac{1}{2}}}{\Delta x^2}\right)U_{i,j}+\frac{\mathcal{E}_{i-\frac{1}{2},j}}{\Delta z^2}U_{i-1,j}+\\&\frac{\mathcal{E}_{i,j+\frac{1}{2}}}{\Delta x^2}U_{i,j+1}+\frac{\mathcal{E}_{i,j-\frac{1}{2}}}{\Delta x^2}U_{i,j-1}=\varrho_{i,j}=q(N_{D_{i,j}}-n_{i,j}+p_{i,j}-N_{A_{i,j}}).\end{aligned} \tag{5.108}$$

Here, Δz and Δx are the grid spacings in z- and x-direction, respectively. The source and drain contacts can be constrained using either Neumann or Dirichlet boundary conditions. In the stationary case, Neumann boundary conditions are commonly used [31, 104, 105]:

$$\begin{aligned}U(x,z)\big|_{x,z\in gate}&=\mu+q\phi_m-q\chi_{ch}-qU_G,\\\frac{\partial U(x,z)}{\partial\eta}\big|_{x,z\notin gate}&=0.\end{aligned} \tag{5.109}$$

For time-dependent problems, Dirichlet boundary conditions are incorporated:

$$\begin{aligned}U(x,z,t)\big|_{x,z\in gate}&=\mu+q\phi_m-q\chi_{ch}-qU_G(t),\\U(x,z,t)\big|_{x,z\in source/drain}&=-qU_{D/S}(t),\\\frac{\partial U(x,z,t)}{\partial\eta}\big|_{x,z\notin gate,source,drain}&=0.\end{aligned} \tag{5.110}$$

This again leads to a matrix-vector system similar to Eq. (5.104).
The solution of the one- or two-dimensional system always follows the same scheme, whose operational steps are executed sequentially:

1. **Decoupling the equations**: The Poisson equation and the continuity equations for electrons and holes are treated as coupled equations.
2. **Initialization**: As an initial guess, the potential is assumed to follow a flat-band profile. Using this potential, the quantum transport equation is solved and the carrier distribution is computed.
3. **Iteration**: In each iteration,
   - the carrier densities are computed from the previous values,

- the electric potential is updated using the Poisson equation,
- the new carrier densities are computed based on the updated potential,

4. **Convergence check**: After each iteration, the algorithm checks whether convergence has been reached (i.e., whether the iteration error falls below a given threshold). If so, the process is terminated. Otherwise, the next iteration begins.

5.8. Mode Space Approximation

The MSA is a numerical technique used to reduce the dimensionality of nano devices in quantum transport simulations [31, 104, 106]. The method relies on projecting the transport equation onto the eigenmodes of the cross-sectional plane. A series of coupled one-dimensional transport equations are derived for the transverse direction. As such, the MSA in combination with the DG method offers substantial computational savings compared to a full two-dimensional DG simulation [31].
To implement the MSA, the modal form of the LVNE is required. From the single-particle SE, the transverse Hamiltonian can be extracted [106]:

$$\imath\hbar\frac{\partial}{\partial t}\psi(x,z,t) = \Bigg\{ -\frac{\hbar^2}{2m_z}\frac{\partial^2}{\partial z^2} \underbrace{-\frac{\hbar^2}{2m_x}\frac{\partial^2}{\partial x^2} + V(x,z,t)}_{\mathcal{H}_{\text{trans}}} \Bigg\}\psi(x,z,t). \tag{5.111}$$

with anisotropic effective masses m_z and m_x. The transverse Hamiltonian $\mathcal{H}_{\text{trans}}$ can be diagonalized in the z' direction, resulting in an eigenvalue problem [106]:

$$\mathcal{H}_{\text{trans}}\Psi_n(x;z',t) = E_n(z',t)\Psi_n(x;z',t). \tag{5.112}$$

The wavefunction ψ is then expanded using the eigenfunctions Ψ_n:

$$\psi(x;z',t) = \textstyle\sum_{n'}\phi_{n'}(z',t)\Psi_{n'}(x;z',t). \tag{5.113}$$

From the already derived LVNE in center-mass and relative coordinates, the modal transport equation is obtained for a negligence of the mode coupling [106]:

$$\frac{\partial}{\partial t}\rho_n(\chi,\xi,t) = \frac{\imath\hbar}{m_z}\frac{\partial^2}{\partial\chi\partial\xi}\rho_n(\chi,\xi,t) + \frac{1}{\imath\hbar}\left\{E_n\left(\chi+\frac{1}{2}\xi,t\right) - E_n\left(\chi-\frac{1}{2}\xi,t\right)\right\}\rho_n(\chi,\xi,t). \tag{5.114}$$

From the modal density matrix $\rho_n(\chi,\xi,t)$, the carrier density and current are computed as [106]:

$$n_{n'}(\chi,t) = \rho_{n'}(\chi,\xi=0,t), \qquad j_{n'}(\chi,t) = q\frac{\hbar}{m_z}\Im\left\{\frac{\partial}{\partial\xi}\rho_{n'}(\chi,\xi=0,t)\right\}. \tag{5.115}$$

Given $\chi = z$ and $\xi = 0$, the transformation to the original coordinate system is direct for $n_{n'}$. For the current, no weighting is necessary. The resulting quantities in two dimensions are [106]:

$$n(x,z,t) = \textstyle\sum_n n_n(z,t)|\psi_n(x;z;t)|^2, \qquad j(z,t) = \sum_n j_n(z,t). \tag{5.116}$$

Summary: The chapter began with a thorough introduction discussing common approximation methods and their limitations. This motivated the use of DG methods, whose mathematical

properties such as uniqueness, existence, coercivity, consistency, and stability were rigorously analyzed. Numerical validation confirmed high accuracy, with absolute errors on the order of 10^{-12}.

Subsequently, the quantum transport models introduced in Chapter 3 were discretized using the DG algorithm. These include the intraband model, the model with spatially varying effective mass, and the interband model. Finally, the discretization of the time domain was addressed using RK2 and RK4 schemes, and the Gummel algorithm was introduced for self-consistent coupling of the Poisson and transport equations.

6. Numerical Validation

This chapter evaluates the applicability of the proposed method to representative quantum devices and assesses the plausibility of the obtained results. Its purpose is to demonstrate the feasibility and physical plausibility of the proposed method through representative examples rather than to provide a comprehensive quantitative validation. For this purpose, a device will be simulated that is well documented in the literature, namely the RTD and provides an initial assessment of the DG approach for device simulation.
This component is thoroughly examined in Section 6.1, which will be the main body of this chapter. In addition, a comparison is carried out with the QTBM, which is considered a standard and reliable tool for quantum device simulation in this field [4, 5]. Both stationary and transient quantum transport are considered. Furthermore, within the stationary regime, thermal equilibrium as well as thermal nonequilibrium scenarios are analyzed. The Poisson equation and, therefore, self-consistency is also incorporated. Finally, the characteristic current-voltage curve of the RTD is computed using the DG method.
To show that the DG is not limited to one use-case, section 6.2 presents a simulation of intraband quantum transport based on a TFET.
Section 6.3 deals with the simulation of the RITD, demonstrating the coupling between conduction and valence bands using the interband quantum transport model.
Moreover, Section 6.4 applies the MSA introduced in Section 5.8 coupled with the DG algorithm to simulate a DGFET, where transport in two spatial directions must be considered.
Section 6.5 concludes this chapter by presenting principles of HPC that can be employed to improve the performance of selected simulations.
At this point, the following notation for the numerical methods used in the simulations will be adopted for the remainder of this work:

- **DGFV** method: The relative coordinate ξ is discretized using the FV technique, while the center-of-mass coordinate is discretized using the DG method.
- **DGFEM** method: The relative coordinate ξ is treated with the FEM, while the center-of-mass coordinate remains as before.
- **DGDG** method: Both the center-of-mass and relative coordinates are discretized using two independent, one-dimensional DG methods.

6.1. Resonant Tunneling Diodes

For the initial evaluation of the DG concept, the RTD is selected, as it has been widely studied in the literature [2, 72, 73, 74, 77]. Quantum transport primarily occurs along the transport direction, as illustrated in Fig. 3.1. Accordingly, the intraband quantum transport model

from Section 3.2, together with its corresponding discretization from Section 5.3, is employed for the simulation. The RTD consists of an $Al_{0.3}Ga_{0.7}As$-GaAs material structure. Fig. 6.1 shows the detailed layer composition and the potential profile induced by the two $Al_{0.3}Ga_{0.7}As$ barriers. This results in the well-known barrier-shaped flat-band profile [73] in the absence

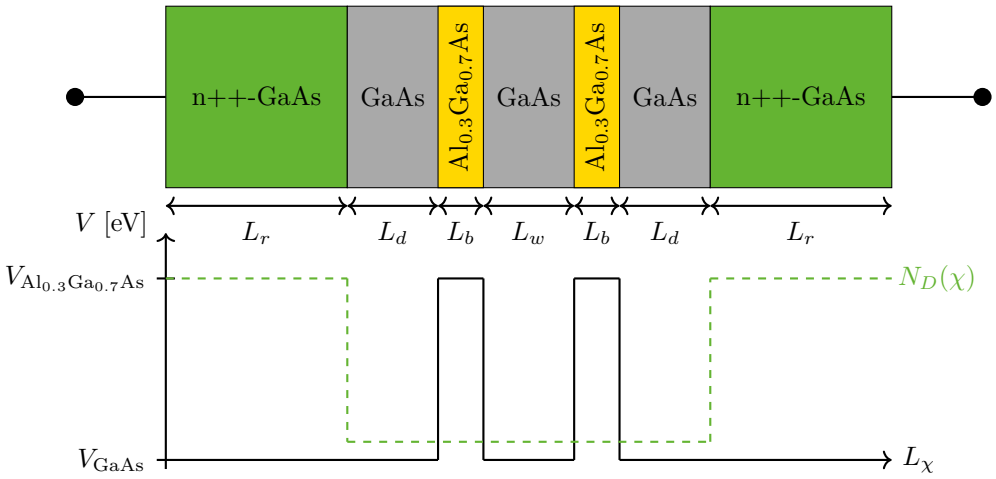

Figure 6.1.: Schematic 2D representation of an RTD with material composition. The lengths of the individual material layers are labeled, and the doping profile $N_D(\chi)$ is shown as a dashed dark green line. The flat-band potential profile is sketched below the RTD in black and exhibits a barrier height of 0.2 eV. Here, L_r denotes the length of the left and right reservoirs, respectively. The regions L_d and L_w around the double barrier are only lightly or completely undoped. The RTD is modeled along the transport direction χ.

of any external bias. The reservoirs are highly doped, each with a donor concentration of $N_D^1 = N_D^{N_\chi} = 10^{24}$ m^{-3}. Tab. 6.1 lists the physical and numerical parameters used in the RTD simulation. To the best of the authors knowledge, directly comparable density matrix distributions for the considered device structures could not be identified in the literature at the time of writing. Most studies of quantum transport devices report derived quantities such as carrier densities or currentvoltage characteristics rather than spatial representations of the full density matrix. Therefore, validation of the numerical method will be performed using the previously introduced quantities. With the known device structure from Fig. 6.1 and the parameters listed in Tab. 6.1, the evaluation can now begin. The first case considered is the stationary regime.

6.1.1. Steady-State Simulation

In the steady-state case, the left-hand side of Eq. (5.77) is set to zero, i.e., $\partial_t \boldsymbol{c}_j^k = 0$. The mass matrix has already been multiplied from the left as an inverse with the right-hand side. However, it is also possible to retain the mass matrix on the left-hand side of Eq. (5.77) as $\boldsymbol{M}\partial_t \boldsymbol{c}_j^k = 0$. While this simplifies implementation, it will have to be done in the transient regime anyway, and is therefore recommended at this stage. Two cases will be considered within the stationary simulation: thermal equilibrium and thermal nonequilibrium.

Table 6.1.: Overview of the physical and numerical parameters of the simulated RTD.

Symbol	Meaning	Value
Physical Parameters		
T	Operating temperature	300 K
m_{GaAs}	Effective electron mass in GaAs	$0.063m_0$
$m_{\mathrm{Al_{0.3}Ga_{0.7}As}}$	Effective electron mass in $Al_{0.3}Ga_{0.7}As$	$0.0796m_0$
L_ξ	Length of the domain Ω_ξ	108 nm
L_χ	Length of the domain Ω_χ	60 nm
L_d	Extension of the voltage drop region	22.5 nm
L_g	Width of the $Al_{0.3}Ga_{0.7}As$ barriers	5 nm
L_w	Width of the GaAs well	5 nm
V_{GaAs}	Potential value of the GaAs material	1.309 eV
$V_{\mathrm{Al_{0.3}Ga_{0.7}As}}$	Potential of $Al_{0.3}Ga_{0.7}As$	1.509 eV
N_D	Donor concentration in GaAs	10^{24} m^{-3}
δ	Effective range of the CAP	$0.2L_\xi$
W_0	Amplitude of the CAP	1
U	Voltage for (non-)equilibrium	(0.2) 0 V
$U_{\max}$	Maximum voltage for IV characteristic	0.35 V
T_{final}	Time window for transient simulation	$1 \cdot 10^{-13}$ s
Numerical Parameters		
N_ξ^{FV}	Number of FV volumes in Ω_ξ	180
N_ξ^{FEM}	Number of FEM elements in Ω_ξ	179
N_ξ^{DG}	Number of DG elements in Ω_ξ	60
$N_p^{\xi,\mathrm{FEM}}$	Nodes per FEM element	2
$N_p^{\xi,\mathrm{DG}}$	Nodes per DG element	3
N_χ	Number of DG elements in Ω_χ	60
N_p^χ	Nodes per DG element	3
N_{qx}	Order of Gauss-Lobatto quadrature	20
N_U	Number of voltage steps for IV curve	50
dt	Time step for transient simulation	$3 \cdot 10^{-17}$ s

Thermal Equilibrium

In the thermal equilibrium case, *no* external voltage is applied to the RTD. The potential profile from Fig. 6.1 thus remains symmetric about the center axis at $\chi = L_\chi/2$. The first simulation in thermal equilibrium is shown in Fig. 6.2 [GS6]. The real part is displayed in Fig. 6.2a and the imaginary part in Fig. 6.2b. Along the ξ-axis, the Fermi distribution at both ends $\chi = 0$ nm and $\chi = 60$ nm are clearly visible. Along the χ-axis, the carrier distribution shows two minima at the locations of the $Al_{0.3}Ga_{0.7}As$ barriers. The imaginary part in Fig. 6.2b reaches an amplitude of

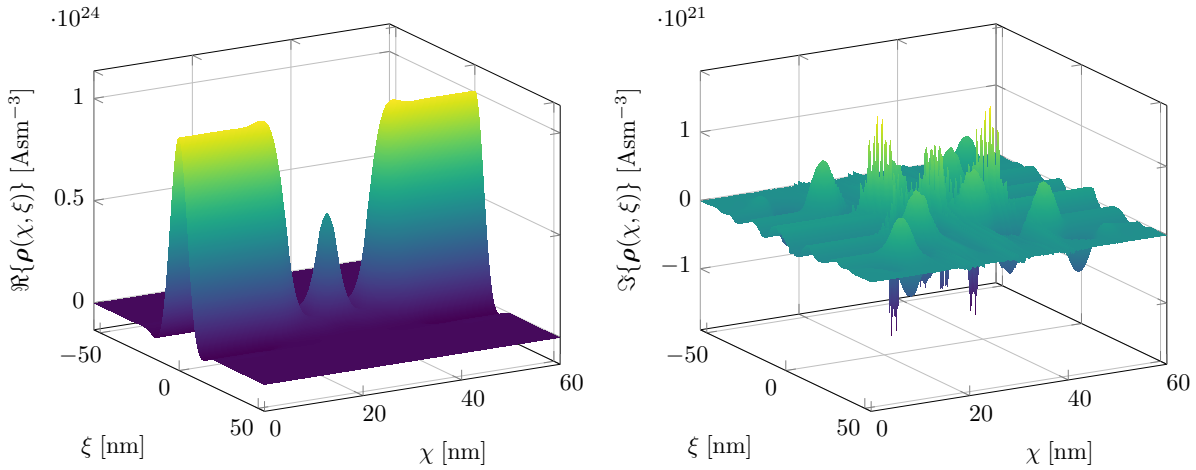

(a) Real part

(b) Imaginary part

Figure 6.2.: Real (a) and imaginary part (b) of the statistical density matrix $\boldsymbol{\rho}$ from the steady-state simulation using the DGFV method under thermal equilibrium. Physical and numerical parameters are listed in Tab. 6.1.

10^{21}, which should not occur when no external voltage is applied. The current density depends on the imaginary part of the statistical density matrix. Thus, a non-zero imaginary part implies a non-zero current flow, which is physically incorrect in this case as no external bias is applied yet. This becomes evident when considering Eq. (5.78). The origin of this error is numerical and stems, among other things, from the upwind flux [15]. Mesh size also greatly affects this issue which will be demonstrated shortly. The numerical flux does **not** account for nonlocal effects induced by the device structure and hence fails to include these effects in the boundary conditions [GS2]. One source of this error is therefore the diffusion term in Eq. (2.22). Increasing the number of elements can reduce this error, and it is thus concluded that the imaginary part converges toward zero with increasing element count, as illustrated in Fig. 6.3a and Fig. 6.3b. Increasing the number of grid points to $N_\xi \times N_{\chi p} = 300 \times 300$ reduces the amplitude from 10^{21} to 10^{20} [GS6], where $N_{\chi p} = N_\chi \cdot N_p^\chi$ is the total number of nodes in the computational χ-domain. While introducing self-consistency in Fig. 6.3b does further reduce the amplitude, it also introduces oscillations especially at the edges of the computational domains. For further comparison with the QTBM, the carrier density n from Eq. (5.78) is used. Fig. 6.4 compares the carrier densities obtained by the DGFV, DGDG, and DGFEM methods with that from the QTBM. Out of all the numerical methods, the DGDG scheme appears to have the closest trajectory to the QTBM. This is confirmed when the L^2, L^∞ and relative errors are compared, which are included in the following Tab. 6.2. Here, the DGDG method achieves the lowest errors with $L^2 = 1.46\ \%$, $L^\infty = 3.39\ \%$ and a relative error of 1.31 %. Meanwhile the DGFV scheme shows the largest errors across the board, which can be traced back to the use of the trapezoidal rule, among others. For an explanation of the notation, see the introduction of Chapter 6. The DGFV method exhibits an overestimated peak between the barriers at $\chi = 30$ nm, whereas the DGFEM method achieves better agreement at this position but fails to reach the correct minimum within the barriers [GS3]. Since the Gauss-Lobatto quadrature was applied to both coordinates of the drift operator in the DGDG and DGFEM methods, their improved accuracy over the DGFV method is expected [GS3].

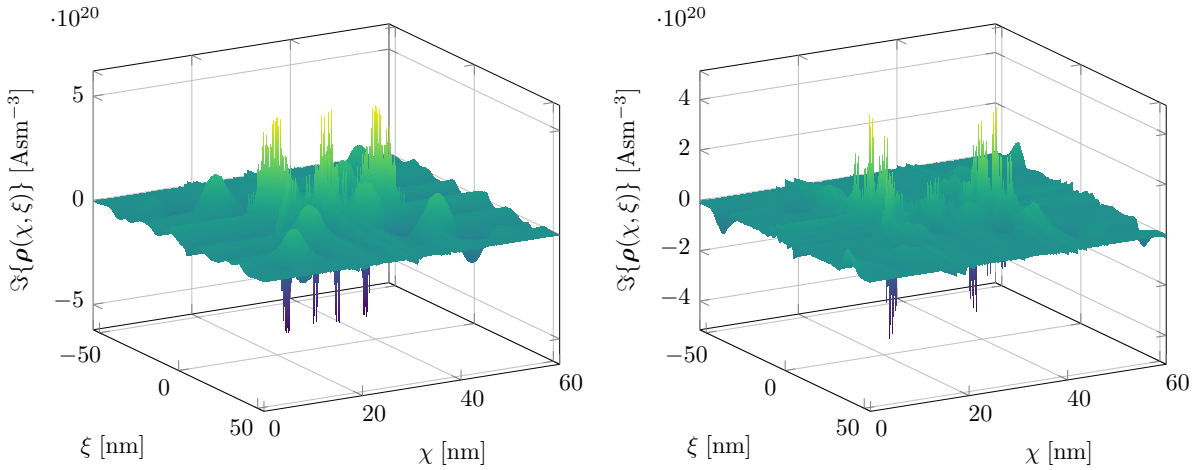

(a) Flatband (b) Self-consistent

Figure 6.3.: Imaginary part of the statistical density matrix $\boldsymbol{\rho}$. The number of elements was increased to $N_\xi = 300$ and $N_\chi = 100$, while the number of nodes per element was kept at $N_p^\chi = 3$. (a) shows was generated using a flatband potential, while (b) was computed utilizing a self-consistent potential.

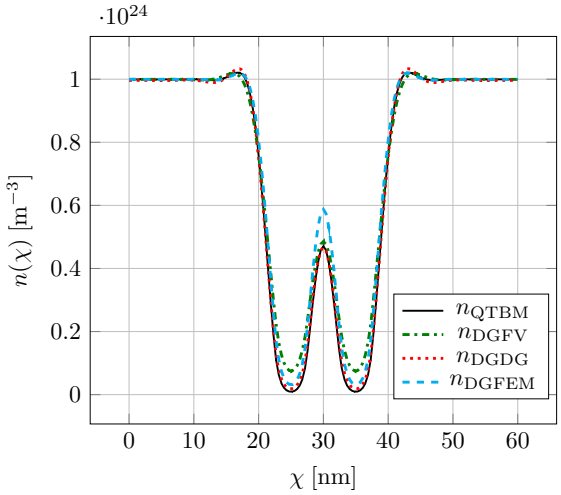

Figure 6.4.: Comparison of carrier densities from QTBM (black) with the DGFV (dark green, dash-dotted), DGDG (red, dotted), and DGFEM (cyan, dashed) methods.

Table 6.2.: Quantitative results of the carrier density comparison from Fig. 6.4. The table shows the L^2, L^∞, and relative errors against the QTBM.

Method	L^2	L^∞	**Rel. Error**
DGFV	3.64 %	8.48 %	3.16 %
DGFEM	2.02 %	4.79 %	1.86 %
DGDG	1.46 %	3.39 %	1.31 %

Thermal Nonequilibrium

Now, an external voltage is applied to the RTD, distorting the potential profile from Fig. 6.1 and resulting in an asymmetric distribution across the device length L_χ. Fig. 6.5 shows the

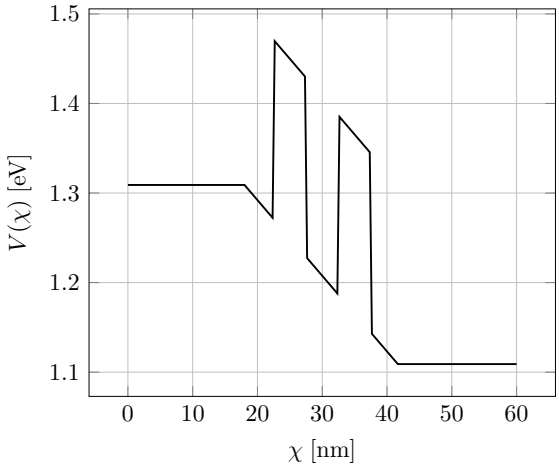

Figure 6.5.: Potential profile of the RTD under thermal nonequilibrium. An external voltage of 0.2 V is applied.

updated potential profile of the RTD for thermal nonequilibrium. It consists of the band-edge potential from Fig. 6.1 and the voltage drop of 0.2 V. A current flow is expected under these conditions, so the amplitude of the imaginary part should exceed that in Fig. 6.2b. As shown

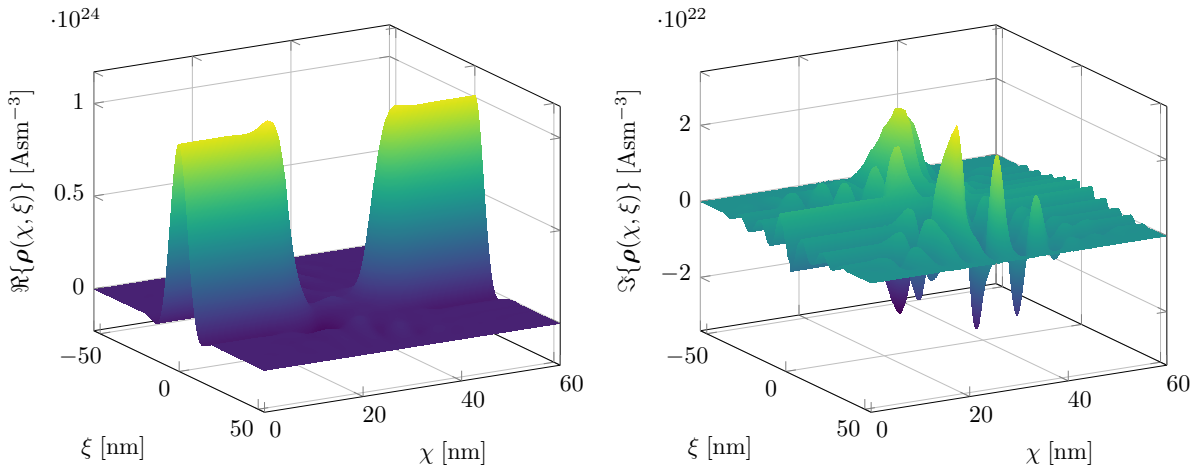

(a) Real part

(b) Imaginary part

Figure 6.6.: Real (a) and imaginary part (b) of the statistical density matrix $\boldsymbol{\rho}$ from the steady-state simulation using the DGFV method under thermal nonequilibrium. Physical and numerical parameters are listed in Tab. 6.1.

in Fig. 6.6b, the amplitude of the imaginary part is 10^{22}, which is indeed higher than in the thermal equilibrium. In this case, a non-zero imaginary part is physically valid, as current flow is expected. The real part in Fig. 6.6a indicates that carriers accumulate before the first barrier

in the χ direction. The asymmetric distribution of carriers along the transport direction further supports the physical plausibility of the solution [58]. In both cases, a flat-band potential was assumed (cf. Figs. 6.1 and 6.5). To account for self-consistency, the implementation described in Section 5.7 will now be applied.

6.1.2. Self-Consistency

A self-consistent potential takes into account the carrier distribution obtained from solving the quantum transport equation in order to determine the potential distribution. The Gummel algorithm is implemented as an iterative process coupling both quantities. The resulting updated potential profiles are shown in Fig. 6.7. Both profiles consist of the flat-band potential, the

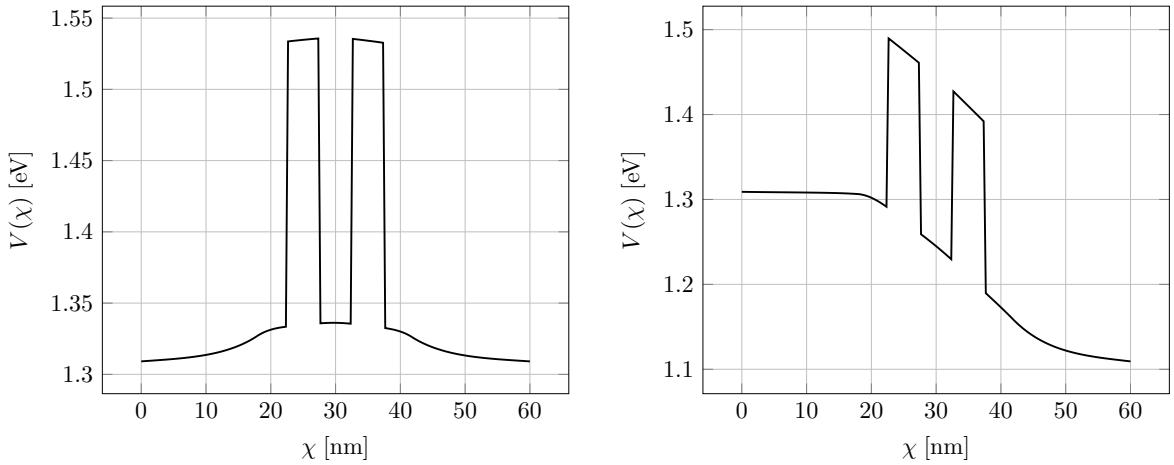

(a) Voltage profile of the RTD under thermal equilibrium.

(b) Voltage profile of the RTD under thermal nonequilibrium. An external voltage of 0.2 V is applied.

Figure 6.7.: Self-consistent potential profiles of the RTD for thermal equilibrium (a) and nonequilibrium (b). Both include the self-consistent Hartree potential.

self-consistent Hartree potential (Figs. 6.7a and 6.7b), and – under nonequilibrium conditions – an additional external bias (Fig. 6.7b). Accordingly, the carrier distributions for equilibrium and nonequilibrium exhibit different behaviors. Fig. 6.8 shows that in both cases, the carrier concentrations decay much more gradually before and after the barriers compared to the results in Figs. 6.2a and 6.6a. The self-consistent Hartree potential captures the expected space-charge behavior. In addition to its influence on the statistical density matrix, the Hartree potential also affects the characteristic current-voltage (IV) curve of the RTD.

6.1.3. Current-Voltage Characteristics

The characteristic IV curve of the RTD shows the current flow across the device length L_χ as a function of the applied voltage. The curve is considered characteristic because it features a region of Negative Differential Resistance (NDR) – meaning the current decreases as the voltage increases [2]. The IV curves are shown in Fig. 6.9a for the flat-band approximation and in Fig. 6.9b for the self-consistent Hartree potential. The current density is determined for voltages

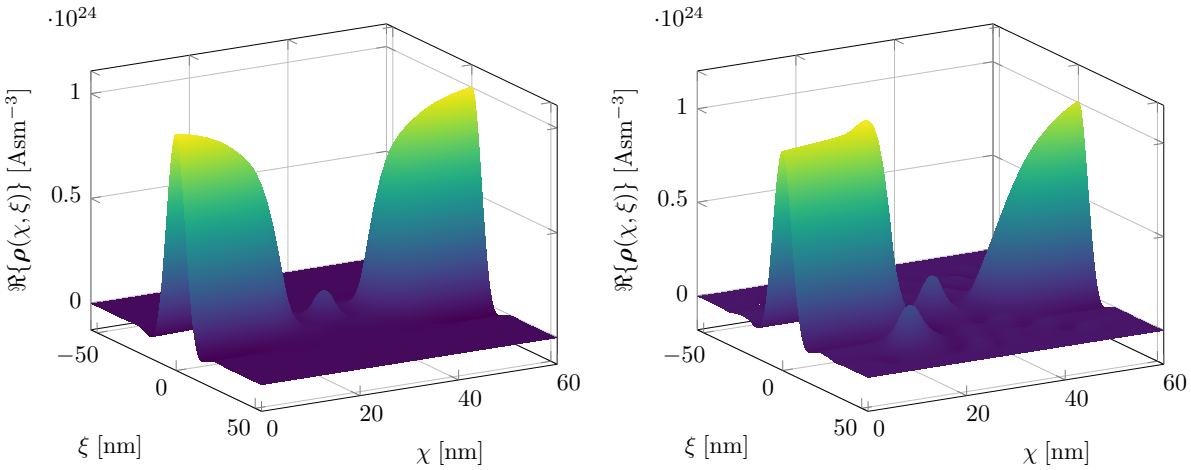

(a) Thermal equilibrium (b) Thermal nonequilibrium

Figure 6.8.: Real part of the statistical density matrices $\Re\{\boldsymbol{\rho}\}$ for thermal equilibrium (a) and thermal nonequilibrium (b) in stationary simulation. The physical and numerical parameters are listed in Tab. 6.1.

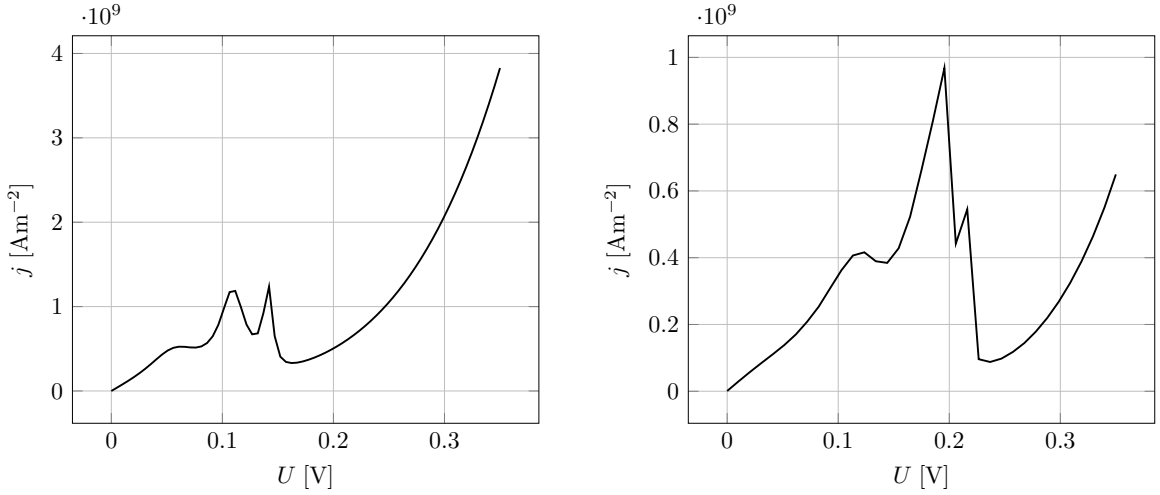

(a) With flat-band potential. (b) With self-consistent Hartree potential.

Figure 6.9.: Characteristic IV curve of an RTD using flat-band potential (a) and self-consistent Hartree potential (b). The current density is plotted over the applied voltage ranging from 0 V to 0.35 V.

ranging from 0 V to 0.35 V. The maximum voltage is limited to 0.35 V because convergence of the self-consistent Hartree solver becomes poor around 0.4 V. For better comparability and to save computational resources and time, this upper limit is applied. For the flat-band case, the first resonance occurs around 0.12 V, where the current reaches a local maximum. Subsequently, the current decreases with increasing voltage, indicating the onset of the NDR region. A non-physical 'jagged' trajectory near the first resonance at approximately 0.12 V in Fig. 6.9a and around 0.2 V in Fig. 6.9b can be observed. This artifact is caused by the CAP. With an effective width of $\delta = 0.2 \cdot L_\xi$, the CAP is insufficient to fully suppress this

effect. Increasing the width to $\delta = 0.4 \cdot L_\xi$ smooths the resonance peak and aligns the result with the literature [2, 15, 72, 73, 77], as seen in Figs. 6.10a and 6.10b. Comparing the results

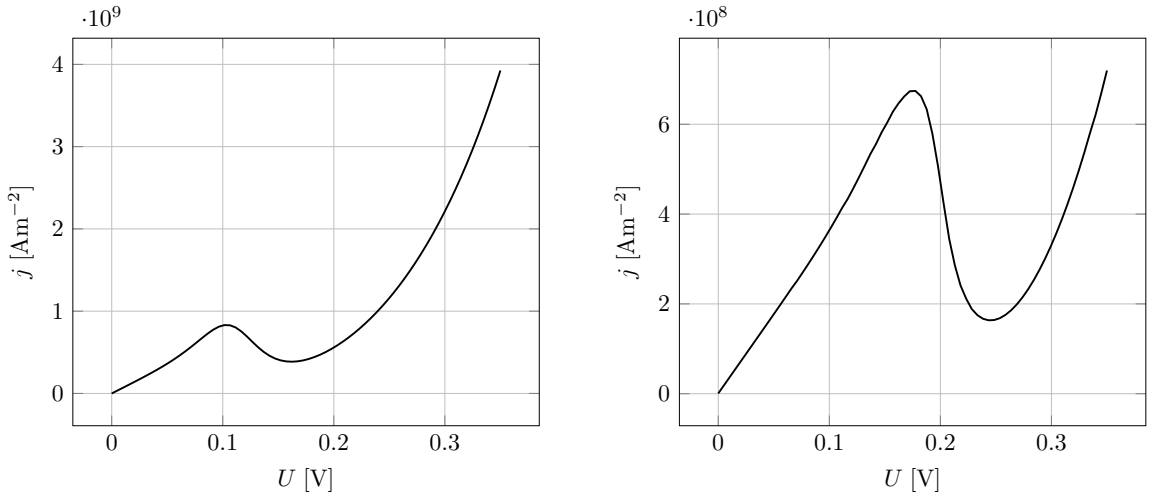

(a) With flat-band potential.

(b) With self-consistent Hartree potential.

Figure 6.10.: Characteristic IV curves of an RTD using flat-band potential (a) and self-consistent Hartree potential (b). The current density is shown as a function of the applied voltage from 0 V to 0.35 V. The width of the CAP was increased to $\delta = 0.4 \cdot L_\xi$.

from Fig. 6.10 to those in Fig. 6.9, one observes that in both cases – the thermal equilibrium and nonequilibrium – the amplitude of the current density decreases due to the larger damping region introduced by the CAP. This is due to a broader portion of the statistical density matrix being damped, which in turn lowers the average amplitude of its imaginary part. Since the current density depends directly on this quantity (see Eq. (5.78)), the resulting current is reduced accordingly.
The next section is dedicated to the transient simulation.

6.1.4. Transient Simulation

The time-dependent regime provides insight into the dynamic switching behavior of a device. This is a crucial aspect that reflects the dynamic response of charge carriers when an external voltage is applied. Eq. (5.77) is implemented under the condition $\partial_t \boldsymbol{c}_j^k \neq 0$. The mass matrix has already been shifted to the right-hand side through inversion.
Furthermore, the thermal equilibrium is defined as the initial condition. It is assumed that at time $t = 0$, an external voltage of 0.2 V is applied. As discussed in Section 5.6, the RK2 or RK4 scheme is used for time discretization. To ensure numerical stability and convergence, the eigenvalues of the system matrix should be examined beforehand. These should all lie in the left half of the complex plane, i.e., their real parts should be negative [68]. As shown in Fig. 6.11, the eigenvalues are located in the left half-plane as expected [GS2],[22]. This confirms the stability analysis presented in Section 5.2.3, where the numerical flux and the CAP were shown to play a crucial role in ensuring stability. Accordingly, the current simulation is carried out under four configurations – alternating between central and upwind flux, each with and without a CAP. This results in four eigenvalue spectra, analyzed below.

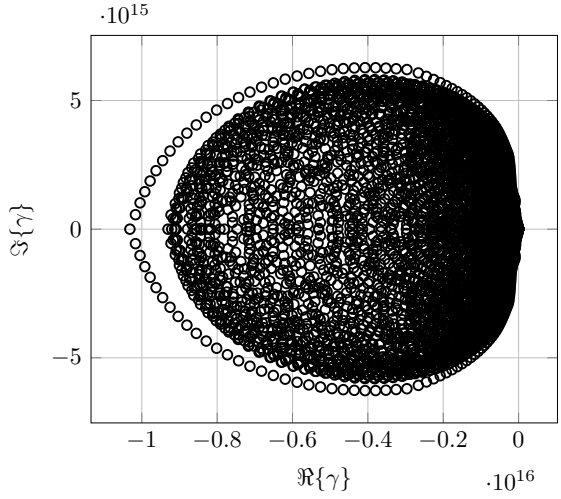

Figure 6.11.: Eigenvalue spectrum of the system matrix.

Comparing Figs. 6.12a and 6.12b as well as 6.12c and 6.12d, it becomes evident that the CAP predominantly influences the real part of the eigenvalues γ. It is also noteworthy that the central flux is unstable in all cases, as a significant number of eigenvalues lie in the right half-plane. The largest real part is $\max(\Re\{\gamma\}) = 1.27 \cdot 10^{14}$ in Fig. 6.12a, and still $\max(\Re\{\gamma\}) = 4.92 \cdot 10^{13}$ in Fig. 6.12b, both of which are sufficiently large to cause divergence during the transient simulation. By contrast, the upwind flux yields no eigenvalues with positive real parts, even without a CAP, as shown in Fig. 6.12c. The addition of a CAP shifts the spectrum even further into the stable region (Fig. 6.12d) [GS7].
This confirms convergence and allows the simulation to proceed using the parameters in Tab. 6.1. Regardless of the numerical scheme used, the same transient behavior is observed. As shown in Fig. 6.13, snapshots of the carrier density n and the current density j are recorded across the full simulation time. Fig. 6.13a illustrates the smooth transition from thermal equilibrium to nonequilibrium. Around $t = 30$ fs, the system converges into the nonequilibrium state. Note that during continued operation, the RTD heats up, altering its properties such as resistance, which also affects the current [77]. A more realistic simulation should account for these thermal effects. However, since this work focuses on conceptual development of the DG method for quantum transport, and assuming that temperature changes are negligible within 100 fs, a constant temperature as defined in Tab. 6.1 is justified. Furthermore, the trajectory of the carrier distribution is qualitatively consistent with transient responses reported in tight-binding studies [107].
Fig. 6.13b shows the current along χ as a function of time t. The trajectory is qualitatively consistent with [108]. The current starts near zero at $t = 0$ fs and rises sharply after switching on the external voltage at about $t = 15$ fs. Note that the current at $t = 0$ fs is not exactly zero, which would be physically correct, but appears slightly offset due to numerical errors in the imaginary part of the statistical density matrix (see Fig. 6.2b). After approximately $t = 30$ fs, the current stabilizes, indicating convergence toward the nonequilibrium state.
In the present implementation, the RK2 formulation requires recomputation of the drift operator at each timestep, whereas the RK4 formulation operates on a preassembled system matrix. Consequently, the observed runtime differences reflect implementation-specific algorithmic structure rather than purely the formal order of the Runge-Kutta schemes. Consequently,

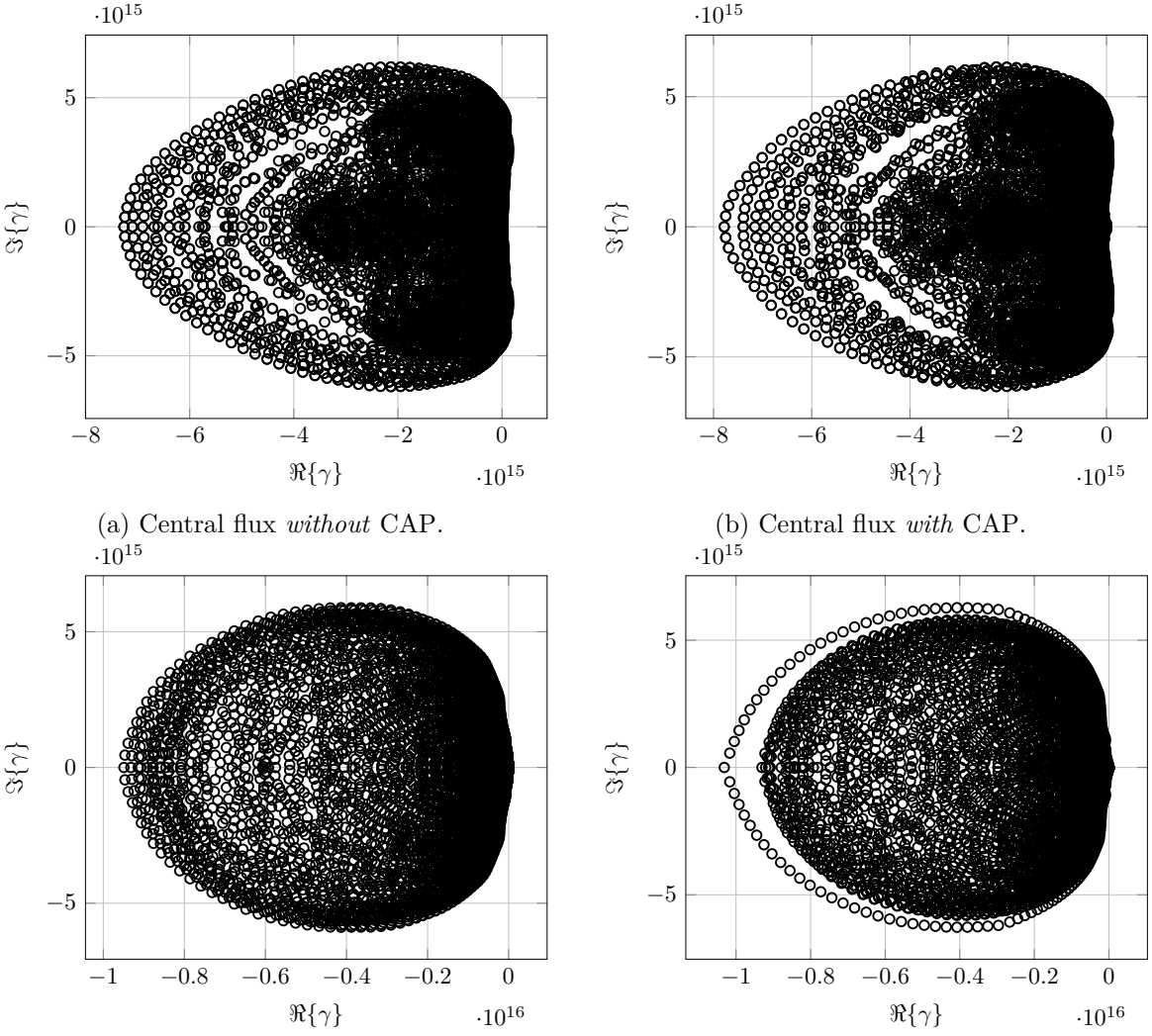

(a) Central flux *without* CAP.

(b) Central flux *with* CAP.

(c) Upwind flux *without* CAP.

(d) Upwind flux *with* CAP.

Figure 6.12.: Stability analysis of the numerical scheme through variation of flux type and CAP. Shown are central flux without (a) and with CAP (b) as well as upwind flux without (c) and with CAP (d).

RK4 is expected to yield better computational performance within the present implementation. As shown in Fig. 6.14, the runtime τ of the RK2 method (blue) increases approximately exponentially with rising N_ξ, while the RK4 method (dark green) exhibits a linear growth. As expected, the RK4 method is more efficient than RK2 [GS6].
This concludes the transient simulation. The next section addresses the final aspect of the RTD simulation.

6.1.5. Spatially Varying Effective Mass

The simulation involving a spatially varying effective mass is based on the model described in Section 5.4. Tab. 6.1 lists the effective electron masses for GaAs and $Al_{0.3}Ga_{0.7}As$. In this case,

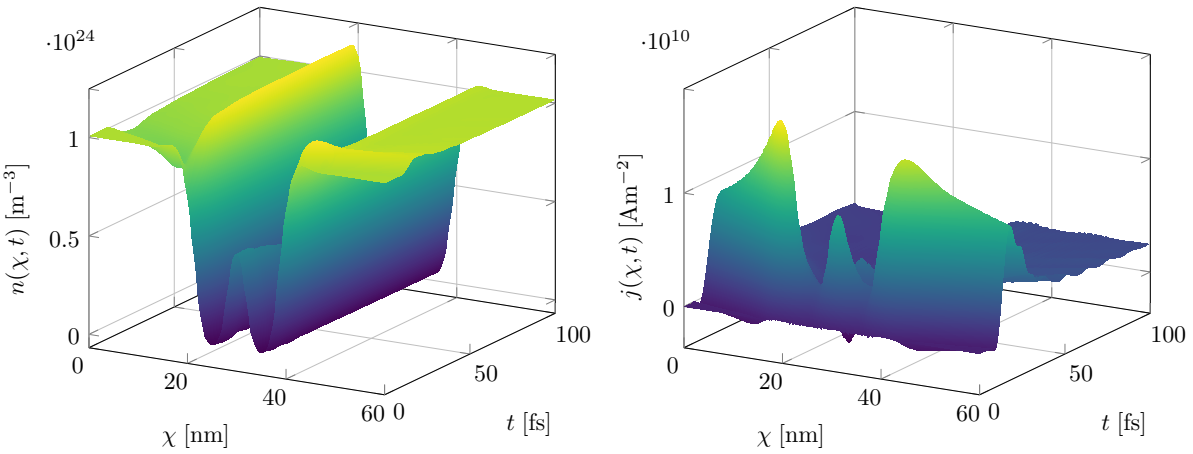

(a) Time-dependent carrier density n in transport direction χ.

(b) Time-dependent current density j in transport direction χ.

Figure 6.13.: Time-dependent carrier density $n(\chi, t)$ (a) and current density $j(\chi, t)$ (b). Both quantities reach convergence after approximately $t = 30$ fs.

electrons in $Al_{0.3}Ga_{0.7}As$ have a higher mass, and thus, greater inertia. The resulting profile is identical to the one shown in Fig. 6.1.
Since the system matrix in this simulation is twice as large, the more efficient (though less accurate) DGFV method is used again. Additionally, a self-consistent Hartree potential is assumed under thermal equilibrium. The carrier density obtained using the spatially varying effective mass n_{ih} is compared to the carrier density assuming a homogeneous effective mass n_h in Fig. 6.15. It can be seen that the local maximum in the quantum well at $\chi = 30$ nm is higher when using the inhomogeneous mass distribution n_{ih} compared to the homogeneous case n_h [GS4]. This is consistent with the literature [14, 71, 75] and demonstrates that the DG method is conceptually suitable for incorporating variable mass distributions and is therefore capable for the simulation of heterostructures.

With this, the simulation of the RTD is concluded, and the next device can be analyzed.

6.2. Tunnel Field-Effect Transistor

In the previously discussed RTD-section, transport was primarily simulated in the conduction band. In the context of intraband quantum transport, a TFET will now be considered. Based on the intraband quantum transport model from Section 5.3, both the conduction and valence bands are simulated – though without coupling between them.
The concept of improving the sub-threshold and leakage currents in Field Effect Transistor (FET)s through tunneling transitions was proposed in 2007 [109]. The idea of incorporating a tunneling structure between the source and channel (see Fig. 6.16) was then implemented in [110, 111]. The TFET is shown schematically in Fig. 6.16. This representation can be interpreted as a cross-section, implying that the overall device structure is a cylindrical TFET. Fig. 6.17a shows the potential drop across the device length as a flat-band potential. The conduction and valence band potential profiles are depicted. The energy gap between both

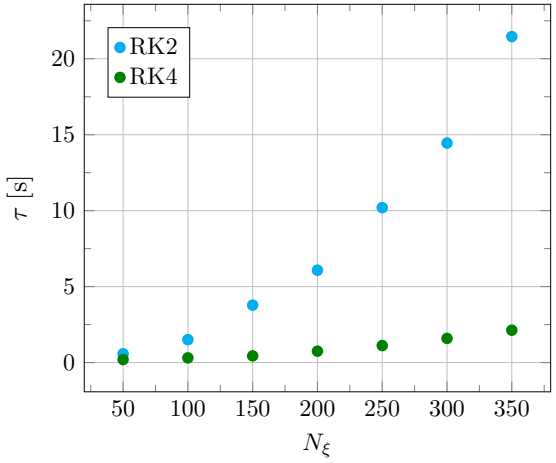

Figure 6.14.: Runtime comparison τ between the RK2 and RK4 methods as a function of the number of elements N_ξ. The simulation was conducted using the DGFV scheme. The number of elements N_ξ was varied in steps of 50 from 50 to 350, while the number of elements N_χ remained constant.

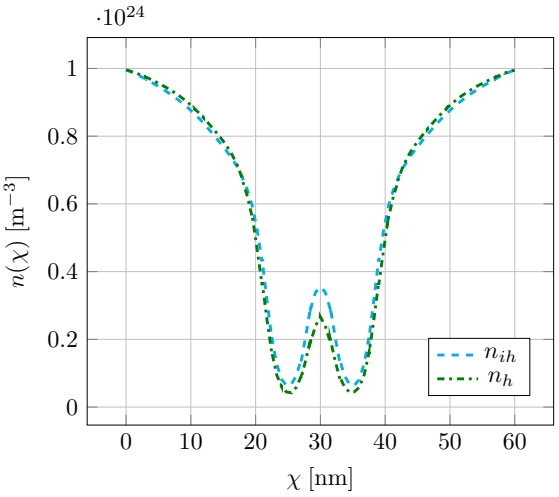

Figure 6.15.: Carrier distribution with spatially varying effective mass n_{ih} (light blue, dashed) and homogeneous effective mass n_h (dark green, dash-dotted), both with a self-consistent Hartree potential.

bands is $E_g = 0.2$ eV, as listed in Tab. 6.3. Additionally, from the same table $U_{GS} = U_g - U_s = -0.15 - 0.1 = -0.25$ V and $U_{DS} = U_d - U_s = -0.35 - 0.1 = -0.45$ V can be derived. In contrast to the previously discussed RTD, electron transport in the ξ-direction (L_ξ in Fig. 6.16) is not symmetric due to the gate contact. Therefore, the TFET can no longer be reduced to a one-dimensional transport problem. To justify the reduction to one dimension, the following assumptions are made:

- The device in Fig. 6.16 is assumed to be symmetric along the z-direction. This reduces the transport problem to two dimensions.
- Additionally, due to the narrow width of the device, electron transport in the y-direction

Table 6.3.: Overview of the physical and numerical parameters of the simulated TFET.

Symbol	**Description**	**Value**
Physical Parameters		
T	Operating temperature	300 K
m	Effective electron mass	$0.023m_0$
L_ξ	Length of domain Ω_ξ	120 nm
L_χ	Length of domain Ω_χ	90 nm
δ	Absorption region of CAP	$0.2L_\xi$
W_0	Amplitude of CAP	1
E_g	Band gap energy	0.2 eV
U_s	Source contact voltage	0.10 V
U_g	Gate contact voltage	−0.15 V
U_d	Drain contact voltage	−0.35 V
Numerical Parameters		
N_ξ^{FV}	Number of FV volumes in Ω_ξ	180
N_χ	Number of DG elements in Ω_χ	60
N_p^χ	Nodes per DG element	3
N_{qx}	Gauss-Lobatto quadrature order	20

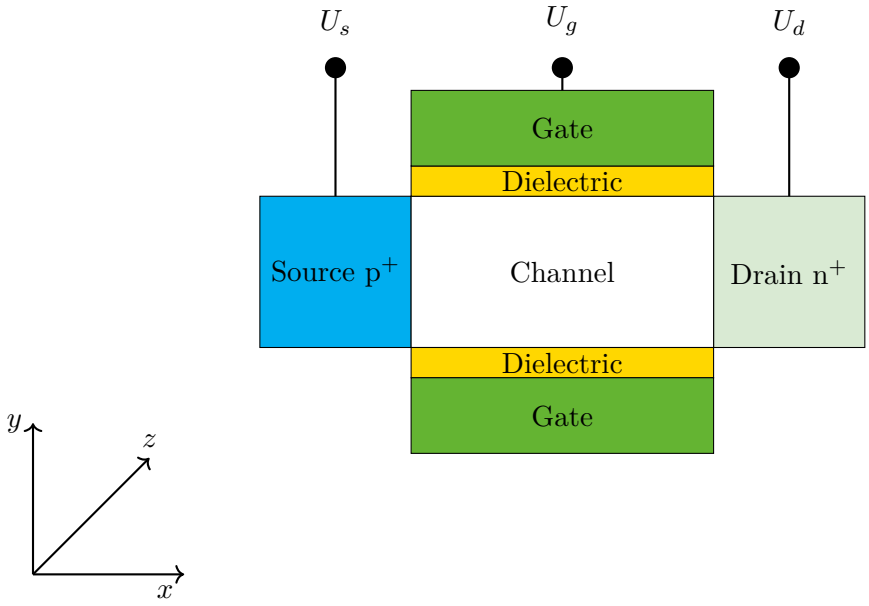

Figure 6.16.: Schematic illustration of a TFET. The transport of electrons is assumed to be dominant exclusively in the direction of the x-axis.

is assumed negligible compared to transport in the x-direction. Thus, a one-dimensional transport model is justified.

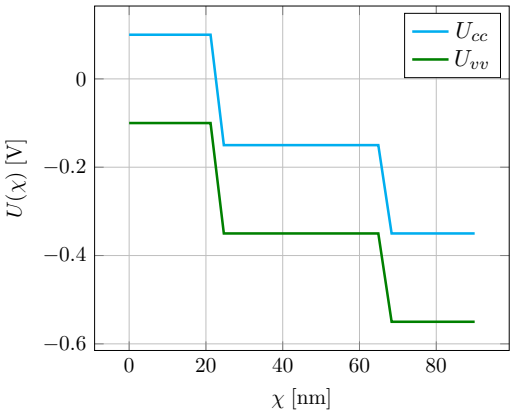

(a) Flatband potential.

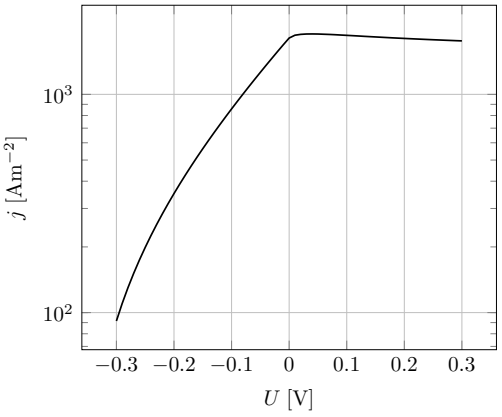

(b) Current-Voltage (IV) curve.

Figure 6.17.: (a) depicts the flat-band potential profile of the TFET. The light blue line corresponds to the conduction band U_{cc}, while the dark green line corresponds to the valence band U_{vv}. (b) shows the characteristic IV curve for a bias sweep of the gate contact between $U_g = -0.3...0.3$ V.

Under these assumptions, the TFET can be approximated using the one-dimensional DG method, and intraband transport can be analyzed. First, Fig. 6.17b displays the characteristic IV curve for a bias sweep of the gate voltage $U_g = -0.3...0.3$ V. Although it is difficult to find perfectly agreeing references, the curve shows a monotonistic rise for negative values of U_g, a clear off state, and a saturation phase for positive values U_g, which are strong indications for the physical correctness of the results [105, 110]. Fig. 6.18 shows the absolute values of the

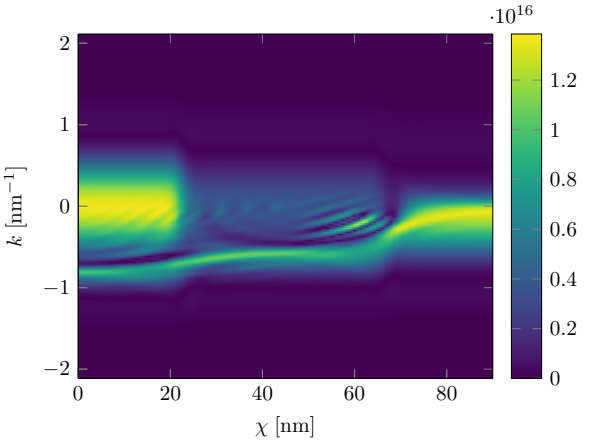

(a) Electron density in the conduction band.

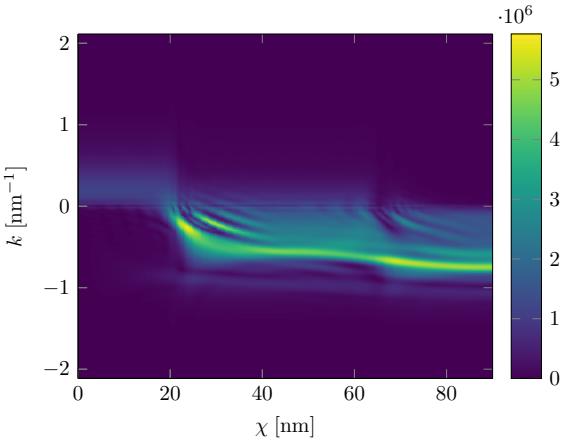

(b) Hole density in the valence band.

Figure 6.18.: Absolute values of the statistical density matrices $\boldsymbol{\rho}$ of the conduction band (a) and valence band (b) from a stationary simulation. The physical and numerical parameters are listed in Tab. 6.3.

density matrices for the conduction band $\boldsymbol{\rho}_{cc}$ and valence band $\boldsymbol{\rho}_{vv}$. It is evident that electrons transition from the conduction to the valence band, visible as a step-shaped loop in negative k-direction in Fig. 6.18a. The analogous transition from the valence to the conduction band is seen in Fig. 6.18b as an inverse loop. This is consistent with results from similar intraband

simulations using established numerical methods [58].
With this, the simulation of intraband quantum transport is concluded. Next, the interband quantum transport wil be solved, for which a new device will be introduced.

6.3. Resonant Interband Tunneling Diode

The RITD is similar to the RTD, with the key difference that multiple bands are considered here. Unlike the device from Section 6.1, no double barrier is used; instead, the simplest form is realized: the *p-n* junction, also known as the Esaki diode [48]. In this type of RTD, interband tunneling effects dominate, where electrons tunnel from the valence band into the conduction band, leaving behind a hole in the valence band. The reverse process, recombination, is also possible (see Section 3.4). In this case, the coupling between both bands is explicitly taken into account.
The physical and numerical parameters of the simulation are listed in Tab. 6.4. Again, only

Table 6.4.: Overview of the physical and numerical parameters for the simulated RITD.

Symbol	**Meaning**	**Value**
Physical Parameters		
T	Operating temperature	300 K
m	Effective electron mass	$0.027m_0$
L_ξ	Length of domain Ω_ξ	140 nm
L_χ	Length of domain Ω_χ	120 nm
δ	CAP absorption width	$0.2L_\xi$
W_0	CAP amplitude	1
U_C	External bias voltage	-0.55 V
E_g	Band gap energy	0.2 eV
P	Kane parameter	$5 \cdot 10^9$
$U_{\max}$	Maximum bias for the IV curve	1.4 V
Numerical Parameters		
N_ξ^{FV}	Number of FV volumes in Ω_ξ	120
N_χ	Number of DG elements in Ω_χ	49
N_p^χ	Number of nodes per DG element	3
N_{qx}	Gauss-Lobatto quadrature order	20
N_U	Number of voltage steps for IV curve	41

the DGFV method is used for the simulation, as the system matrix dimensions – demonstrated in Section 5.5 – are even larger than for the intraband model. Due to its minimal memory footprint (smallest matrix dimensions), the DGFV is justified given the hardware limitations during development. The potential profile of the RITD is shown in Fig. 6.19. The conduction band flat-band potential U_{cc} is represented by the light blue curve, while the valence band

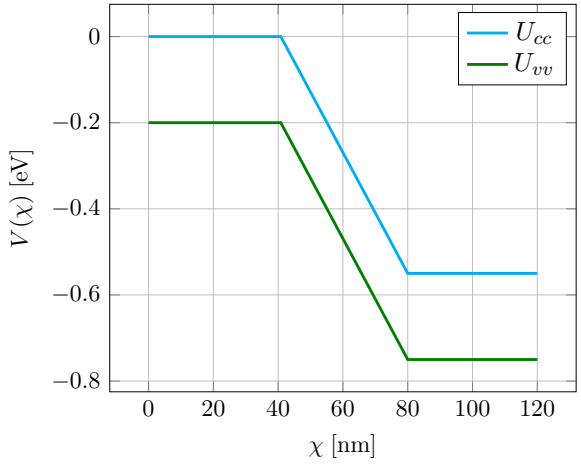

Figure 6.19.: Voltage profile of the RITD as a flat-band potential. The light blue line corresponds to the conduction band potential U_{cc}, and the dark green line corresponds to the valence band potential U_{vv}.

potential U_{vv} is depicted in dark green. They result from the difference between the emitter and collector biases $U = U_E - U_C = 0.00 - 0.55 = -0.55$ V and are separated by the band gap energy $E_g = 0.2$ eV (see Tab. 6.4).
The stationary simulation yields the density matrices $\boldsymbol{\rho}_{cc}$, $\boldsymbol{\rho}_{cv}$, $\boldsymbol{\rho}_{vc}$, and $\boldsymbol{\rho}_{vv}$, which are shown in Fig. 6.20. Figs. 6.20a and 6.20d show the characteristic transitions between the conduction and valence bands as seen before in Fig. 6.18. The transitions in the conduction band (6.20a) correspond directly to those in the valence band (6.20d). The off-diagonal density matrices in Figs. 6.20b and 6.20c indicate interband coupling, localized around the center of the domain where the potential gradient is largest. This supports the main hypothesis of the MEF approach, which states that coupling occurs only where potential gradients exist [GS5],[56]. Note that the density matrices shown in Fig. 6.20 represent absolute values. Especially for the coupling components (6.20b and 6.20c), this implies that the shown density matrix pairs do not have to necessarily be of the same shape and amplitude. Absolute values are used here since the QLE formulation remains in eigenvalue space and is not transformed back into real space, to enable better comparability with results from the literature [58]. Nonetheless, the density matrices exhibit physically plausible behavior, which justifies proceeding to compute the current-voltage characteristic to verify and further demonstrate the capabilities of the DG approach.
As indicated in Tab. 6.4, the external voltage is swept from 0 V to 1.4 V in 41 steps with an increment of $\Delta V = 0.035$ V. At each step, the current is evaluated at the midpoint of the device. The IV curves in Fig. 6.21 are all computed using the DG method. The three curves differ in the resolution of their discretization. The light blue curve corresponds to the finest mesh, using $N_\xi = 94$ finite volumes in the ξ-direction and $N_\chi = 34$ finite elements in the χ-direction, each with $N_{\chi p} = 3$ nodes. This was the maximum mesh resolution achievable with the available hardware, consisting of an Intel Core i9-14000K, 128 GB RAM, and an RTX 4080 Super graphics unit. The dark green curve uses $N_\xi = 68$, $N_\chi = 24$, and $N_{\chi p} = 3$, while the yellow curve is generated with a coarse mesh of $N_\xi = 24$, $N_\chi = 10$, and $N_{\chi p} = 3$.
It is evident that with increasing mesh refinement, the resonance peak shifts toward higher voltages. Moreover, the region of NDR exhibits a lower current amplitude, which is consistent with known results in the literature [GS5],[58, 71].

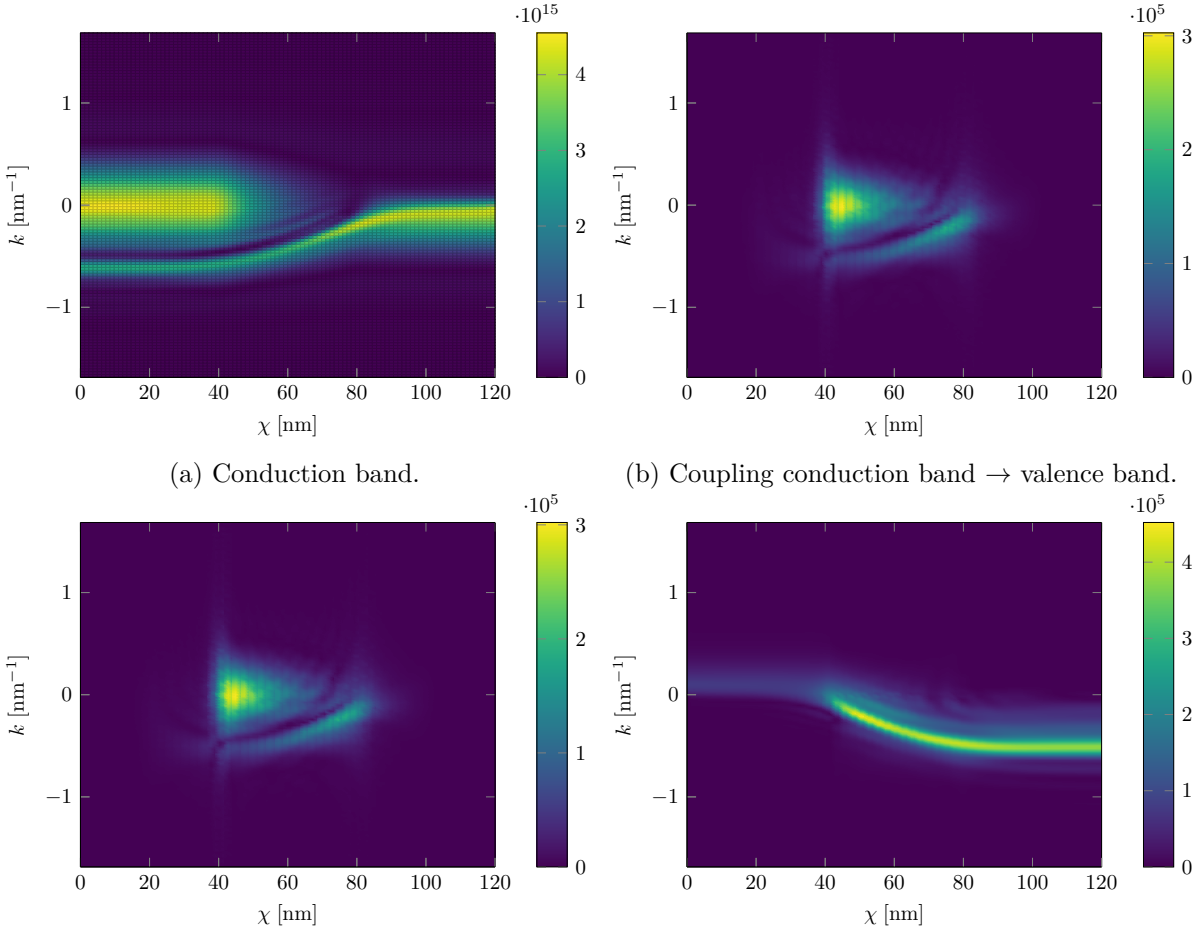

(a) Conduction band.

(b) Coupling conduction band → valence band.

(c) Coupling valence band → conduction band.

(d) Valence band.

Figure 6.20.: Absolute values of the statistical density matrices $\boldsymbol{\rho}_{\lambda\lambda'}$: conduction band (a), valence band (d), and interband couplings (b, c) from stationary simulation. The physical and numerical parameters are listed in Tab. 6.4.

Thus, the DG method is capable of realistically reproducing interband quantum transport. With this, the first spatial dimension is fully mastered by the numerical method. The next section will now turn to the second spatial dimension using a new device concept.

6.4. Dual-Gate Field-Effect Transistors

To simulate two-dimensional devices, the MSA introduced in Section 5.8 is employed to reduce a two-dimensional transport problem to an effective one-dimensional model by dividing the transversal axis of a device into individual modes. This reduced system can then be discretized and solved using the established numerical techniques for each individual mode [106].
For validation, a DGFET is used, which resembles the TFET shown in Fig. 6.16. In this case, the dimensions in the transverse direction are too large to justify neglecting the second spatial dimension.

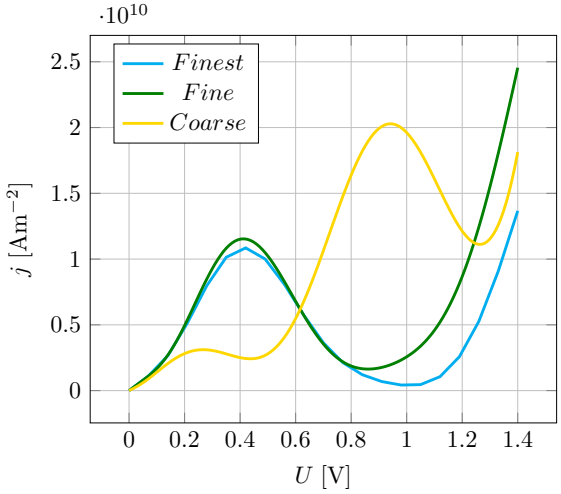

Figure 6.21.: Characteristic IV curves of the RITD for different mesh resolutions. The yellow curve uses the coarsest mesh, the dark green curve uses a finer mesh, and the light blue curve corresponds to the finest resolution.

A simulation is carried out using a self-consistent Hartree potential, which requires solving the two-dimensional Poisson equation (see Section 5.7). The physical and numerical parameters are listed in Tab. 6.5. Fig. 6.22 shows the potential profile along the transport direction χ, consisting of both the flat-band potential and the self-consistent Hartree potential. In this example, only a gate voltage is applied. The simulation procedure is as follows: for each mode,

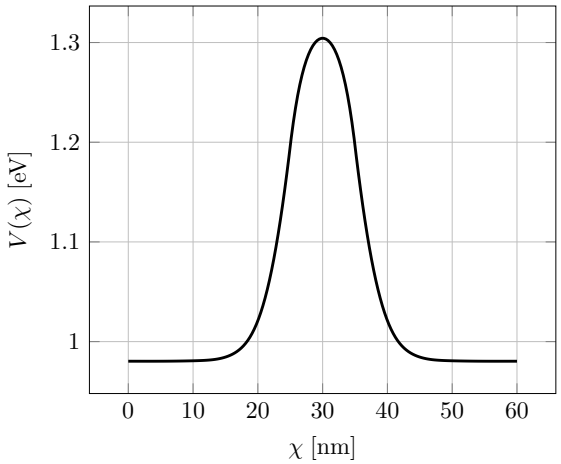

Figure 6.22.: Potential profile of the DGFET as a flat-band potential including the self-consistent Hartree component.

the carrier density is computed using the one-dimensional DGFV method and passed to the iteration loop for solving the Poisson equation numerically. After six iterations, the solution converges, and the process is repeated for the next mode. The resulting two-dimensional carrier density at thermal equilibrium is shown in Fig. 6.23. To validate the result shown in Fig. 6.23, it is compared with existing results from a conventional FV method and the NEGF, where the

Table 6.5.: Overview of the physical and numerical parameters for the simulated DGFET.

Symbol	**Meaning**	**Value**
Physical Parameters		
T	Operating temperature	300 K
m_{ch}	Effective electron mass (channel)	$0.041m_0$
m_{ox}	Effective electron mass (oxide)	$0.5m_0$
L_c	Channel length	10 nm
L_s	Length of source contact	25 nm
L_d	Length of drain contact	25 nm
W_c	Channel width	3 nm
W_{ox}	Oxide width Ω_χ	1.5 nm
L_y	Total length in transverse direction	6 nm
δ	CAP absorption width	$0.2L_\xi$
W_0	CAP amplitude	1
N_s	Doping in source contact	$2 \cdot 10^{25}$ m^{-3}
N_d	Doping in drain contact	$2 \cdot 10^{25}$ m^{-3}
$U_{\max}$	Max. external voltage for IV curve	1 V
U_g	Gate voltage	1.2 V
U_s	Source voltage	0.0 V
U_d	Drain voltage	0.0 V
Numerical Parameters		
N_ξ^{FV}	Number of FV volumes in Ω_ξ	120
N_χ	Number of DG elements in Ω_χ	60
N_p^χ	Number of nodes per DG element	3
N_{qx}	Gauss-Lobatto quadrature order	20
N_U	Number of voltage steps for the IV curve	21

latter serves as the reference. The relative error according to

$$\mathcal{E}_{L^2} = \sqrt{\frac{|Q_{\text{approx.}} - Q_{\text{ref.}}|^2}{|Q_{\text{ref.}}|^2}} \tag{6.1}$$

is determined for both the standard FV and the DGFV method, and the maximum percentage deviation is evaluated. Simulations are conducted at $U_d = 0$ V, $U_d = 0.5$ V, and $U_d = 1.0$ V external bias, using identical values for N_ξ and N_χ. Error values and average runtime per iteration are summarized in Tab. 6.6. It is evident that the DGFV method consistently achieves lower error across all bias voltages compared to the standard FV approach. With increasing voltage, both methods show higher error, but the performance gap also increases. This again highlights the advantage of the Gauss-Lobatto quadrature over the trapezoidal rule, which the first is used by the DG method and the latter by the FV technique. The runtime per iteration

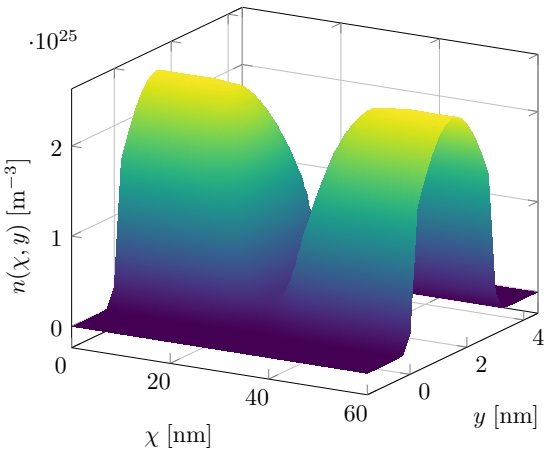

Figure 6.23.: Two-dimensional carrier density n of the DGFET obtained using the DGFV method. Physical and numerical parameters are listed in Tab. 6.5.

Table 6.6.: Comparison of absolute error and runtime between the DGFV and standard FV method. Runtime is averaged over all iterations.

Method	Voltage	N_ξ	Rel. Error	Avg. Runtime
DGFV	0.0 V	120	2.50 %	7.89 s
FV	0.0 V	120	2.71 %	7.95 s
DGFV	0.5 V	120	2.83 %	7.59 s
FV	0.5 V	120	3.32 %	7.99 s
DGFV	1.0 V	120	3.27 %	7.62 s
FV	1.0 V	120	4.78 %	7.96 s

is nearly identical, with DGFV being slightly faster by a few milliseconds.
The significant error discrepancy, especially at 1.0 V, motivates a second comparison using equal-error criteria. Here, the error of the FV method is taken as a target, and the number of elements N_ξ in the DGFV method is reduced accordingly to match this error. The updated

Table 6.7.: Comparison at matched error levels between DGFV and standard FV. Runtime is the average per iteration.

Method	Voltage	N_ξ	Rel. Error	Avg. Runtime
DGFV	0.0 V	114	2.72 %	7.09 s
FV	0.0 V	120	2.71 %	7.95 s
DGFV	0.5 V	80	3.28 %	3.54 s
FV	0.5 V	120	3.32 %	7.99 s
DGFV	1.0 V	34	4.71 %	0.84 s
FV	1.0 V	120	4.78 %	7.96 s

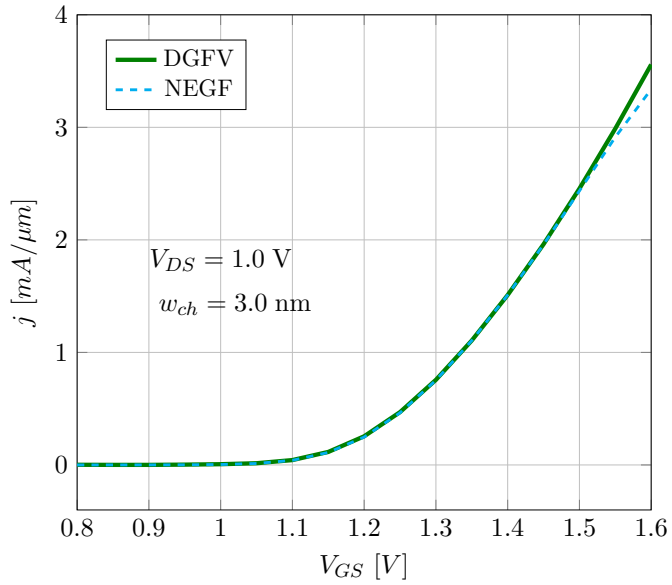

Figure 6.24.: Comparison of the normalized IV-curves for the DGFET obtained with the DGFV method and the NEGF reference for a bias sweep between $V_{\mathrm{GS}} = 0.8...1.6$ V.

comparison in Tab. 6.7 reveals a drastic drop in runtime, down to 0.84 s per iteration at 1.0 V, due to the reduced number of elements. This further displays the DG method's ability to outperform conventional approaches in computational efficiency.
Next, the characteristic IV-curve for the DGFET can be analyzed for which a bias sweep of $V_{GS} = 0.8...1.6$ V is executed, while $V_{DS} = 1.0$ V. Fig. 6.24 shows the comparison between the DGFV concept (darkgreen full line) and the NEGF reference (cyan dashed line). Over all, both lines show close agreement. Only towards the end at approx. $V_{GS} = 1.5$ V does the reference line diverge from the approximation. However, the error comparison yields a value of

$$\mathcal{E}_{L\infty} = 0.44\ \%,$$

when compared to the NEGF results.
In conclusion, the DG method, combined with the MSA, offers a highly efficient framework for solving two-dimensional quantum transport problems.

6.5. High-Performance Computing

High-Performance Computing (HPC) refers to the development of highly efficient and high-performance algorithms [112]. This also includes the DG methodology. In order to assess the performance benefits provided by the DG method, a comparison will now be made with established numerical solution techniques such as the FV method, the QTBM, or the NEGF method. In particular, Subsection 6.5.1 focuses on the runtime of simulations compared to other numerical methods. Subsection 6.5.2 then addresses the resource management of the DG method, highlighting ways to reduce and more efficiently use hardware resources. Finally, Subsection 6.5.3 introduces a technique aimed at further improving the runtime of the DG method.

6.5.1. Runtime Analysis

Fig. 6.14 presented the runtime comparison between the RK2 and RK4 schemes. It was shown that the RK4 method yielded more efficient runtimes. In both cases, explicit time discretization schemes were applied. However, if the model is discretized using a different method, such as the FV technique, an implicit time integration scheme is employed, which is typically slower [GS6],[71]. Fig. 6.25 shows the runtime comparison between the DG/RK4

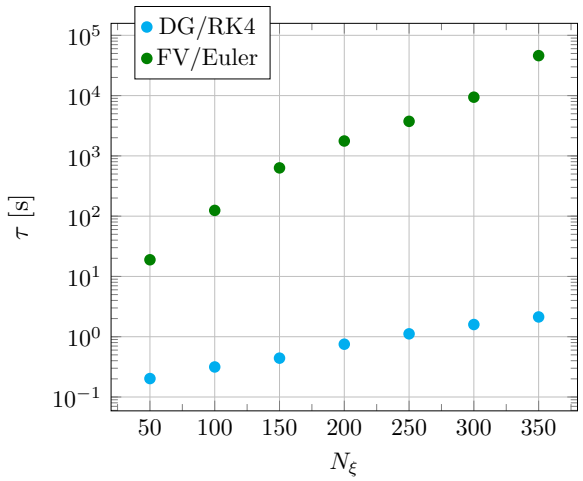

Figure 6.25.: Runtime comparison τ between the FV/Euler and DG/RK4 methods with variation in the number of elements in the ξ-direction. The number of elements N_ξ was varied in increments of 50 from 50 to 350, while the number of elements N_χ in the χ-direction remained unchanged.

method and the FV/Euler approach. The runtimes per time step were computed as the average across all time steps of the transient simulation shown in Fig. 6.13. It can be seen that the combination of the FV technique with an implicit time integration scheme significantly increases the computational effort [GS6]. Notably, the runtime grows more rapidly with increasing N_ξ in the FV/Euler method than in the DG-based comparison.
Furthermore, it is of interest how the runtime behaves among the different DG-based variants developed in this work, namely the DGFV, DGFEM, and DGDG schemes. As shown in Fig. 6.26, the runtimes of the three methods are summarized. Among them, the DGFV scheme exhibits the shortest runtime, followed by the DGFEM method, and finally the DGDG scheme with the longest runtime across the entire range of element numbers N_ξ [GS3].
When also considering the absolute error of all three methods, a different perspective becomes relevant – namely, that of error parity. This means analyzing the accuracy of each method at different discretization levels and determining which mesh configuration is required to reach the same error. To this end, the QTBM method is again used as the reference. The absolute error is computed using the L^∞ norm as

$$\mathcal{E}_{L^\infty} = \frac{|n_{\mathrm{QTBM}} - n_{\mathrm{DG}*}|}{|n_{\mathrm{QTBM}}|} \tag{6.2}$$

Here, the carrier density n_{QTBM} from Eq. (6.2) corresponds to the result obtained from the QTBM, while $n_{\mathrm{DG}*}$ represents the carrier density from the respective DG-based approaches,

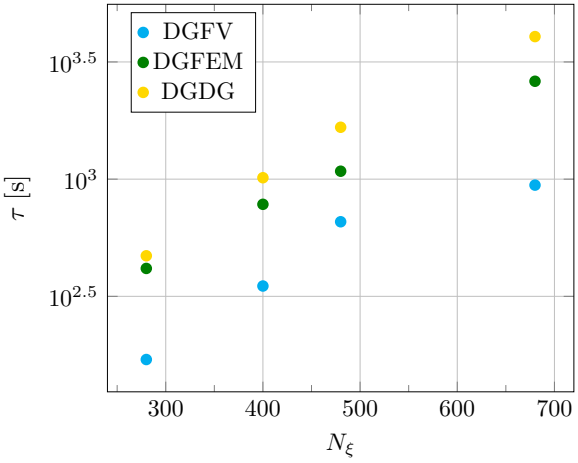

Figure 6.26.: Runtime comparison τ between the DGFV, DGFEM, and DGDG methods for varying numbers of elements in the ξ-direction. The number of elements N_ξ was increased from 280 to 680, while the number of elements N_χ in the χ-direction remained fixed as defined in Tab. 6.1.

i.e., DGFV, DGFEM, or DGDG. The computed error can then be plotted as a function of runtime τ. As illustrated in Fig. 6.27, the DGDG method offers the most efficient runtime

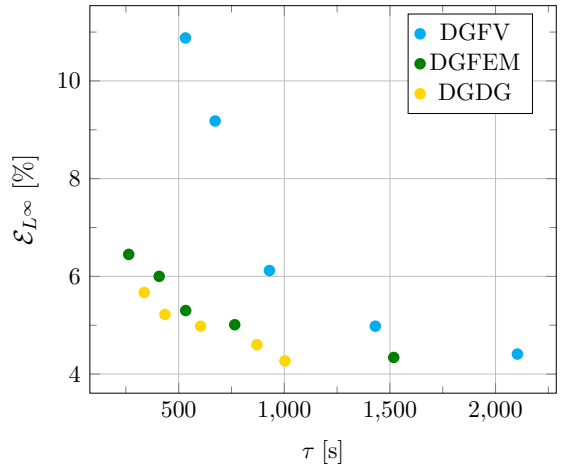

Figure 6.27.: Comparison of the absolute error $\mathcal{E}_{L^\infty}$ versus runtime τ between the QTBM reference and the DGFV, DGFEM, and DGDG approaches.

when accounting for error [GS3], followed closely by the DGFEM and DGFV schemes. The relatively poor performance of the DGFV variant is mainly due to the use of the trapezoidal rule for potential integration in the ξ-direction, rather than the more accurate Gauss-Lobatto quadrature. While the trapezoidal rule is computationally faster, it is also less accurate. Since the DGFEM and DGDG methods yield higher accuracy, a coarser grid is sufficient to reach the same error, allowing the DGDG method to cut runtime by nearly half.

A similar trend can be observed for interband quantum transport. Here, a comparison is performed with the UDS method from [71], evaluating both runtime and accuracy against

the DG scheme. To compute the absolute error $\mathcal{E}_{L^\infty}$, Eq. (6.2) is applied once again. This time,

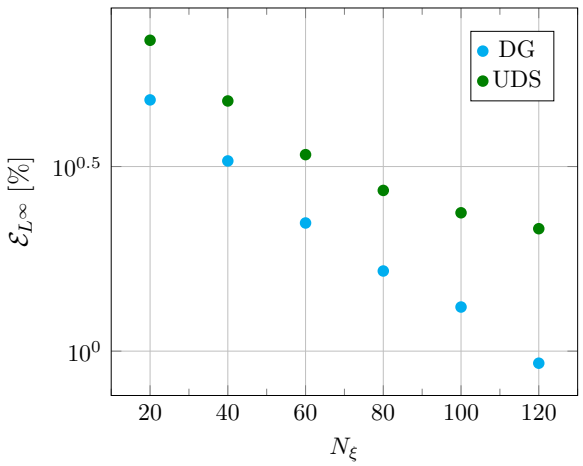

Figure 6.28.: Comparison of the absolute L^∞ error between the DG and UDS methods. The number of elements N_ξ was increased from 20 to 120 in increments of 20. All other numerical parameters are listed in Tab. 6.4.

however, the reference is the DG solution obtained using the finest available mesh. This choice is justified by the fact that the DG implementation has been shown to offer improved accuracy and thus qualifies as a suitable benchmark. As shown in Fig. 6.28, the error for all N_ξ values is lower for the DG method than for UDS [GS5]. Naturally, the DG solution (cyan markers in Fig. 6.28) converges to the reference with increasing element count N_ξ. The same applies to UDS, albeit with a consistent margin of a few percentage points.

When runtime is now considered, a familiar pattern emerges: As shown in Fig. 6.29,

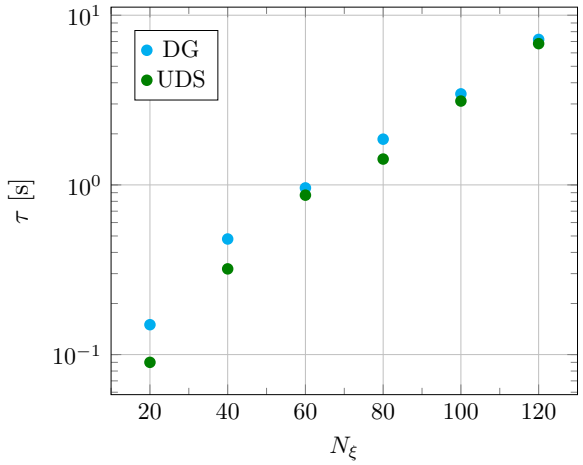

Figure 6.29.: Runtime comparison τ between the DG and UDS methods. The number of elements N_ξ was increased from 20 to 120 in increments of 20. All other numerical parameters are provided in Tab. 6.4.

the DG method is once again slower. However, this is to be expected, since the FD method is known for its high efficiency, albeit at the cost of accuracy. Nevertheless, the DG scheme holds

its ground when the error from Fig. 6.28 is considered. Fig. 6.30 shows the relationship between

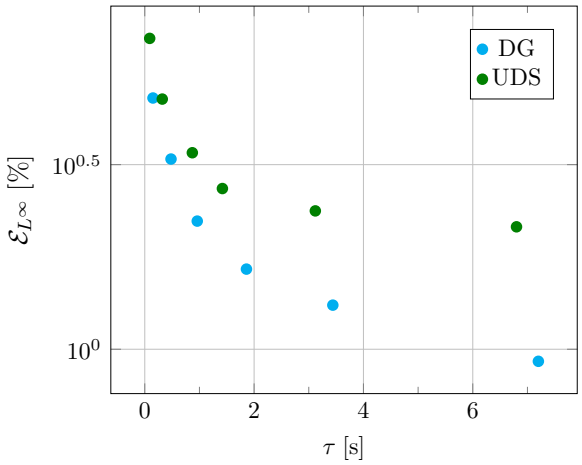

Figure 6.30.: Comparison of runtime τ and absolute error $\mathcal{E}_{L^\infty}$ between the DG and UDS methods. The number of elements N_ξ was increased from 20 to 120 in steps of 20. The remaining numerical parameters are given in Tab. 6.4.

absolute error $\mathcal{E}_{L^\infty}$ and runtime τ. Once again, it is evident that the DG method becomes the more efficient scheme when targeting the same error, as it requires fewer discretization elements to achieve the same accuracy as the UDS method.
Overall, it is apparent that while the DG method incurs a longer runtime for the same number of elements, a coarser mesh is sufficient to attain the same accuracy as commonly used numerical methods.

Next, the focus will be on resource management.

6.5.2. Resource Management

In this context, resource management refers to how a numerical method utilizes available hardware resources to perform a simulation. First, an aspect that is less dependent on the numerical method itself and more influenced by programming style is considered.
Every matrix generated during the simulation process must be stored in the system's main memory. Since, for instance, the DG method uses local matrices (defined per element) to assemble global matrices (defined for the entire computational domain), it is reasonable to assume that many matrices must be assembled and stored during runtime. A simplistic programming approach would involve creating a single script that generates all necessary matrices and retains them until the simulation ends. This style is referred to as the **Single Script (SS)** approach [GS3].
A more efficient and memory-saving alternative is to delete the local matrices once the global matrices have been assembled. This reduces memory usage by limiting the number of matrices stored simultaneously. In MATLAB, this can be achieved by breaking the SS into multiple functions, passing only the variables needed for subsequent calculations. This programming style is referred to as the **Functional Programming (FP)** approach [GS3].
The previously introduced DGFV, DGFEM, and DGDG methods were implemented using both

programming styles. The differences in memory usage and runtime are shown in Tab. 6.8. Two

Table 6.8.: Differences in runtime and RAM usage for the three approaches using the SS and FP programming styles.

Method	**Runtime [s]**		**RAM Usage [GB]**	
	SS	*FP*	*SS*	*FP*
DGFV	532	1545	45.13	37.77
DGFEM	920	2361	354.98	42.02
DGDG	1003	1600	863.67	46.95

main observations can be made from Tab. 6.8:

1. The runtime of all methods increases significantly under the **FP** style.
2. RAM usage is substantially reduced with the **FP** style, particularly for the DGFEM and DGDG methods.

The first point can be attributed to the fact that FP requires large amounts of data to be transferred between functions. Due to the limited read/write speed of RAM, this increases runtime. The DGDG method experiences the most significant slowdown due to its larger matrix dimensions and higher number of nonzero entries [GS3].
Regarding point two, RAM usage is significantly reduced by deleting local and partially global matrices that are no longer needed. These are not passed between functions after execution. The DGFEM and DGDG methods, in particular, benefit from this memory saving, especially due to reduced execution of Gauss-Lobatto quadrature routines [GS3].
This optimization allows both the DGFEM and DGDG methods to be executed on a standard laptop with 32 GB of RAM, rather than requiring a LiDO3[1] compute node with one terabyte of RAM, which was used to generate Tab. 6.8. Furthermore, the mesh can now be significantly refined. The reduced memory usage brings another key advantage for all methods: parallelization.

To take advantage of parallelization, the IV characteristic shown in Fig. 6.9 is revisited, which was generated using a `for`-loop that iterates over a vector of voltage values, simulating the device at each value. In the case of the RTD, for instance, voltages from 0 V to 0.35 V are divided into 50 steps. Since each iteration is independent of previous ones, they can be computed in parallel.
Modern computers typically feature multicore processors, where each core can handle an independent task in MATLAB. In the case of a parallel `for`-loop, each core executes one iteration, meaning that a processor with eight cores (including threads) can perform eight RTD simulations simultaneously. All eight simulations are stored in RAM, making it critical to minimize memory usage to allow full utilization of all processor cores.

[1]The LiDO3 (Linux Cluster at the TU Dortmund) is a tool for scientific computing and data science for researches at the Technischen Universität Dortmund and consists of multiple CPU and GPU units with RAM capacities of up to one terabyte. The author gratefully acknowledges the computing time provided on the Linux HPC cluster at Technical University Dortmund (LiDO3), partially funded in the course of the Large-Scale Equipment Initiative by the Deutsche Forschungsgemeinschaft (DFG, German Research Foundation) as project 271512359.

In the following section, a post-processing method will be introduced that aims to improve the accuracy of the DG method.

6.5.3. Slope Limiter

As the name suggests, a Slope Limiter (SL) limits the slope of the solution, thereby damping excessive gradients and restricting potential jumps at element interfaces [113].
In general, SLs are post-processing tools, since they only manipulate the final solution. Therefore, expectations regarding their effectiveness should remain moderate. The adjustment of the solution is performed in elements where discontinuities may occur – the so-called problematic elements, which can be detected algorithmically. The goal of a SL is to suppress oscillations specifically in these elements [23, 114].
In the following, three different SLs are examined: the Problem Independent (PI), Total Variation Diminishing (TVD), and Moment SL. These differ in the degree of their smoothing characteristics, ranging from rather *mild* to *aggressive* smoothing [113]. Their functionality and implementation can be found in standard references such as [23, 113, 114, 115]. Here, a focus is put exclusively on their effect on the DG method.
Once again, an RTD according to Tab. 6.1 is simulated using the DGDG method. A mesh with $N_\chi \cdot N_{\chi p} \times N_\xi \cdot N_p^\xi = 240 \times 360$ is used. First, the transport direction χ is investigated. As shown

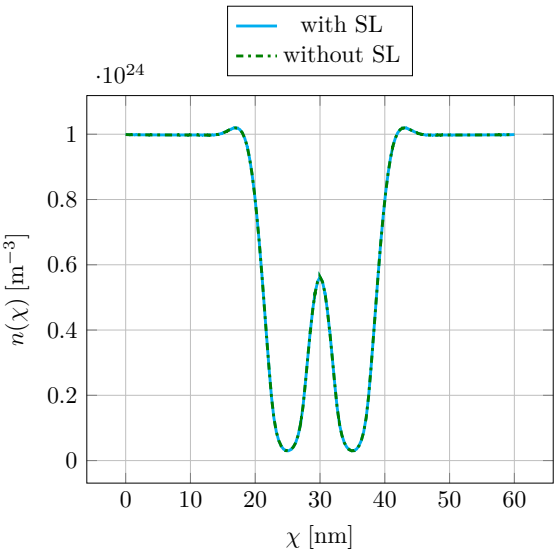

Figure 6.31.: Comparison of the charge carrier density n_{DGDG} with (light blue) and without (dark green) slope limiter.

in Fig. 6.31, the charge carrier distributions with and without limiting largely coincide. One can conclude that the transport direction is already sufficiently smooth and that the application of a SL has no significant effect. Next, the relative direction ξ is examined. Fig. 6.32 illustrates the effects of the different SLs on the charge carrier distribution. Notably, strong smoothing is visible in the regions around $\xi = \pm 18$ nm for all SLs. The moment limiter achieves the strongest smoothing, as seen in Fig. 6.32b, closely followed by the PI limiter, which produces a slightly weaker smoothing. In both cases, the peak at $\xi = 0$ nm is preserved. The TVD limiter, on the

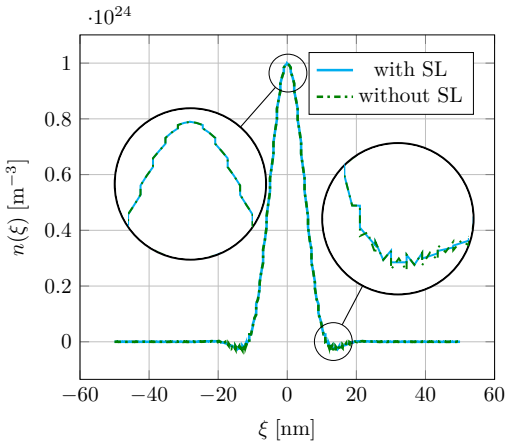

(a) Charge carrier distribution with and without PI-limiter

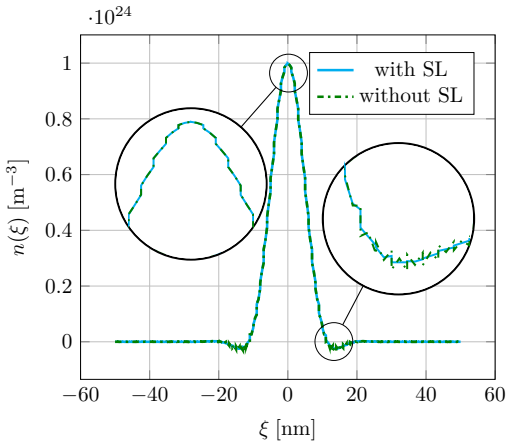

(b) Charge carrier distribution with and without moment-limiter

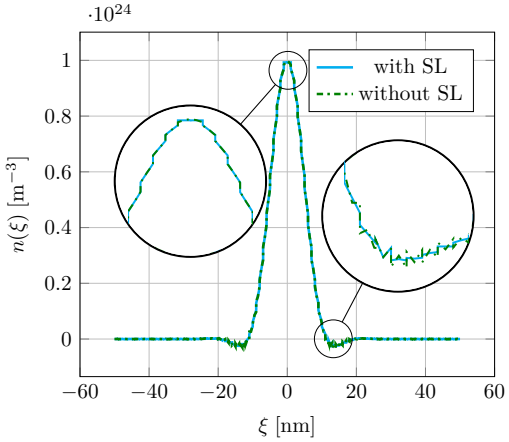

(c) Charge carrier distribution with and without TVD-limiter

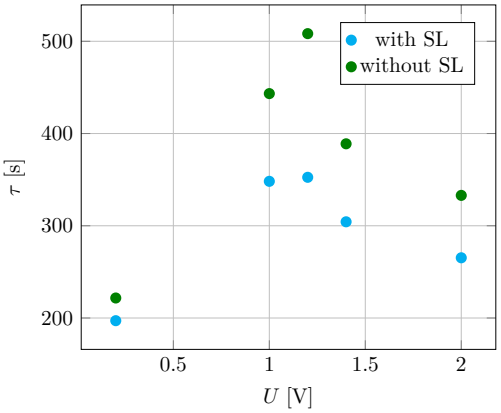

(d) Runtime comparison of the Poisson-loop with and without moment-limiter

Figure 6.32.: Smoothed charge carrier distributions in ξ-direction using the PI-limiter (a), the moment-limiter (b), and the TVD-limiter (c). Subfigure (d) shows a runtime comparison with and without limiter for the Poisson loop.

other hand, shows its greatest weakness in Fig. 6.32c, where not only the peak is dampened, but the smoothing around $\xi = \pm 18$ nm is also the weakest [GS8].
The smoothed solutions can be compared with the reference, namely the QTBM, and the error can be computed using the L^p norm for $p = 1, 2, \infty$. The results are summarized in Tab. 6.9. With a runtime of 0.06 s, the moment limiter is the most efficient and also yields the lowest L^p error.
In a final step, the RTD is simulated with a self-consistent Hartree potential for different values of externally applied voltages. In each iteration, the charge carrier distribution n is smoothed using the moment limiter prior to calculating the self-consistent potential, as this limiter was identified as the more accurate method in Tab. 6.9. A comparison of the simulation times with and without the moment limiter is shown in Fig. 6.32d. Here, five random voltage values between 0 V and 2 V were chosen for the RTD simulation. It is evident that especially at higher voltages, simulation times can be significantly reduced. This is due to the error reduction

Table 6.9.: Overview of the L^p error and runtime for the individual SLs.

Error	**No limiter**	**PI**	**Moment**	**TVD**
L^1	11.62 %	8.58 %	7.89 %	8.04 %
L^2	7.83 %	7.38 %	7.25 %	7.46 %
L^∞	8.07 %	8.07 %	8.07 %	9.36 %
Runtime		0.13 s	0.06 s	0.07 s

achieved by the limiter, which in turn reduces the number of required iteration steps in the Gummel algorithm, resulting in an average runtime reduction of approximately 21 % [GS8].

7. Summary and Outlook

The present work aimed at the development of a DG concept suitable for solving quantum transport equations. Particular emphasis was placed on achieving high accuracy and efficiency in order to justify its use alongside established numerical methods such as the Finite Difference (FD), Finite Element method (FEM), and Finite Volume (FV) approaches.
On the basis of quantum transport models for the intraband, as well as interband quantum transport and the inclusion of a spatially varying effective electron mass, boundary conditions were introduced in the form of inflow/outflow boundaries and the CAP to account for the open boundaries in the relative direction. A thorough investigation of the CAP coupled with the DG methodology in Section 5.2.3 revealed a substantial influence of the CAP on the stability of the numerical method. The analysis furthermore showed that the numerical flux of the DG scheme is another major contributor to the algorithm's stability. A comparison between the upwinding and central flux showed that the upwinding flux is the best choice to ensure numerical stability.

The transport models were then comprehensively discretized using the DG method. In comparison with reference methods such as QTBM and NEGF, the developed numerical method showed low error, proving its suitability for discretization. In a first step, the intraband transport model was treated. In this context, three numerical schemes were derived, all of which employ the DG method for discretizing particle transport. Both spatial directions were treated independently with one-dimensional numerical methods. This resulted in the DGFV, the DGFEM, and the DGDG methods. To discretize the model with spatially varying effective mass as well as the interband transport model, the DGFV method was used exclusively since implementing them with DGFEM or DGDG would result in prohibitively high matrix occupancy and hardware usage. Lastly, time discretization using the RK2 and RK4 schemes was outlined, and the Gummel algorithm was discussed for solving the Poisson equation numerically. Finally, the MSA was implemented for the treatment of two-dimensional transport problems in conjunction with the DG method.
First, one-dimensional transport was validated using an RTD. In the framework of stationary simulations, both thermal equilibrium and non-equilibrium were covered, and the flat-band potential could be combined with a self-consistent Hartree potential. By manipulating the CAP, the DG method produced comparable IV curves, both with and without the self-consistent potential. Moreover, using the previously introduced RK2 and RK4 schemes, the transient switching behavior of the RTD was successfully simulated. An initial efficiency analysis revealed that the RK4 method yielded shorter runtimes than RK2. Finally, the model with the spatially varying effective mass was successfully validated as well.
With the introduction of the TFET, the intraband transport model was further tested. The density matrices of the conduction and valence bands agreed with the literature and demonstrated that the DG method is well suited for this type of simulation.
The interband model was subsequently validated using an RITD. Again, the DG method produced plausible density matrix profiles for the pure and mixed states. The IV curves were in

agreement with previous works, confirming the suitability of the DG approach for simulating interband quantum transport.
To test the interplay between the MSA and the DG method, and to allow simulations of two-dimensional quantum transport, the DGFET was introduced. A comparison with a standard FV method, using the NEGF as a reference, showed that the DG algorithm achieved lower approximation errors while maintaining shorter runtimes in the evaluated examples.
Runtime analysis was particularly relevant since the development of a time-efficient method was a primary objective of this work. A comparison with the FV method and an implicit time integration scheme for transient simulations showed that the DG method offers significant efficiency gains by allowing for explicit schemes such as RK4. The comparison of the three proposed schemes – DGFV, DGFEM, and DGDG – revealed that while DGFV was most memory-efficient, the DGFEM and DGDG methods achieved higher accuracy. Ultimately, it was shown that, under the condition of error parity, the DGDG method required a shorter runtime. Following the same rationale, it was shown for the interband transport model that the investigated FV implementation yielded higher errors and/or runtimes in the presented experiments when compared to the DG alternative.
In addition, resource management was investigated. Two programming paradigms – SS and FP – were identified. While the SS style resulted in shorter runtimes, the FP approach led to a 95 % reduction in RAM usage for the DGDG method. This came at the cost of increased runtime. However, reduced memory usage enabled parallel execution of certain simulation loops such that the increased runtime could be remedied to en extent.
With the introduction of SLs, a post-processing technique was included to further increase the accuracy of the DG method. By limiting the slope of the solution, global smoothing could be achieved. Increased accuracy, in turn, led to a reduction in the number of required iterations during self-consistent IV curve simulations, which significantly reduced runtime.

In summary, the DG method offers a framework that supports a wide range of one-dimensional quantum transport simulations. Its increased accuracy compared to conventional methods, combined with shorter runtimes in all simulation scenarios, demonstrates its flexibility and suitability for leveraging modern HPC principles.

Naturally, there remain further opportunities related to the DG method: For example, the use of so-called flux limiters could be investigated. While slope limiters act only in post-processing, flux limiters directly modify the numerical flux, which may lead to a greater impact on the final solution.
MATLAB offers various options for integrating GPU support. To further enhance efficiency, the matrix-vector multiplication in the DG method could be offloaded to high-end GPUs. Compared to CPUs, GPUs offer significantly more cores, enabling higher computational throughput, especially when combined with dedicated GPU memory. For this, the system matrix must be transferred to the GPU memory. The size of this matrix is therefore constrained by the available memory. With their block-diagonal structure, DG methods are particularly well suited for clever matrix partitioning to make optimal use of limited GPU resources.

Clearly, the DG methods offer advantages that could not be fully exploited in the scope of this project – a fact underlined by the approval of the second phase of this DFG project.

List of Publications

[GS1] Ganiu, V. ; Loesing, P. ; Jaeger, M. ; Schulz, Dirk: Stabilizing Quantum-Liouville equations with complex absorbing potentials in discontinuous Galerkin frameworks. In: *Journal of Applied Mathematics and Computing* (2025). http://dx.doi.org/10.1007/s12190-025-02598-7. – DOI 10.1007/s12190–025–02598–7

[GS2] Ganiu, V. ; Jaeger, M. ; Schulz, D.: Hybrid Discontinuous Galerkin Approach for the Solution of Quantum Liouville-Type Equations. In: *IEEE Transactions on Nanotechnology* 22 (2023), S. 696–705. http://dx.doi.org/10.1109/TNANO.2023.3322541. – DOI 10.1109/TNANO.2023.3322541

[GS3] Ganiu, V. ; Schulz, D.: Efficiency analysis of discontinuous Galerkin approaches for the application onto quantum Liouville-type equations. In: *Journal of Computational Electronics* 23 (2024), S. 718–727. http://dx.doi.org/10.1007/s10825-024-02178-1. – DOI 10.1007/s10825–024–02178–1

[GS4] Ganiu, V. ; Schulz, D.: Application of a Hybrid Discontinuous Galerkin Scheme onto Quantum-Liouville-type Equations for Heterostructure Devices. In: *2023 International Conference on Simulation of Semiconductor Processes and Devices (SISPAD)*, 2023, S. 261–264

[GS5] Ganiu, V. ; Schulz, D.: Efficient quantum transport simulations in nanodevices using multi-band discontinuous Galerkin methods. In: *Journal of Computational Electronics* 24 (2025), Nr. 1, 167. http://dx.doi.org/10.1007/s10825-025-02398-z. – DOI 10.1007/s10825–025–02398–z

[GS6] Ganiu, V. ; Schulz, D.: Discontinuous Galerkin concept for Quantum-Liouville type equations. In: *Solid-State Electronics* 200 (2023), 108536. http://dx.doi.org/https://doi.org/10.1016/j.sse.2022.108536. – DOI https://doi.org/10.1016/j.sse.2022.108536. – ISSN 0038–1101

[GS7] Ganiu, V. ; Schulz, D.: Application of discontinuous Galerkin methods onto quantum-Liouville type equations. In: *Proceedings of the International Workshop on Computational Nanotechnology (IWCN)*, 2023

[GS8] Ganiu, V. ; Arnaut, B ; Neu, J. ; Schulz, D.: Impact of Slope Limiters on DG Methods Solving Quantum-Liouville Type Equations. In: *Proceedings of the International Workshop on Computational Nanotechnology (IWCN)*, 2025

Bibliography

[1] Schrödinger, E.: An Undulatory Theory of the Mechanics of Atoms and Molecules. In: *Phys. Rev.* 28 (1926), Dec, 1049–1070. http://dx.doi.org/10.1103/PhysRev.28.1049. – DOI 10.1103/PhysRev.28.1049

[2] Frensley, William R.: Wigner-function model of a resonant-tunneling semiconductor device. In: *Phys. Rev. B* 36 (1987), Jul, 1570–1580. http://dx.doi.org/10.1103/PhysRevB.36.1570. – DOI 10.1103/PhysRevB.36.1570

[3] Schulz, L. ; Inci, B. ; Pech, M. ; al. et: Subdomain-based exponential integrators for quantum Liouville-type equations. In: *Journal of Computational Electronics* 20 (2021), S. 2070–2090. http://dx.doi.org/10.1007/s10825-021-01797-2. – DOI 10.1007/s10825–021–01797–2

[4] Lent, Craig S. ; Kirkner, David J.: The Quantum Transmitting Boundary Method. In: *Journal of Applied Physics* 67 (1990), Nr. 10, S. 6353–6359

[5] Frensley, W. R.: Numerical evaluation of resonant states. In: *Superlattices and Microstructures* 11 (1992), Nr. 3, S. 347–350. http://dx.doi.org/10.1016/0749-6036(92)90396-M. – DOI 10.1016/0749–6036(92)90396–M. – ISSN 0749–6036

[6] Jacoboni, Carlo ; Bordone, Paolo: The Wigner-function approach to non-equilibrium electron transport. In: *Reports on Progress in Physics* 67 (2004), jun, Nr. 7, 1033. http://dx.doi.org/10.1088/0034-4885/67/7/R01. – DOI 10.1088/0034–4885/67/7/R01

[7] Rossi, F ; Jacoboni, C ; Nedjalkov, M: A Monte Carlo solution of the Wigner transport equation. In: *Semiconductor Science and Technology* 9 (1994), may, Nr. 5S, 934. http://dx.doi.org/10.1088/0268-1242/9/5S/143. – DOI 10.1088/0268–1242/9/5S/143

[8] Datta, S.: The non-equilibrium Green's function (NEGF) formalism: An elementary introduction. In: *Digest. International Electron Devices Meeting,*, 2002, S. 703–706

[9] Lake, Roger ; Datta, Supriyo: Nonequilibrium Green's-function method applied to double-barrier resonant-tunneling diodes. In: *Phys. Rev. B* 45 (1992), Mar, 6670–6685. http://dx.doi.org/10.1103/PhysRevB.45.6670. – DOI 10.1103/PhysRevB.45.6670

[10] Jauho, Antti-Pekka ; Wingreen, Ned S. ; Meir, Yigal: Time-dependent transport in interacting and noninteracting resonant-tunneling systems. In: *Phys. Rev. B* 50 (1994), Aug, 5528–5544. http://dx.doi.org/10.1103/PhysRevB.50.5528. – DOI 10.1103/PhysRevB.50.5528

[11] Gaury, Benoit ; Weston, Joseph ; Santin, Matthieu ; Houzet, Manuel ; Groth, Christoph ; Waintal, Xavier: Numerical simulations of time-resolved quantum electronics.

In: *Physics Reports* 534 (2014), Nr. 1, 1-37. http://dx.doi.org/https://doi.org/10.1016/j.physrep.2013.09.001. – DOI https://doi.org/10.1016/j.physrep.2013.09.001. – ISSN 0370–1573. – Numerical simulations of time-resolved quantum electronics

[12] Vogl, P. ; Kubis, T.: The non-equilibrium Green's function method: An introduction. In: *Journal of Computational Electronics* 9 (2010), 12, S. 237–242. http://dx.doi.org/10.1007/s10825-010-0313-z. – DOI 10.1007/s10825–010–0313–z

[13] Frensley, William R.: Boundary conditions for open quantum systems driven far from equilibrium. In: *Rev. Mod. Phys.* 62 (1990), Jul, 745–791. http://dx.doi.org/10.1103/RevModPhys.62.745. – DOI 10.1103/RevModPhys.62.745

[14] Tsuchiya, H. ; Ogawa, M. ; Miyoshi, T.: Simulation of quantum transport in quantum devices with spatially varying effective mass. In: *IEEE Transactions on Electron Devices* 38 (1991), Nr. 6, S. 1246–1252. http://dx.doi.org/10.1109/16.81613. – DOI 10.1109/16.81613

[15] Schulz, Dirk ; Mahmood, Azhar: Approximation of a Phase Space Operator for the Numerical Solution of the Wigner Equation. In: *IEEE Journal of Quantum Electronics* 52 (2016), Nr. 2, S. 1–9. http://dx.doi.org/10.1109/JQE.2015.2504086. – DOI 10.1109/JQE.2015.2504086

[16] Schulz, Lukas ; Schulz, Dirk: Numerical Analysis of the Transient Behavior of the Non-Equilibrium Quantum Liouville Equation. In: *IEEE Transactions on Nanotechnology* 17 (2018), Nr. 6, S. 1197–1205. http://dx.doi.org/10.1109/TNANO.2018.2868972. – DOI 10.1109/TNANO.2018.2868972

[17] Rosati, Roberto ; Dolcini, Fabrizio ; Iotti, Rita C. ; Rossi, Fausto: Wigner-function formalism applied to semiconductor quantum devices: Failure of the conventional boundary condition scheme. In: *Phys. Rev. B* 88 (2013), Jul, 035401. http://dx.doi.org/10.1103/PhysRevB.88.035401. – DOI 10.1103/PhysRevB.88.035401

[18] Béland, Michel ; Côté, Jean ; Staniforth, Andrew: The Accuracy of a Finite-Element Vertical Discretization Scheme for Primitive Equation Models: Comparison with a Finite-Difference Scheme. In: *Monthly Weather Review* 111 (1983), Nr. 12, 2298 - 2318. http://dx.doi.org/10.1175/1520-0493(1983)111<2298:TAOAFE>2.0.CO;2. – DOI 10.1175/1520–0493(1983)111<2298:TAOAFE>2.0.CO;2

[19] Tokhi, M O. ; Mohamed, Z ; Azad, A K M.: Finite difference and finite element approaches to dynamic modelling of a flexible manipulator. In: *Proceedings of the Institution of Mechanical Engineers, Part I: Journal of Systems and Control Engineering* 211 (1997), Nr. 2, 145-156. http://dx.doi.org/10.1243/0959651971539966. – DOI 10.1243/0959651971539966

[20] Gerstenmayer, Alexander ; Jüngel, Ansgar: Comparison of a finite-element and finite-volume scheme for a degenerate cross-diffusion system for ion transport. In: *Computational and Applied Mathematics* 38 (2019), Nr. 108. http://dx.doi.org/10.1007/s40314-019-0882-9. – DOI 10.1007/s40314–019–0882–9

[21] Reed, W. H. ; Hill, T. R.: Triangular Mesh Methods for the Neutron Transport Equation / Los Alamos Scientific Laboratory. Version: oct 1973. https://digital.library.unt.edu/ark:/67531/metadc1036080/. 1973. – Technical Report. – Accessed July 3, 2025. University of North Texas Libraries, UNT Digital Library. Crediting UNT Libraries Government Documents Department

[22] Cockburn, Bernardo ; Karniadakis, George E. ; Shu, Chi-Wang: The Development of Discontinuous Galerkin Methods. In: Cockburn, Bernardo (Hrsg.) ; Karniadakis, George E. (Hrsg.) ; Shu, Chi-Wang (Hrsg.): *Discontinuous Galerkin Methods*. Berlin, Heidelberg : Springer Berlin Heidelberg, 2000. – ISBN 978–3–642–59721–3, S. 3–50

[23] Shu, Chi-Wang: A brief survey on discontinuous Galerkin methods in computational fluid dynamics. In: *Advances in Mechanics* 43 (2013), Nr. 3, 541. http://dx.doi.org/10.6052/1000-0992-13-059. – DOI 10.6052/1000–0992–13–059. – ISSN 1000–0992

[24] Schwarz, Hans R.: *Methode der Finiten Elemente: eine Einführung unter besonderer Berücksichtigung der Rechenpraxis*. 3., neubearbeitete Auflage. Stuttgart : Teubner, 1991. – ISBN 3–519–22349–X

[25] Case, William B.: Wigner functions and Weyl transforms for pedestrians. In: *American Journal of Physics* 76 (2008), 10, Nr. 10, 937-946. http://dx.doi.org/10.1119/1.2957889. – DOI 10.1119/1.2957889. – ISSN 0002–9505

[26] Ducry, Fabian ; Aeschlimann, Jan ; Luisier, Mathieu: Electro-thermal transport in disordered nanostructures: a modeling perspective. In: *Nanoscale Adv.* 2 (2020), S. 2648–2667. http://dx.doi.org/10.1039/D0NA00168F. – DOI 10.1039/D0NA00168F

[27] Wang, Lin-Wang: *Calculating Quantum Transports Using Periodic Boundary Conditions*. 2004

[28] Schulz, Lukas ; Schulz, Dirk: Complex Absorbing Potential Formalism Accounting for Open Boundary Conditions Within the Wigner Transport Equation. In: *IEEE Transactions on Nanotechnology* 18 (2019), S. 830–838. http://dx.doi.org/10.1109/TNANO.2019.2933307. – DOI 10.1109/TNANO.2019.2933307

[29] Eslahchi, M.R. ; Masjed-Jamei, M. ; Babolian, E.: On numerical improvement of GaussLobatto quadrature rules. In: *Applied Mathematics and Computation* 164 (2005), Nr. 3, 707-717. http://dx.doi.org/https://doi.org/10.1016/j.amc.2004.04.113. – DOI https://doi.org/10.1016/j.amc.2004.04.113. – ISSN 0096–3003

[30] Guo, Wenfei ; Cai, Zizhe ; Xiong, Zhongfei ; Chen, Weijin ; Chen, Yuntian: Efficient and accurate numerical-projection of electromagnetic multipoles for scattering objects. In: *Frontiers of Optoelectronics* 16 (2023), dec, Nr. 1. http://dx.doi.org/10.1007/s12200-023-00102-2. – DOI 10.1007/s12200–023–00102–2. – ISSN 2095–2767

[31] Venugopal, R. ; Ren, Z. ; Datta, S. ; Lundstrom, M. S. ; Jovanovic, D.: Simulating quantum transport in nanoscale transistors: Real versus mode-space approaches. In: *Journal of Applied Physics* 92 (2002), 10, Nr. 7, 3730-3739. http://dx.doi.org/10.1063/1.1503165. – DOI 10.1063/1.1503165. – ISSN 0021–8979

[32] Rahman, A. ; Guo, Jing ; Datta, S. ; Lundstrom, M.S.: Theory of ballistic nanotransistors. In: *IEEE Transactions on Electron Devices* 50 (2003), Nr. 9, S. 1853–1864. http://dx.doi.org/10.1109/TED.2003.815366. – DOI 10.1109/TED.2003.815366

[33] Mai, D. ; Schulz, D.: Applying POD-methods onto electron-phonon scattering in the Wigner equation. In: *Proceedings of the International Workshop on Computational Nanotechnology (IWCN)*, 2025

[34] Madelung, O.: *Festkörpertheorie I.* 1972. http://dx.doi.org/https://doi.org/10.1007/978-3-642-80673-5. http://dx.doi.org/https://doi.org/10.1007/978-3-642-80673-5

[35] Madelung, O.: *Festkörpertheorie II: Wechselwirkungen.* 2013. http://dx.doi.org/https://doi.org/10.1007/978-3-642-65413-8. http://dx.doi.org/https://doi.org/10.1007/978-3-642-65413-8

[36] Ashcroft, N.W. ; Mermin, N.D.: *Solid State Physics.* Holt, Rinehart and Winston, 1976 (HRW international editions). https://books.google.de/books?id=oXIfAQAAMAAJ. – ISBN 9780030839931

[37] VonNeumann, John: *Mathematische Grundlagen der Quantenmechanik.* Springer, 1932 http://eudml.org/doc/203794

[38] Landsman, Klaas: *Foundations of Quantum Theory: From Classical Concepts to Operator Algebras.* Cham, 2017

[39] Weyl, H.: *The Theory of Groups and Quantum Mechanics.* Dover Publications, 1950 (Dover Books on Mathematics). https://books.google.de/books?id=jQbEcDDqGb8C. – ISBN 9780486602691

[40] Case, William B.: Wigner functions and Weyl transforms for pedestrians. In: *American Journal of Physics* 76 (2008), 10, Nr. 10, 937-946. http://dx.doi.org/10.1119/1.2957889. – DOI 10.1119/1.2957889. – ISSN 0002–9505

[41] Wigner, E.: On the Quantum Correction For Thermodynamic Equilibrium. In: *Phys. Rev.* 40 (1932), Jun, 749–759. http://dx.doi.org/10.1103/PhysRev.40.749. – DOI 10.1103/PhysRev.40.749

[42] Griffiths, D.J.: *Introduction to Quantum Mechanics.* Cambridge University Press, 2017 https://books.google.de/books?id=0h-nDAAAQBAJ. – ISBN 9781107179868

[43] Nielsen, Michael A. ; Chuang, Isaac L.: *Quantum Computation and Quantum Information: 10th Anniversary Edition.* Cambridge University Press, 2010

[44] Bell, J. S. ; Aspect, Alain: *Speakable and Unspeakable in Quantum Mechanics: Collected Papers on Quantum Philosophy.* 2. Cambridge University Press, 2004

[45] Datta, Supriyo: *Electronic Transport in Mesoscopic Systems.* Cambridge University Press, 1995 (Cambridge Studies in Semiconductor Physics and Microelectronic Engineering)

[46] Ferry, D.K. ; Goodnick, S.M. ; Bird, J.: *Transport in Nanostructures.* Cambridge University Press, 2009 https://books.google.de/books?id=8j8gAwAAQBAJ. – ISBN 9781139480833

[47] Born, Max: *The statistical interpretation of quantum mechanics*. Nobel lecture. https://www.nobelprize.org/prizes/physics/1954/born/lecture/. Version: 1954. – Retrieved from the Nobel Prize website

[48] Esaki, L. ; Tsu, R.: Superlattice and Negative Differential Conductivity in Semiconductors. 14 (1970), Nr. 1, S. 61–65. http://dx.doi.org/10.1147/rd.141.0061. – DOI 10.1147/rd.141.0061

[49] Jiang, Zhang ; Sung, Kevin J. ; Kechedzhi, Kostyantyn ; Smelyanskiy, Vadim N. ; Boixo, Sergio: Quantum Algorithms to Simulate Many-Body Physics of Correlated Fermions. In: *Phys. Rev. Appl.* 9 (2018), Apr, 044036. http://dx.doi.org/10.1103/PhysRevApplied.9.044036. – DOI 10.1103/PhysRevApplied.9.044036

[50] Chuang, S.L.: *Physics of Optoelectronic Devices*. Wiley, 1995 (Wiley Series in Pure and Applied Optics). https://books.google.de/books?id=ect6QgAACAAJ. – ISBN 9780471109396

[51] Voon, L.C.L.Y. ; Willatzen, M.: *The k p Method: Electronic Properties of Semiconductors*. Springer Berlin Heidelberg, 2009 https://books.google.de/books?id=t46OZQrEd8QC. – ISBN 9783540928720

[52] Kittel, Charles: *Introduction to Solid State Physics*. 8. Wiley, 2004 http://www.amazon.com/Introduction-Solid-Physics-Charles-Kittel/dp/047141526X/ref=dp_ob_title_bk. – ISBN 9780471415268

[53] Kane, Evan O.: Band structure of indium antimonide. In: *Journal of Physics and Chemistry of Solids* 1 (1957), Nr. 4, 249-261. http://dx.doi.org/https://doi.org/10.1016/0022-3697(57)90013-6. – DOI https://doi.org/10.1016/0022–3697(57)90013–6. – ISSN 0022–3697

[54] Luttinger, J. M. ; Kohn, W.: Motion of Electrons and Holes in Perturbed Periodic Fields. In: *Phys. Rev.* 97 (1955), Feb, 869–883. http://dx.doi.org/10.1103/PhysRev.97.869. – DOI 10.1103/PhysRev.97.869

[55] Morandi, Omar ; Modugno, Michele: Multiband envelope function model for quantum transport in a tunneling diode. In: *Phys. Rev. B* 71 (2005), Jun, 235331. http://dx.doi.org/10.1103/PhysRevB.71.235331. – DOI 10.1103/PhysRevB.71.235331

[56] Schulz, L. ; Schulz, D.: Multiband Phase Space Operator for Narrow Bandgap Semiconductor Devices. In: *2020 International Conference on Simulation of Semiconductor Processes and Devices (SISPAD)*, 2020, S. 383–386

[57] Ahn, D. ; Park, S.H.: *Engineering Quantum Mechanics*. Wiley, 2011 (IEEE Press). https://books.google.de/books?id=KPyO9OpVzgkC. – ISBN 9781118017814

[58] Schulz, Lukas: *Numerische Methoden für die Analyse von Quantenbauelementen auf Grundlage der Liouville-von-Neumann-Gleichung*. Technische Universität Dortmund, 2021

[59] Mizuta, H ; Goodings, C J.: Transient quantum transport simulation based on the statistical density matrix. In: *Journal of Physics: Condensed Matter* 3 (1991), may, Nr. 21, 3739. http://dx.doi.org/10.1088/0953-8984/3/21/007. – DOI 10.1088/0953–8984/3/21/007

[60] Ferry, David K. ; Nedjalkov, Mihail ; Weinbub, Josef ; Ballicchia, Mauro ; Welland, Ian ; Selberherr, Siegfried: Complex Systems in Phase Space. In: *Entropy* 22 (2020), Nr. 10. http://dx.doi.org/10.3390/e22101103. – DOI 10.3390/e22101103. – ISSN 1099–4300

[61] Vyas, Pratik B. ; Put, Maarten L. d. ; Fischetti, Massimo V.: Master-Equation Study of Quantum Transport in Realistic Semiconductor Devices Including Electron-Phonon and Surface-Roughness Scattering. In: *Phys. Rev. Appl.* 13 (2020), Jan, 014067. http://dx.doi.org/10.1103/PhysRevApplied.13.014067. – DOI 10.1103/PhysRevApplied.13.014067

[62] Iotti, Rita C. ; Dolcini, Fabrizio ; Rossi, Fausto: Wigner-function formalism applied to semiconductor quantum devices: Need for nonlocal scattering models. In: *Physical Review B* 96 (2017), sep, Nr. 11. http://dx.doi.org/10.1103/physrevb.96.115420. – DOI 10.1103/physrevb.96.115420. – ISSN 2469–9969

[63] Weyl, Hermann V.: Quantenmechanik und Gruppentheorie. In: *Zeitschrift für Physik* 46 (1927), 1-46. https://api.semanticscholar.org/CorpusID:121036548

[64] Case, William B.: Wigner functions and Weyl transforms for pedestrians. In: *American Journal of Physics* 76 (2008), 937-946. https://api.semanticscholar.org/CorpusID:32442131

[65] Biegel, B. A. ; Plummer, J. D.: Comparison of self-consistency iteration options for the Wigner function method of quantum device simulation. In: *Phys. Rev. B* 54 (1996), Sep, 8070–8082. http://dx.doi.org/10.1103/PhysRevB.54.8070. – DOI 10.1103/PhysRevB.54.8070

[66] Armagnat, Pierre ; Waintal, Xavier ; Houzet, Matthieu: The self-consistent quantum-electrostatic problem in strongly non-linear regime. In: *arXiv preprint* (2019). https://arxiv.org/abs/1905.01271

[67] Gummel, H. K.: A self-consistent iterative scheme for one-dimensional steady state transistor calculations. In: *IEEE Transactions on Electron Devices* 11 (1964), Nr. 10, S. 455–465. http://dx.doi.org/10.1109/T-ED.1964.15364. – DOI 10.1109/T–ED.1964.15364

[68] Hesthaven, Jan S. ; Warburton, Tim: *Texts in Applied Mathematics*. Bd. 54: *Nodal Discontinuous Galerkin Methods: Algorithms, Analysis, and Applications*. New York, NY : Springer, 2008. http://dx.doi.org/10.1007/978-0-387-72067-8. http://dx.doi.org/10.1007/978-0-387-72067-8. – ISBN 978–0–387–72065–4

[69] Shockley, W.: *Electrons and Holes in Semiconductors: With Applications to Transistor Electronics*. Van Nostrand, 1959 (Bell Telephone Laboratories series). https://books.google.de/books?id=279EAAAAIAAJ. – ISBN 9780882753829

[70] Pankove, J.I.: *Optical Processes in Semiconductors*. Dover, 1975 (Dover books explaining science and mathematics). https://books.google.de/books?id=HHM9Vo0DYZAC. – ISBN 9780486602752

[71] Schulz, Lukas ; Schulz, Dirk: Formulation of a phase space exponential operator for the Wigner transport equation accounting for the spatial variation of the effective mass. In: *J. Comput. Electron.* 19 (2020), dec, Nr. 4, 13991415. http://dx.doi.org/10.1007/s10825-020-01551-0. – DOI 10.1007/s10825–020–01551–0. – ISSN 1569–8025

[72] Dorda, Antonius ; Schürrer, Ferdinand: A WENO-solver combined with adaptive momentum discretization for the Wigner transport equation and its application to resonant tunneling diodes. In: *Journal of Computational Physics* 284 (2015), 95-116. http://dx.doi.org/https://doi.org/10.1016/j.jcp.2014.12.026. – DOI https://doi.org/10.1016/j.jcp.2014.12.026. – ISSN 0021–9991

[73] Jiang, Haiyan ; Cai, Wei ; Tsu, Raphael: Accuracy of the Frensley inflow boundary condition for Wigner equations in simulating resonant tunneling diodes. In: *Journal of Computational Physics* 230 (2011), Nr. 5, 2031-2044. http://dx.doi.org/https://doi.org/10.1016/j.jcp.2010.12.002. – DOI https://doi.org/10.1016/j.jcp.2010.12.002. – ISSN 0021–9991

[74] Jensen, K. L. ; Buot, F. A.: Numerical aspects on the simulation of IV characteristics and switching times of resonant tunneling diodes. In: *Journal of Applied Physics* 67 (1990), 02, Nr. 4, 2153-2155. http://dx.doi.org/10.1063/1.345551. – DOI 10.1063/1.345551. – ISSN 0021–8979

[75] Kim, Kyoung-Youm ; Lee, Byoungho: Simulation of quantum transport by applying second-order differencing scheme to Wigner function model including spatially varying effective mass. In: *Solid-State Electronics* 43 (1999), Nr. 1, 81-86. http://dx.doi.org/https://doi.org/10.1016/S0038-1101(98)00201-9. – DOI https://doi.org/10.1016/S0038–1101(98)00201–9. – ISSN 0038–1101

[76] Bir, G. L. ; Pikus, G. E. ; Hensel, J. C. ; Louvish, D.: *Symmetry and Strain-Induced Effects in Semiconductors*. New York : Wiley, 1974

[77] Sun, Jian P. ; Haddad, G.I. ; Mazumder, P. ; Schulman, J.N.: Resonant tunneling diodes: models and properties. In: *Proceedings of the IEEE* 86 (1998), Nr. 4, S. 641–660. http://dx.doi.org/10.1109/5.663541. – DOI 10.1109/5.663541

[78] Seabaugh, A. C. ; Zhang, Q.: Low-Voltage Tunnel Transistors for Beyond CMOS Logic. In: *Proceedings of the IEEE* 98 (2010), Nr. 12, S. 2095–2110. http://dx.doi.org/10.1109/JPROC.2010.2070830. – DOI 10.1109/JPROC.2010.2070830

[79] Morandi, Omar: Multiband Wigner-function formalism applied to the Zener band transition in a semiconductor. In: *Phys. Rev. B* 80 (2009), Jul, 024301. http://dx.doi.org/10.1103/PhysRevB.80.024301. – DOI 10.1103/PhysRevB.80.024301

[80] Borgioli, Giovanni ; Frosali, Giovanni ; Zweifel, Paul F.: Wigner Approach to the Two-Band Kane Model for a Tunneling Diode. In: *Transport Theory and Statistical Physics* 32 (2003), Nr. 3-4, S. 347–366. http://dx.doi.org/10.1081/TT-120024768. – DOI 10.1081/TT–120024768

[81] Poluektov, Yu M.: Quantum relativistic equation for a probability amplitude. In: *arXiv preprint arXiv:2312.04212* (2023). https://arxiv.org/abs/2312.04212

[82] Hadley, G. R.: Transparent boundary condition for beam propagation. In: *Opt. Lett.* 16 (1991), May, Nr. 9, 624–626. http://dx.doi.org/10.1364/OL.16.000624. – DOI 10.1364/OL.16.000624

[83] Ahland, A. ; Schulz, D. ; Voges, E.: Accurate mesh truncation for Schrödinger equations by a perfectly matched layer absorber: Application to the calculation of optical spectra. In: *Phys. Rev. B* 60 (1999), Aug, R5109–R5112. http://dx.doi.org/10.1103/PhysRevB.60.R5109. – DOI 10.1103/PhysRevB.60.R5109

[84] Gedney, S.D.: An anisotropic perfectly matched layer-absorbing medium for the truncation of FDTD lattices. In: *IEEE Transactions on Antennas and Propagation* 44 (1996), Nr. 12, S. 1630–1639. http://dx.doi.org/10.1109/8.546249. – DOI 10.1109/8.546249

[85] Galerkin, B.G.: On electrical circuits for the approximate solution of the Laplace equation. In: *Vestnik Inzhenerov* 19 (1915), S. 897–908

[86] Strikwerda, John C.: *Finite Difference Schemes and Partial Differential Equations*. 2nd Edition. Philadelphia, PA : Society for Industrial and Applied Mathematics (SIAM), 2004. – ISBN 978–0–89871–567–5

[87] LeVeque, Randall J.: *Finite Volume Methods for Hyperbolic Problems*. Cambridge, UK : Cambridge University Press, 2002. http://dx.doi.org/10.1017/CBO9780511791253. http://dx.doi.org/10.1017/CBO9780511791253. – ISBN 978–0–521–00924–9

[88] Toro, Eleuterio F.: *Riemann Solvers and Numerical Methods for Fluid Dynamics: A Practical Introduction*. 2nd Edition. Berlin, Heidelberg : Springer, 1997. http://dx.doi.org/10.1007/b79761. http://dx.doi.org/10.1007/b79761. – ISBN 978–3–540–65966–9

[89] Karniadakis, George E. ; Sherwin, Spencer J.: *Spectral/hp Element Methods for Computational Fluid Dynamics*. 2nd Edition. Oxford, UK : Oxford University Press, 2005. – ISBN 978–0–19–852869–2

[90] Roe, P.L: Approximate Riemann solvers, parameter vectors, and difference schemes. In: *Journal of Computational Physics* 43 (1981), Nr. 2, S. 357–372. http://dx.doi.org/https://doi.org/10.1016/0021-9991(81)90128-5. – DOI https://doi.org/10.1016/0021–9991(81)90128–5. – ISSN 0021–9991

[91] *Encyclopedia of Mathematics*. https://www.springer.com/encyclopaedia-mathematics. Version: 2023

[92] Ciarlet, Philippe G.: *The Finite Element Method for Elliptic Problems*. Society for Industrial and Applied Mathematics, 2002 http://dx.doi.org/10.1137/1.9780898719208. – ISBN 0898715148

[93] Carvalho, Alexandre ; Cholewa, Jan ; Dlotko, Tomasz: Abstract parabolic problems in ordered Banach spaces. In: *Colloquium Mathematicum* 90 (2001), 01, S. 1–17. http://dx.doi.org/10.4064/cm90-1-1. – DOI 10.4064/cm90–1–1

[94] Drivaliaris, Dimosthenis ; Yannakakis, Nikos: Generalizations of the Lax-Milgram theorem. In: *Boundary Value Problems* 2007 (2007), S. 1–9

[95] Brenner, Susanne C. ; Scott, L. R.: *Texts in Applied Mathematics*. Bd. 15: *The Mathematical Theory of Finite Element Methods*. Springer Science und Business Media, 2007 http://dx.doi.org/10.1007/978-0-387-75934-0. – ISBN 9780387759333

[96] Evans, Lawrence C.: *Graduate Studies in Mathematics*. Bd. 19: *Partial Differential Equations*. 2. American Mathematical Society, 2010

[97] Shahbazi, Khosro: An explicit expression for the penalty parameter of the interior penalty method. In: *Journal of Computational Physics* 205 (2005), Nr. 2, S. 401–407. http://dx.doi.org/https://doi.org/10.1016/j.jcp.2004.11.017. – DOI https://doi.org/10.1016/j.jcp.2004.11.017. – ISSN 0021–9991

[98] Arnold, Anton ; Lange, Horst ; Zweifel, Paul F.: A discrete-velocity, stationary Wigner equation. In: *Journal of Mathematical Physics* 41 (2000), 11, Nr. 11, 7167-7180. http://dx.doi.org/10.1063/1.1318732. – DOI 10.1063/1.1318732. – ISSN 0022–2488

[99] Lesaint, P. ; Raviart, P. A.: On a Finite Element Method for Solving the Neutron Transport Equation. In: *Publications des séminaires de mathématiques et informatique de Rennes* S4 (1974), Nr. 8, S. 1–40

[100] Khalid, Khuram S. ; Schulz, Lukas ; Schulz, Dirk: Self-Energy Concept for the Numerical Solution of the Liouville-von Neumann Equation. In: *IEEE Transactions on Nanotechnology* 16 (2017), Nr. 6, S. 1053–1061. http://dx.doi.org/10.1109/TNANO.2017.2747622. – DOI 10.1109/TNANO.2017.2747622

[101] Yueh, W.-C. ; Cheng, S. S.: Explicit Eigenvalues and Inverses of Tridiagonal Toeplitz Matrices with Four Perturbed Corners. In: *The ANZIAM Journal* 49 (2008), Nr. 3, S. 361–387. http://dx.doi.org/10.1017/S1446181108000102. – DOI 10.1017/S1446181108000102

[102] Eslahchi, M.R. ; Masjed-Jamei, M. ; Babolian, E.: On numerical improvement of Gauss Lobatto quadrature rules. In: *Applied Mathematics and Computation* 164 (2005), S. 707–717. http://dx.doi.org/10.1016/j.amc.2004.04.113. – DOI 10.1016/j.amc.2004.04.113

[103] LeVeque, R. J.: *Numerical Methods for Conservation Laws*. Basel : Birkhäuser, 1990 (Lectures in Mathematics). http://dx.doi.org/10.1007/978-3-0348-5116-9. http://dx.doi.org/10.1007/978-3-0348-5116-9. – ETH Zürich

[104] Jiang, H. ; Cai, W.: Effect of boundary treatments on quantum transport current in the Greens function and Wigner distribution methods for a nano-scale DG-MOSFET. In: *Journal of Computational Physics* 229 (2010), Nr. 12, S. 4461–4475. http://dx.doi.org/10.1016/j.jcp.2010.02.008. – DOI 10.1016/j.jcp.2010.02.008. – ISSN 0021–9991

[105] Liu, Y. u. a.: Device Physics and Performance Potential of III-V Field-Effect Transistors. Version: 2010. http://dx.doi.org/10.1007/978-1-4419-1547-43. In: *Fundamentals of III-V Semiconductor MOSFETs*. Boston, MA : Springer US, 2010. – DOI 10.1007/978–1–4419–1547–4 3, S. 31–50

[106] Schulz, Lukas ; Schulz, Dirk: Time-Resolved Mode Space based Quantum-Liouville type Equations applied onto DGFETs. In: *2020 International Conference on Simulation of Semiconductor Processes and Devices (SISPAD)*, IEEE, 2020, S. 331–334

[107] Abdi, A. ; Schulz, D.: Application of the tight-binding method onto the Von Neumann equation. In: *Journal of Computational Electronics* 23 (2024), S. 707–717. http://dx.doi.org/10.1007/s10825-024-02173-6. – DOI 10.1007/s10825–024–02173–6

[108] Frensley, William R.: Transient Response of a Tunneling Device Obtainefrom the Wigner Function. In: *Phys. Rev. Lett.* 57 (1986), Dec, 2853–2856. http://dx.doi.org/10.1103/PhysRevLett.57.2853. – DOI 10.1103/PhysRevLett.57.2853

[109] Knoch, Joachim ; Mantl, Siegfried ; Appenzeller, Joerg: Impact of the dimensionality on the performance of tunneling FETs: Bulk versus one-dimensional devices. In: *Solid-State Electronics* 51 (2007), Nr. 4, S. 572–578. http://dx.doi.org/10.1016/j.sse.2007.02.001. – DOI 10.1016/j.sse.2007.02.001

[110] Venkatagirish, Nagavarapu ; Tura, Ahmet ; Jhaveri, Ritesh ; Chang, Hsu-Yu ; Woo, J. C.: Novel Asymmetric Tunneling Devices for Low Power ULSI. In: *ECS Transactions* 22 (2009), Nr. 1, S. 273–278. http://dx.doi.org/10.1149/1.3152984. – DOI 10.1149/1.3152984

[111] Verhulst, Anne S. ; Vandenberghe, William G. ; Maex, Karen ; Groeseneken, Guido: Scaling theory of tunnel field-effect transistors. In: *ECS Transactions* 25 (2009), Nr. 4, S. 455–464. http://dx.doi.org/10.1149/1.3203983. – DOI 10.1149/1.3203983

[112] Hager, Georg ; Wellein, Gerhard: *Introduction to High Performance Computing for Scientists and Engineers*. 1st. USA : CRC Press, Inc., 2010. – ISBN 143981192X

[113] Zou, L.: Understand slope limiter graphically. In: *arXiv preprint arXiv:2101.07610* (2021). https://arxiv.org/abs/2101.07610

[114] Kuzmin, Dmitri: A new perspective on flux and slope limiting in discontinuous Galerkin methods for hyperbolic conservation laws. In: *Computer Methods in Applied Mechanics and Engineering* 373 (2021), 113569. http://dx.doi.org/10.1016/j.cma.2020.113569. – DOI 10.1016/j.cma.2020.113569. – ISSN 0045–7825

[115] Shu, Chi-Wang: Total-Variation-Diminishing Time Discretizations. In: *SIAM Journal on Scientific and Statistical Computing* 9 (1988), Nr. 6, 1073–1084. http://dx.doi.org/10.1137/0909073. – DOI 10.1137/0909073

[116] Datta, Supriyo: *Quantum Transport: Atom to Transistor*. Cambridge University Press, 2005. – ISBN 1107127955, 9781107127951

A. Non-Equilibrium Green's Function

To also capture the time variance of a quantum system, the NEGF method is presented here in necessary brevity. It serves as a reference for comparison with the DG algorithm.

The NEGF formalism is based on Greens functions, which are mathematical tools used to describe the dynamics of quantum systems [12]. Moreover, the NEGF method is particularly well suited for incorporating external influences and, most importantly, scattering mechanisms such as electronphonon interactions [8, 12], which is the most notable advantage of NEGF over the QTBM. For modeling ballistic transport regimes, however, both methods are considered equivalent [58].

The foundation of the NEGF approach is the retarded Greens function, which reflects the impulse response of the quantum system and is defined as:

$$\boldsymbol{G}^R = \{E - \boldsymbol{H} - \boldsymbol{\Sigma}^R\}^{-1}. \tag{A.1}$$

Here, $\boldsymbol{\Sigma}^R$ is the retarded self-energy, which includes the interaction between the device and the contacts. Scattering mechanisms can also be incorporated through this term [116]. Next, the so-called *broadening matrix* and the *in-scattering* self-energy are required. They are defined as:

$$\boldsymbol{\Gamma}_1 = \imath(\boldsymbol{\Sigma}_1 - \boldsymbol{\Sigma}_1^\dagger), \qquad \boldsymbol{\Gamma}_N = \imath(\boldsymbol{\Sigma}_N - \boldsymbol{\Sigma}_N^\dagger), \tag{A.2}$$

and

$$-\imath\boldsymbol{\Sigma}^< = \textstyle\sum_c \boldsymbol{\Gamma}_c f_{2D}(E - \mu_c), \tag{A.3}$$

respectively. The broadening matrix accounts for the modification of discrete energy levels due to the interaction with contacts. From this matrix, the in-scattering self-energy of contact c can be determined.

Finally, with the lesser Greens function

$$-\imath\boldsymbol{G}^< = \boldsymbol{G}^R(-\imath\boldsymbol{\Sigma}^<)\boldsymbol{G}^{R\dagger}, \tag{A.4}$$

the statistical density matrix can be computed as

$$\boldsymbol{\rho} = \int \frac{dE}{2\pi}(-\imath\boldsymbol{G}^<(E)). \tag{A.5}$$

B. Quantum Transmitting Boundary Method

The QTBM is a standard approach for solving the SE with open boundary conditions, first introduced by Lent and Kirkner in [4], and is based on solving the stationary 1D SE using the FD approximation. Assuming a discrete basis $\boldsymbol{\Phi}$ is given, the SE can be written as [116]

$$E\boldsymbol{\Phi} = \boldsymbol{H}\boldsymbol{\Phi} + \boldsymbol{\Sigma}\boldsymbol{\Phi} + \boldsymbol{s}. \tag{B.1}$$

As shown in [116], the basis $\boldsymbol{\Phi}$ can be obtained either from spatial discretization or expansion in local orbital functions. The matrix $\boldsymbol{H}$ captures the quantum system in the form of the Hamiltonian. The formulation of open boundary conditions [116] yields the matrix $\boldsymbol{\Sigma}$ and the source vector $\boldsymbol{s}$. $\boldsymbol{\Sigma}$ is the self-energy of the contacts and describes the interaction between them and the device. The source term $\boldsymbol{s}$ models carrier injection. Using the standard Hamiltonian definition (2.18), the diagonal elements of the matrix from the FD method are given by [58]:

$$H_{i-1} = -\frac{\hbar^2}{m_0 {\Delta_z}^2} \cdot \frac{1}{m_{eff,i} + m_{eff,i-1}}, \tag{B.2}$$

$$H_{i+1} = -\frac{\hbar^2}{m_0 {\Delta_z}^2} \cdot \frac{1}{m_{eff,i} + m_{eff,i+1}}, \tag{B.3}$$

$$H_I = -(H_{i+1} + H_{i-1}) + V_i. \tag{B.4}$$

The electron mass is defined as $m = m_0 \cdot m_{eff}(z)$, with m_0 being the material dependant constant and $m_{eff}(z)$ is the free electron mass dependent on the position z. The matrix elements of $\boldsymbol{\Sigma}$ are defined as [58]:

$$\Sigma_{11} = -\frac{\hbar^2}{2m_0 m_{eff,1} {\Delta_z}^2} \cdot e^{ik_1\Delta z}, \qquad \Sigma_{NN} = -\frac{\hbar^2}{2m_0 m_{eff,N} {\Delta_z}^2} \cdot e^{ik_N\Delta z}, \tag{B.5}$$

describing the injection from the left and outflow to the right, respectively, where N is the number of discretization points in the transport direction z. The corresponding source terms are given as [58]:

$$s_1 = \frac{\imath\hbar^2}{m_0 m_{eff,1} {\Delta_z}^2} \sin(k_1\Delta z), \qquad s_N = \frac{\imath\hbar^2}{m_0 m_{eff,N} {\Delta_z}^2} \sin(k_N\Delta z). \tag{B.6}$$

As before, s_1 and s_N represent the injection from the left and right, respectively. In order to compute the statistical density matrix $\boldsymbol{\rho}$, a linear system must be solved for each relevant energy E and for each injection from the respective contacts [58]. From the scattering states $\Phi_c(E)$, the density matrix can then be obtained as [58]:

$$\boldsymbol{\rho} = \sum\nolimits_c \int \frac{dE}{2\pi} \left| \frac{dE(k_c)}{dk_c} \right|^{-1} \Phi_c(E) f_{2D}(E - \mu_c) \Phi_c^\dagger(E). \tag{B.7}$$

Although the QTBM provides accurate results for stationary simulations, it is unsuitable for time-dependent (transient) regimes [4]. Therefore, it is primarily used in this work to benchmark the accuracy of the DG method in steady-state simulations. For time-domain comparisons, a different approach must be used namely, the NEGF formalism discussed in Section A.

C. Nomenclature

CAP	Complex Absorbing Potential
CFD	Computational Fluid Dynamics
DG	Discontinuous Galerkin
DGDG	Discontinuous Galerkin-Discontinuous Galerkin
DGFEM	Discontinuous Galerkin-Finite Element method
DGFV	Discontinuous Galerkin-Finite Volume
DGFET	Dual-Gate Field Effect Transistor
FD	Finite Difference
FEM	Finite Element method
FET	Field Effect Transistor
FP	Functional Programming
FV	Finite Volume
HPC	High-Performance Computing
IV	Current-Voltage
LVNE	Liouville-von Neumann equation
MEF	Multiband Envelope Function
MSA	Mode Space Approximation
MSD	Multi-Stage Discretization
NDR	Negative Differential Resistance
NEGF	Non-Equilibrium Green's Function
PDE	Partial Differential Equation
PI	Problem Independent
PML	Perfectly Matched Layer
QLE	Quantum-Liouville Equation
QTBM	Quantum Transmitting Boundary Method
RK2	Runge-Kutta 2nd order
RK4	Runge-Kutta 4th order
RITD	Resonant Interband Tunneling Diode
RTD	Resonant Tunneling Diode
SE	Schrödinger equation
SL	Slope Limiter
SS	Single Script
TFET	Tunnel Field Effect Transistor
TVD	Total Variation Diminishing
TVDM	Total Variation Diminishing Methods
UDS	Upwinding Difference Scheme
WTE	Wigner transport equation

D. List of Symbols

α Coordinate index; scaling factor in the numerical flux ($0 \leq \alpha \leq 1$); multi-index in weak derivatives D^{α}

β CAP (Complex Absorbing Potential) coefficient; coefficient in the eigenvalue decomposition

χ Centre-of-mass coordinate (transport coordinate after coordinate transformation)

δ Effective width / absorption region of the CAP; Kronecker delta $\delta_{n,m}$

ϵ Arbitrary constant ($0 < \epsilon < 1$) in the arithmetic-geometric inequality

η Damping coefficient

γ Eigenvalue of the DG system matrix (stability analysis); constant for internal penalty method ($\gamma = 0$ or $\gamma = 1$)

κ Local stabilisation factor in the DG method ($\kappa = \tilde{\kappa}^k / h$)

λ Energy band index ($\lambda = c$ for conduction band, $\lambda = v$ for valence band); eigenvalue of the discretisation matrix

μ Chemical potential / Fermi level; scalar regulating the jump contribution in the numerical flux

ϕ Electrostatic potential; wave function in the reservoir; test function in the weak formulation

π Circular constant, $\pi \approx 3.14159$

ψ Wave function / single-particle state

ρ Statistical density matrix / density operator; charge carrier distribution

σ Cross-section / standard deviation

τ Runtime / simulation time; triangulation of the computational domain

φ Test function in the weak formulation; function in Sobolev space

ϱ Space charge density in the Poisson equation

ξ Relative coordinate (rotated coordinate after coordinate transformation)

ζ Integration coordinate in Weyl quantization (Fourier transform coordinate in momentum space)

Δ Difference / discretisation step size ($\Delta\chi$, $\Delta\xi$, Δz)

Γ Boundary of the computational domain; broadening matrix in the NEGF formalism (Γ_1, Γ_N)

Ω Computational domain (Ω_{χ}, Ω_{ξ}, Ω_{Γ})

Φ Transformation matrix (eigenvector matrix); Bloch function; basis function

Ψ Quantum state vector / wave function (many-particle state)

Σ Self-energy matrix in the NEGF / QTBM formalism (Σ^R, $\Sigma^<$, Σ_1, Σ_N)

Δ_z Grid spacing in the QTBM transport direction z

∞ Infinity

$\int$ Integral

∇ Nabla operator (gradient, divergence)

$\oint$ Contour integral (line integral)

∂ Partial derivative

$\sum$ Summation

$\hbar$ Reduced Planck constant, $\hbar = h/(2\pi) \approx 1.055 \times 10^{-34}\,\mathrm{J\,s}$

$\imath$ Imaginary unit, $\imath^2 = -1$

$\lfloor s \rfloor$ Floor function (integer part)

$\forall$ For all (universal quantifier)

$\in$ Element of

$\propto$ Proportional to

$\subset$ Subset of

$\{u\}$ Average at element boundaries

$\mathcal{C}(\xi)$ Complex Absorbing Potential (CAP)

$\mathcal{E}$ Permittivity $\mathcal{E} = \mathcal{E}_0\mathcal{E}_r$; also used as electric field (context-dependent)

$\mathcal{E}_0$ Vacuum permittivity ($\mathcal{E}_0 \approx 8.854 \times 10^{-12}\,\mathrm{F/m}$); note: written ϵ_0 in some equations – same quantity

$\mathcal{E}_{L^2}$ Relative error in the L^2-norm

$\mathcal{E}_{L^\infty}$ Relative error in the L^∞-norm

$\mathcal{E}_r$ Relative permittivity

$\mathcal{H}$ Hamiltonian operator (in Hilbert space)

$\mathcal{H}_{cc}$ Hamiltonian operator for the conduction band

$\mathcal{H}_{vv}$ Hamiltonian operator for the valence band

$\mathcal{I}$ Imaginary-part operator $\Im\{\cdot\}$; stabilisation term; identity matrix (context-dependent)

$\mathcal{K}$ Crystal momentum operator ($\mathcal{K} = \mathcal{P}/\hbar$)

$\mathcal{L}$ Liouville operator (in the LVNE); lift operator in the DG coercivity analysis (context-dependent)

$\mathcal{P}$ Momentum operator

$\mathcal{P}_N$ Polynomial space of degree N

$\mathcal{R}$ Real-part operator $\Re\{\cdot\}$; residual; Real part of the drift operator

$\mathcal{W}(\chi, \xi, t)$ Imaginary part of the drift operator

$\mathcal{X}$ Position operator in the Weyl quantisation formalism

$\mathbb{C}$ Field of complex numbers

$\mathbb{N}_0$ Natural numbers including zero

$\mathbb{R}$ Field of real numbers

$\hat{\boldsymbol{G}}$ Transformed drift-reaction matrix in the DG formulation; $\hat{\boldsymbol{G}} = \boldsymbol{\Phi}^\dagger \boldsymbol{B} \boldsymbol{\Phi}$

$\hat{\rho}$ Density operator (quantum-mechanical operator)

$\hat{H}$ Hamiltonian operator

$\hat{n}$ Unit normal vector at element boundaries

$\boldsymbol{\Lambda}$ Diagonal matrix of eigenvalues

$\boldsymbol{\Phi}$ Eigenvector matrix / transformation matrix

$\boldsymbol{\Sigma}^R$ Retarded self-energy; In-scattering self-energy

$\boldsymbol{\rho}$ Density matrix vector (in the semi-discrete system)

$\boldsymbol{A}$ Diffusion matrix / discretisation matrix

$\boldsymbol{B}$ Drift matrix (potential-related)

$\boldsymbol{G}^R$ Retarded Green's function (NEGF); Lesser Green's function (NEGF)

$\boldsymbol{H}$ Hamiltonian matrix

$\boldsymbol{I}_p$ Identity vector

$\boldsymbol{K}$ Global system matrix of the DG method

$\boldsymbol{M}$ Mass matrix; $\boldsymbol{M}^k_{i,j}(\sigma) = \int_{D^k} l^k_i(\sigma)\, l^k_j(\sigma)\, d\sigma$

$\boldsymbol{R}$ Lattice vector

$\boldsymbol{S}$ Stiffness (derivative) matrix of the DG method; $\boldsymbol{S}^k_{i,j}(\sigma) = \int_{D^k} l^k_i(\sigma)\, \partial_\sigma l^k_j(\sigma)\, d\sigma$

$\boldsymbol{c}$ Vector of expansion coefficients

$\boldsymbol{k}$ Wave vector / crystal momentum; Lateral component of the wave vector (parallel to interfaces); Longitudinal / transport component of the wave vector

$\boldsymbol{p}$ Momentum / momentum element

$\boldsymbol{r}$ Position vector

$\boldsymbol{y}$ Integration coordinate in Weyl quantisation (Fourier conjugate of crystal momentum in position space)

E. List of Figures

F. List of Tables